ROYAL HOLLOWAY UNIVERSITY OF LONDON

Influence of tectonic setting and extension velocity on the basement architecture of rifted continental margins

Maria Elena Ros Bernabeu

Supervised by
Prof. Marta Pérez-Gussinyé
Prof. Jason Phipps Morgan

A thesis submitted in fulfilment of the requirements for the degree of Doctor of Philosophy

Department of Earth Sciences

Egham, April 2018

Declaration of Authorship

I, Maria Elena Ros Bernabeu, hereby declare that this thesis and the work presented in it is entirely my own. Where I have consulted the work of others, this is always clearly stated.

Signed:

_____

Date: April 13, 2018

_____

Abstract

Magma-poor rifted margins portray a wide range of tectonic styles. These differences arise from the variability in key factors controlling continental rifting, such as the initial lithospheric strength and extension velocity. The aim of this work is to use thermomechanical numerical experiments to shed light on the processes controlling the modes of continental extension and their impact on margin tectonic architecture and nature of the continent-ocean transition (COT).

Firstly, I further developed a 2D thermodynamic model by including melt productivity, melt emplacement below the extending continental crust, heat release by the emplaced melt and serpentinization. Additionally, I carried out a series of sensitivity tests of the main parameters controlling the evolution of the model in order to establish appropriate conditions for the pre-rift lithospheric structure and for the involved mechanisms.

Secondly, I systematically varied the lower crustal strength and extension velocity to analyze the modes of extension, distribution of surface heat flow and crustal and lithospheric depth dependent thinning (DDT). I showed how different types of lower crustal flow localize upper crustal faulting either in single or multiple faults. This type of flow is linked to the formation of a low viscosity channel within the deep crust, whose extent and thickness varies with the mode of extension (i.e. narrow, sequential faulting, wide and core complex). The distribution of crustal DDT in our models was compared to natural rifted margins, and inferred that the lower crustal flow generally occurs at a fault-block scale, which induces small-scale crustal DDT, except for the core complex extensional mode.

Finally, I showed the importance of the lower crustal strength in controlling also the amount and onset of melting and serpentinization during rifting. I proposed that the relative timing between both events controls the nature of the COT. Subsequently, I presented a genetic link between margin tectonic style and nature of the COT that strongly depends on the lower crustal strength. Based on this conceptual template, I predicted different natures for the COTs in the South Atlantic central segment.

To Jesús.

This dissertation is dedicated to my husband and pillar of my life.
He has been an endless source of support, love and pancakes
during these years and has helped me in finding a better work-life balance.
You are the best person I know and
I am very grateful to God for having you in my life.

Contents

CHAPTER

1

Introduction

1.1 Continental rifts

Continental rifts are regions of extensional deformation that results in lithospheric thinning and eventually rupture, leading to the formation of two conjugate rifted margins and a mid-ocean ridge. The continental lithosphere may deform under the influence of two different mechanisms, based on the origin of the extensional forces. **Passive rifting** refers to the mechanism by which far-field stresses at the boundaries of the lithosphere, or within, create the extensional field that thins the lithosphere, which induces a 'passive' upwelling of the mantle and decompressional melting. **Active rifting** refers to an 'active' upwelling of the mantle in the form of a plume that heats and weakens the base of the lithosphere producing crustal doming and abundant melts. Thus, in a passive mode melts are syn- or post-rift while in an active mode melts are pre-rift (Sengör and Burke, 1978).

Continental margins can be also active or passive depending whether these are tectonically active or inactive, respectively. **Active continental margins** are located near or adjacent to a plate boundary, most commonly a subduction zone, and are characterized by volcanic activity, earthquakes and mountain building. In contrast, **passive continental margins** are located far from plate boundaries, typically surrounding a mid-ocean ridge.

Passive rifted margins have been typically classified as **volcanic** and **non-volcanic** depending on the volume of magmatism (Mutter et al., 1988). However, since non-volcanic margins also exhibit some degree of magmatism, Sawyer et al. (2007) proposed to rename these two end-members as **magma-rich** and **magma-poor** margins. This dichotomy would represent more reliably the extremes of the passive margins spectrum. The classification scheme relies on whether magmatism is more or less than expected from passive continental rifting of normal temperature mantle (i.e. undepleted mantle with a potential temperature of 1300°C according to Reston

(2009a)). The timing of magmatism and continental break-up will also influence on the outcome. The characterization of either end-member does not imply the type of rifting undergone (i.e. passive versus active) (Hopper et al., 1992; Wijk et al., 2001). Figure 1.1 shows the worldwide distribution of magma-poor and magma-rich margins. This map includes a separate type of margins, the **transform margins** (e.g., Edwards et al., 1997), which form during continental break-up and exhibit scarce magmatism accompanying abrupt crustal thinning (Reston, 2009a).

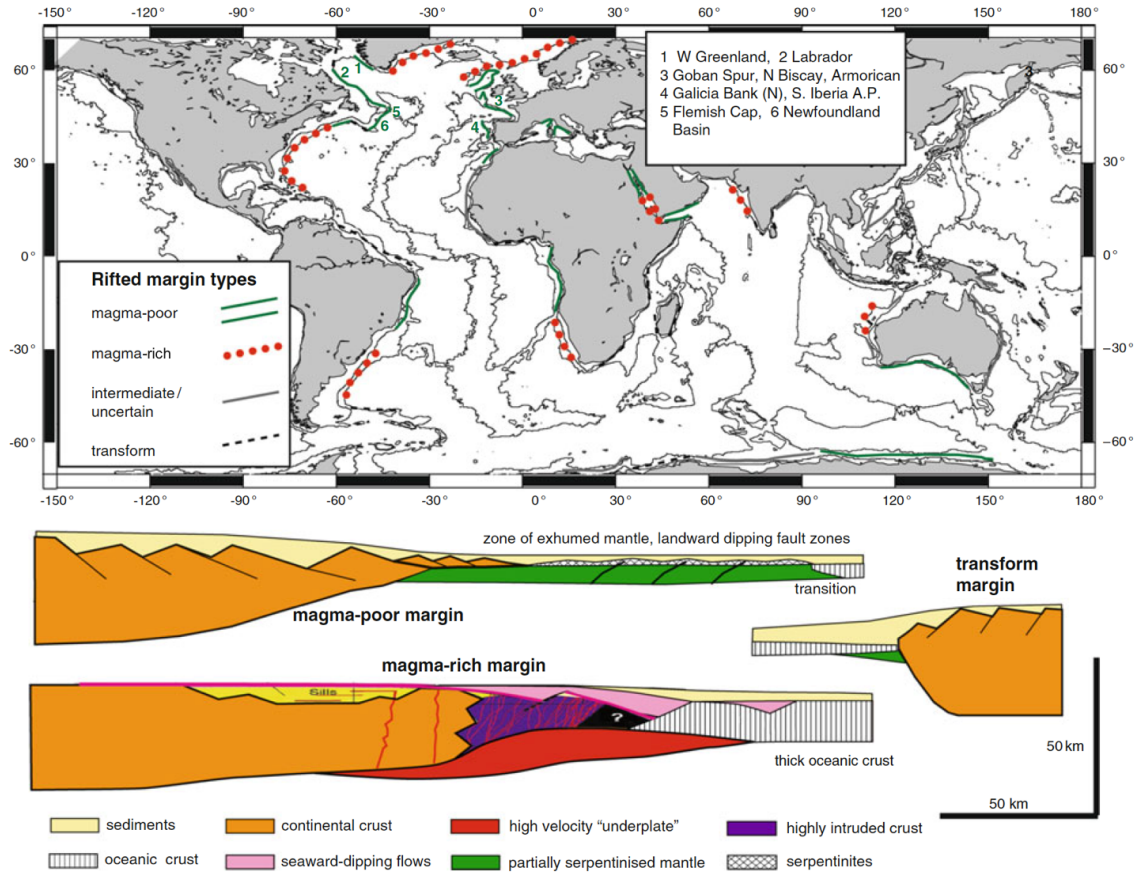

Figure 1.1: Top panel: Worldwide map of rifted margin types. Bottom panel: Cartoon of the archetype margin sections for magma-poor, magma-rich and transform types. Numbers indicate locations of typical examples of magma-poor margins. From Reston and Manatschal (2011).

Magma-rich margins involve voluminous extrusive magmatism during the syn-rift, manifested as seaward dipping reflectors and intrusions within the lower crust (i.e. underplating)(Fig. 1.1). The excessive magmatism in these margins results in the emplacement of igneous material with a thickness over 10 km (Kelemen and Holbrook, 1995; Reston and Manatschal, 2011). This estimation is higher than the expected thickness produced in passive normal mantle upwelling, which typically leads to 6-7 km, i.e. the thickness of normal oceanic crust (e.g., Bown and White, 1995). It may be explained by fast extension of the lithosphere with a potential temperature for

the mantle above 1300°C. This increase in mantle temperature may be caused by the presence of a thermal anomaly, that could be related or not to the activity of a plume. Alternative causes include enhanced melt source fertility of the mantle (Korenaga, 2004; Korenaga and Kelemen, 2000) or small-scale mantle convection (Boutilier and Keen, 1999; Mutter et al., 1988).

Alternatively, **magma-poor margins** are typically characterized by limited syn-rift magmatism, wide domains of extremely thinned crust and the exhumation of partially serpentinized mantle prior to oceanic crust (Fig. 1.1). The scarcity of magmatism may be related to a depleted mantle (Müntener and Manatschal, 2006; Pérez-Gussinyé et al., 2006), cold mantle temperatures (Reston and Morgan, 2004), very slow extension velocities (Minshull et al., 2001; Pérez-Gussinyé et al., 2006) or depth-dependent distribution of lithospheric strain whereby the lithosphere locally thins less than the crust (Huismans and Beaumont, 2008).

1.2 Magma-poor passive margins

Further knowledge of magma-poor passive margins is fundamental for academic and economic purposes. The oil industry explores these margins searching for mature source rocks that form hydrocarbon systems. For a successful exploration in deep water margins (500-2500 m below sea level), a quantitative understanding of the tectonic and thermal history is required to identify prolific margins (White et al., 2003). More importantly, these margins are of scientific interest because they result from the extension and rupture of continental lithosphere, the initial stage of the Wilson Cycle (Wilson et al., 1966) where continents repeatedly dismember and reassemble forming oceanic lithosphere that subducts and recycles.

Around 30% of the passive margins are magma-poor (Fig. 1.1, McDermott, 2013). Estimations of half-extension velocities at magma-poor margins are in the range of the ultra-slow spreading domain for mid-ocean ridges, i.e. $<=$ 10 mm/yr (Dick et al., 2003; Heine et al., 2013; Pérez-Gussinyé, 2013). Examples of magma-poor margins comprise the Labrador-West Greenland conjugates (Chian et al., 1995), Flemish Cap–Galicia conjugates (Funck et al., 2003; Zelt et al., 2003), Newfoundland Basin-Southern Iberia Abyssal Plain conjugates (Dean et al., 2000; Van Avendonk et al., 2006), Nova Scotia–Morocco conjugates (Contrucci et al., 2004a; Funck et al., 2004), Angolan margin (Contrucci et al., 2004b) and Exmouth Plateau (Kusznir and Park, 1987). Figure 1.2 shows the sections of these magma-poor margins after combining multi-channel seismic (MCS) and wide-angle data to fit well the crustal velocities (Reston, 2009b). These margins exhibit diverse conjugate asymmetry, width, crustal thinning and type of continent-ocean transition. For example, the Galicia Bank margin shows a wide domain of crustal thinning followed by a zone of highly attenuated crust underlain by serpentinized mantle and a narrow

zone of exhumed mantle before the oceanic crust. In contrast, the Iberian Abyssal Plain shows a narrow domain of crustal thinning and a broad transition of exhumed mantle to oceanic crust.

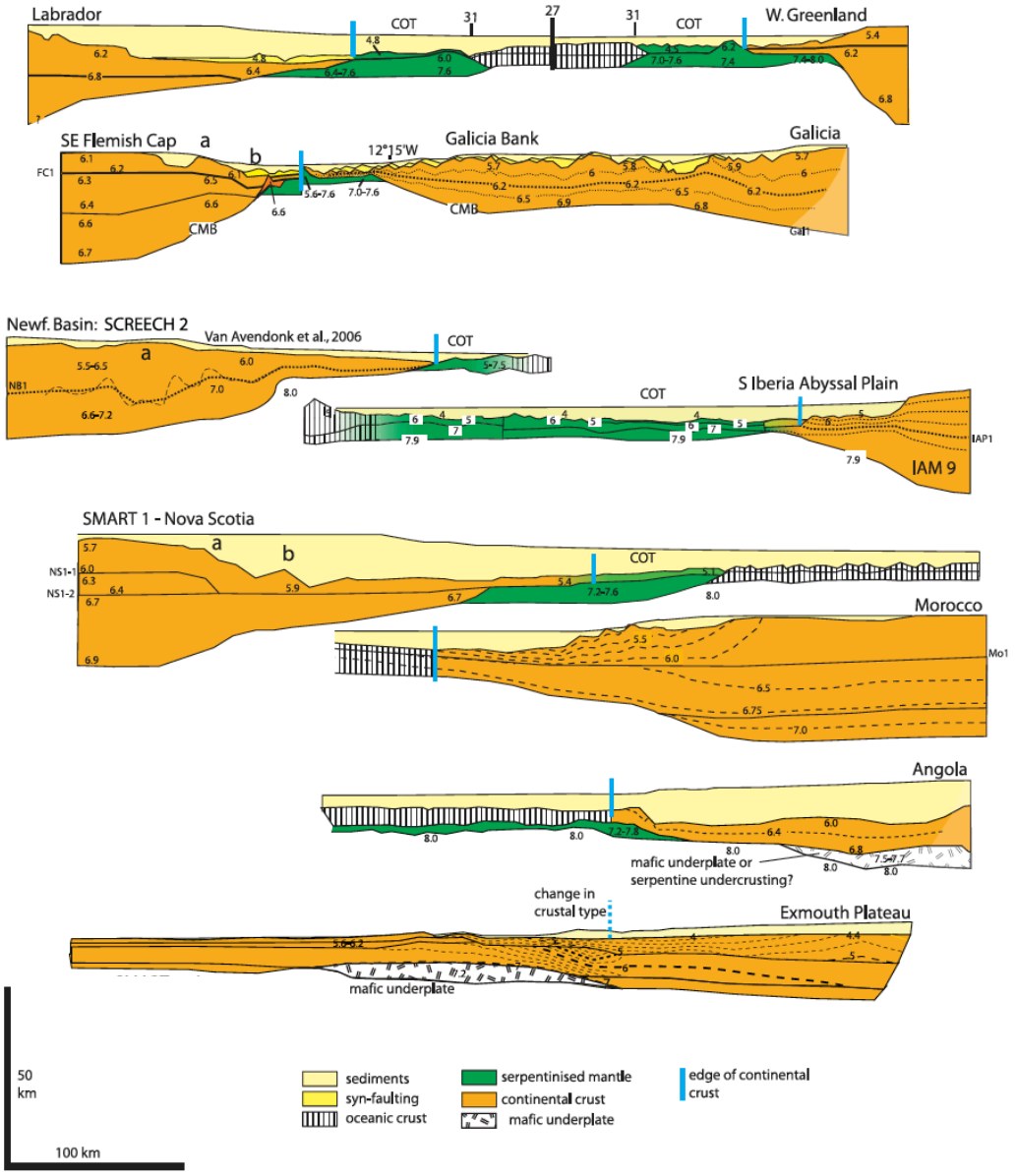

Figure 1.2: Magma-poor margin profiles. CMB, crust–mantle boundary and COT, continent–ocean transition. After Reston (2009b).

Different models of magma-poor rifting have been proposed in the past years to explain the observed margin features. The classical conceptual models of pure-shear (McKenzie, 1978) and simple-shear (Lister et al., 1986; Wernicke, 1981, 1985) fail to approach the observed architectural variability, while the pure-shear model predicts only symmetric margins, the simple-shear type models propose the development of a crust- or lithosphere-scale fault that allows for an asymmetric

configuration (see also Introduction to Chapter 4). More recent models have been based on the very well studied asymmetric margins of Newfoundland-Iberia and the Alpine Tethyan system (Lavier and Manatschal, 2006; Manatschal, 2004; Péron-Pinvidic and Manatschal, 2009; Whitmarsh et al., 2001) and extrapolated to other margins such as the Espirito Santo-Angola, Campos-Angola, Santos and offshore Eastern India (e.g., Nemčok et al., 2013; Peron-Pinvidic et al., 2013; Unternehr et al., 2010; Zalán et al., 2011). It has been proposed that all magma-poor margins can be described by five extensional phases: stretching, thinning-coupling, hyperextension, exhumation, and finally magmatic oceanization, which describe particular tectonic, subsidence, heat flow and magmatic histories. The idea is that identification of the areas of margins affected by these phases can help us unravel their extensional histories by analogy with the archetypal magma-poor margins (Péron-Pinvidic et al., 2017). Mohn et al. (2012) describes the common features between these archetypal conjugates and worldwide magma-poor margins assuming that any difference may be related to inheritance and particular rift histories. This indicates that the idealized magma-poor margin (Fig.1.3) is characterized by first-order architectural elements, such as the presence of high-angle listric faults and limited crustal thinning in the proximal domain, an abrupt crustal thinning over a relatively narrow area (about 50 km wide) in the necking domain, an hyper-extended crust (thickness $<$ 10 km) in the distal domain and a zone of exhumed mantle in the transition to oceanic crust (i.e. continent-ocean transition, COT).

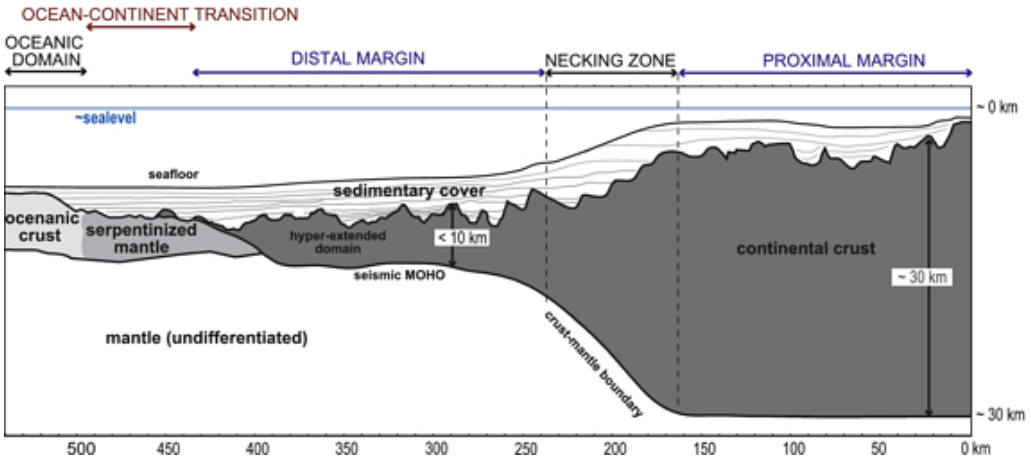

Figure 1.3: Archetype magma-poor rifted margin based on West Iberia margin. From Mohn et al. (2012).

However, a wider range of margins classified as magma-poor show significant differences to these structural features. For instance, the symmetric conjugate margins of the Great Australian Bight (southern Australia) and central Wilkes Land (East Antarctica), which lack of a zone of exhumed mantle (Direen et al., 2011). Geodynamical modelling also showed that not all magma-

poor margins undergo the phases of the rifting model proposed by Lavier and Manatschal (2006) (Svartman Dias et al., 2015a). Therefore this highlights the need for models based on the inner processes and key parameters controlling continental rifting.

It is well known that the overall extensional style, tectonic architecture and subsidence history of margins are importantly controlled by the strength of the lower crust (Bassi, 1995; Brune et al., 2017b; Buck, 1991; Hopper and Buck, 1996; Huismans and Beaumont, 2014; Sharples et al., 2015; Svartman Dias et al., 2015a; Tetreault and Buiter, 2017; Wijns et al., 2005). Distinct modes of continental extension have been defined according to lower crustal strength and the locus of deformation: the narrow, wide, core complex (Buck, 1991) and sequential faulting modes (Brune et al., 2014, 2017b; Ranero and Pérez-Gussinyé, 2010) (see Introduction to Chapter 4). The efficiency of the lower crust to flow is also an important control on the mechanism of crustal depth-dependency during continental extension (e.g., Brun and Beslier, 1996; Driscoll and Karner, 1998, see also Introduction to Chapter 4). Therefore, this thesis aims to investigate the variability in the architecture of magma-poor margins that results from different strengths of the lower crust and its relation to the extensional modes history and rheological behavior of the lower crust. This work is conceived as a conceptual study where observational data from the central South Atlantic margins are used to constrain the initial and boundary conditions of the numerical models (e.g., initial crustal thickness, extension velocity and rheological properties).

1.3 Continent-ocean transition

A key piece to understand the processes that control final stages of continental extension is the nature of the COT, defined as the transition between the oceanward end of the thinned continental crust and the first occurrence of magmatic oceanic crust. The relative lack of sediments above the COT of the Newfoundland-West Iberia magma-poor margins has encouraged many geophysical expeditions to focus on the study of its nature (Chian et al., 1999; Pickup et al., 1996; Russell and Whitmarsh, 2003; Tucholke et al., 1989). The drilled serpentinized mantle exhumed along the COT of these archetype margins has served many studies to conclude that other magma-poor margins with similar architectonical characteristics present also an exhumed serpentinized mantle at the COT (Fig. 1.4a), as commented above. This has cast doubt about the viability of the classic model of continental break-up followed by magmatic oceanic spreading for magma-poor margins (Fig. 1.4b). However, many wide-angle and multichannel seismic data show no evidence of an exhumed serpentinized mantle along margins such as the Tyrrenian basin (Prada et al., 2014), the northwestern South China Sea (Cameselle et al., 2017) and the Moroccan margin (Fig. 1.2

Contrucci et al., 2004a). In contrast, these margins show more abrupt magmatic transition to oceanic crust, following the classical model from rifting to sea-floor spreading (Fig. 1.4b).

Hence, controversy exists regarding the nature of the COT on magma-poor margins. For example, the Exmouth Plateau, northwest Australia, with either interpretations of serpentinized exhumed mantle (Tischer, 2006) or thinned continental crust with underplating (Fig. 1.2, Reston, 2009b), and also the easternmost part of the Santos basin that Zalán et al. (2011) interprets as exhumed serpentinized mantle by analogy with the Iberian Margin while Klingelhoefer et al. (2014) and Evain et al. (2015) interpret is as proto-oceanic crust, i.e. composed of magmatic products not yet forming typical oceanic crust. The characterization of the COT nature results then from the relative contribution of the processes of serpentinization and decompressional melting during continental rifting (see Introduction Chapter 5). This thesis also explores the integration of these processes in the study of magma-poor continental extension.

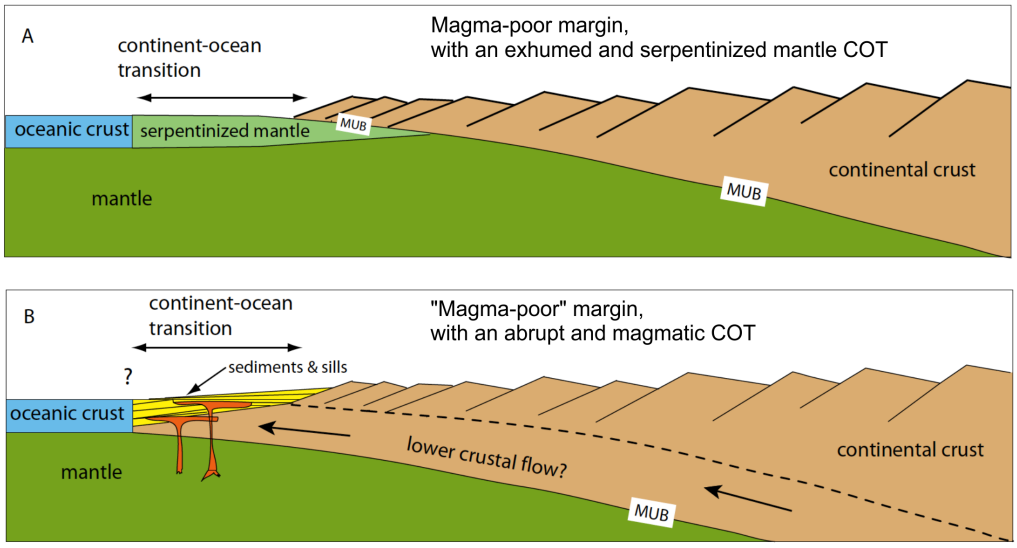

Figure 1.4: a) Cartoon of a magma-poor end-member with COT of exhumed and serpentinized mantle (e.g., Iberia-Newfoundland). b) Cartoon of a magma-poor non-end-member with an abrupt and magmatic COT (e.g., northern Gulf of California). MUB is mafic-ultramafic boundary. Modified from Sawyer et al. (2007).

1.3.1 Decompressional melting

During continental rifting, the passive upwelling of the mantle generates changes in temperature and pressure that produce partial melt of rocks (McKenzie, 1984). The amount of melt generated depends on factors such as the potential temperature of the asthenospheric mantle, the initial thickness of the lithosphere or the duration of extension (White et al., 1995). Although the

migration, retention and extraction of melt is very poorly constraint in rifting scenarios, results from mid-ocean ridges can be extrapolated to the continental rifting (Nielsen and Hopper, 2004). In a mid-ocean ridge basalt (MORB) the preservation of isotopic disequilibria indicates a fast vertical migration of melt (for a review on melt migration processes see Kelemen et al. (1997)), on the order of meters per year (e.g., Faul, 2001).

There is evidence of solidified mantle melts intruding and underplating the crust (e.g., Mackenzie et al., 2005; Thybo and Artemieva, 2013). Most igneous bodies found in continental crust are dikes and sills (Mathieu et al., 2008; Menand, 2011). Dikes are vertical sheet-shaped intrusions cross-cutting the crust and sills are horizontal-sheet crustal intrusions. Both igneous bodies have lengths of meters up to kilometers and thickness of meters. The crystallization of melts underplating the crust or forming oceanic crust implies the release of latent heat, which is partly removed by conduction and hydrothermal circulation (Maclennan et al., 2005).

An average crustal thickness of 6-7 km is observed over most of the spreading rate range (Cannat et al., 2009; White et al., 2001). Although early studies of MORBs established a strong dependence of the oceanic crustal thickness with the spreading rate (Goslin et al., 1972; Reid and Jackson, 1981), Dick et al. (2003) recently showed how the crustal thickness has a strong dependency for velocities below 20 mm/yr full-extension (ultra-slow spreading ridges) while it diminishes for faster spreading ridges (Fig. 1.5).

1.3.2 Serpentinization

Serpentinization is the process that transforms dry mantle peridotite into wet serpentinite. As the mantle is serpentinized, it experiences an increase in volume of approximately 40% and a decrease in density, which may result in abnormal subsidence of the forming basin. Throughout the exothermic reaction that generates serpentinites, the strength of the rock is reduced and new patterns of heat flow emerge, which could affect the distribution of strain during continental rifting (Rüpke et al., 2013). In nature, the serpentinization reaction is complex, but can be simplified to

$$Olivine + water = serpentine + brucite \tag{1.1}$$

In natural systems, the process of rocks serpentinization process lasts $10^4 - 10^6$ years (Iyer et al., 2012; Skelton et al., 2005). The olivine reacts with significant amounts of seawater under appropriate temperature conditions (Emmanuel and Berkowitz, 2006; Pérez-Gussinyé and Reston, 2001).

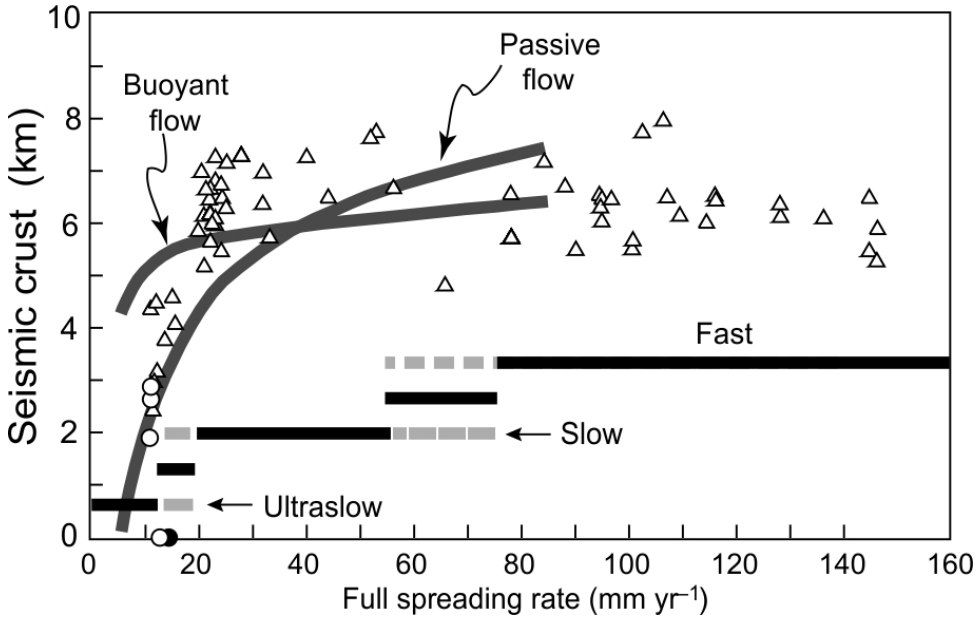

Figure 1.5: Seismic crustal thickness versus spreading rate is represented by white triangles, (White et al., 2001). White circles are Gakkel ridge values black filled circle is for SWIR 98–168 E oblique supersegment. Zero values are based on dredging. Crustal thickness curves calculated for passive flow and buoyant flow models. A revised ridge classification scheme is shown by the heavy black straight lines giving the spreading-rate ranges for ultraslow-, slow-, fast- and the two transitional classes. Broken lines indicate the typical overlap of tectonic styles for each of the three principal classes of ocean ridge that give rise to the two transitional ridge classes. From Dick et al. (2003).

During continental extension, crustal thinning brings crustal rocks to shallower and cooler depths (e.g., Müntener et al., 2000). The initial ductile crustal layers become progressively more brittle and, eventually, the total embrittlement of the crust allows the formation of crustal-scale faults. Then, seawater can flow through the active crustal faults and serpentinize the mantle (Bayrakci et al., 2016; Pérez-Gussinyé and Reston, 2001). According to Pérez-Gussinyé and Reston (2001), total crustal embrittlement depends on the extension rate. For fast extension, the high temperatures and strain rates promote ductile deformation and delays the crustal embrittlement. However, for slow extension, the low temperatures and strain rates promote brittle deformation.

1.4 Motivation

The extensional processes of continental lithosphere have been a hot topic in the geoscientific community since Wilson et al. (1966) first described the opening and closing of the oceans, i.e. the Wilson Cycle, and particularly since the modern theory of Plate Tectonics was developed (Le Pichon, 1968; McKenzie and Parker, 1967; Morgan, 1968). Many field studies, geophysical surveys, petrological analysis, analogue and numerical modelling have been carried out in

order to gain insight into the processes that control the tectonic evolution of continental rifting and the style of rifted margins. The great versatility of numerical modelling as a tool to do theoretical experiments of continental rifting has led it to a recent proliferation. In particular, dynamic approaches of numerical models for continental rifting use the constitutive equations of lithospheric rocks to address the underlying processes that control the contrasting styles of rifting. This thesis focuses on the development and use of numerical modelling for the study of the feedbacks between dynamic processes that occur under ultra-slow continental extension and magma-poor conditions.

Numerical models are typically used to investigate the influence of extension velocity and initial conditions of the lithospheric structure (i.e. composition, thickness and temperature) on the faulting pattern, geometry, subsidence and heat flow of continental margins. However, there is still a lack of unified comprehension due to the compositional and structural complexity of the continental lithosphere. Here, I investigate continental rifting extended by velocities within the ultra-slow range (<=10 mm/yr half-extension), which reign in the formation of magma-poor margins, to understand the role of the lower crustal strength in the variability of the margins tectonic style (Chapter 4).

Most of the continental rifting numerical models neglect the processes of magmatism and serpentinization, which are important for the characterization of the COT. In order to get a more complete picture of the rifted margins, I also analyze the development of melts and serpentinites during continental extension for different initial lithospheric states, with a particular focus on the influence of the lower crustal strength (Chapter 5). Since the presence of salt, carbonates and volcanism hinders the visibility of structures in the seismic profiles, many worldwide margins that lack of a detailed wide-angle seismic data and drilling at their COTs cannot be accurately interpreted. The margins of the central segment of the South Atlantic present unfavourable conditions for the determination of the COTs nature and extension, such as the lack of magnetic data, due to the quiet magnetic Cretaceous period over which break-up occurred, and the thick Aptian salt layer present above these margins (Aslanian et al., 2009). However, the evolution of these margins is relatively well-constraint because continental rifting evolved during a single episode, in contrast to the North Atlantic that underwent two episodes (Aslanian et al., 2009). This makes it possible to relate the type of COT that results from the numerical model to the expected COT along conjugate margins in this study zone.

The ultimate goal of this thesis is to better our understanding on the deformation style and production of magmatism and serpentinization during continental lithospheric extension. Moreover, based on the numerical modelling results, this dissertation aims to develop a conceptual model linking the COT nature and tectonic style of magma-poor margins for the ultra-slow velocity

category. Thus, I focus on addressing the following questions: (i) can we relate tectonic styles of margins with the type of COT?, (ii) how the lower crustal strength influences the onsets and amounts of melts and serpentinites?, (iii) how does the relative timing between melting and serpentinization control the characterization of the COT?, (iv) how the different modes of extension are controlled by the lower crustal strength?, (v) which factors control margin width and conjugate asymmetry?, (vi) what is the influence of the upper and lower crust thickness ratio on the exhumation of lower crust?, (vii) how is the heat flow history affected by the different modes of extension?, (viii) can models of depth dependent thinning be applied to natural cross-sections? and (ix) what is the effect of viscous strain softening on melt productivity?. Questions (i)-(iii) are addressed in Chapter 5, (iv)-(vii) in Chapter 4 and (ix) in Chapter 3.

1.5 Thesis outline

This thesis consists of an introductory chapter (Chapter 1), two chapters explaining the geodynamic numerical modelling (Chapters 2 and 3), two core chapters written in scientific paper format (Chapters 4 and 5) and final chapters for the critical discussion of the results and conclusions (Chapters 6 and 7). Additional information is presented in Appendix A at the end of the thesis manuscript.

Chapter 2 - Numerical model

Chapter 2 describes the general numerical methodology used in this thesis. The first part includes mathematical definitions of basic rheological terms, governing equations, rock rheologies and an overview of the finite element method (FEM) used in the numerical code. The second part focuses on the new contributions to the model, including the algorithms for melting, magmatic crustal thickness, melt emplacement and underplating, heat release of solidified melt and the further development of the serpentinization numerical code.

Chapter 3 - Testing the sensitivity of margin development to input parameters: a general study

Chapter 3 presents the initial rheological and thermal profiles of the numerical models used throughout the thesis and investigates the model sensitivity to mesh resolution, water content in the mantle and different mechanisms of strain softening. The aim of this chapter is to analyze the influence of the default parameters and implemented processes on model evolution.

Chapter 4 - Understanding the variability in tectonic architecture of margins: a numerical modelling study

Chapter 4 is one of the main core chapters, prepared for submission to Tectonics. This study investigates the influence of the lower crustal strength on the modes of deformation during magma-poor continental rifting and the controls on conjugate asymmetry and lower crustal exhumation. I also examine the link between lithospheric depth dependent thinning and heat flow history. And compare crustal depth dependent stretching observed in the numerical models to examples of wide-angle seismic profiles.

Chapter 5 - Lower crustal strength controls on melting and serpentinization at magma-poor margins: potential implications for the South Atlantic

Chapter 5 is one of the main core chapters and an article published in Geochemistry, Geophysics, Geosystems in 2017. Here I integrate the studies of the influence of lower crustal strength on rifted continental margins and continent-ocean transitions for ultra-slow extension velocities. The nature of the continent-ocean transition is characterized by the relative timing between the processes of melting and serpentinization. A conceptual model is proposed and applied to selected central South Atlantic margins for the prediction of the type of continent-ocean transition.

Chapter 6 - General discussion and critical evaluation

Chapter 6 discusses the main results presented in previous chapters, critically evaluates the limitations of the numerical model and presents future lines of work.

Chapter 7 - Conclusions

Chapter 7 provides a summary of the concluding remarks.

Appendix

Appendix A

CHAPTER

2

Numerical model

2.1 The lithosphere as a continuum

Geodynamical models approximate the lithosphere as a continuum and apply the equations that govern its mechanism. Conservation of mass, momentum and energy equations are solved for the crust-mantle system with the Boussinesq approximation. This approximation considers that a variation in density only affects the body force term (i.e. it has gravitational consequences) but does not imply a change in volume. Therefore, the incompressible fluid approximation is assumed to remain valid as buoyancy forces are included.

2.1.1 Stress in rocks

In an incompressible fluid at rest (*hydrostatic state of stress*) all shear stresses are null and all normal stresses are equal to each other

$$\sigma_{ij} = \left\{ \begin{array}{ll} -P & \text{if } i = j \\ 0 & \text{if } i \neq j \end{array} \right\} \tag{2.1}$$

where P is the *hydrostatic pressure* and equal to the vertical pressure due to the weight of the fluid. Similarly, the *lithostatic pressure* is defined as the pressure caused by the weight of the rock overburden $P(z) = P_0 + g \int_0^z \rho(z) dz$, where P_0 is Earth's surface pressure and g is gravity. The case of *lithostatic stress state* assumes that the stress state at depth z has become entirely hydrostatic due to relaxation of all shearing stresses by some creep process so that the the pressure works equally on all sides because of the weight of the overlying rock. However, rocks undergo deformation within the Earth, which deviates their normal stresses from the lithostatic stress state. These deviations are called deviatoric stresses

$$\sigma'_{ij} = \sigma_{ij} + P\delta_{ij} \tag{2.2}$$

where δ_{ij} is the Kronecker delta ($\delta_{ij} = 1$ if $i = j$ and $\delta_{ij} = 0$ if $i \neq j$). The pressure is defined in continuum mechanics as the mean normal stress $P = -\sigma_{kk}/3$ (positive with depth). Deviatoric stresses are the stress components that are not equal in all directions: they push or pull in a particular direction. Shear stresses are completely deviatoric.

2.1.2 Deformation, strain and strain rate in rocks

Rock deformation describes the collective displacements of points in a body, i.e., the complete transformation from the initial to the final geometry, which may include translation, rotation, distortion (strain) and dilatation.

The displacement of any rock point, under the assumption of incompressible fluid, can be expressed as the sum of three components (Fig. 2.1)

$$u_i + du_i = u_i + \varepsilon_{ij}dx_i + w_{ij}dx_i \tag{2.3}$$

where u_i, being common to neighbouring points, is the rigid-body translation, du_i is the difference in displacement, ε_{ij} is the non rigid-body strain and w_{ij} is the rigid-body rotation (Ranalli, 1995). The *non rigid-body strain tensor* is defined as $\varepsilon_{ij} = \frac{1}{2}\left(\frac{\partial u_i}{\partial x_j} + \frac{\partial u_j}{\partial x_i}\right)$, which measures the internal deformation produced by a shape change. The *rigid-body rotation tensor* is defined as $w_{ij} = \frac{1}{2}\left(\frac{\partial u_i}{\partial x_j} - \frac{\partial u_j}{\partial x_i}\right)$ and quantifies the rotation. These two terms form the so-called *displacement gradient tensor*

$$\frac{\partial u_i}{\partial x_j} = \frac{1}{2}\left(\frac{\partial u_i}{\partial x_j} + \frac{\partial u_j}{\partial x_i}\right) + \frac{1}{2}\left(\frac{\partial u_i}{\partial x_j} - \frac{\partial u_j}{\partial x_i}\right) \tag{2.4}$$

Therefore, equation 2.3 can be written as

$$u_i + du_i = u_i + \frac{\partial u_i}{\partial x_j}dx_i \tag{2.5}$$

Hereafter, the terms strain and deformation will be used indistinctly. The *strain tensor* ε_{ij} characterizes the total amount of deformation compared to the initial state and its time derivative $\dot{\varepsilon}_{ij}$, the *strain rate tensor*, describes the dynamics of changes in the internal deformation (Gerya, 2009)

$$\dot{\varepsilon}_{ij} = \frac{1}{2}\left(\frac{\partial v_i}{\partial x_j} + \frac{\partial v_j}{\partial x_i}\right) \tag{2.6}$$

where the velocity v_i is the time derivative of the displacement, $v_i = \frac{Du_i}{Dt}$, and $\frac{\partial v_i}{\partial x_j}$ is the *velocity gradient tensor*. The tensor can be decomposed into two parts, the isotropic, which is an invariant, $\dot{\varepsilon}_{kk}$ and the deviatoric $\dot{\varepsilon}'_{ij}$

$$\dot{\varepsilon}'_{ij} = \dot{\varepsilon}_{ij} - \delta_{ij}\frac{1}{3}\dot{\varepsilon}_{kk} \tag{2.7}$$

where i, j and k are coordinate indices.

Using the incompressibility assumption (Section 2.2.1), all normal strains are zero

$$\dot{\varepsilon}_{kk} = \frac{\partial v_k}{\partial x_k} = div(\vec{v}) = 0 \quad \Rightarrow \quad \dot{\varepsilon}'_{ij} = \dot{\varepsilon}_{ij} \tag{2.8}$$

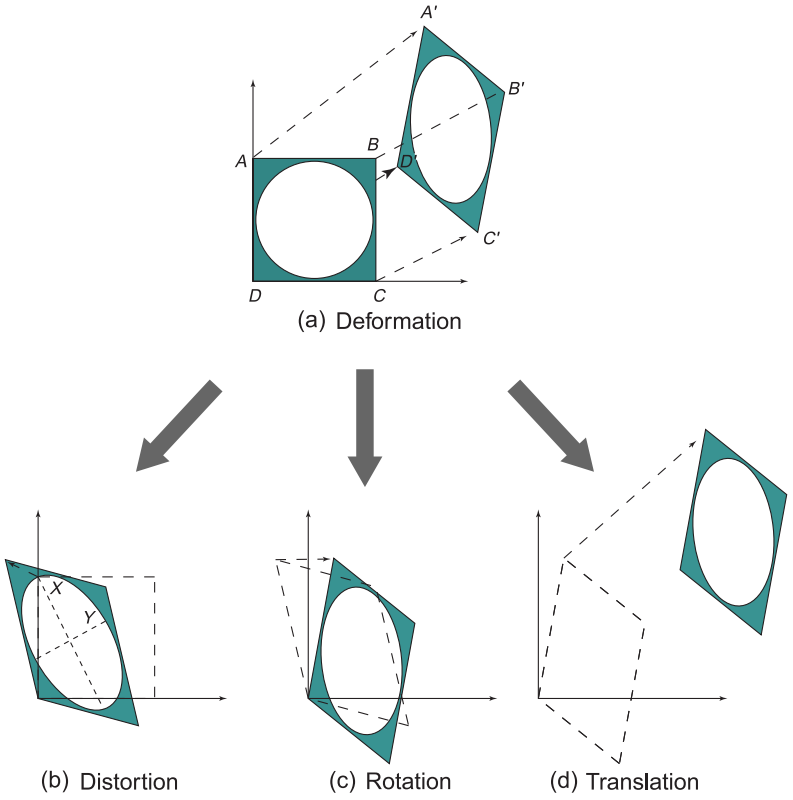

Figure 2.1: A deformed square (a) is categorized into three independent components: (b) distortion, (c) rotation and (d) translation, and shows the corresponding strain ellipse. Four corners of the initial square are labelled with A, B, C and D to represent the displacement of each material point within the square. The principal strain axes are X and Y along with distortion occurs. Adapted from Van der Pluijm and Marshak (2005).

2.1.3 Second invariants

Geodynamic models should be defined independent of their particular coordinate system. Thus, flow laws are formulated in terms of the second deviatoric stress or strain rate invariants. The *second invariant of the deviatoric stress tensor* is defined as $J_2' = \frac{1}{2}{\sigma_{ij}'}^2$ in the mathematical theory of plasticity. However, in geodynamic modelling, it is more common to use the square root of the invariant

$$\sigma_{II} = \sqrt{J_2'} = \sqrt{\frac{1}{2}{\sigma_{ij}'}^2} \tag{2.9}$$

Similarly, the *second invariant of the the deviatoric strain rate tensor* is defined as

$$\dot{\varepsilon}_{II} = \sqrt{\frac{1}{2}\dot{\varepsilon'}_{ij}^2} = \{incompressibility\} = \sqrt{\frac{1}{2}\dot{\varepsilon}_{ij}^2} \tag{2.10}$$

Hereafter, when referring in the text to the second invariants, I will use σ_{II} and $\dot{\varepsilon}_{II}$.

2.2 Governing equations

2.2.1 Conservation of mass

The *equation of continuity* describes the conservation of mass for a moving continuous media, which, in a Lagrangian system of reference has the form

$$\frac{D\rho}{Dt} + \rho\frac{\partial v_i}{\partial x_i} = 0 \tag{2.11}$$

where v_i are velocity components, ρ is local density, x_i are spatial coordinates and $\frac{D\rho}{Dt}$ is the Lagrangian or material time derivative of density.

In numerical modelling, the lithosphere and asthenosphere are commonly approximated as an incompressible fluid (i.e. material density is constant with time), thus the previous equation becomes

$$\frac{\partial v_i}{\partial x_i} = 0 \tag{2.12}$$

2.2.2 Conservation of energy

The Lagrangian *heat conservation equation* relates temperature changes to the heat balance in a continuum according to

$$\rho C_p\frac{DT}{Dt} = -\frac{\partial q_i}{\partial x_i} + H \tag{2.13}$$

where ρ is density ($kg\ m^{-3}$), C_p is heat capacity at constant pressure ($Jkg^{-1}K^{-1}$), $\frac{DT}{Dt}$ is the Lagrangian time derivative of temperature, $\frac{\partial q_i}{\partial x_i}$ is the partial derivative of heat flux (Wm^{-2}) and H is volumetric heat production (Wm^{-3}). The heat flux is defined as $q_i = -k\frac{\partial T}{\partial x_i}$ (Fourier's law of heat conduction), where k is thermal conductivity ($Wm^{-1}K^{-1}$).

2.2.3 Conservation of momentum

Following Newton's second law of motion, the Lagrangian *conservation of momentum* is the balance between the acting forces on the continuous media and the change of momentum

$$\frac{\partial \sigma_{ij}}{\partial x_j} + \rho g_i = \rho \frac{Dv_i}{Dt} \tag{2.14}$$

where σ_{ij} are stresses, i and j denote coordinate indices, x_j spatial coordinates, g_i gravity acceleration, and $\frac{Dv_i}{Dt}$ is the Lagrangian time derivative of velocity.

2.2.4 Stokes equation

On geological time scale, rocks undergo viscous deformation, which is caused by deviatoric stresses related to the velocity gradients. If these stresses are linearly proportional to the strain rate, the fluids are called Newtonian. The viscous constitutive equation that relates the deviatoric stress σ'_{ij} and strain rate $\dot{\varepsilon}'_{ij}$ tensors is

$$\sigma'_{ij} = 2\eta\dot{\varepsilon}'_{ij} + \delta_{ij}\eta_{bulk}\dot{\varepsilon}_{kk} \tag{2.15}$$

where η is the (dynamic shear) viscosity, η_{bulk} is the bulk viscosity, $\dot{\varepsilon}'_{kk}$ is the bulk strain rate and δ_{ij} is the Kronecker delta: $\delta_{ij} = 1$ if $i = j$ and $\delta_{ij} = 0$ if $i \neq j$ (i and j are coordinate indices). Assuming the incompressible fluid approximation (Section 2.2.1), the *Newtonian constitutive equation* (2.15) becomes

$$\sigma'_{ij} = 2\eta\dot{\varepsilon}_{ij} \tag{2.16}$$

which is the *Navier-Poisson relation for Newtonian incompressible fluids*. The viscosity η I use is defined as the ratio between the shear stress σ_s and twice the shear strain rate $\dot{\varepsilon}_s$ for a Newtonian fluid with dimensions of $Pa\ s$

$$\eta = \frac{1}{2}\frac{\sigma_s}{\dot{\varepsilon}_s} \tag{2.17}$$

The viscosity decreases with increasing stress or strain rate. It is worth mention that in geodynamics the following 'geological' shear strain rate definition can also be found

$$\dot{\gamma}_{ij} = \left(\frac{\partial v_i}{\partial x_j} + \frac{\partial v_j}{\partial x_i} \right) = 2\dot{\varepsilon}_{ij} \tag{2.18}$$

which leads to the definition of viscosity as simply $\eta = \frac{\sigma_s}{\dot{\gamma}_s}$ (Ranalli and Murphy, 1987; Stüwe, 2007).

The equation of motion for a Newtonian fluid is the momentum equation (2.14) written in terms of pressure and deviatoric stresses (2.2)

$$\frac{\partial \sigma'_{ij}}{\partial x_j} - \frac{\partial P}{\partial x_i} + \rho g_i = \rho \frac{Dv_i}{Dt} \tag{2.19}$$

where x_i and x_j are spatial coordinates, P is pressure, ρ is density, g_i is gravity and $\frac{Dv_i}{Dt}$ is the Lagrangian time derivative of velocity. This equation is the *Navier-Stokes equation of motion*, which governs the motion of fluids in a gravity field. In the case of slow motion of highly viscous fluids, inertial forces can be neglected ($\rho \frac{Dv_i}{Dt} = 0$) with respect to gravitational forces and viscous resistance. In this case, the equation becomes the *Stokes equation for slow creeping flow*

$$\frac{\partial \sigma'_{ij}}{\partial x_j} - \frac{\partial P}{\partial x_i} + \rho g_i = 0 \tag{2.20}$$

2.3 Rock rheology

Earth's interior undergoes a series of forces that deform its rocks. Rheology is responsible for studying the deformation and flow of Earth materials and establishes constitutive laws that describe this behavior. The major rheological model for the lithosphere combines elasticity, viscous creep and plastic yielding. These three modes of the mechanical behavior of rocks depend on how long an applied load lasts. The mantle behaves elastically at time scales of hundreds of seconds, while it behaves viscously in time scales of hundreds to thousands of years. On very long geological times (>1 Myr), the upper crust and upper mantle behave as thin elastic and plastic plates overlying an inviscid substratum.

2.3.1 Viscous creep

Rocks generally deform as non-Newtonian fluids, so the strain rate is proportional to the nth power of stress as given by the power law

$$\dot{\varepsilon} = A\sigma^n \tag{2.21}$$

where $n > 1$ is the dimensionless material exponent with values usually between 2 and 4 for rocks; A is a material constant, with units of $Pa^{-n}s$, that generally depends on temperature, pressure and material parameters. Two main creep mechanisms dominate the behavior of rocks in the mantle: dislocation and diffusion creep. *Dislocation creep* typically occurs in the upper mantle and deep crustal rocks, where high temperatures and stresses are reached and lead to dislocation glide and climb within the crystal lattice. *Diffusion creep* occurs by motion of vacancies through the crystal lattice. This process generally operates at high temperatures and small stresses by the deformation mechanisms of volume diffusion (favoured at higher temperatures) and grain-boundary diffusion (favoured at lower temperatures). Karato and Wu (1993) suggested that, in the upper mantle, there is a transition from dislocation to diffusion creep with depth. The dislocation and diffusion creep of rocks can be described by the following *power-law creep equation* (Hirth and Kohlstedt, 2003)

$$\dot{\varepsilon} = A\sigma^n d^{-m} f H_2O^r exp\left(\frac{-E + PV}{RT}\right) \tag{2.22}$$

where $\dot{\varepsilon}$ is the strain rate, A is the preexponential factor, σ is the differential stress, d is the grain size, m is the grain-size exponent, fH_2O is the water fugacity, r is the water fugacity exponent, E is the activation energy, P is the (dynamic) pressure, V is the activation volume , R is the universal gas constant and T is the temperature. For geodynamic problems, Hirth and Kohlstedt (2003) proposed the change of the variable water fugacity (MPa) for the water content ($H/10^6Si$) in the power-law equation following the relationship from Hirth and Kohlstedt (1996)

$$C_{OH} = A_{H_2O}\, exp\left(\frac{-E_{H_2O} + PV_{H_2O}}{RT}\right) fH_2O \tag{2.23}$$

where $A_{H_2O} = 26\ H/10^6 Si/MPa$, $E_{H_2O} = 40\ kJ/mol$, $V_{H_2O} = 10\text{x}10^{-6}\ m^3/mol$ and fH_2O is water fugacity in MPa.

In order to use a valid power law equation for any reference system (which is fulfilled in the Newtonian equation), the equation is reformulated as a function of the second invariants (Ranalli, 1995) as $\dot{\varepsilon}_{II} = \widehat{A}\,\sigma_{II}^n$. The power-law creep viscosity can be defined by analogy to the Newtonian viscosity (Eq. 2.17)

$$\eta = \frac{\sigma_{II}}{2\dot{\varepsilon}_{II}} \tag{2.24}$$

where the second invariant of the deviatoric stress (σ_{II}) and strain rate ($\dot{\varepsilon}_{II}$) are related to the differential stress and strain rate depending on the type of rheological experiment used to establish the flow law: in a simple shear laboratory experiment, the sample is deformed by a non-zero shear

stress while in a triaxial compression experiment it is deformed by a differential stress (difference between the maximal and minimal applied stress) (Ranalli, 1995).

Thus, by substituting Eq.2.22 in Eq.2.24 with the corresponding conversion factor F for the second invariants

$$\eta = F A^{\frac{-1}{n}} \dot{\varepsilon}_{II}^{\frac{1-n}{n}} d^m C_{OH}^{-r} exp\left(\frac{E+PV}{nRT}\right) \tag{2.25}$$

where $F = 2^{(1-2n)/n}$ is for simple shear experiments and $F = 2^{(1-n)/n}/3^{(1+n)/2n}$ for triaxial compression experiments (Gerya and Stöckhert, 2006).

Finally, the effective power law creep viscosity is given by

$$\eta_{eff} = \frac{1}{\frac{1}{\eta_{dis}} + \frac{1}{\eta_{diff}}} \tag{2.26}$$

where $_{dis}$ and $_{diff}$ is dislocation and diffusion respectively.

2.3.2 Elasticity

Rocks deform elastically at small stresses and strains. Once the load ceases, deformation is recovered. The elastic constitutive equation that relates the stress σ_{ij} and strain ε_{ij} tensors is

$$\sigma_{ij} = 2\mu\varepsilon_{ij} + \delta_{ij}\lambda\varepsilon_{kk} \tag{2.27}$$

where μ, the shear modulus, and λ are Lamés constants (elastic parameters dependent on temperature, pressure and composition), η_{bulk} is the bulk viscosity, ε_{kk} is the bulk strain and δ_{ij} is the Kronecker delta: $\delta_{ij} = 1$ if $i = j$ and $\delta_{ij} = 0$ if $i \neq j$ (i and j are coordinate indices). Similarly, the deviatoric stress σ'_{ij} are

$$\sigma'_{ij} = 2\mu\varepsilon'_{ij} \tag{2.28}$$

where the deviatoric stress tensor is equation (2.2) $\sigma'_{ij} = \sigma_{ij} + P\delta_{ij}$, pressure is $P = -\frac{\sigma_{kk}}{3} = -(\lambda + \frac{2}{3}\mu)\varepsilon_{kk}$, and the deviatoric strain tensor is given by equation (2.7) $\varepsilon'_{ij} = \varepsilon_{ij} - \frac{1}{3}\delta_{ij}\varepsilon_{kk}$.

In order to obtain a relationship between the deviatoric stress rate tensor and the deviatoric strain rate tensor, we can not just derive equation (2.28) because, although the (Cauchy) stress is objective, its stress rate (Lagrangian derivative) is not. In continuum mechanics, objective stress rates are used to deal with this problem, which are time derivatives of stress that are independent of the reference system. The *Jaumann objective derivative* preserves the deviatoric property of a

tensor (Gerya, 2009). Its general form is

$$\sigma_{(J)} = \dot{\sigma} - w \cdot \sigma + \sigma \cdot w \tag{2.29}$$

where $\dot{\sigma}$ is the time derivative of the stress and w is the rotation. Thus, the objective Lagrangian derivative of the deviatoric stress is (Moresi et al., 2003)

$$\sigma'_{ij(J)} = \frac{D\sigma'_{ij(J)}}{Dt} - w_{ik}\sigma'_{kj} + \sigma'_{ik}w_{kj} \tag{2.30}$$

where $w_{ij} = \frac{1}{2}\left(\frac{\partial v_i}{\partial x_j} + \frac{\partial v_j}{\partial x_i}\right)$ is the rotation tensor. Therefore, the Jaumann objective derivative includes the effects of the stresses rotation (Gerya, 2009). The constitutive equation that relates deviatoric stress tensor and strain rate tensor yields to

$$\dot{\sigma}'_{ij(J)} = 2\mu\dot{\varepsilon}'_{ij} \tag{2.31}$$

2.3.3 Visco-elasticity

The rheology of rocks is assumed to be Maxwell visco-elastic: for an applied stress, deformation is initially elastic and then viscous. Once stress ceases, the elastic component is recovered while the viscous component remains. The constitutive equation of a Maxwell rheology is the addition of the elastic and the viscous strain rate constitutive laws (Eq. (2.31) and (2.16) respectively)

$$\dot{\varepsilon}'_{ij} = \dot{\varepsilon}'^{el}_{ij} + \dot{\varepsilon}'^{visc}_{ij} = \frac{\dot{\sigma}'_{ij(J)}}{2\mu} + \frac{\sigma'_{ij}}{2\eta} \tag{2.32}$$

where the viscous strain rate is the addition of the strain rates of the dislocation and the diffusion creep $\dot{\varepsilon}'^{visc}_{ij} = \dot{\varepsilon}'^{dis}_{ij} + \dot{\varepsilon}'^{diff}_{ij}$. In order to solve the constitutive equation numerically, the Jaumann stress rate (Eq. 2.30) can be expressed in a difference form (Moresi et al., 2003)

$$\sigma'_{ij(J)} = \frac{\sigma'_{ij} - \sigma'^{old}_{ij}}{\triangle t} - w^{old}_{ik}\sigma'^{old}_{kj} + \sigma'^{old}_{ik}w^{old}_{kj} \tag{2.33}$$

where the superscript old indicates values at the past time step and $\triangle t$ is a time step with the relevant timescale for the elastic stresses changes.

Therefore, rearranging, Eq. 2.32 results (Kaus, 2010)

$$\sigma'_{ij} = 2\eta_{ve}\dot{\varepsilon}'_{ij} + \chi\sigma'^{old}_{ij(J)} \tag{2.34}$$

where

$$\eta_{ve} = \frac{1}{\frac{1}{\eta} + \frac{1}{\mu \triangle t}} \tag{2.35}$$

$$\chi = \frac{1}{1 + \frac{\mu \triangle t}{\eta}} \tag{2.36}$$

$$\sigma'^{old}_{ij(J)} = \sigma'^{old}_{ij} - \triangle t \left(-w_{ik}\sigma'_{kj} + \sigma'_{ik}w_{kj} \right) \tag{2.37}$$

$\sigma'^{old}_{ij(J)}$ are the Jaumann deviatoric stress from the previous time step.

2.3.4 Visco-elasto-plasticity

Below a critical stress or elastic limit σ_c, rocks behave elastically. Above this elastic limit, rock deformation starts being viscous until the stress reaches the yield strength σ_y and the rock fails plastically (Ranalli, 1995).

In order to define a yield strength σ_y, we need a criterion that is appropriate for describing plastic yielding in rocks. The Drucker-Prager yield criterion (Drucker and Prager, 1952) states that the onset of plastic yielding occurs for a critical combination of the second invariant of the deviatoric stress σ_{II} and the pressure P

$$\sigma_y = \sigma_{II} = Psin(\phi) + Ccos(\phi) \tag{2.38}$$

where ϕ is the angle of friction and C is the cohesion.

Recalling equation (2.32), the addition of the plastic component gives

$$\dot{\varepsilon}'_{ij} = \dot{\varepsilon}'^{el}_{ij} + \dot{\varepsilon}'^{visc}_{ij} + \dot{\varepsilon}'^{pl}_{ij} = \frac{\dot{\sigma}'_{ij(J)}}{2\mu} + \frac{\sigma'_{ij}}{2\eta} + \dot{\varepsilon}'^{pl}_{ij} \tag{2.39}$$

where the plastic strain rate $\dot{\varepsilon}'^{pl}_{ij}$ is related to the stresses following a plastic flow rule. The plastic flow rule defines the deviatoric plastic strain rates as the derivatives of the plastic potential G with respect to the deviatoric stresses (Vermeer and De Borst, 1984), given by $\dot{\varepsilon}'^{pl}_{ij} = \dot{\lambda}\frac{\partial G}{\partial \sigma'_{ij}}$, where $\dot{\lambda}$ is the plastic multiplier and $G(Pa)$ is a scalar function that represents the amount of mechanical energy per unit volume employed in plastic deformation (Gerya, 2009). The Prandtl-Reuss law is the plasticity flow rule obtained by taking the von Mises yield function $\sigma_y = \sigma_{II}$ (Oller, 2014) as the flow potential G. Thus, the plastic flow rule results

$$\dot{\varepsilon}'^{pl}_{ij} = \left\{ \begin{array}{cc} 0 & \text{if } \sigma'_{ij} < \sigma_y \\ \dot{\lambda}\frac{\partial G}{\partial \sigma'_{ij}} = \dot{\lambda}\frac{\partial \sigma_{II}}{\partial \sigma'_{ij}} = \dot{\lambda}\frac{\sigma'_{ij}}{2\sigma_{II}} & \text{if } \sigma'_{ij} \geq \sigma_y \end{array} \right\} \tag{2.40}$$

in other words, plastic deformation starts when the second deviatoric invariant is higher than the yield strength given by Eq. (2.38). The non-linear plastic flow rule requires the plastic multiplier to be solved iteratively in order to reach the equilibrium state. The constitutive equation (2.34) can be written now as

$$\sigma'_{ij} = 2\eta_{ve}(\dot{\varepsilon}'_{ij} - \dot{\varepsilon}'^{pl}_{ij}) + \chi\sigma'^{old}_{ij(J)} \tag{2.41}$$

where η_{ve} and χ are defined in equations (2.35) and (2.36), respectively. Once the yield criterion is satisfied $\sigma_{II} \geq \sigma_y$, stresses are brought back to the yield surface so that σ_{II} is equal to σ_y, which is expressed by the equation (Kaus, 2010)

$$\sigma_y = 2\eta_{ve}(\dot{\varepsilon}'_{II} - \dot{\varepsilon}'^{pl}_{II}) + \chi\,\sigma'^{old}_{II(J)} \tag{2.42}$$

or

$$\sigma_y = 2\eta_{vep}\,\dot{\varepsilon}_{II} + \chi\,\sigma'^{old}_{II(J)} \tag{2.43}$$

where $\sigma'^{old}_{II(J)}$ is the second invariant of the Jaumann deviatoric stress from the previous time step and the viscoelastoplastic effective viscosity is $\eta_{vep} = \frac{\sigma_y - \chi\,\sigma'^{old}_{II(J)}}{2\,\dot{\varepsilon}_{II}}$.

Consequently, rocks behave as visco-elasto-plastic materials that follow the constitutive equation

$$\sigma'_{ij} = 2\eta_{eff}\dot{\varepsilon}'_{ij} + \chi\sigma'^{old}_{ij(J)} \tag{2.44}$$

where the effective viscosity η_{eff} is equal to η_{ve} if the yield criterion is not reached or to η_{vep} if it is satisfied.

2.4 2D FEM numerical model

To model continental extension that occurs normal to plate boundaries, the numerical model adopts the plane strain approximation. Therefore, the flow is parallel to the vertical cross-section and independent on the third axis (Ranalli, 1995).

The solutions of the heat diffusion equation (Eq. 2.13) and the Stokes flow (Eq. 2.20) for the continental extension problem are calculated with a Lagrangian numerical code based on the MATLAB-solver MILAMIN for finite elements (Dabrowski et al., 2008). The mechanical and thermal solvers are solved sequentially at each time step and are coupled via the temperature dependence of viscosity and density. The MILAMIN solver consists of three sections: a preprocessor to generate the unstructured mesh of the geometrical problem and introduce the input data, a processor to discretize and solve the governing conservation equations, and a postprocessor to analize the results (see Appendix A for the mechanical and thermal workflows).

The Finite Element Method (FEM) is a numerical method for solving boundary-value problems that are described by partial differential equations. The main steps of the FEM are the following:

1. The physical system of interest is divided into a series of non-overlapping finite elements that are connected by a discrete number of nodal points.
2. The interpolation functions are chosen to interpolate the field variables over the element.
3. The matrix relating the nodal values of each element is defined, which is obtained through a mathematical process that uses weighted residual methods.
4. The elementary matrices are combined to form the algebraic equations describing the global system. Elements connectivities are used in the assembly process. The matrix of coefficients of the global problem is known as the global stiffness matrix.
5. The boundary conditions are incorporated in the global matrix and the equations are solved through an adequate matrix method.

On the basis of the weak formulation, the Galerkin method is used to obtain approximate solutions of the temperature, pressure and velocity unknowns of the boundary-value problem. The method is characterized for employing the same weighting and interpolation functions, i.e, the so-called shape functions. The temperature solutions for the thermal problem are calculated in the nodes, where the shape functions N_i interpolate the temperature T^i to the neighboring elements

$$\hat{T}(x,y) = \sum_{i=1}^{nnod} N_i(x,y) T^i \tag{2.45}$$

where $nnod$ is the number of nodes in the discretized domain. Similarly, the approximate solutions for the velocity components and pressure are

$$\hat{v}_x(x,y) = \sum_{i=1}^{nnod} N_i(x,y) {v_x}^i \tag{2.46}$$

$$\hat{v}_y(x,y) = \sum_{i=1}^{nnod} N_i(x,y) {v_y}^i \tag{2.47}$$

$$\hat{P}(x,y) = \sum_{i=1}^{nnod} \Pi_i(x,y) p^i \tag{2.48}$$

where N_i and Π_i are the velocity and pressure shape functions, respectively.

The numerical code uses a two-dimensional mesh generator that creates stable triangular elements

(Shewchuk, 1996). The triangles are of Crouzeix-Raviart type, with seven nodes, quadratic shape functions enhanced by a cubic bubble function for velocities and discontinuous linear interpolation for pressures.

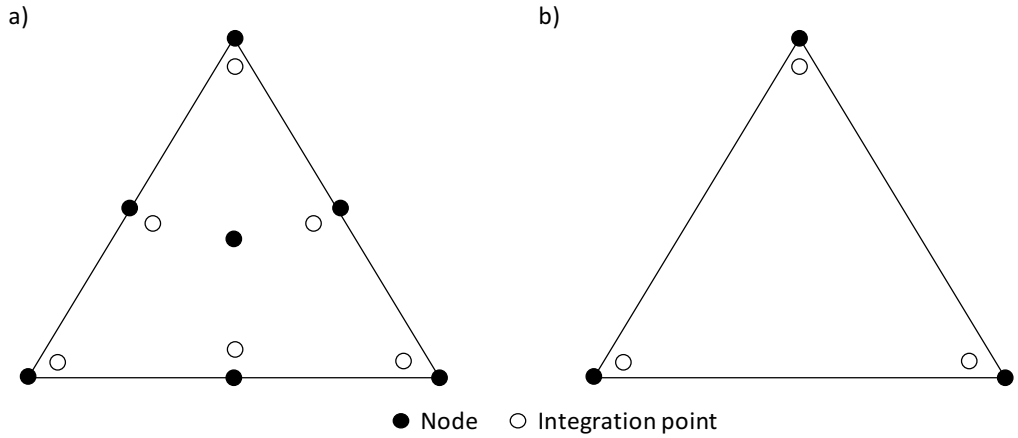

Figure 2.2: Crouzeix-Raviart triangular element for a) velocities and temperatures and b) pressures.

2.4.1 Thermal solver

The heat conservation equation in strong form is (Eq. 2.13)

$$\rho C_p \frac{DT}{Dt} = -\frac{\partial q_i}{\partial x_i} + H \tag{2.49}$$

which can be expressed in a weak form as

$$\iint \rho\, Cp\, \mathbf{N}^T \frac{\partial(\mathbf{NT})}{\partial t} dxdy = \iint \mathbf{N}^T \bigtriangledown^T (\mathbf{D} \bigtriangledown (\mathbf{NT}) dxdy + \iint \mathbf{N}^T H\, dxdy \tag{2.50}$$

where $\mathbf{D}$ is the isotropic thermal conductivity tensor, $\mathbf{N}$ are the shape functions, T is the temperature, t is time, ρ is the density, C_p is the heat capacity and H is the heat source.

The term on the left-hand side has second order derivatives, which will cause the linear shape functions to vanish, therefore the application of the Green's Theorem (integration by parts) yields

$$\begin{aligned} \left[\iint \rho\, Cp\, \mathbf{N}^T\mathbf{N}\, dxdy\right] \frac{\partial \mathbf{T}}{\partial t} = \\ \left[\iint \bigtriangledown(\mathbf{N})^T (\mathbf{D} \bigtriangledown (\mathbf{N}) dxdy\right] \mathbf{T} + \oint_\Gamma \mathbf{N}^T \mathbf{q}^T \mathbf{n} dxdy + \iint \mathbf{N}^T H\, dxdy \end{aligned} \tag{2.51}$$

The Galerkin finite element approximation can be rewritten in a matrix form as

$$M\frac{\partial T}{\partial t} + CT = Rhs \tag{2.52}$$

where C is the so-called conductivity matrix, M the heat capacity or "mass" matrix and the Rhs includes the thermal load. It is also necessary to discretize in time the equation $\frac{\partial T}{\partial t} \simeq \frac{T_n - T_{n-1}}{\triangle t}$

$$(M + \triangle t\, C)T_n = MT_{n-1} + \triangle t\, Rhs \tag{2.53}$$

Reformulated as

$$K_T T = Rhs \tag{2.54}$$

where K_T is the (global) stiffness matrix, T are temperature solutions and Rhs is the Right-hand side where the forces are included. An elementary contribution to the global stiffness matrix, the so-called elementary stiffness matrix, in the thermal problem is given by

$$K_T^e = \int_\Omega \int \left(k^e \left(\frac{\partial N_i}{\partial x}\frac{\partial N_j}{\partial x} + \frac{\partial N_i}{\partial y}\frac{\partial N_j}{\partial y} \right) + \rho C_p N_i N_j \right) dxdy \tag{2.55}$$

where k^e is the conductivity of the element.

2.4.2 Mechanical solver

The strong formulation of the plane strain Stokes flow 2.20 is

$$\frac{\partial}{\partial x}\left(\eta \left(\frac{4}{3}\frac{\partial v_x}{\partial x} - \frac{2}{3}\frac{\partial v_y}{\partial y} \right) \right) + \frac{\partial}{\partial y}\left(\eta \left(\frac{\partial v_x}{\partial y} + \frac{\partial v_y}{\partial x} \right) \right) - \frac{\partial P}{\partial x} = 0 \tag{2.56}$$

$$\frac{\partial}{\partial y}\left(\eta \left(\frac{4}{3}\frac{\partial v_y}{\partial y} - \frac{2}{3}\frac{\partial v_x}{\partial x} \right) \right) + \frac{\partial}{\partial x}\left(\eta \left(\frac{\partial v_x}{\partial y} + \frac{\partial v_y}{\partial x} \right) \right) - \frac{\partial P}{\partial y} = -\rho g_y \tag{2.57}$$

where η is the effective viscosity.

The incompressibility condition is satisfied by penalizing with a large bulk modulus the bulk deformation (Dabrowski et al., 2008)

$$\frac{\partial v_x}{\partial x} + \frac{\partial v_y}{\partial y} + \frac{P}{\kappa} = 0 \tag{2.58}$$

The weak mechanical problem is of the form

$$\begin{pmatrix} A & Q^T \\ Q & \kappa^{-1}M \end{pmatrix} \cdot \begin{pmatrix} v \\ P \end{pmatrix} = \begin{pmatrix} F \\ 0 \end{pmatrix}$$

where the element stiffness matrix for the Stokes problem is

$$K_M^e = \begin{pmatrix} A & Q^T \\ Q & \kappa^{-1}M \end{pmatrix} = \iint \begin{pmatrix} \eta^e B^T D B & -B_{vol}^T \Pi^T \\ -\Pi B_{vo} l & -\kappa^{-1} \Pi \Pi^T \end{pmatrix} \tag{2.59}$$

where B is the kinematic matrix that transforms velocity into strain rate and D is the matrix extracting the deviatoric part of the strain rate. The global system yields

$$K_M \, b = Rhs \tag{2.60}$$

where K_M is the stiffnex matrix of the global system, b is a columnwise vector with the velocity and pressure unknowns and Rhs the Right-hand side.

2.4.3 **Remeshing**

The Lagrangian formulation is limited by the large deformations that accumulate after many time steps, which causes mesh distortion. The FEM elements composing the mesh evolve during deformation and hence their shapes and locations change. The numerical code uses shape functions that are defined geometrically, therefore, for a very distorted element, the interpolation given by the shape functions will be less accurate than for an undistorted element. This results in a poor numerical solution. To overcome this problem, remeshing is introduced each time step that the defined deformation threshold is exceeded or that two interfaces overlap.

A new non-deformed triangular mesh is generated by the program Triangle (Shewchuk, 1996). The mesh generator Triangle requires quality factors for the angles and size of the triangles. We introduce as inputs the maximum area of the triangular element for each rheological layer and the minimum angle constraint of 33°. The model calls the function Triangle every time step that the quality of the mesh is poor, which is given by angles smaller than 7° or higher than 170° or a quality factor smaller than 0.2, given by $q_n = min(4\sqrt{3}area)/(l_{12}^2 + l_{23}^2 + l_{31}^2)$, where l_{ij} indicate the side of the triangle from vertex i to vertex j and $area$ is the triangular area.

Then, the variables fields are interpolated to the new mesh. The scheme for the process is as follows:

1. The defined variables at the integration points are interpolated to the nodes of the deformed mesh.

2. The integration points of the new undeformed mesh are located onto the deformed triangular elements given by the three vertex or nodes.

3. The values of the nodes in the deformed mesh are interpolated to the integration points of the new undeformed mesh.

Errors arise from the interpolation of the variables, as a result, the mechanical and temperature solution may not be in equilibrium until another time step after the remeshing.

2.4.4 Boundary conditions

The prescribed boundary conditions to the 2D extensional model are shown in Figure 2.3. In the thermal regime, constant temperatures are imposed at the top surface ($T_0 = 0°C$) and at the asthenosphere layer ($T_{LAB} = T_{bot} = 1300°C$) with zero heat flux across the lateral boundaries. All the mantle temperatures are potential temperatures due to the non-inclusion of the adiabatic temperature gradient with depth (see also Hasenclever, 2010).

The extensional model is prescribed with normal velocity boundary conditions and tangential free slip at each lateral. A free surface top boundary is added to the model (Andrés-Martínez et al., 2015), which allows the deformation of topography. The bottom boundary has tangential free-slip and normal velocity that results from the law of mass conservation.

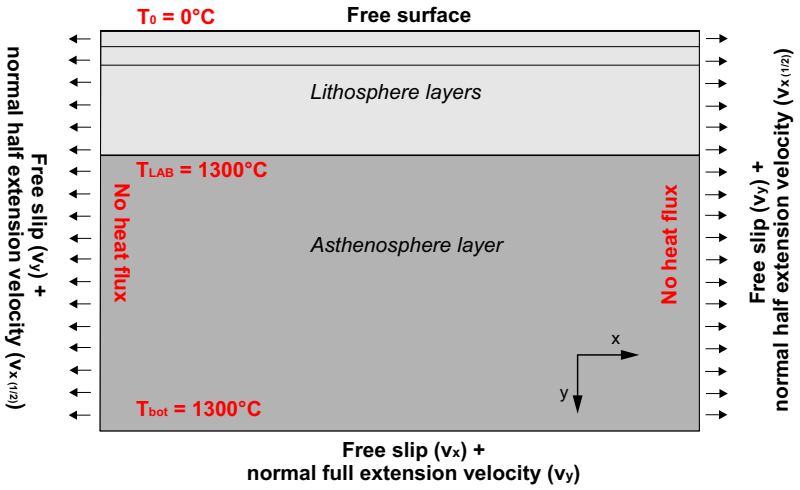

Figure 2.3: 2D model showing mechanical and thermal boundary conditions.

2.5 New contributions to the model

2.5.1 Melt generation

In order to calculate the amount of melting produced at each time step, the melting curve (solidus) needs to be defined. Although the mantle dehydrates as it melts, dry melting is more

productive than wet melting (Hirth and Kohlstedt, 1996). Therefore, the model uses a first-order approximation of melting for a dry solidus temperature and homogeneous fertile peridotite mantle (for a heterogeneous multi-component solid mantle see Hasenclever, 2010). Melt production is defined as 'the fractional melt per unit mass that melts' (Phipps Morgan, 2001). Generally, melting studies estimate melt production using a constant solidus and latent heat of melting (Reid and Jackson, 1981; Sparks et al., 1993). In this thesis, the melt generation formulation is based on that of Phipps Morgan (2001), where melting is approximated as a reversible adiabatic process. During adiabatic ascent, the thermodynamic variable entropy S is conserved, thus $dS = 0$ (isentropic process). The entropy of a parcel of mantle that follows an isentropic path has thermal dT, pressure dP and mass fraction dF contributions

$$dS(F,T,P) = 0 = \left(\frac{\partial S}{\partial T}\right)_{P,F} dT + \left(\frac{\partial S}{\partial P}\right)_{T,F} dP + \left(\frac{\partial S}{\partial F}\right)_{T,P} dF \tag{2.61}$$

For a pure component, the entropy of melting $\triangle S_s$ is related to the latent heat of melting L and melting temperature T_s as

$$\triangle S_s = L/T_s \tag{2.62}$$

which can be an approximation for $\left(\frac{\partial S}{\partial F}\right)_{T,P} \approx \triangle S_s$.

The temperature needed to melt mantle rocks increases with pressure (depth) and melt extraction (depletion). The mantle temperature cannot be over the solidus temperature since the melting will start immediately and hence the temperature will be reduced to the solidus as the latent heat is consumed. Therefore, the change in the upwelling mantle temperature associated to melting is equal to the change in solidus temperature and controlled by the pressure drop dP and depletion dF

$$dT = dT_s = \left(\frac{\partial T_s}{\partial P}\right)_F dP + \left(\frac{\partial T_s}{\partial F}\right)_P dF \tag{2.63}$$

where $\left(\frac{\partial T_s}{\partial P}\right)_F$ is the solidus-pressure dependence and $\left(\frac{\partial T_s}{\partial F}\right)_P$ is called the solidus-depletion dependence.

Substituting equation (2.62) and (2.63) into the relation (2.61), and further arrangements (Phipps Morgan, 2001), lead to the melt productivity formula

$$\left(\frac{dF}{dP}\right)_S = \frac{\left(-\frac{\partial T_s}{\partial P}\right)_F + \frac{\alpha T}{\rho c_p}}{\frac{L}{c_p} + \left(\frac{\partial T_s}{\partial F}\right)_P} \tag{2.64}$$

Melt productivity is defined as the amount of melting per increment of mantle decompression (Hirschmann et al., 1994).

The numerical formulation of melting that I have implemented in the 2D model is described below. It is assumed that all temperatures are 'potential temperatures', e.g., adiabatic effects are assumed to be uniform. In each time step, for each mantle particle (node) advected from position 1 to position 4 (Figure 2.4), the melting process is divided in two operations, where the mantle partially melts, firstly, as the temperature increases and, secondly, as the pressure decreases (Phipps Morgan, 2001). This is (1) a change in temperature at constant pressure that reflects the addition/removal of heat at constant pressure, and (2) a change in temperature at constant entropy that reflects the decrease/increase in pressure on an adiabatic system. First, I check whether the new temperature after heat diffusion at the same old node depth is above or below the solidus (Figure 2.4 a, position 1). The solidus is given by

$$T_s = T_s^0 + \frac{\partial T_s}{\partial P} P + \frac{\partial T_s}{\partial F} F \tag{2.65}$$

where, for fertile peridotite, T_s^0 =1081°C is the solidus temperature at the surface, $\frac{\partial T_s}{\partial P}$ = 132°C/GPa is the solidus-pressure dependence and $\frac{\partial T_s}{\partial F}$ = 350°C is the solidus-depletion dependence (Hasenclever, 2010; Phipps Morgan, 2001).

As soon as the geotherm of the mantle crosses its solidus (Figure 2.4 a, position 2), melt starts and hence the temperature will be reduced since latent heat is consumed till the mantle temperature equals the solidus. The melting production associated to this step is calculated as (Asimow et al., 1997)

$$dF = \frac{dT}{\frac{L}{c_p} + \frac{\partial T_s}{\partial F}} \tag{2.66}$$

where $\frac{L}{c_p}$ = 550°C for partial melting of mantle peridotite and dT is the difference between the end-position of the mantle rock and solidus temperatures.

In the nodes where melting has been produced the temperature is corrected to the solidus (Figure 2.4 a, position 3)

$$\frac{\partial T}{\partial P} = \frac{\partial T_s}{\partial P} + \frac{\partial T_s}{\partial F}\frac{\partial F}{\partial P} \tag{2.67}$$

and the depletion variable and the solidus are updated.

Second I calculate the production of melting of the upwelled mantle rock as a function of the pressure drop. The solidus is calculated for the new (advected) position of the node (Figure 2.4 b, position 3). The drop in pressure is calculated for each node, i.e. difference in pressure before and after the advection ($dP = dP_0 + dP_1$) but only taken into account the drop pressure over the solidus (dP_1). I make equal the slopes of the triangles to obtain the value of dP_0

$$\frac{dP}{T_{s0} - T_{s1}} = \frac{dP_0}{dT_0} \implies dP_0 = \frac{dP dT_0}{T_{s0} - T_{s1}} \tag{2.68}$$

where $dT_0 = T_{s0} - T$. So the considered pressure drop will be $dP = dP_1$.

Then calculate the melting production associated to advection is calculated as

$$dF = \frac{dF}{dP} dP \tag{2.69}$$

where $\frac{dF}{dP}$ is the melt productivity over dP

$$\frac{dF}{dP} = \frac{-\frac{dT_s}{dP}}{\frac{L}{c_p} + \frac{dT_s}{dF}} \tag{2.70}$$

And finally the advected temperature as

$$T_4 = T_3 + \frac{dT}{dP} \triangle P \tag{2.71}$$

where $\frac{dT}{dP}$ is given by Eq. 2.67.

The depletion is updated by adding the calculated dF and hence the new solidus. The final melting production of a node in a time step is the addition of both step productivities (diffusion and advection).

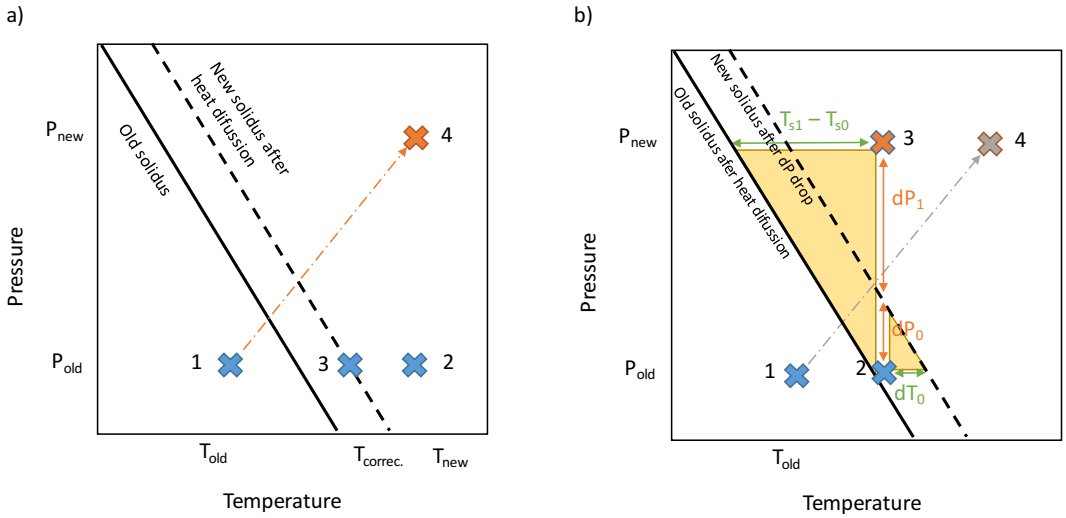

Figure 2.4: Steps for the numerical formulation of melt generation: changes in pressure and temperature as the mantle ascends and the corresponding solidus. Solid lines represent starting solidus and dashed lines represent new solidus after the mantle has upwelled in a time step. The modelling of a decompressional melting process can be divided in two: a) The melting related to the increase in temperature and b) the melting related to the decrease in pressure. See text for further details.

2.5.1.1 Magmatic crustal thickness

A useful measure of the melt productivity is the magmatic crustal thickness (Bown and White, 1995; Ito et al., 1996; Sotin and Parmentier, 1989). This measure assumes that all melt is focused and accreted at the rift axis. At each time step, I estimate the magmatic crustal thickness by weightening the degree of melting per node area, integrating over the area of melt and dividing the total amount of melt by a length proportional to the opening extension during the time step $2vdt$ (v is the half-extension velocity). The estimate provides an upper limit of the crustal thickness since, in nature, part of the melt stops during its ascent (Cannat et al., 2009).

The amount of magmatic crustal thickness over time is a good proxy to be compared to the magmatic products that result in natural rifting examples. However, the numerical calculation is sensitive to different parameters such as pressures involved in the calculation of melt, temperature remesh for the melt calculation and type of integration of the melting area. The first approximation I used for these factors showed a magmatic crustal thickness curve with scattered points. Figure 2.5a shows how the remesh interpolation influenced on the magmatic crustal thickness resulting in points out of the trend. Remeshing creates new nodes, where the values from the old nodes have to be interpolated, and small errors in the interpolation of depletion and temperature (about $2°C$ over 800 $°C$ background temperature) resulted in these outliers.

To improve the calculation of the total melt, I used two functions developed by Hasenclever (2010): the first one splits each old 6-node element into 4 new linear elements and the second one interpolates the temperature variable from these new triangular elements into the remeshed triangles by using quasi-cubic interpolation functions. The resulting magmatic crustal thickness is shown in Figure 2.5b.

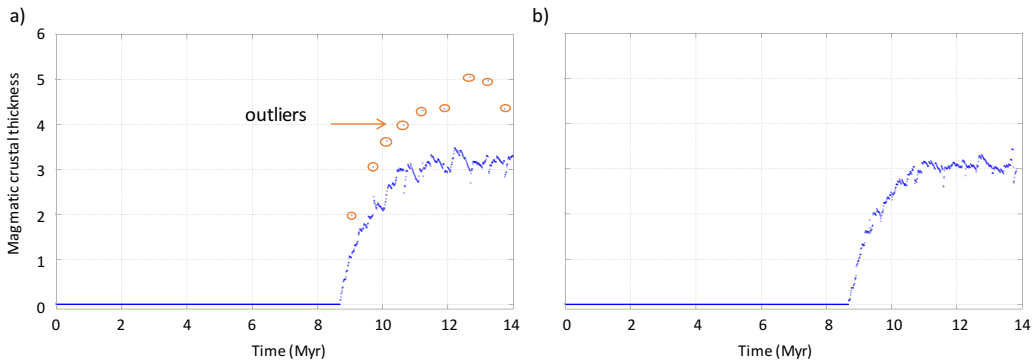

Figure 2.5: Magmatic crustal thickness over time. a) Before corrections: the crustal thickness presented scattered outputs (outliers) every time step with a regridding of the deformed lagrangian mesh. b) After corrections: crustal thickness with a better interpolation function.

In order to test the feasibility of the integration of the melt area, I compared the results from two type interpolations. The first one assumed a regular mesh over the melt area where each node is given an area of $1km^2$ and the melt per node is interpolated to the regular grid and integrated. The second one used another function developed by Hasenclever (2010) which consisted of assigning an area proportional to the element size to each node. Figure 2.6 shows that both interpolations give very similar results for the magmatic crustal thickness.

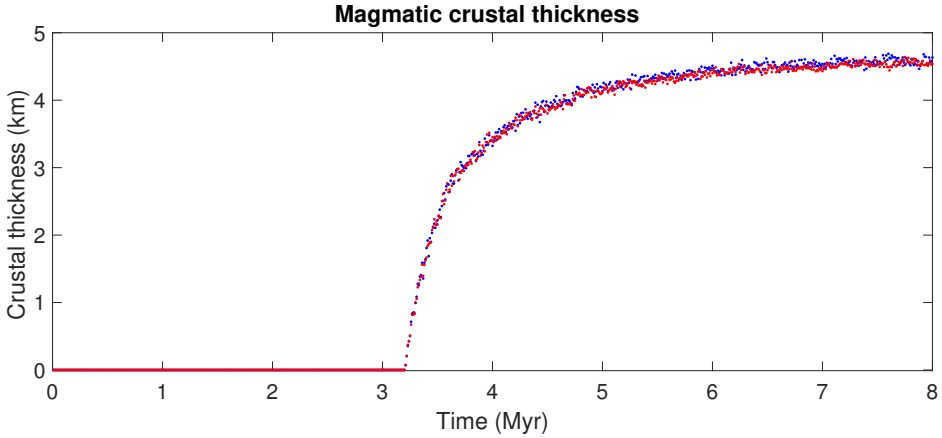

Figure 2.6: Two approximations for the integration of the melt area: a regular grid (red) and a numerical mesh-based triangular grid (blue) to interpolate the amount of melt from each node and integrated the total amount. Both approximations give similar results.

Another numerical issue was the pressures involved in the solidus temperature calculation, which were initially lithostatic and resulted in a more scattered crustal thickness curve. After using the pressure outputs from the mechanical (dynamic pressures), the resulting curve was smoother.

2.5.2 Melt emplacement and underplating

In continental rifting, melt migrates from the melt region to the area of lowest potential energy at the surface (where the extension is taking place). In its way, it can be emplaced in magma-chambers or fractures where it solidifies. The main stopping of melt relates to contrasts in mechanical properties, common in layers of different properties that are in contact, where melt accumulates. There are three main mechanisms for stopping in the shape of a dike: Cook-Gordon delamination (mainly at shallow depth, the contact opens), stress barrier (the maximum principal compressive stress, σ_1, flips 90 $^\circ$ from being vertical to being horizontal and favouring dike arrest and/or sill formation), and elastic mismatch (difference in Young's moduli across a contact in relation to that of the contact itself) (Gudmundsson, 2011).

Based on these considerations, I have modelled two end-member scenarios for melt emplacement below the Moho discontinuity. In the first scenario, melt flows to the area beneath the Moho where the strain rate is maximum, i.e. the rift center. There it is emplaced as a vertical column, i.e. a dike, of width $2v_x dt$ and thickness the magmatic crustal thickness (Fig. 2.7a), where v_x is the horizontal velocity applied to each model side and dt is the time step of the model (i.e. 10 kyr). In the second scenario, melt migrates vertically upwards from the area where it is produced and it is emplaced below the Moho as a concave-upward layer, i.e. a sill (Fig. 2.7b). To build the sill at each time step, I interpolate the area of melt to a regular mesh and discretize it in columns, as it was a layer composed of individual dikes. Figure 2.8 shows the evolution of two models with the dike and the sill approximation, respectively.

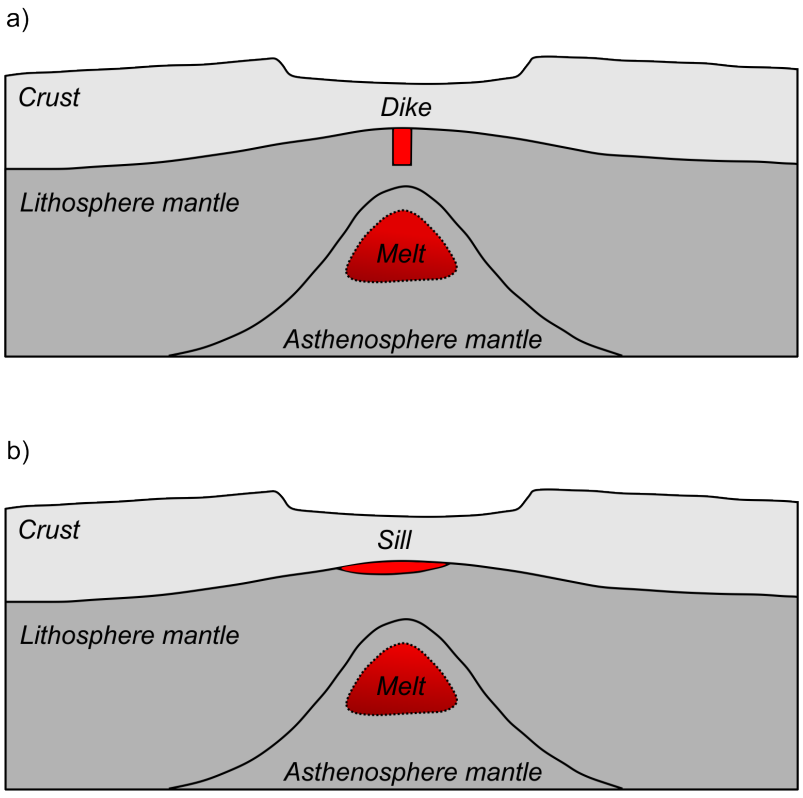

Figure 2.7: Two end-member scenarios for ad-hoc melt emplacement: a) dike and b) sill.

In both cases all melt is assumed to pond and underplate the thinning continental crust. I call 'underplating' the addition of dikes (or sills) during continental rifting that direct pond at the Moho (Thybo and Artemieva, 2013). Although this is a traditional concept, it shows in a simplistic way how melts emplace at the base of the crust and/or intrude the lower crust as dike- or sill-like bodies. In nature, the presence of underplating may be detected at lower crustal areas without reflectivity from the reflection seismic lines. As first-order approximation of the accumulation of

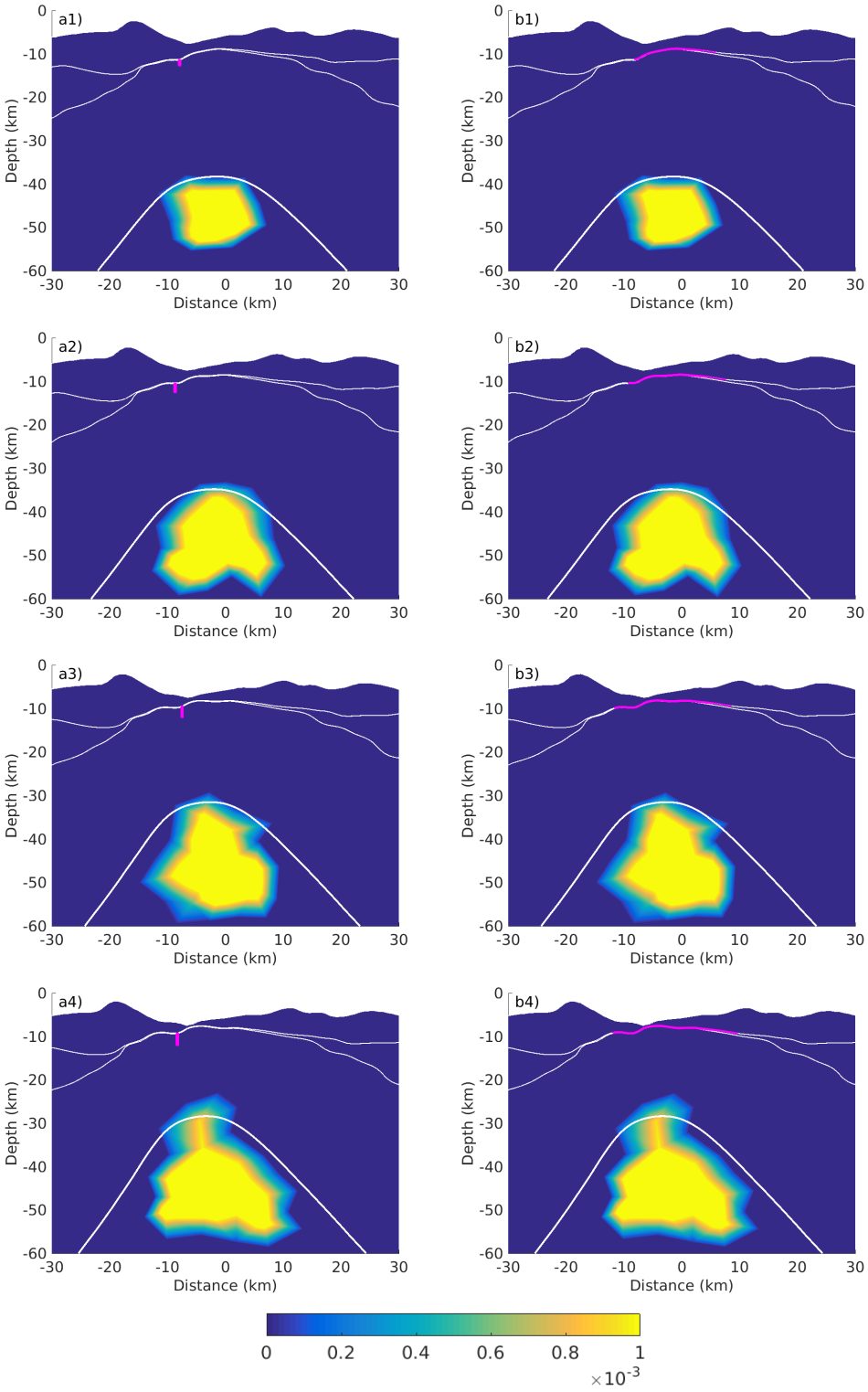

Figure 2.8: Amount of melting after 3.3, 3.4, 3.5 and 3.6 Myr of deformation (from top to bottom) for two types of magmatic underplating: a) dike and b) sill. Colorbar indicates the percentage of melting generated, white lines are lithospheric layers boundaries, vertically-shape pink accumulated melt represents a dike (a1 to a4) and horizontally-shape accumulated melt represents a sill (b1 to b4).

melts during continental rifting, I have included the underplating model in the numerical code. At each time step, the dike is decomposed as a combination of tracers that move with the nodal velocity field of the mantle. These tracers are modelled as semi-transparent circles with radius scaled by the time step amount of melt (Fig. 2.9). Two dikes for different time steps (4 and 9 Myr) are shown in Figure 2.9. The increasing number of dike tracers during the evolution of the rift leads to zones where their accumulation shows more opacity and represents the higher density of underplated magmatic crust (Fig. 2.10b).

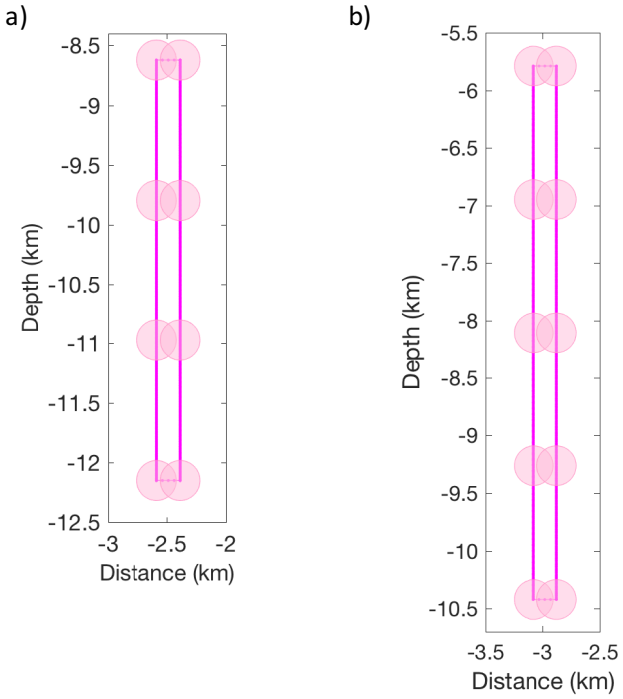

Figure 2.9: Decomposition of the area of a dike (magenta rectangle) into tracers (light pink circles) for the times steps a) 4 Myr and b) 9 Myr. The amount of melt increases with time, hence, the dike is thicker and the number of tracers increases as well (compare a) with b)).

The location of the dike during continental rifting, as explained above (beneath the Moho where the strain rate is maximum), is compared in Figure 2.11 to the approximation of migrating all melt to the shallowest part of the Moho as modelled in previous studies of mid-ocean ridges and continental rifting (e.g., Behn and Ito, 2008; Behn et al., 2006; Daniels et al., 2014). The model is extended by 5 mm/yr (half-extension), with a crust of wet quartzite, lithosphere mantle of dry olivine and asthenosphere of wet olivine. The distribution of the underplating, or accumulated dikes, on both models is very similar. The wide margin is underplated by magmatic products as it becomes longer, and both the maximum strain rate at the Moho and the thinnest crustal domain at each time step are concomitant most of the time in the rifting history.

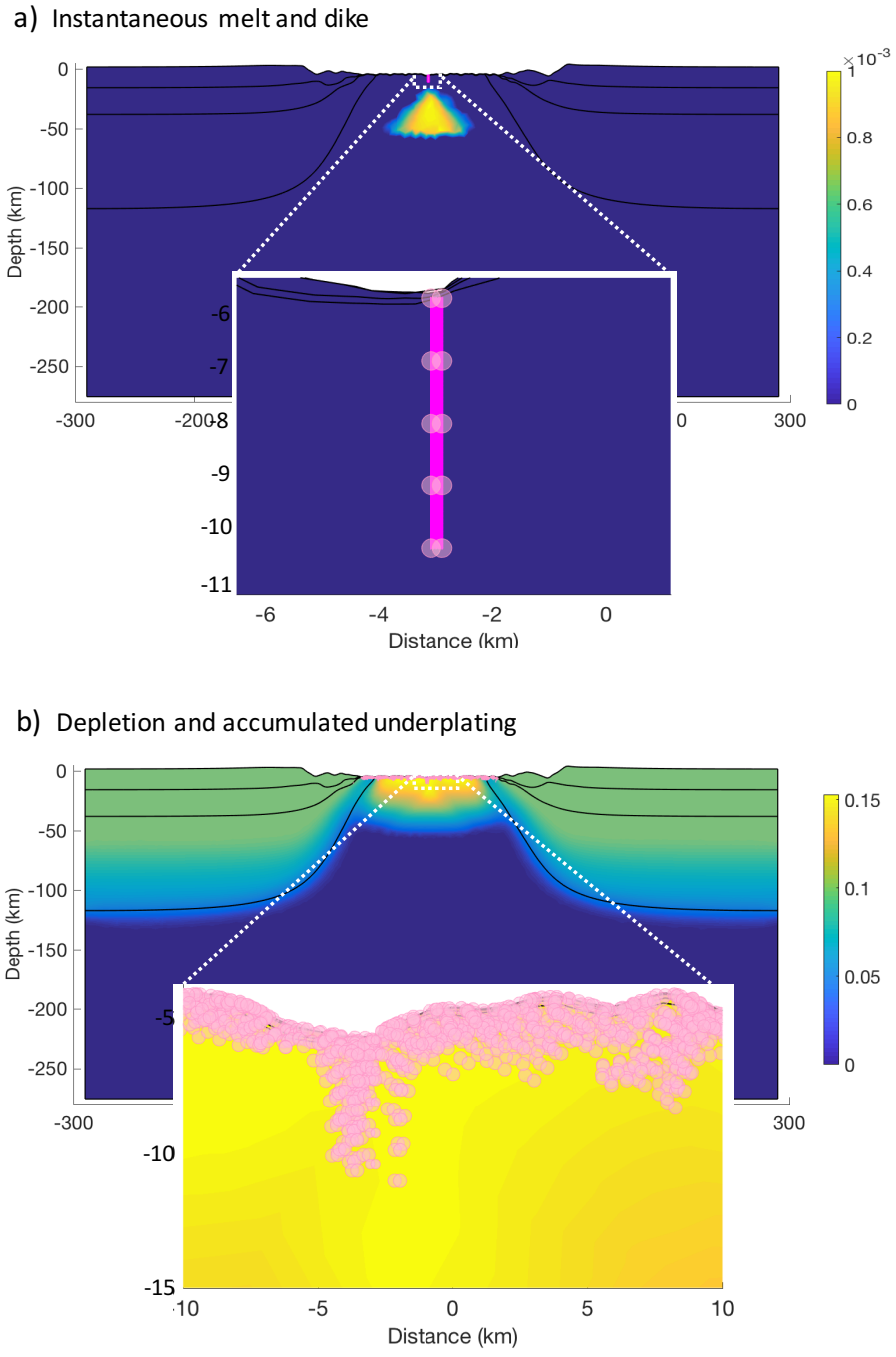

Figure 2.10: Distribution of underplating after lithospheric continental break-up (9 Myr). a) Instantaneous melt and its integration into a dike (magenta rectangle) and the area of the dike divided into circular tracers (light pink circles). b) Depletion and magmatic accumulated underplating.

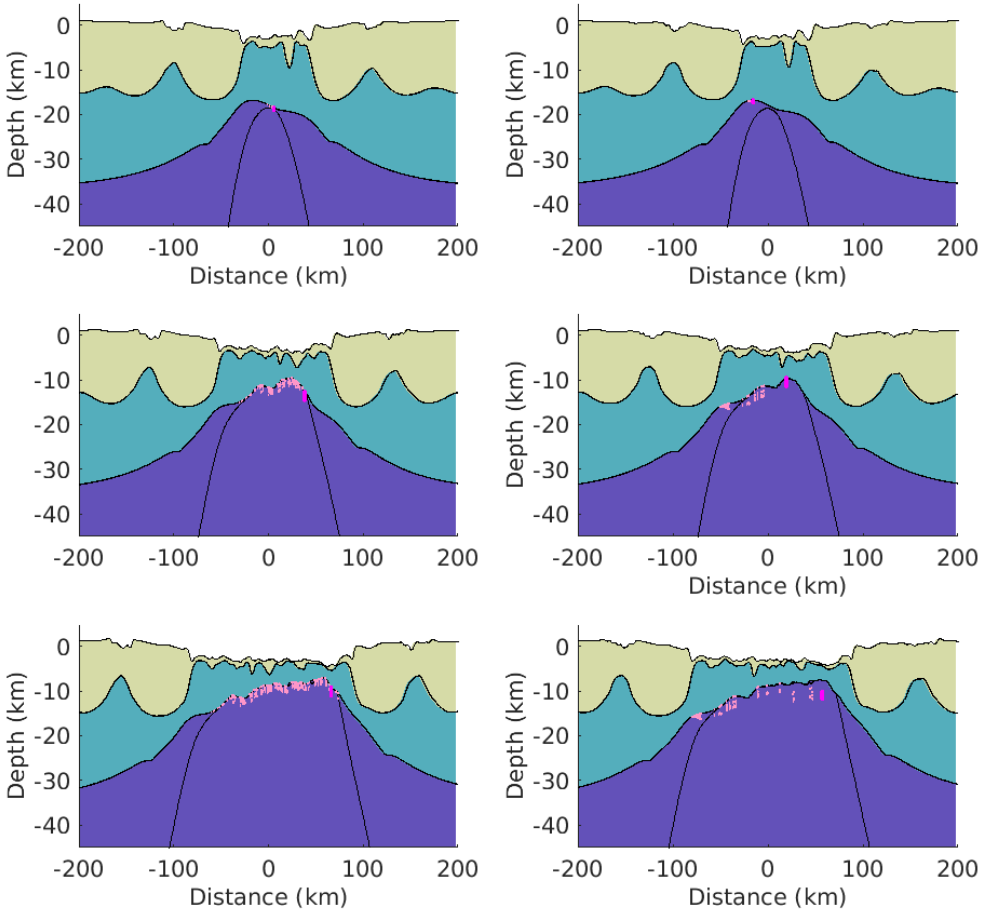

Figure 2.11: Model evolution for types of dike emplacement (from top to bottom: 22, 32 and 42 Myr). Left panel shows the emplacement of a dike below the Moho at the maximum strain rate. Right panel shows the emplacement of a dike at the shallowest level below the Moho.

2.5.3 **Heat release of cooling solidified melt**

The emplacement of dikes - or sills - at temperatures of $\sim 1000°C$ will increase the temperature of the rocks below the Moho, which typically are at $\sim 500 - 800°C$. Although the heating of the country rock is restricted to a very narrow zone, the continuous emplacement of dikes during continental rifting can have significant thermal impact on the surroundings. It is interesting therefore to address the dikes heat release and its effect on localization of strain and hence rift evolution.

The heating of a dike is effective for a distance into adjacent rocks, and will depend on the emplacement dike temperature, the thermal diffusivity and the distance to the dike. I have

modelled two different estimations of the heat that a dike releases during its cooling. The first estimation only evaluates the thermal history after complete solidification of a dike, by solving the one-dimensional heat conduction equation in an infinite region to find the temperature field surrounding the dike (Turcotte and Schubert, 2014). For an initial temperature distribution $T'(y)$ of the dike and its surroundings, the Laplace's solution determines the subsequent temperature distribution T

$$T = \frac{1}{2\sqrt{\kappa\pi t}} + \int_{-\infty}^{+\infty} T'(x')\, e^{\frac{-(y-y')^2}{4\kappa t}} dx' \tag{2.72}$$

where κ is the thermal diffusivity ($m^2 s^{-1}$), x' is a dummy variable for integration, t is relaxation time and x is distance from dike center line. To solve for temperatures, the model evaluates the numerical integration of the temperature distribution at each time step. Dikes are assumed to be emplaced instantaneously at high temperature $T'(x) = 1100°C$. A typical value for the relaxation time is $t = 100$ yr.

To include the solidification of the dike we should treat it as a Stefan problem, which involves the growth of a solidified region (Wangen, 2010). The liquid melt cools to its melting temperature T_m and begins to solidify, there is a phase change from liquid to solid at the melting temperature and a release of heat, i.e. the latent heat of fusion, which is transported by conduction through the solid part. This requires to graphically solve an equation including the latent heat L, the heat capacity c and the difference between the melting T_m and the background temperature T.

Based on this approximation, for the second estimation I consider that the dike has solidified instantaneously and therefore its initial temperature is the melting temperature T_m plus the temperature increase of the heat released during solidification L/c. The temperature distribution at the time $t > t_1$, after a dike intrusion of thickness a_1 at depth z_1 and at the time t_1 with a temperature $T_1 = T_m + \frac{L}{c}$, is given by

$$T(z,t) = T_n(z,t) + [T_1 - T_n(z_1,t_1)]\, \hat{T}\left(\frac{z-z_1}{a}, \frac{t-t_1}{t_0}\right) \tag{2.73}$$

where $T_n(z,t)$ is the temperature solution in absence of the dike, which is added to the temperature distribution given by the dike (second adding term). In the second term, the $\hat{T} - function$ is given by

$$\hat{T}(\hat{z},\hat{t}) = \frac{1}{2}\left(erf\left(\frac{\hat{z}+1}{2\sqrt{\hat{t}}}\right) - erf\left(\frac{\hat{z}-1}{2\sqrt{\hat{t}}}\right)\right) \tag{2.74}$$

The center line of the dike is $\hat{z} = 0$ and extends from $\hat{z} = -1$ to $\hat{z} = 1$. The initial conditions

are $\hat{T} = 1$ inside the dike and $\hat{T} = 0$ outside the dike. The boundary conditions give no thermal impact on the country rock far from the dike $\hat{T}(\hat{z} = -\inf, \hat{t}) = 0$ and $\hat{T}(\hat{z} = \inf, \hat{t}) = 0$. The characteristic temperature of the dike is T_0, the characteristic length is half-width of the dike a and the characteristic time is $t_0 = \frac{a^2}{\kappa}$. The temperature $T_n(z_1, t_1)$ is subtracted from the temperature of the dike T_1 to in front of the $\hat{T} - function$ to satisfy the initial condition $T_n(z_1, t_1) = T_1$. This is a good approximation except for a short time interval right after solidification. And I use $T_1 = T_m + \frac{L}{c} = 1100 + 278 = 1378°C$.

The first approximation using the Laplace's solution is less accurate since it considers that the cooling and solidification of the dike has already occurred and it only model the time of postsolidification, so, once all melts have been solidified the Laplace's solution is applied. The second approximation is more realistic since it uses the error function to account for the solidification of the instantaneous dike emplacement at high temperature.

Both approximations calculate the cooling of an instantaneously solidified dike, however, the second estimation also takes into account the heat released during solidification for the calculation of the thermal distribution on the surroundings.

I show in Figure 2.12 the implementation of the second type of heat release. Figure 2.12a shows the emplacement of a dike at a time step and the surrounding nodes with their temperatures given by the colors, this is before releasing heat. Subsequently, heat is released and the nodes closer to the dike increase their temperatures, as seen in Figure 2.12b. Figure 2.12c shows a zoom of the dike after the release of heat. The regular grid of points that appears is over which the heat of the dike is extrapolated following the approximation of the error function. It can be seen how the temperature decreases with horizontal distance. The points that appear shifted from the regular grid are the actual nodes of the model mesh in this area. Figure 2.12d shows the same image without the regular grid, where the mesh nodes have acquired a new increased temperature that depends on the horizontal distance relative to the dike's position.

Some snaphots of the evolution of a model with wet quartzite crust of 35 km thickness (10 mm/yr half-extension) are shown in Figure 2.13, where the thermal effect of the dike on the country side is compared to the thermal structure of the same model without heat release.

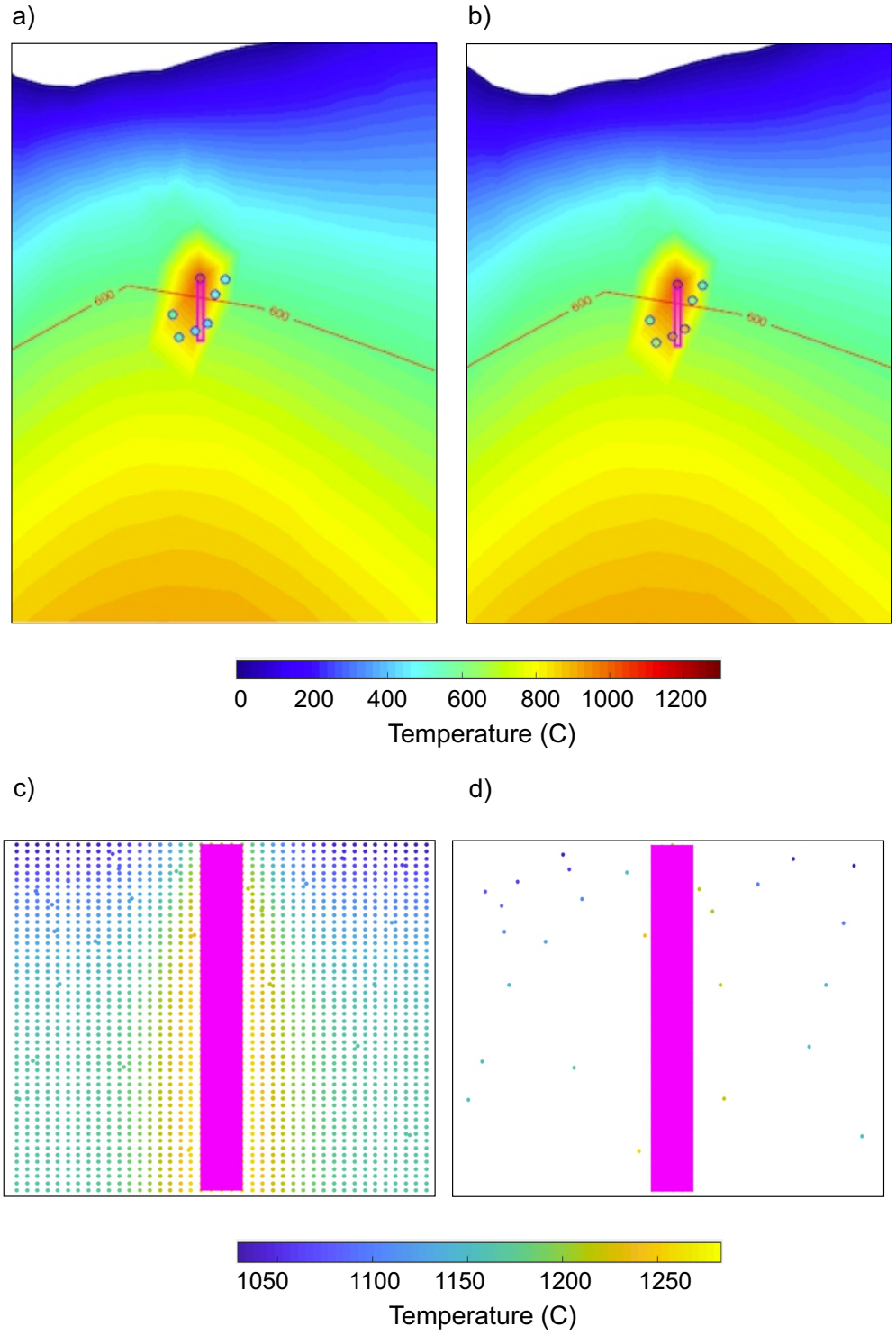

Figure 2.12: Thermal field before and after heat release of a dike: a) Dike emplacement prior to the release of heat and b) after the release of heat. Red line is the isotemperature of 600°.

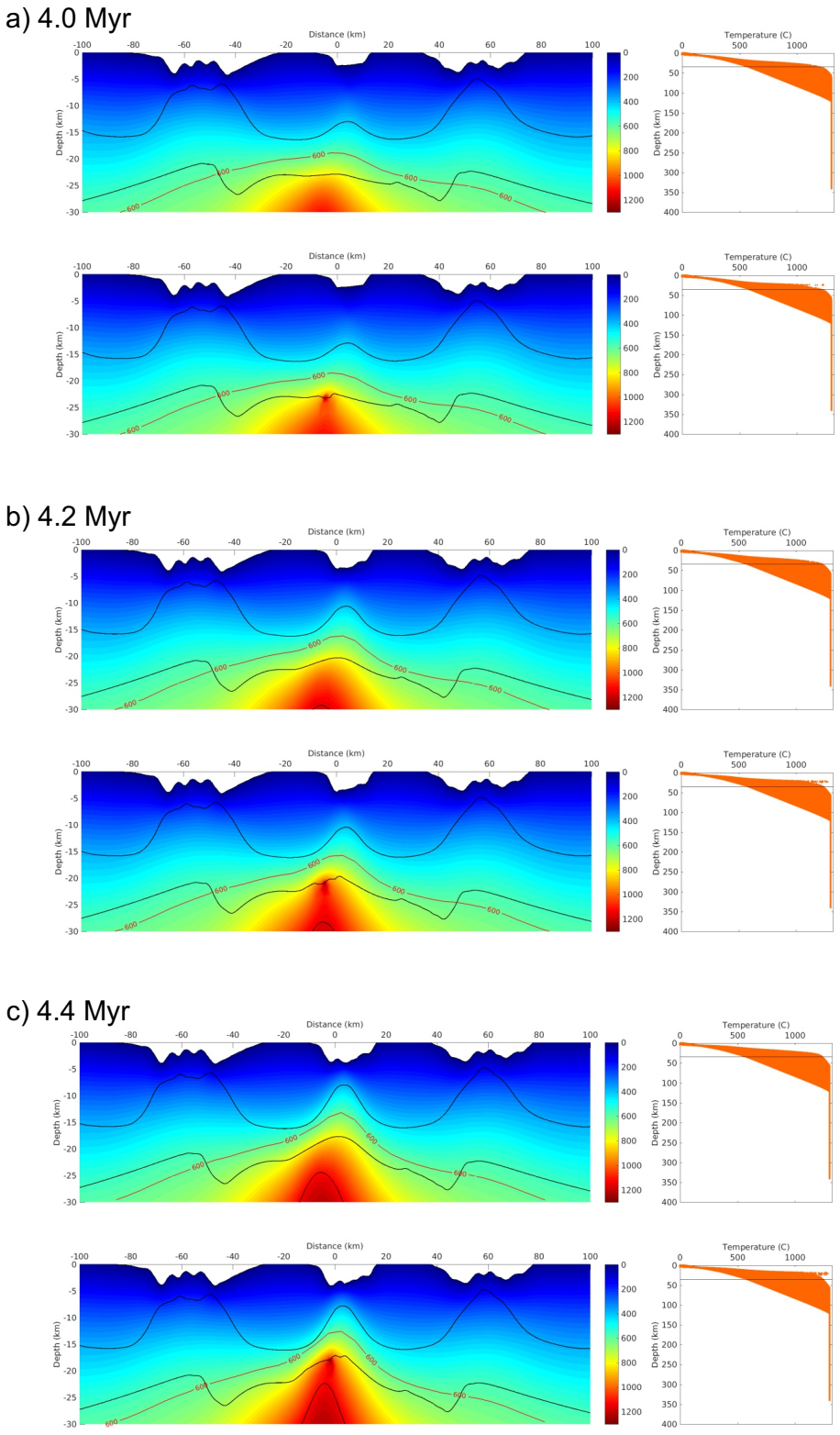

Figure 2.13: Effect of heat release on the thermal structure of the extending lithosphere for a model with wet quartzite lower crust, 35 km thick-crust and extension of 100 mm/yr. Temperature is in °. Snapshots at a) 4.0 Myr, b) 4.2 Myr and c) 4.4 Myr for model without heat release (top) and with heat release (bottom). Right panels show the lithospheric geotherm, where the scattered points at about 20 km depth show the increased temperature in the nodes surrounding the dike.

2.5.4 Serpentinization

In the numerical models, serpentinization of the mantle occurs when faults cutting through the crust are active and the mantle is within the temperature range for serpentinization ($\sim 100 - 450°C$). Active faults are assumed to be 'open' crustal-scale channels so that the seawater can reach the underlying mantle and participate in the reaction of serpentinization. This was first proposed by Pérez-Gussinyé and Reston (2001) and later demonstrated by Bayrakci et al. (2016). Two criteria are checked each time step. First, whether the crustal nodes within the brittle regime, calculated with the mechanical solver, connect the surface to the uppermost mantle (Pérez-Gussinyé et al., 2006). Here I introduced a cut-off depth of 20 km where the deepest serpentinites are expected to be found. Second, the parameter that defines 'active' faults is calculated based on the background strain rate.

This threshold parameter is subject of discussion. Faults are considered to be active when they have larger strain rates than a threshold value $\dot{\epsilon}_{th}$, which is calculated from the maximum and minimum strain rates ($\dot{\epsilon}_{max}$ and $\dot{\epsilon}_{min}$) along the model domain, $\dot{\epsilon}_{th} = f \cdot (\dot{\epsilon}_{max} - \dot{\epsilon}_{min}) + \dot{\epsilon}_{min}$, where f is an arbitrary factor ranging from 0 to 1. Sensitivity tests of the f factor were carried out by varying its value from 0.001 to 0.5 (corresponding to the 0.1 and the 50 $\%$ of the strain rate variation, respectively). The two models used consisted of a 35 km crustal thickness, mafic granulite and wet quartzite lower crust, and were extended by 3 mm/yr (half-extension). Models with a larger f resulted in a slight delay of the onset of serpentinization ($\sim$ 0.1 to 0.4 Myr, for mafic granulite and wet quartzite, respectively) and less amounts of serpentinized mantle. The difference in the parameter influences mainly the depth at which water reaches the mantle, and therefore the depth of the serpentinized zone, which changes by about 5 km. Consequently, the degree of serpentinization is also affected, obtaining larger zones of 100 $\%$ serpentinized mantle for the lower parameter. From drill holes in the Iberia Abyssal Plain, highly serpentinized mantle up to 100 $\%$ has been estimated at the COT, which decreases with depth (Chian et al., 1999). Despite the small differences, the general outcomes for the nature and composition of the COTs hold after varying this numerical threshold within a reasonable range (Fig. 2.14). The threshold parameter value assumed for the models of this thesis is 0.15. Although this modelling parameter is not well constrained, I consider that this assumption for crust-cutting active faults improves the estimation of the locations for generation of serpentinization in comparison to the condition of having the entire crust within the brittle regime as modelled by previous studies (e.g., Pérez-Gussinyé and Reston, 2001; Rüpke et al., 2013).

If the criteria above is satisfied and the mantle is at appropriate temperature conditions for serpentinization, then rate of serpentinization is calculated as a function of temperature. Although,

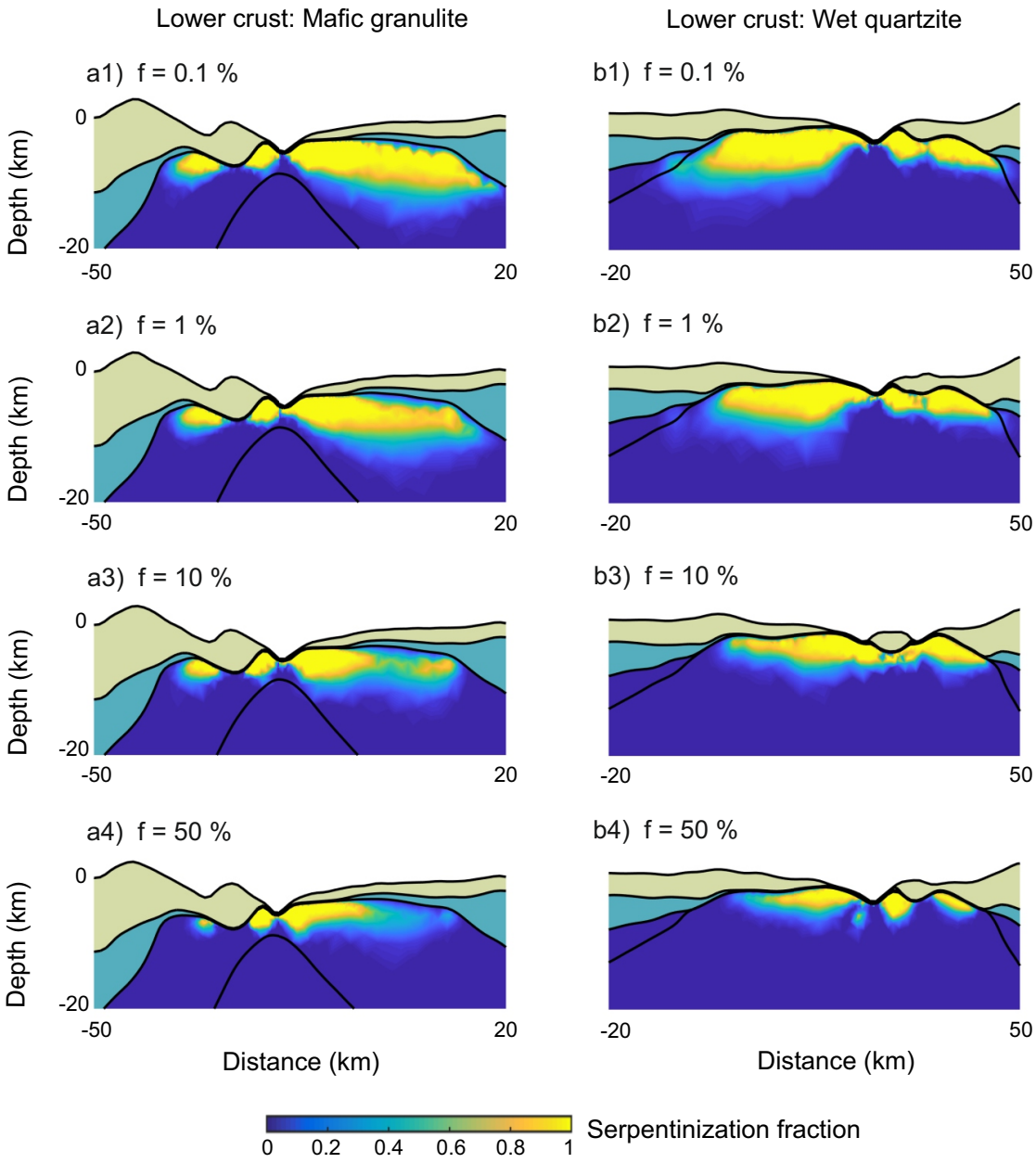

Figure 2.14: Numerical models testing the sensitivity of the amount of serpentinization on the parameter f that defines active faults that allow water downflow. a1-a4) Mafic granulite lower crust. The value of the active fault parameter f is: a1) 0.1%, a2) 1%, a3) 10 % and a4) 50%. b1-b4) Wet quartzite lower crust. The value of the active fault parameter f is: b1) 0.1%, b2) 1%, b3) 10 % and b4) 50%. In both models, as the parameter increases the resulting serpentinized zone slightly decreases in amount and depth.

in nature, the serpentinization reaction depends on many factors (e.g., initial rock, temperature, water supply, etc), it is possible to establish a simple parametrization in agreement with experimental

data, which is only dependent on temperature (Emmanuel and Berkowitz, 2006):

$$\frac{\partial \rho_m}{\partial t} = -k_r(T)\rho_m \tag{2.75}$$

where ρ_m is the mass of fosterite per unit volume, t is time and $k_r(T)$ is the temperature-dependent serpentinization rate. Following the study of Emmanuel and Berkowitz (2006), I approximate the rate of serpentinization by a bell-shaped function on the form $k_r(T) = Ae^{-b(T-c)^2}$, where T is absolute temperature, $A = 10^{-10}s^{-1}$ is a kinetic coefficient, $b = 2.5 \cdot 10^{-4}K^{-2}$ determines the temperature range for the reaction and $c = 270°C$ determines the peak temperature at which k_r equals A (Fig. 2.15), thereby the serpentinization reaction occurs for temperatures between $100°C$ and $400°C$ with the maximum value at $270°C$. The transformation of peridotites into serpentinites releases heat to the surrounding rock $Q = H\frac{\partial \rho_m}{\partial t}$, where H is the heat reaction per unit mass of forsterite. In this numerical model, the assumed temperature raise is of $T_s = \frac{Q}{C_p} = 300°C$ for complete serpentinization (Iyer et al., 2012). In the current version of the code, the effect of serpentinization on rheology and density is not yet introduced.

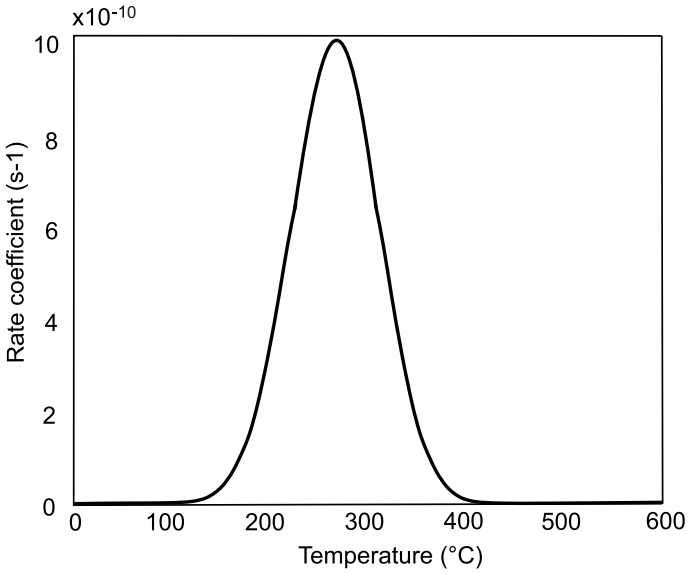

Figure 2.15: Temperature-dependent serpentinization rate. The serpentinization of the dominant form of olivine (i.e. forsterite) initiates at $100°C$ and reaches a maximum at around $270°C$. For higher temperatures, the kinetics of the serpentinization reaction is retrograde and stops at temperatures above $400°C$(Emmanuel and Berkowitz, 2006).

I assume that serpentinized mantle may act as an 'impermeable' barrier to melt transport. This assumption is based on the fact that, in subduction zones, serpentinites have been proposed to be impermeable in the direction perpendicular to shearing at the subducting plate interface (Katayama et al., 2009; Kawano et al., 2011). This suggests that, in extensional environments, a layer of

serpentinized mantle may also act as a barrier to vertical melt migration. Second, if melt is intruding by diking in the brittle regime, then non-dilatant brittle deformation of serpentinite (Escartin et al., 1997) may act as an additional stress barrier that the dike has to overcome. Alternatively, other magma/serpentine interactions could lead to serpentinites being a natural barrier to dike propagation. For example, if the hot dike magma induces rapid devolitilization of serpentine at the serpentine contact, this large pulse of volatiles could induce fracture along the serpentinized mantle interface that favors the dike propagating alongside, rather than into the region of serpentinized mantle. Furthermore, serpentine devolitilization is strongly endothermic, thus favoring more rapid dike cooling/freezing. This does not exclude the possibility that melt eventually intrudes the serpentinite layer, but the presence of serpentinite can hinder the intrusion of melt through serpentine to reach shallower crustal levels and/or reach the surface (Fig. 2.16a1-a3).

In contrast, if melt ascends to underplate the crust prior to serpentinization, will deepen regions of potential serpentinization to hotter levels in the mantle, where serpentinization is less likely. Hence, I have modelled that where there is underplating serpentinization cannot be generated (Fig. 2.16b1-b3).

Although some melt could be intruded within the crust and /or extruded, I am not considering this at the moment but instead it would be interesting to explore how the heat released by the instantaneous dikes affects the serpentinization process. In Figure 2.17 I show a preliminary test comparing the effect of heat release on the region of serpentinized mantle for the model with mafic granulite lower crust, 40 km thick-crust and extended by 3 mm/yr. It can be seen that the potential zone for the generation of serpentinites is affected by the input of heat emerging from the subsequent emplacement of dikes. In the model with heat release (Fig. 2.17b) the zone of serpentinized mantle in the distal margins is smaller because the temperature structure has been shifted from the thermal stability limits of serpentinization. This feedback between heat release and generation of serpentinization may have an impact in the amount of serpentinization resulting in other settings as well.

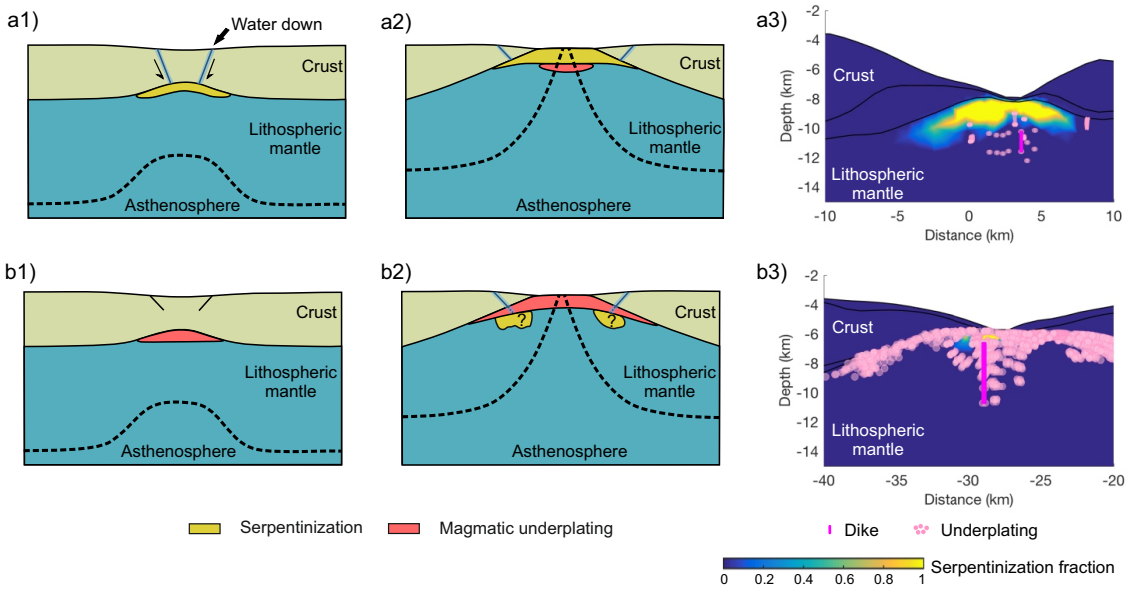

Figure 2.16: Cartoons and numerical models showing two break-up styles of magma-poor continental rifting. a1) Serpentinization starts due to the formation of crustal-scale faults that act as conduits for the water and reach the mantle before melting starts. a2) The serpentinized layer acts as an 'impermeable' barrier for upwelling melts. a3) Numerical model where the dikes are located below the serpentinized zone, the resulting COT shows exhumed and serpentinized mantle underlain by frozen magmatic portions. b1) Melting starts before serpentinization because the formation of crustal-scale faults is delayed. b2) The underplated melt reduces the formation of serpentinites because the potential mantle zone for serpentinization goes deeper and hence, hotter. b3) Numerical model where the underplating inhibits larger generation of serpentinization, therefore, no exposed serpentinized mantle is observed at resulting COT.

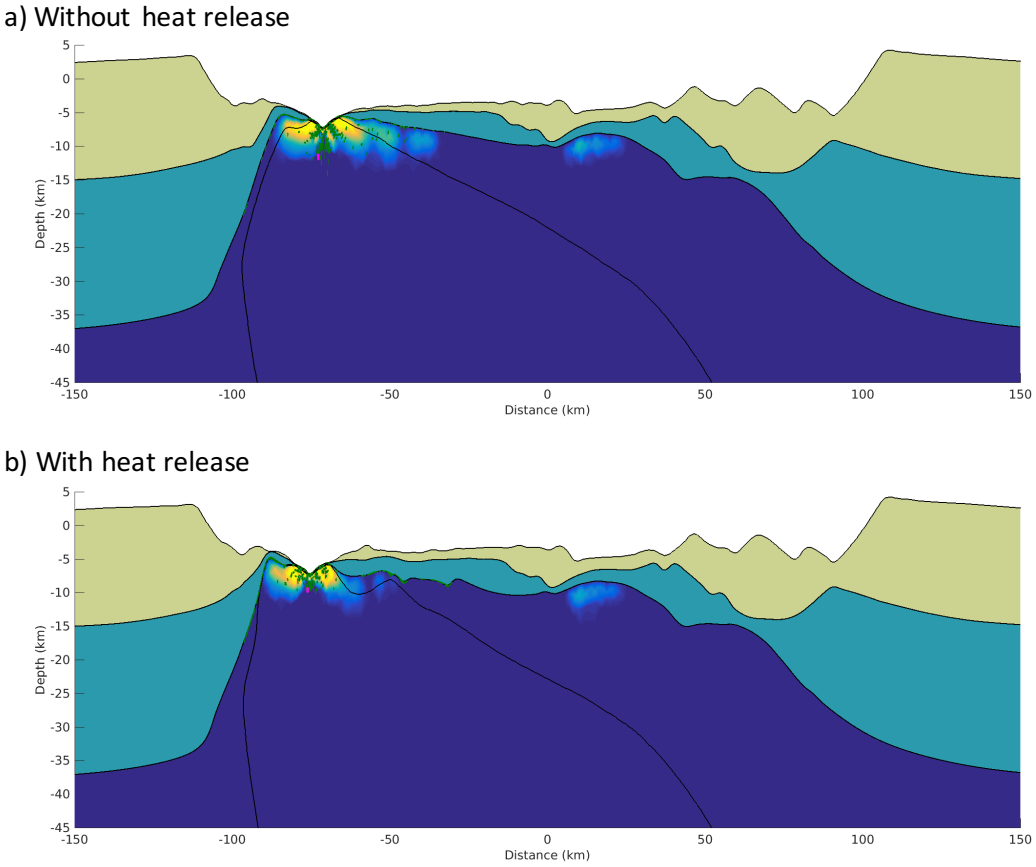

Figure 2.17: Effect of heat release on the final region of serpentinized mantle for a model with mafic granulite, 40 km crustal thickness and half-extension of 3 mm/yr. a) Without including heat release of dikes and b) including heat release.

CHAPTER

3

Testing the sensitivity of margin development to input parameters: a general study

3.1 Model setup

During the PhD research, the numerical code has been in constant evaluation and improvement with the aim of achieving increasingly realistic models that can be compared to natural examples. It is well known that numerous factors can influence the style of deformation during continental extension, and many studies have already thoroughly explored a range of them, such as lithospheric temperature or composition. Therefore, this chapter focuses on the selection of a set of fixed parameters that will be common to all models presented in this dissertation. The choice of these parameters is based on geological observations and/or sensitivity tests. Here I first explain and discuss the default features of the model setup, such as the initial thermo-rheological properties of the lithosphere and asthenosphere, and secondly, I present sensitivity tests of the model to mesh resolution, water content in the mantle and mechanisms of strain localization.

3.1.1 Rheological profile

The tests ran in this thesis have model dimensions of 400 km deep by 400 km wide, where half-extension velocities are applied to the lateral boundaries (as shown in Fig. 2.3) to model continental rifting. The stratification of the crust and mantle is shown in Fig. 3.1, composed of upper and lower crusts and lithospheric and asthenospheric mantles. For the upper crust, a wet quartzite rheology is used. For the lower crust, two end-member rheologies are chosen to address the variability in styles of the tectonic rifted margins and the continent-ocean transition (strong mafic granulite and weak wet quartzite). Chapter 4 also includes a rheology of intermediate

strength (wet anorthite) and Chapter 5 includes a very weak rheology (dry quartzite) for comparison with previous numerical models. Figure A.1 shows the effective viscosity for the range of lower crustal rocks used in this study and few more examples for strength comparison. I use dry olivine for the lithospheric mantle and wet olivine for the asthenospheric mantle. Table 3.1 shows the rheological parameters used for these rheologies.

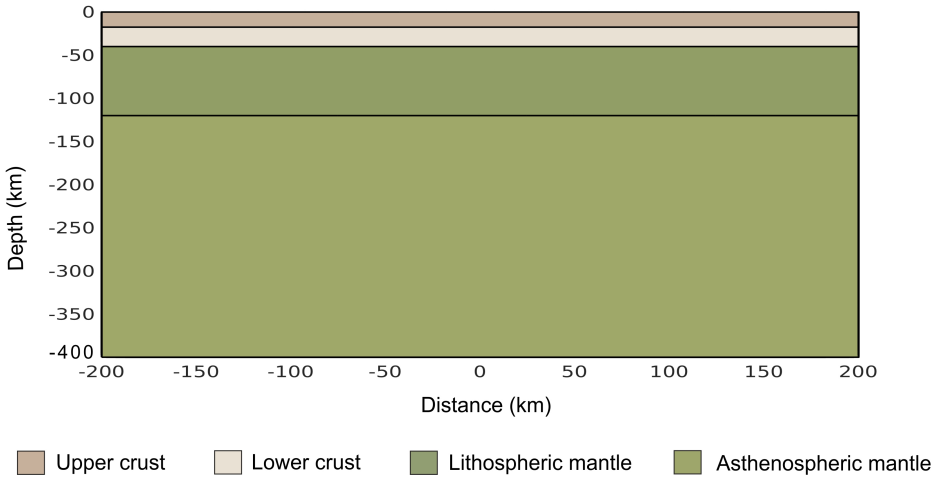

Figure 3.1: Initial setup of the numerical model with stratification of the crust and mantle.

Rock type	$\boldsymbol{log(B_{dis})}$ $(log(Pa^{-n}s^{-1}))$	$\boldsymbol{n_{dis}}$	$\boldsymbol{E_{dis}}$ $(kJmol^{-1})$	$\boldsymbol{log(B_{diff})}$ $(log(Pa^{-n}s^{-1}))$	$\boldsymbol{n_{diff}}$	$\boldsymbol{E_{diff}}$ $(kJmol^{-1})$
Wet quartzite	-28.00	4.0	223	0	0	0
Mafic granulite	-21.05	4.2	445	0	0	0
Wet anorthite	-15.40	3.0	356	0	0	0
Dry olivine	-15.56	3.5	530	-8.65	1	375
Wet olivine	-15.05	3.5	480	-8.65	1	335

Table 3.1: Rheological parameters. Mafic granulite (Wilks and Carter, 1990), wet anorthite (Rybacki and Dresen, 2000), wet quartzite (Gleason and Tullis, 1995), wet and dry olivine (Hirth and Kohlstedt, 2003)

.

3.1.2 Thermal age

In the numerical model, the volumetric heat production H of the heat conservation equation (Eq. 2.13) includes the sum of two terms: H_p, the decay of radioactive isotopes ^{238}U, ^{232}Th and ^{40}K and H_s, the heat dissipation from irreversible non-elastic deformation, i.e. shear heating. Radioactive heat production depends on the rock type, with values typically of $2 \cdot 10^{-6} Wm^{-3}$ in granites, $2 \cdot 10^{-7} Wm^{-3}$ in basalts and $2 \cdot 10^{-8} Wm^{-3}$ in mantle rocks (Turcotte and Schubert,

2002). Shear heating is important for the localization of lithospheric shear zones (White et al., 1980) since it transforms inelastic deformational work to heat, and it is calculated as (Lu et al., 2011)

$$H_s = \sigma'_{ij}\dot{\varepsilon}^{inel}_{ij} = \sigma'_{ij}\left(\dot{\varepsilon}_{ij} - \frac{1}{2\mu}\frac{D\sigma'_{ij}}{Dt}\right) \tag{3.1}$$

where σ'_{ij}, ε_{ij} and ε^{inel}_{ij} are deviatoric stress, deviatoric strain rate and deviatoric inelastic strain rate respectively, μ is the elastic shear modulus and $\frac{D\sigma'_{ij}}{Dt}$ is the Lagrangian time derivative of stress.

The estimation of the thermal lithospheric structure is based on assuming the steady-state solution of the heat conduction equation. The depth to the thermal lithosphere asthenosphere boundary (LAB) can be defined as the depth to a constant isotherm (e.g., 1300°C) or the intersection of the geotherm and the mantle adiabat (Artemieva, 2011). In this thesis, the thermal boundary conditions assume a surface temperature $T_0 = 0°C$ and a LAB temperature $T_{LAB} = 1300°$ at 120 km depth, below which the temperature is held constant with depth. Initially, the temperature of the model is set at 1300°C and the thermal solver runs for 500 Myr to obtain an initial steady-state geotherm (Fig. 3.2). This thermal profile corresponds to a Moho temperature of 634°C for a 40 km depth (and 574°C for a 35 km depth). The thermophysical parameters used in the thermal calculations are given in Table 3.2.

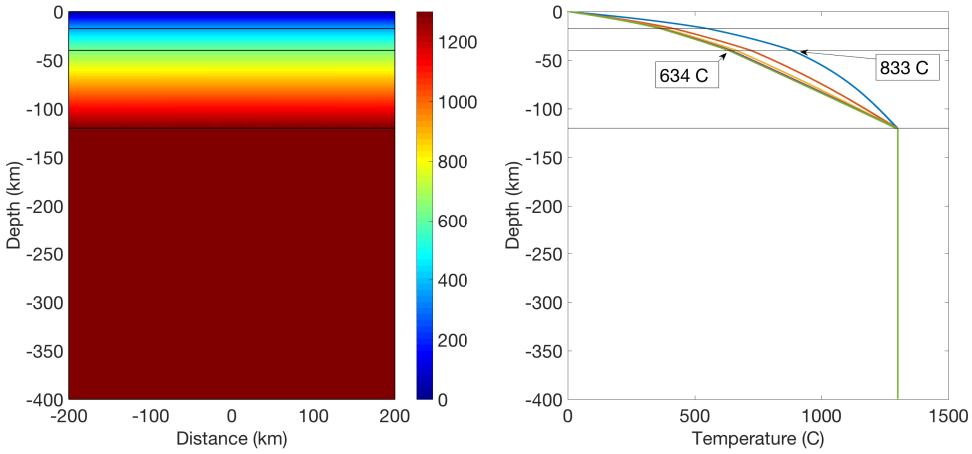

Figure 3.2: Temperature (°C). Left figure: Initial thermal profile (500 Myr). Right figure: Geotherm from 100 Myr (blue) to 500 Myr (green). The temperature at the Moho is 833 °C after 100 Myr and 634 °C after 500 Myr for a crustal thickness of 40 km.

Numerous studies have focused on the effect of the initial thermal structure on continental rifting (e.g., Buck, 1991; Gueydan et al., 2008; Ruppel, 1995; Svartman Dias et al., 2015a), thus, this thesis does not aim to further explore the temperature control parameter and assumes a common starting thermal age for all the models. Unraveling the initial thermal age of a continental

Lithospheric layer	k $(Wm^{-1}K^{-1})$	C_p $(J\,Kg^{-1}K^{-1})$	H_p (μWm^{-3})	ρ $(kg\,m^{-3})$
Upper crust	2.1	1200	1.3	2700
Lower crust	2.5	1200	0.2	2850
Lithospheric mantle	3.3	1200	0	3300
Asthenospheric mantle	3.3	1200	0	3300

Table 3.2: Thermophysical parameters for the rheologies used in this thesis (κ heat conductivity, C_p heat capacity, H_p radioactive heat production and ρ density). Thermal parameters are based on values from Currie and Hyndman (2006),Chapman (1986) and Hacker et al. (2015).

lithosphere prior to rifting is complicated but can be approximated to the 'tectono-thermal age', which accounts for the age of the last major tectonic episode that affected the crust and assumes that the underlying mantle has the same age (Artemieva, 2006). According to the tectono-thermal age global model of Artemieva (2009), the South Atlantic continental lithosphere varies from the Archean to the Proterozoic (Fig. 3.3), which is a region of interest to apply the parameter study of this thesis (see Chapter 5). The final stage of extension in the South America and Africa rift started at the conjugate Santos-Benguela margins about 113 Ma and ended at the Equatorial Atlantic domain at 103 Ma (Heine et al., 2013). This means that our initial thermal age of 500 Myr corresponds to the late Proterozoic Eon (613 Ma) in agreement with the tectono-thermal ages of the mobile belts at theses margins (Fig. 3.3). The surface heat flow that results from this initial geothermal gradient is 55 mWm^{-2}, that compared to the present-day onshore values is in the range for the South Atlantic margins (Artemieva, 2009; Hamza and Vieira, 2012).

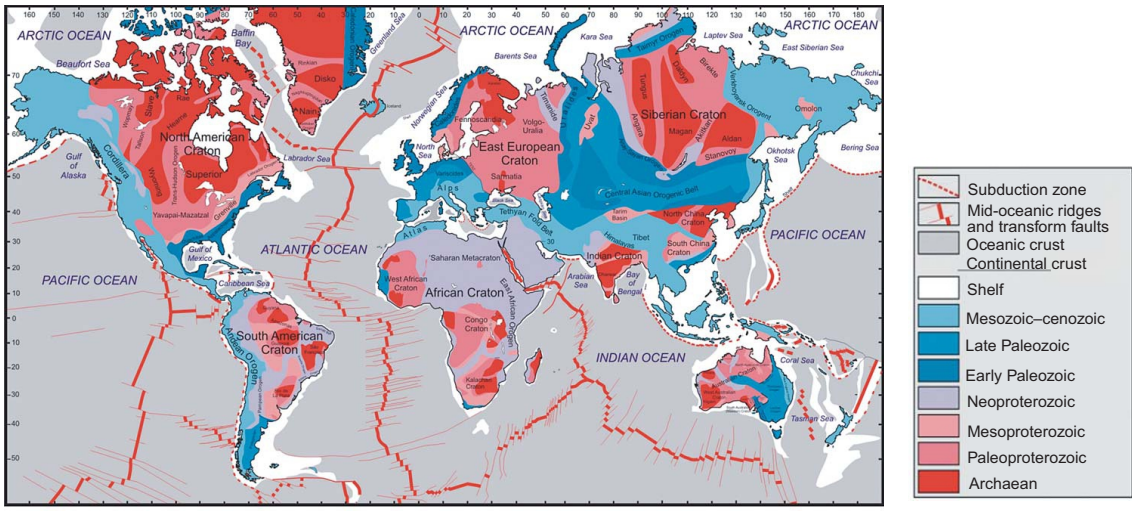

Figure 3.3: Tectono-thermal age of the continental lithosphere: Mesozoic-Cenozoic (250-0 Ma), Late Paleozoic (400-250 Ma), Early Paleozoic (543-400 Ma), Neoproterozoic (1.0-0.54 Ga), Mesoproterozoic (1.6-1.0 Ga), Paleoproterozoic (2.5-1.6 Ga) and Archean (3.8-2.5 Ga). Modified from Schubert (2015).

3.1.3 Compositional lithosphere

The initial version of the numerical code used constant densities for the four rheological layers composing the lithosphere-asthenosphere system. Figure 3.4 shows the first and last stage of a model extended at a constant half-rate of 5 mm/yr with constant densities. However, rocks density typically decreases with increasing temperature because of thermal expansion and with melt depletion due to compositional changes.

Hence, I implemented the equation of density as a function of temperature and depletion

$$\rho = \rho_0(1 - \alpha(T - T_0) - \beta F) \tag{3.2}$$

where ρ_0 and T_0 are the reference density and temperature, respectively, α is the coefficient of thermal expansion $\alpha = -\frac{1}{\rho}\frac{\partial \rho}{\partial T}$, β represents the decrease in density of the residue with melt depletion (Armitage et al., 2013; Nielsen and Hopper, 2004), with a value of 0.044 for Proterozoic lithosphere, and F is melt depletion, for example F = 0.2 denotes a solid residue of 20% melting. In absence of phases transformations, lithospheric rocks have small thermal expansion, on the order of $10^{-5}K^{-1}$ (Gerya, 2009), which is assumed to be independent on temperature, so we use a constant value of $2.4{\cdot}10^{-5}K^{-1}$ for the crust and $3.0{\cdot}10^{-5}K^{-1}$ for the mantle.

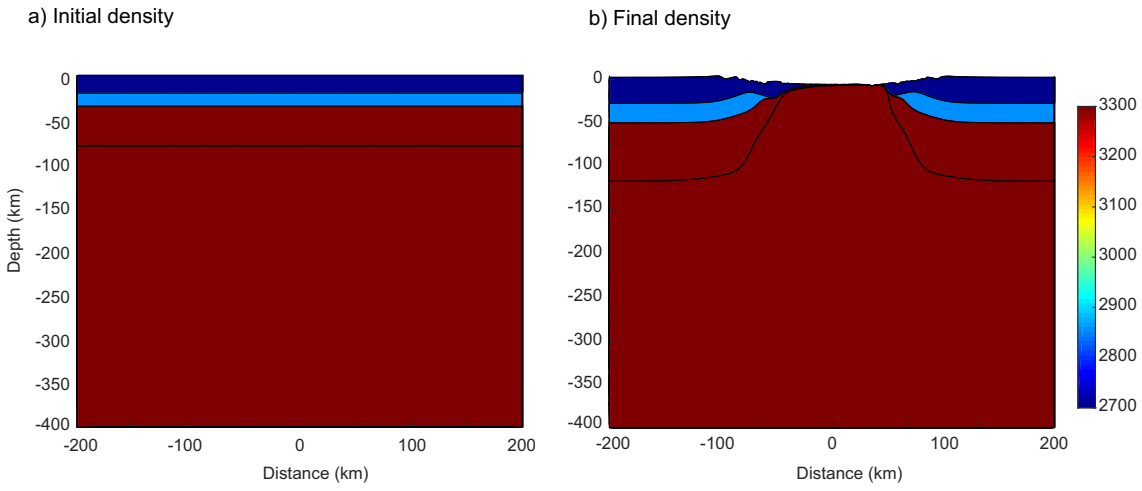

Figure 3.4: Model with constant density for each compositional layer: upper crust 2700 kg/m^3, lower crust 2850 kg/m^3 and mantle 3300 kg/m^3. Rheologies are upper crustal wet quartzite, lower crustal mafic granulite, lithosphere mantle dry olivine and asthenospheric wet olivine. Half-extension velocity of 5 mm/yr. a) Initial densities . b) Densities after lithospheric break-up.

I also included the effects of the compositional layers on the calculation of density (Fig. 3.5). For that, I initialized a 3-layers model with a melt depletion profile. The degree of depletion is 0% from the bottom of the model (400 km) to 130 km depth. From 130 km to the base of the thermal lithosphere (120 km) the degree of depletion increases linearly until 4%. From the base

of the lithosphere to 60 km depth depletion linearly increases to 10%. Finally, the depletion has a constant value of 10% for the first lithospheric 60 km. These depletion-discontinuities are based on the change from spinel to garnet at approximately 60 km depth that implies a decrease in density of about 3%. The rheology of the mantle depends on the degree of depletion. When the mantle is 0% depleted, the rheology used is wet olivine with a water content of 125 ppm H/Si (Hirth and Kohlstedt, 2003; Rüpke et al., 2006). When the mantle is 4% depleted, the rheology used is dry olivine assuming that all water has been extracted (Morgan, 1997). The transition from 0 to 4% depletion uses a mixture of both rheologies (wet and dry olivine) proportional to the degree of depletion. Also, as progressive partial melting occurs in the ascending asthenospheric mantle, the increasing depletion affects the mantle rheology, changing from wet olivine to dry olivine after a depletion of 4%.

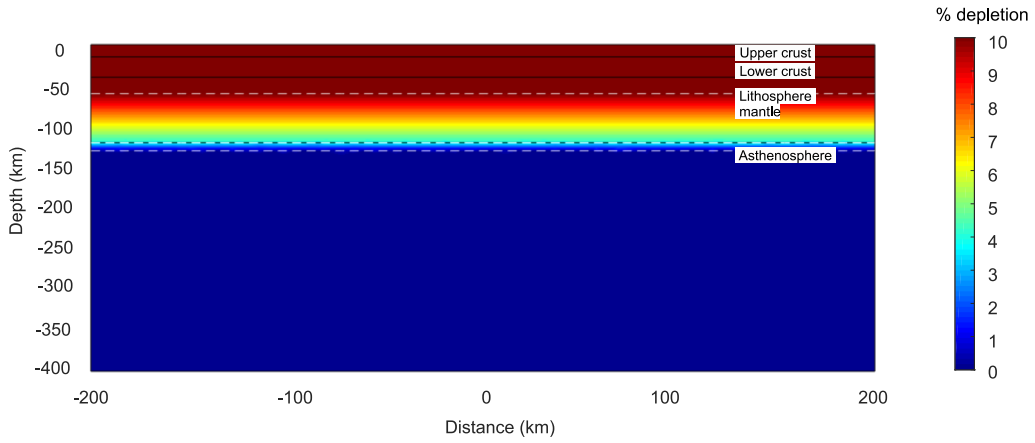

Figure 3.5: Initial depletion profile for the numerical models. White dashes lines indicate changes in the depletion amount. Black solid lines show lithospheric and asthenospheric layers. A gradual increasing in depletion occurs in the mantle, from 0% at 130 km depth to 4% at 120 km depth and to 10% at 60 km depth.

It is important to notice then that I define the thermal LAB at 120 km with a temperature of 1300 $°C$ (Fig. 3.2) and the compositional LAB as a 10 km thick transition, from 120 to 130 km, where depletion decreases from 4 to 0%. Although it is well-established that the LAB corresponds to a decrease in depth of seismic wave speeds, there is still debate regarding the sharpness of this transition. A sharp transition is defined when the presence of partial melt or water in the asthenosphere is taking into account as another mechanism involved in the contrasting properties of the lithosphere and the asthenosphere (Bartzsch et al., 2011). Based on studies of Sp and Ps receiver functions, a sharp LAB velocity gradient is estimated for Phanerozoic continental regions (Fischer et al., 2010, and references therein). A maximum thickness of 11 km is suggested for these tectonic environments, which matches the contrast between a chemically depleted lithosphere mantle and a partially melted or hydrated asthenosphere. Therefore, the

modeled compositional LAB in this study is a good estimation for the transitional thickness. Hereafter, I will refer to the 120 km deep thermal boundary when I speak of the LAB.

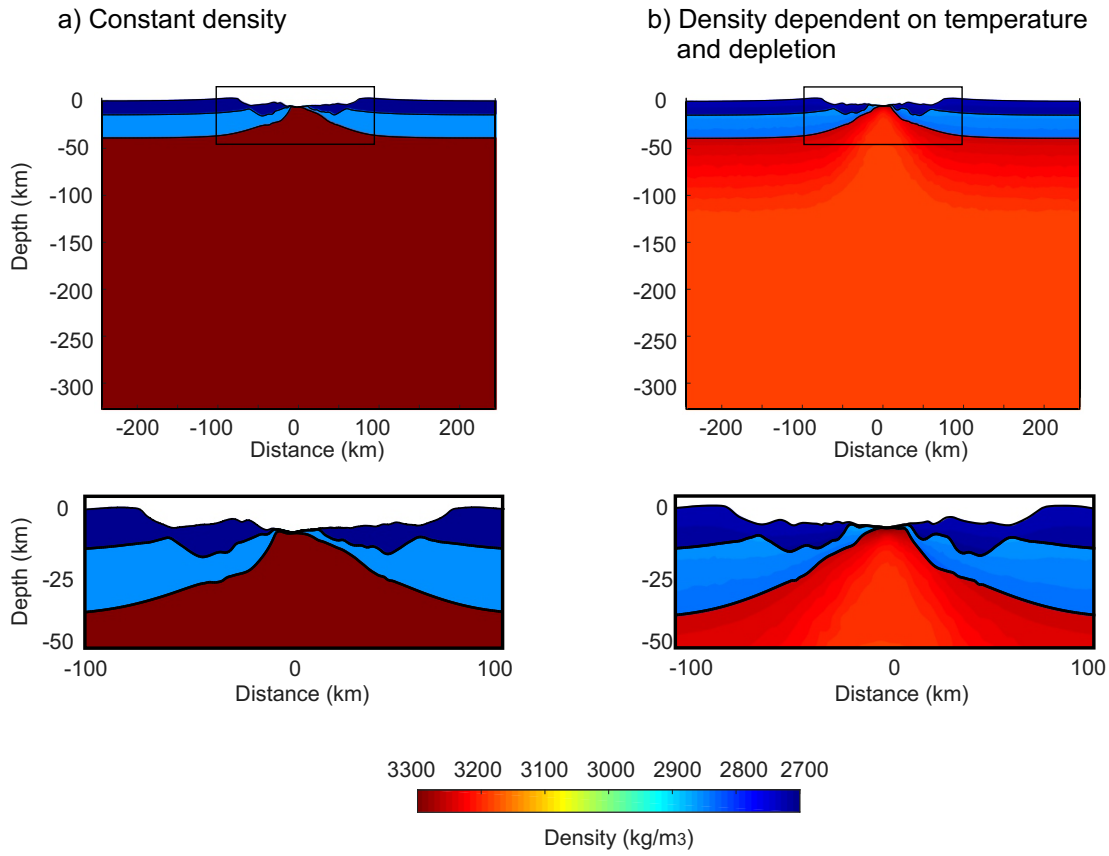

Figure 3.6: Comparison of models with a) constant density and b) density dependent on temperature and melt depletion. Both models with initial densities of 2700 kg/m^3 for the upper crust, 2850 kg/m^3 for the lower crust and 3300 kg/m^3 for the mantle. These tests do not include shear heating or water loading.

I compare the results of a reference model with constant densities and a second model with temperature- and depletion-dependent densities (Fig. 3.6a and b, respectively). The second model shows a decrease in density with depth within each layer, for the crust is about 20 kg/m^3 and for the lithospheric mantle about 100 kg/m^3. Including the dependence on depletion influences the density of the continental rifting mantle, it produces a less dense layer than in the case of density dependence on temperature alone and delays the formation of lithospheric drips deepening into the asthenosphere (Fig. 3.7), here the initial thermal boundary of the model has been fixed at the model bottom instead of the standard depth of 120 km. More depletion implies more buoyancy and less small-scale convection in the mantle and the curves of the magmatic crustal thickness over time vary as a consequence. Differences in the subsidence and uplift of the rift are also important implications that result from considering the temperature and depletion effects.

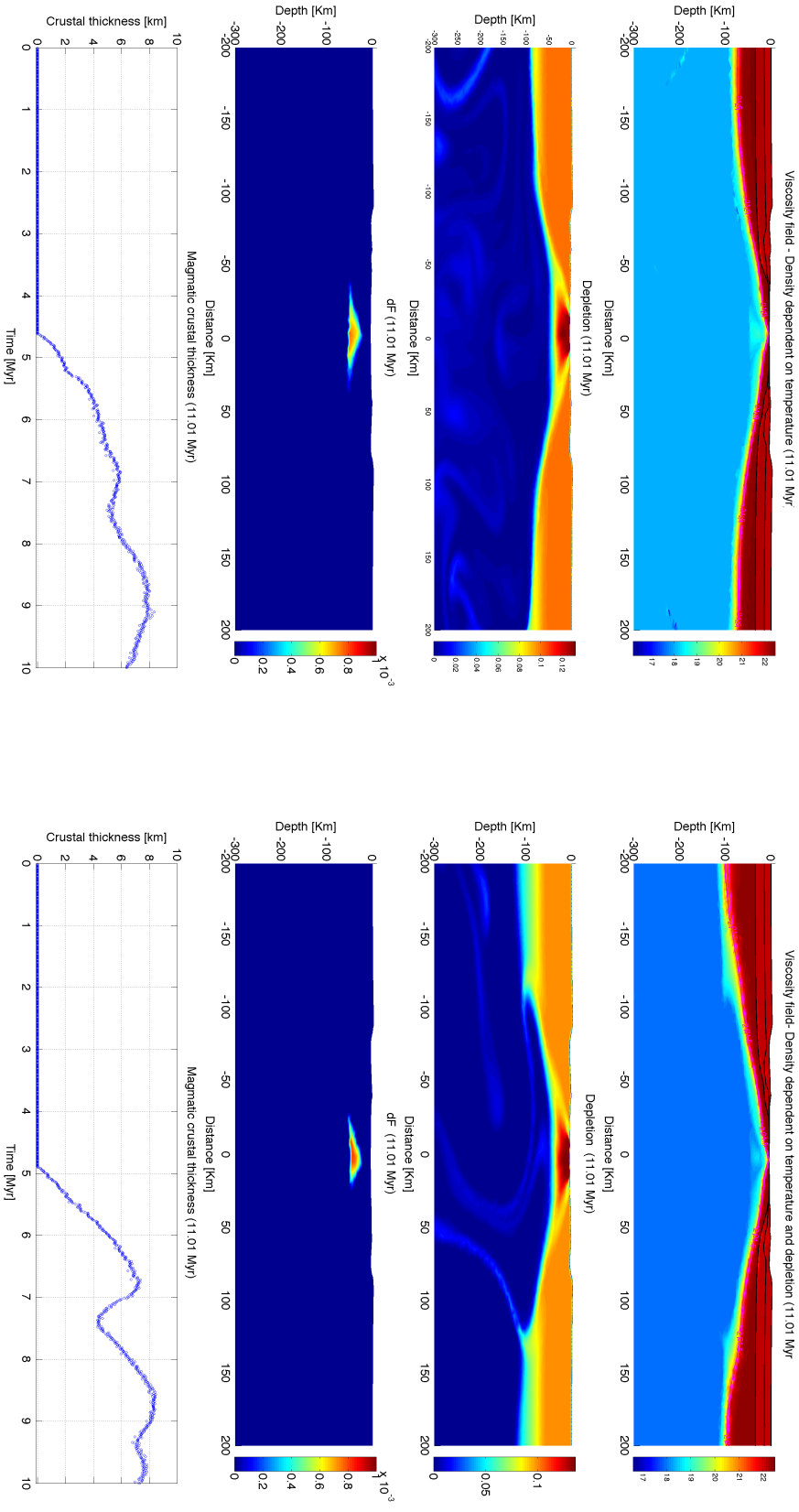

Figure 3.7: Comparison of models with density dependent on temperature (left panel) and density dependent on temperature and melt depletion (right panel). Both models with initial densities of 2700 kg/m^3 for the upper crust, 2850 kg/m^3 for the lower crust and 3300 kg/m^3 for the mantle. Left and right panels show from top to bottom: viscosity field, melt depletion (dF), instantaneous melting and magmatic crustal thickness. Thermal bottom boundary fixed at 400 km depth.

3.2 Sensitivity tests

3.2.1 Mesh resolution

The numerical models used in this thesis have a mesh resolution of about 1 km for the upper crust and 5 km for the lower crust and mantle, with 79841 nodes and 26385 triangular elements (Fig. 3.8a). The model has a significant higher spatial resolution in the upper crust to better resolve the topography and the development of faults in the brittle regime. In order to test the dependence of the mesh resolution on the model results, the same test was ran with an optimized resolution of about 1 km for each rheological layer, resulting in 815069 nodes and 271156 elements (Fig. 3.8b). Model parameters are shown in Table 3.1.

Figure 3.9 shows the strain rate evolution for the two models: the reference model and the optimized model (higher resolution). The model with higher resolution shows more defined shear zones in the lower crust 1 Myr after the onset of rifting, which promotes an initial basin slightly deeper and shorter in width (Fig. 3.9b). After 2.5 Myr, 5 blocks develop in the upper crust for both mesh resolutions but differ in the number and position of the active faults, being a bit more diffused in the case with lower resolution (Fig. 3.9c). Higher resolution promotes more rapid localization since the strain is accumulating at a higher rate, therefore, lithospheric break-up is reached at 4.91 Myr in the reference model and at 4.68 Myr in the optimized model. After lithospheric break-up, the main difference can be found in the topology of the interface separating upper and lower crust, however, the architecture of the rifted margins is very similar (Fig. 3.9e and f), both models show narrow and symmetric margins, with similar subsidence and uplift of the shoulders. Figure 3.10 shows that, close to the interfaces, the change in the second invariant of the deviatoric stress that is better resolved for the optimized model. Finally, Figure 3.11 depicts the evolution of viscosity for both models, the lower resolution in the mantle does not have a impact on the general model results.

I conclude that the reference model provides an adequate mesh resolution to test the different parameters controlling the pattern of rifted margin architecture. A higher resolution would not change the general outcomes and would increase the computational cost in approximately 8 times the resolution of a time step.

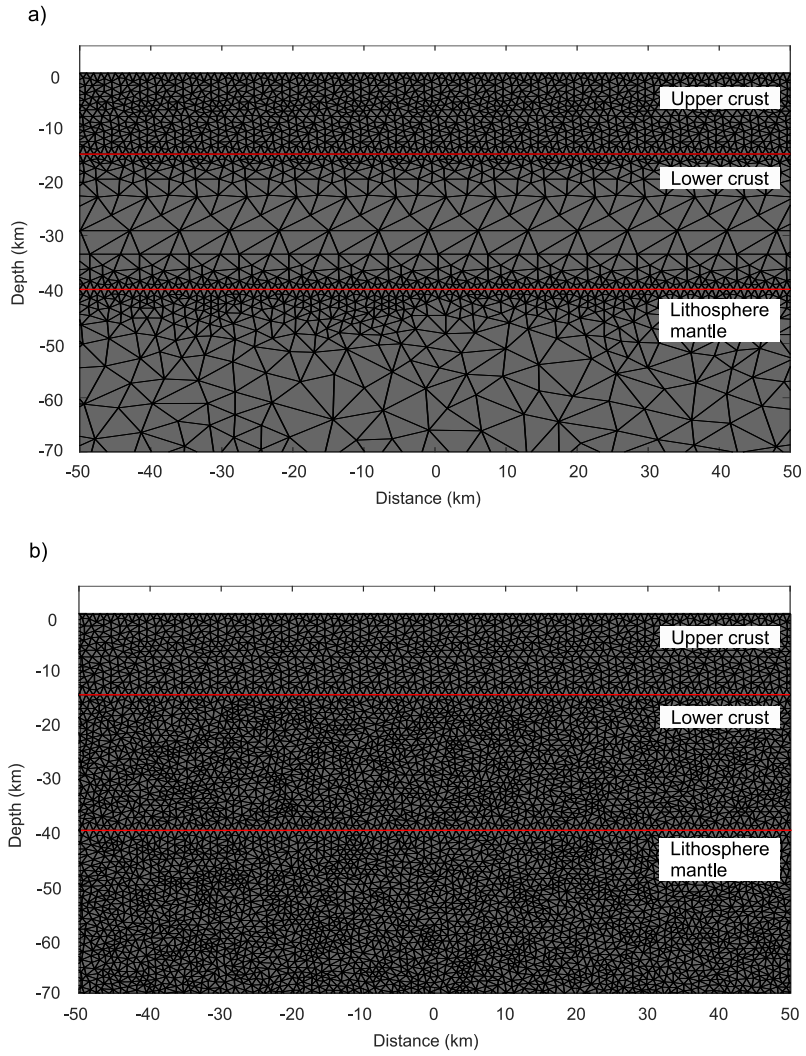

Figure 3.8: Initial mesh resolution. a) Reference model resolution b) Optimized model with higher resolution. Red solid lines are the lithospheric interfaces.

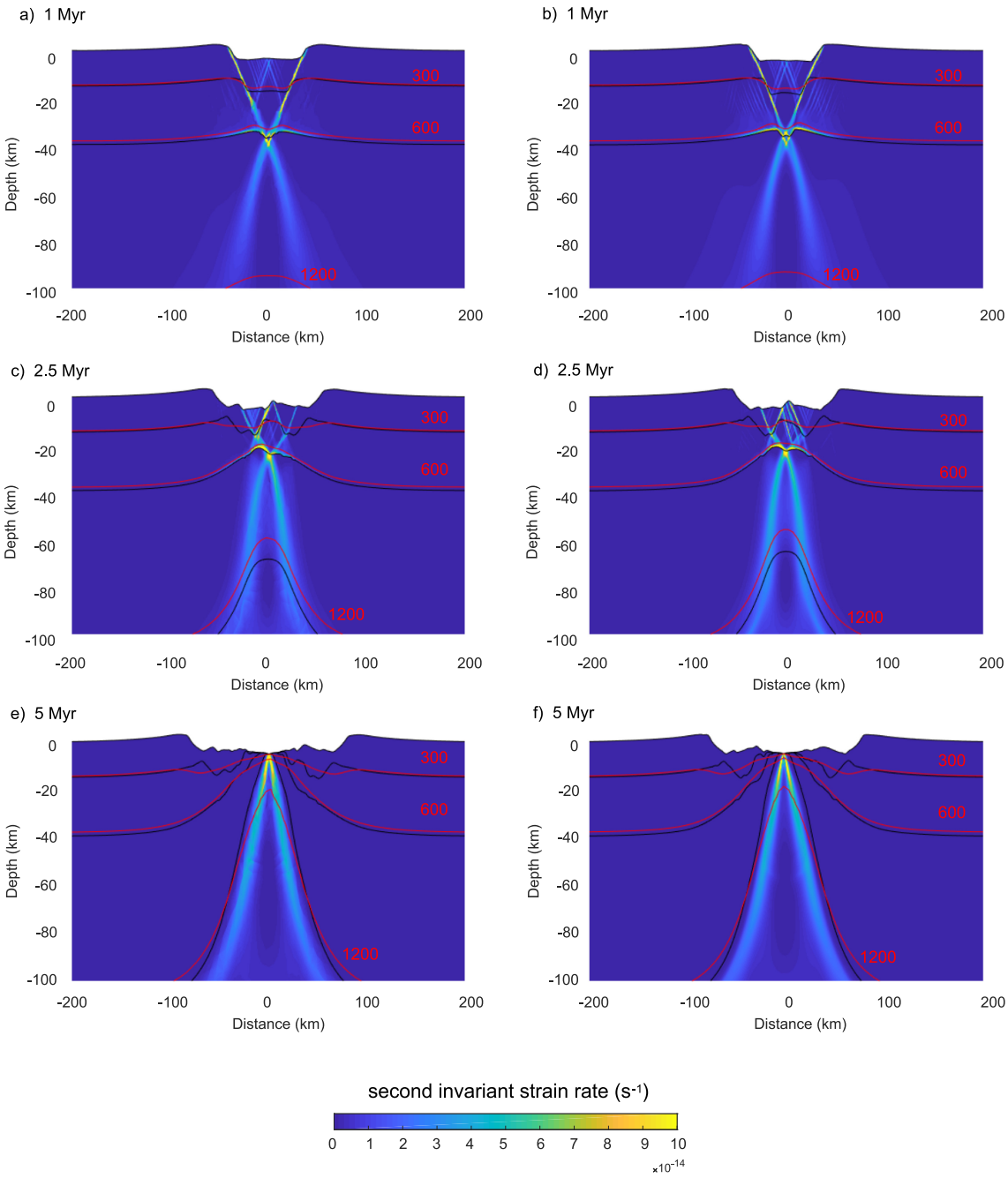

Figure 3.9: Model evolution of the second invariant of the strain rate. Left panel shows the model with a reference resolution and right panel with an optimized resolution. Black solid lines show the lithospheric interfaces. Red solid lines are isotherms ($^{\circ}C$).

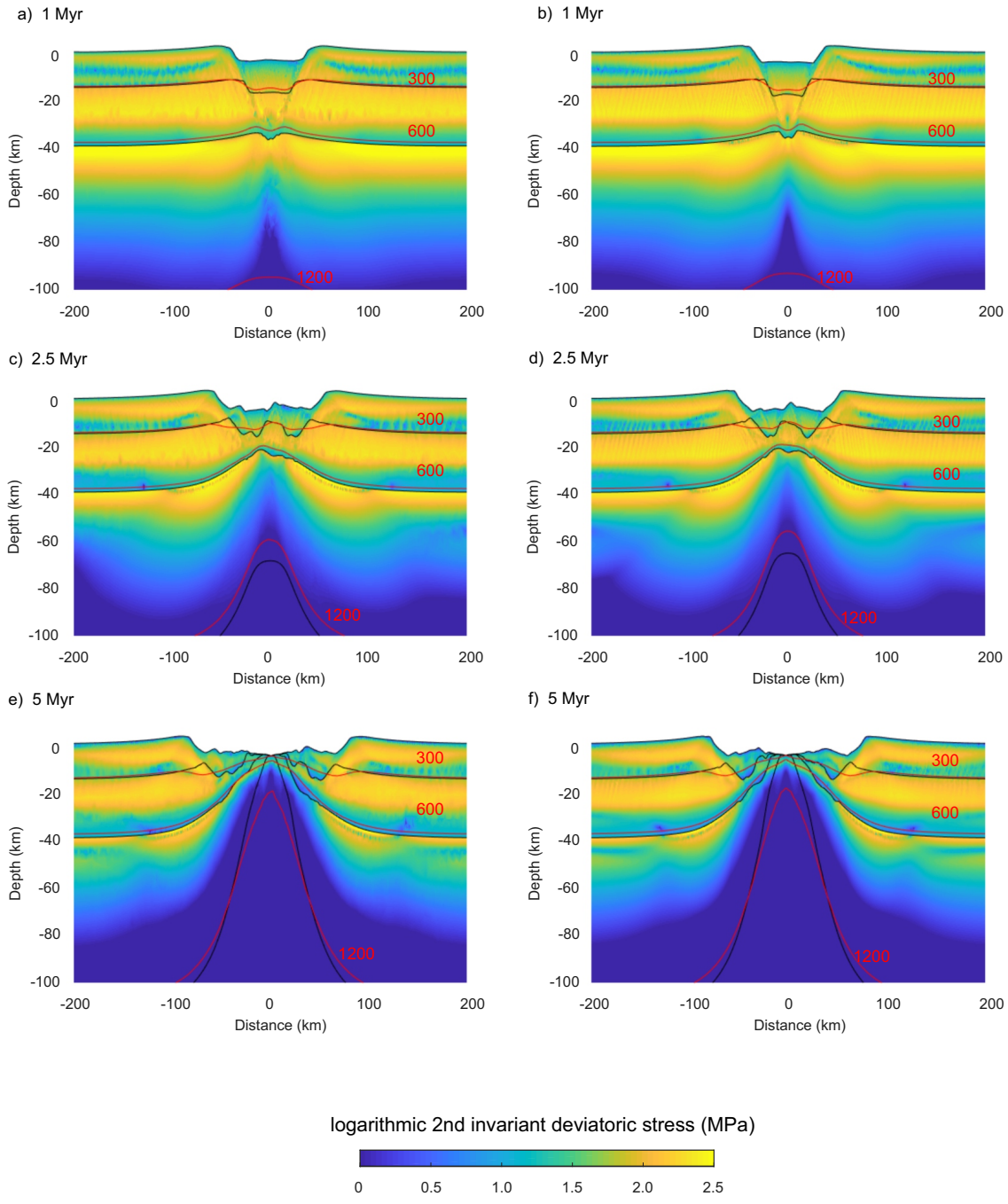

Figure 3.10: Model evolution of the second invariant of the deviatoric stress. Left panel shows the model with a reference resolution and right panel with an optimized resolution. Black solid lines show the lithospheric interfaces. Red solid lines are isotherms ($^{\circ}C$).

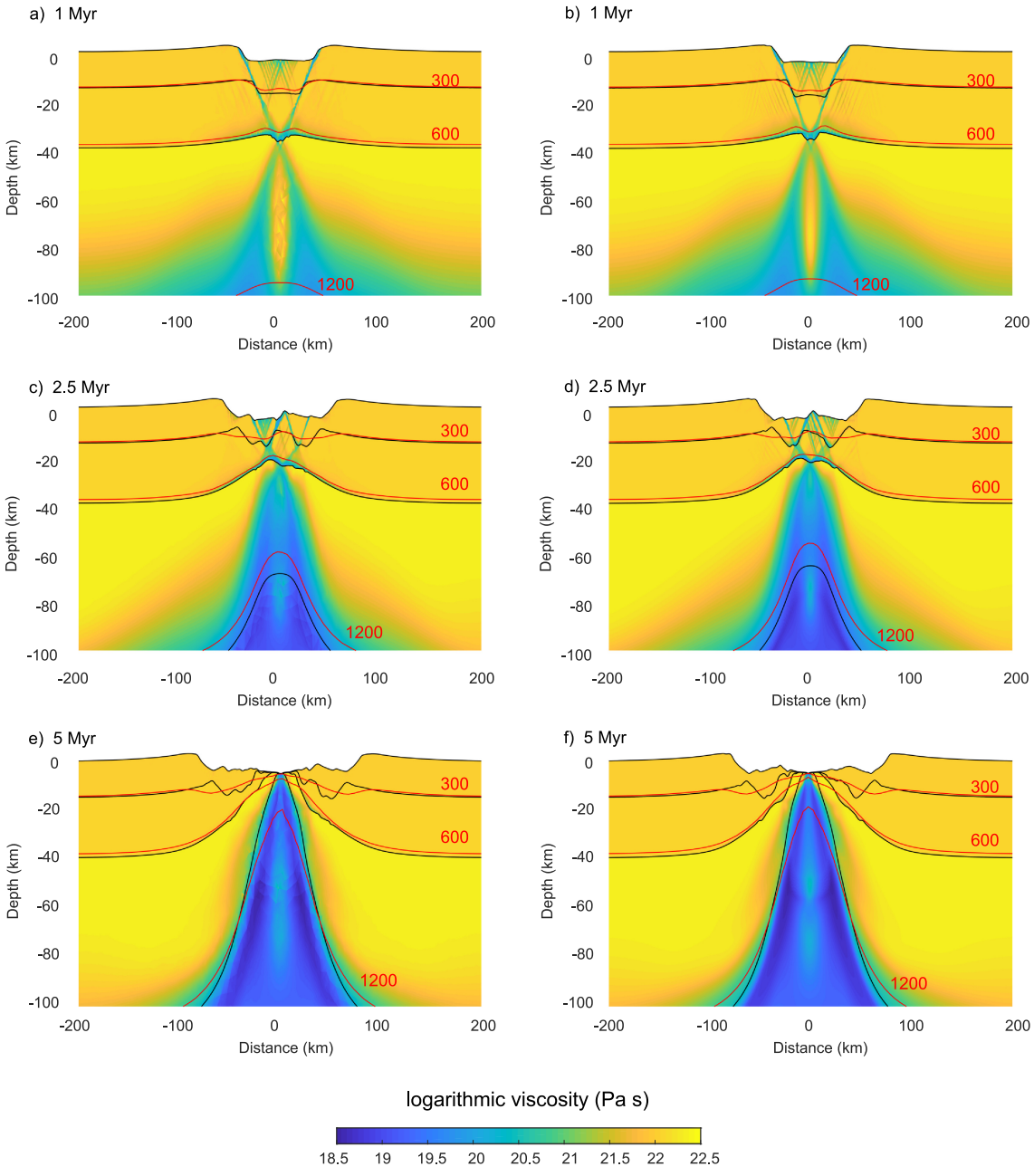

Figure 3.11: Model evolution of the viscosity. Left panel shows the model with a reference resolution and right panel with an optimized resolution. Black solid lines show the lithospheric interfaces. Red solid lines are isotherms ($^{\circ}C$).

3.2.2 Water content

Changes in the water content C_{OH} of rocks (Eq. 2.23) have an impact on the viscous behavior. The dominant effective viscosity will be the one with the lower viscosity between the dislocation and diffusion creeps (Eq. 2.25), where $m = 0$ for dislocation and $n = 1$ for diffusion gives

$$\eta_{dis} = FA^{-\frac{1}{n_{dis}}} C_{OH}^{-\frac{r}{n_{dis}}} \dot{\varepsilon}_{II}^{\frac{1-n_{dis}}{n_{dis}}} \; exp\left(\frac{E_{dis} + PV_{dis}}{n_{dis}RT}\right) \tag{3.3}$$

$$\eta_{dif} = FA^{-1} \, d^m \, C_{OH}^{-r} \; exp\left(\frac{E_{dis} + PV_{dif}}{RT}\right) \tag{3.4}$$

$$\eta_{eff} = \frac{1}{\frac{1}{\eta_{dis}} + \frac{1}{\eta_{dif}}} \tag{3.5}$$

The olivine flow law parameters used in this thesis are summarized in Table 3.3. The viscosity of the asthenosphere is lower than that of the lithosphere mantle in part because of the higher content in water. Different estimates for water content of the upper mantle are in the range of 50 to 200 $ppm\ H_2O$ (Hirschmann, 2006; Hirth and Kohlstedt, 2003; Rüpke et al., 2006). The COH values in the flow laws 3.3 and 3.4 have to be in unit of $ppm\ H/Si (= H/10^6 Si)$. The conversion factor is 12.5 for the bulk upper mantle, so the minimum estimate of 50 $ppm\ H_2O$ is 625 $ppm\ H/Si$ and the maximum estimate of 200 $ppm\ H_2O$ is 2500 $ppm\ H/Si$ (Warren and Hauri, 2014).

Rock type	**Creep**	$\boldsymbol{A}$ $(MPa^{-n}s^{-1})$	$\boldsymbol{n}$	$\boldsymbol{E}$ $(kJmol^{-1})$	$\boldsymbol{V}$ $(10^{-6}\,m^3mol^{-1})$	$\boldsymbol{m}$	$\boldsymbol{r}$
Dry olivine	dislocation	$1.1 \cdot 10^5$	3.5	530	13	0	0
	diffusion	$1.5 \cdot 10^9$	1	375	6	3	0
Wet olivine	dislocation	90	3.5	480	11	0	1.2
	diffusion	$1.1 \cdot 10^6$	1	335	4	3	1

Table 3.3: Rheological parameters of dry and wet olivine for the flow laws from Hirth and Kohlstedt (2003). Wet olivine parameters are for a water content C_{OH} constant with time.

Figure 3.12a shows the effect of water content in dislocation and diffusion creeps for a standard temperature range of the upper mantle (800 to 1600 K). For dislocation creep, a difference from 50 to 200 $ppm\ H_2O$ slightly varies the viscosity, however, for diffusion creep the change in water content reduces the viscosity about half an order of magnitude. Wet olivine rheologies have several orders of magnitude lower than dry olivine rheologies. The figure shows that dislocation creep is the dominant deformation mechanism in the lithosphere mantle (Karato, 2010) and diffusion creep dominates at temperatures closer to the LAB temperature (1600 K in our model). Since a dry olivine rheology may be more suitable to model old mantle regions, I compare the dislocation

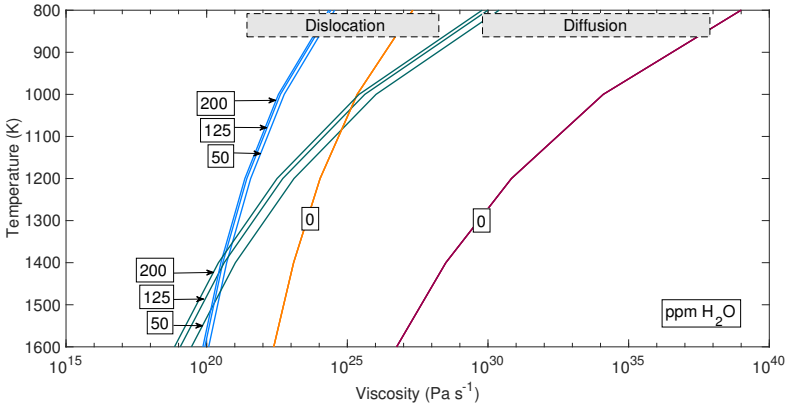

(a) Viscosity profile for dislocation and diffusion creep for different water content ($ppmH_2O$).

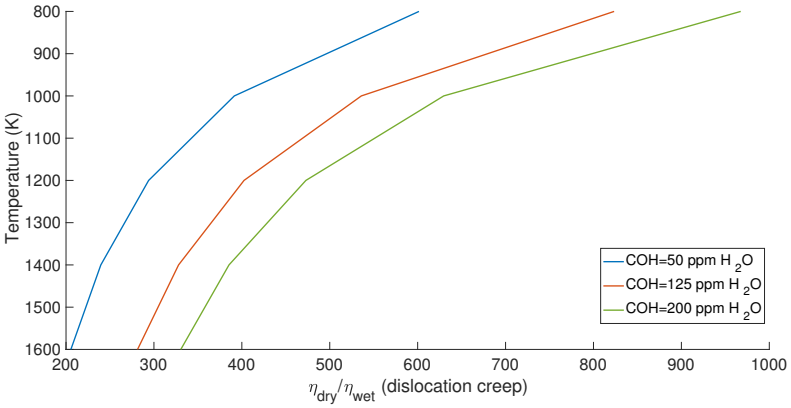

(b) Dislocation viscosity ratio η_{dry}/η_{wet}.

Figure 3.12: Water content effect on effective viscosity. a) Influence of water content and temperature in viscosity for dislocation and diffusion creep. Blue and orange lines are for dislocation creep. Red and green lines are for diffusion creep. b) Ratio of dry to wet dislocation creep viscosity. Based on a constant strain rate 10^{-14} and grain size of 6 mm.

viscosity ratio of dry olivine to wet olivine η_{dry}/η_{wet} for the variability in water content (Figure 3.12b). Hereinafter, I will assume the standard water content of 125 $ppm\ H_2O$ for the primitive wet asthenosphere of my numerical models. This water content for the wet mantle causes the viscosity of the dry mantle to be up to 500-fold the viscosity of the wet mantle, as suggested by Hirth and Kohlstedt (1996), Morgan (1997) and Lee et al. (2011).

Moreover, grain size d has a strong control on the diffusion creep (Eq. 3.4). As the grain size decreases diffusion creep becomes more important. I use a constant grain size of $6mm$ in this study which is a standard value for the continental lithosphere that ranges from 0.1 to 10 mm (Karato, 2010).

3.2.3 Strain localization mechanisms

The factors that control the asymmetry of continental rifted margins are still not understood. However, some progress has been made in defining the mechanisms that promote asymmetric rifting. Strain softening, shear heating and initial weaknesses are some of these processes in numerical modelling that I review in this section.

3.2.3.1 Strain softening

Shear zones develop in the viscous domain when the accumulated strain leads to dynamic recrystallization causing a reduction in the grain-size, which may reduce the effective viscosity (Brune et al., 2014; Huismans and Beaumont, 2003) (Figure 3.13 a, c). Other processes have been suggested to explain strain softening in viscous shear zones, such as dissipative heating (Regenauer-Lieb et al., 2006), phase changes (Brodie and Rutter, 1987) and the development of lattice preferred orientations (LPO) in the upper mantle (Tommasi et al., 2000).

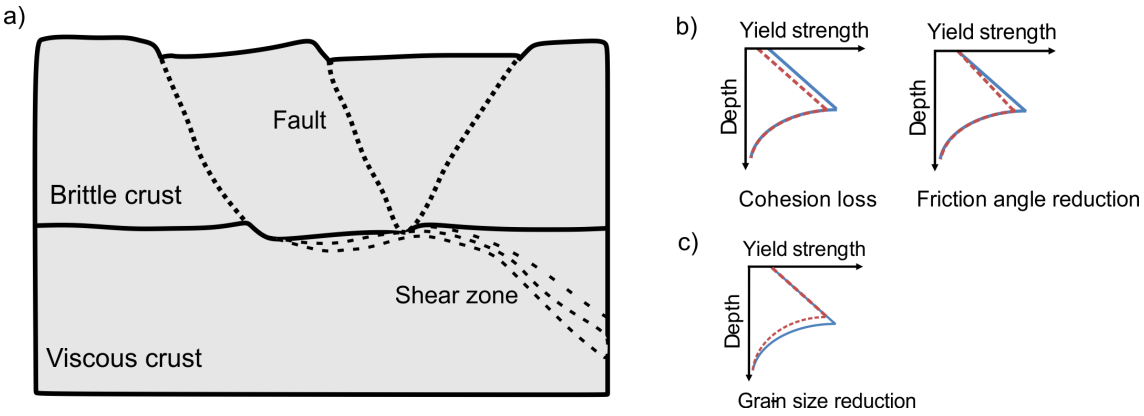

Figure 3.13: Weakening mechanisms for rock strength reduction. a) Faults develop where the crust behaves in a brittle manner and shear zones develop where the crust behaves viscously. b) Weakening processes for the formation of faults: cohesion loss and friction angle reduction. c) Weakening process for the formation of shear zones: grain size reduction. Blue solid lines represent the initial strength envelopes and red dashed lines represent the weakened strength envelopes. Modified after Buck et al. (1999).

Among these processes, dynamic recrystallization, and hence grain size reduction, is considered to have a dominant role (e.g., Platt and Behr, 2011). Therefore, the numerical code includes a factor α in the pre-exponential factor of the viscosity equation (Eq. 3.6) that linearly increases from α_1 to α_2 over an accumulated strain interval. The grain-size reduction promotes a change from dislocation to diffusion creep. However, this change will be temporary because of the fast grain growth occurring in diffusion creep. Even so, significant softening by grain size reduction will localize in shear zones if grain growth is inhibited (De Bresser et al., 2001). Previous studies show

that mantle strain softening via dislocation-accommodated grain boundary sliding decreases with temperature and is limited at temperatures higher than $800°C$ (Précigout and Gueydan, 2009). Based on this laboratory results, I introduce a temperature dependence on the strain viscous softening used in the numerical model. The strain- and temperature-dependent factor α in the viscosity equation reduces the effective viscosity as deformation accumulates

$$\eta = (\alpha A)^{-1/n} d^{p/n} f_{H_20}^{-r/n} \dot{I}_2^{(1-n)/2n} exp\left(\frac{E+PV}{nRT}\right) \tag{3.6}$$

The dependence of the α-factor on the accumulated strain is given by

$$\alpha(T) = (\epsilon_{IIh} - \epsilon_{IIh_1}) \frac{\alpha_2(T) - \alpha_1}{\epsilon_{IIh_2} - \epsilon_{IIh_1}} + \alpha_1 \tag{3.7}$$

where α_2 is temperature-dependent, with a value of 30 between $0°C$ and $800°C$ followed by an exponential decrease from $\alpha_2 = 30$ at $800°C$ to $\alpha_2 = 1$ at $1200°C$; $\alpha_1 = 1$, $\epsilon_{IIh_1} = 0$ and $\epsilon_{IIh_2} = 1$ (see Figure 3.14). In the viscosity equation (Eq. 3.6), α is raised to the inverse of n, meaning that a value of $\alpha = 30$ corresponds to a change in viscosity of about 0.4 compared to the undeformed rock.

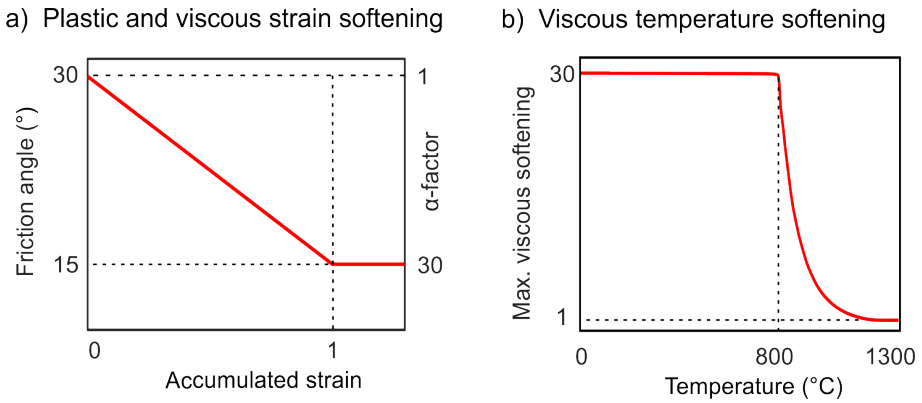

Figure 3.14: Weakening mechanisms to simulate the generation of faults and shear zones. a) Plastic and viscous strain softening: friction angle decreases from 30 to 15° and α-factor increases from 1 to 30 over an accumulated strain range of 0 to 1. b) Viscous softening: dependence of the maximum viscous softening factor with temperature (α in Eq. 3.7).

Figure 3.15 compares the viscous softening distribution with time for the models dependent on strain and on strain and temperature. The first model shows an increasing viscous softening in the lithosphere mantle and uppermost asthenosphere while the temperature cut-off of the second model inhibits the softening at temperatures higher than ca. 800°, so the viscous softening is focused at the upper part of the lithosphere and does not affect the asthenospheric mantle

upwelling.

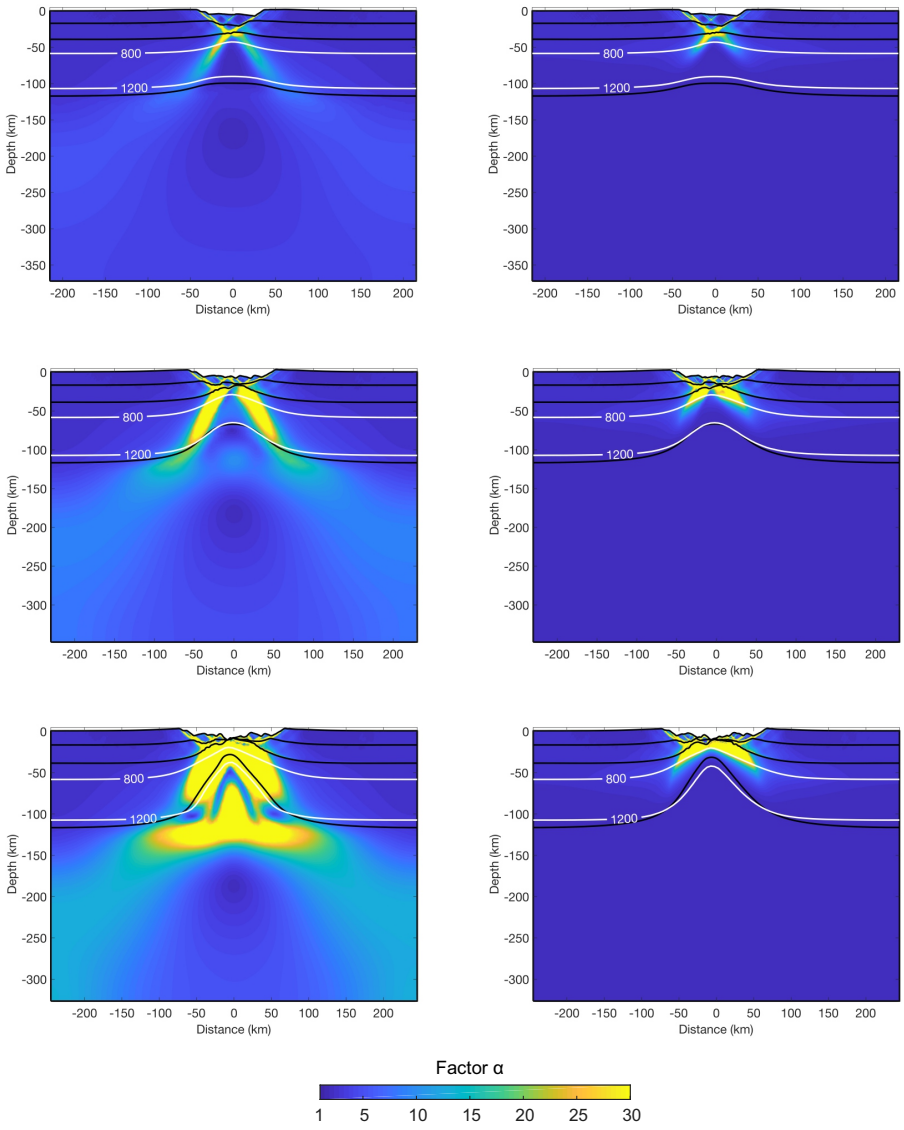

Figure 3.15: Viscous softening. Left panel: Only dependent on accumulated strain. Right panel: Dependent on accumulated strain and temperature.

In nature, fault planes or gouges represent mechanical discontinuities along which rock strength decreases. A reduction in the cohesion (Buck and Lavier, 2001) or in the angle of friction (Bos and Spiers, 2002) are two possible causes for rocks weakening. The cohesion is a pressure-insensitive rock property that results from the electrostatic grain bonding (Nemčok, 2016). Cohesion rock values are estimated between 10 and 20 MPa for sedimentary rocks and up to 50 MPa for crystalline rocks (Handin, 1966). Hereafter I assume a cohesion value of 10 MPa unless otherwise indicated. The angle of friction is a pressure-sensitive rock property controlled by the physical friction among grains (Nemčok, 2016). Examples of typical natural values are of 48° for Sioux

quartzite and 23° for quartz diorite (for more values see Nemčok, 2016). In numerical modelling, the rock values used for the angle of friction are in the range of 20 to 30°. Both cohesion loss and friction angle reduction imply that faults are typically weaker than the surrounding undamaged rock and susceptible of strain localization (Fig. 3.13 a, b; Kirby, 1985). Among the natural mechanisms that may result in fault weakening are the mineral transformations, foliation formation and high values of fluid pressure (Bos and Spiers, 2002; Sibson, 1990).

Plastic strain softening is commonly included in numerical models to simulate cohesion and friction angle weakening at faults, which is achieved by defining a parametrical function of some type of finite strain (Buck and Poliakov, 1998; Huismans and Beaumont, 2002; Lavier et al., 1999; Moresi et al., 2007). Scholz and Cowie (1990) showed how the loss of strength of faults as strain increases is very fast, approximately after 2 percent of strain.

Based on the above studies, I have used two approaches for plastic softening, both dependent on the friction angle ϕ. The first approach defines the friction angle as a function of the accumulated second strain invariant ϵ_{IIh}

$$\phi = (\epsilon_{IIh} - \epsilon_{IIh_1})\frac{\phi_2 - \phi_1}{\epsilon_{IIh_2} - \epsilon_{IIh_1}} + \phi_1 \tag{3.8}$$

where ϕ_1 is the initial friction angle, ϕ_2 is the softened friction angle and $\epsilon_{IIh_2} - \epsilon_{IIh_1}$ is the strain interval where plastic strain softening takes place. We set $\phi_1 = 30°$, $\phi_2 = 15°$, $\epsilon_{IIh_1} = 0$ and $\epsilon_{IIh_2} = 1$ (see Fig. 3.14a). The accumulated strain tensor ϵ_{IIh} is calculated from the deformation gradient (see Andrés-Martínez, 2016; Malvern, 1969).

The second approach reduces the friction angle with the accumulated plastic strain ϵ_p

$$\phi = (\epsilon_p - \epsilon_{p_1})\frac{\phi_2 - \phi_1}{\epsilon_{p_2} - \epsilon_{p_1}} + \phi_1 \tag{3.9}$$

with equivalent values to Eq. 3.8. In this case, the accumulated plastic strain ϵ_p is calculated following the formulation of Moresi et al. (2007) (see de Montserrat et al., 2018). I compare the distribution of both types of plastic softening in Figure 3.16. Although the differences in the distribution of the reduced friction angle arise from the choice of the plastic strain softening (Figure 3.16), the style of lithospheric thinning and geometries of the rifted margins remain similar for both cases. Figure 3.17 shows a zoom into the first 40 km of the lithosphere. A larger number of active shear bands appears in the model with softening dependent on ϵ_p. While the model dependent on ϵ_{IIh} accumulates significant strain and generates shear bands with longer slips at crustal-scales, the model dependent on ϵ_p shows shear bands not connecting upper and lower crusts until later in time. The resulting strength distribution is more accurate in the second case,

where plastic softening depends only on the plastic accumulated strain and can be compared to the results of previous studies (e.g., Naliboff and Buiter, 2015; Van Avendonk et al., 2009).

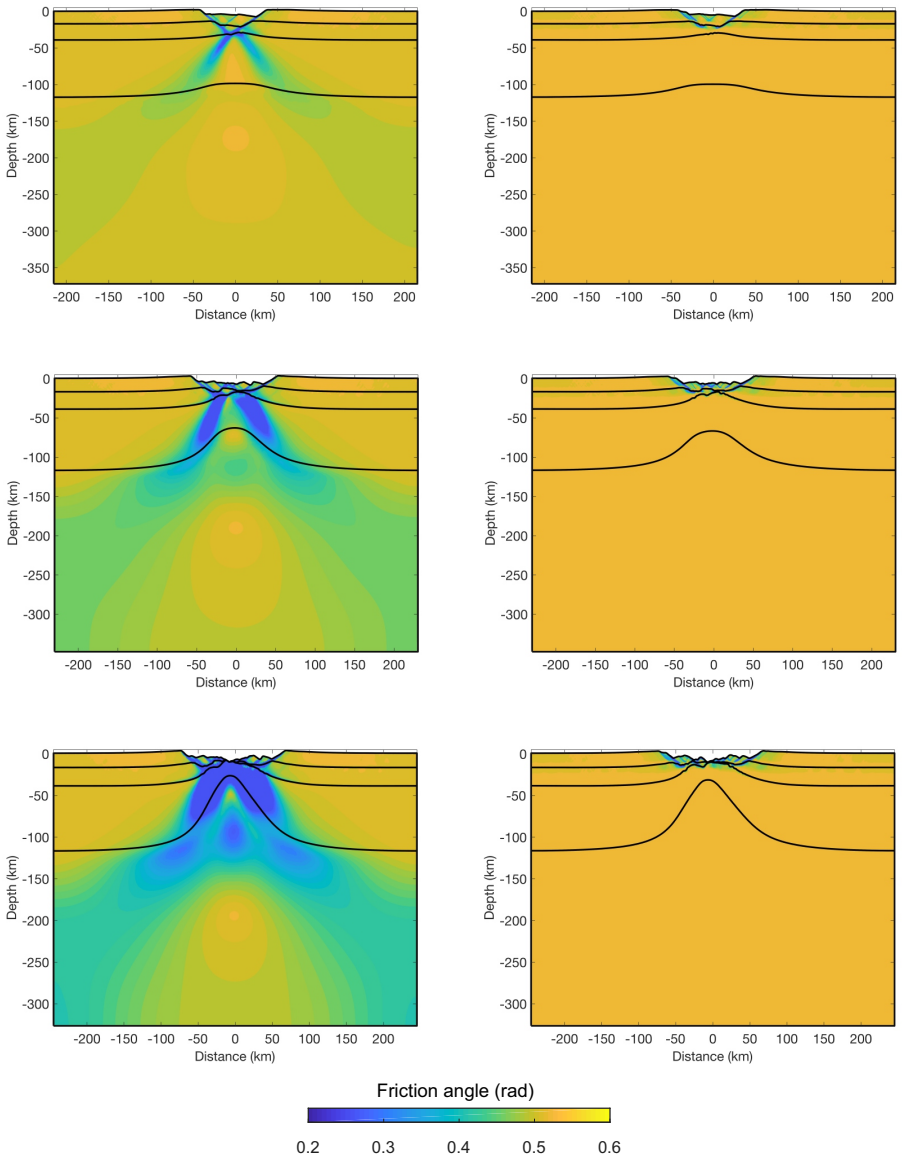

Figure 3.16: Plastic strain softening evolution. Left panel: dependent on the accumulated second strain invariant. Right panel: dependent on accumulated plastic strain.

Recently, Duretz et al. (2016) have explored the initiation of deformation in continental rifting by simulating tectonically inherited heterogeneities of kilometer scale resolution that reproduce similar results to the passive margins architectures. This structural softening does not require an ad-hoc weakening of material properties with accumulated strain, however the number and distribution of the weak/strong layers has to be determined in order to promote different modes of extension.

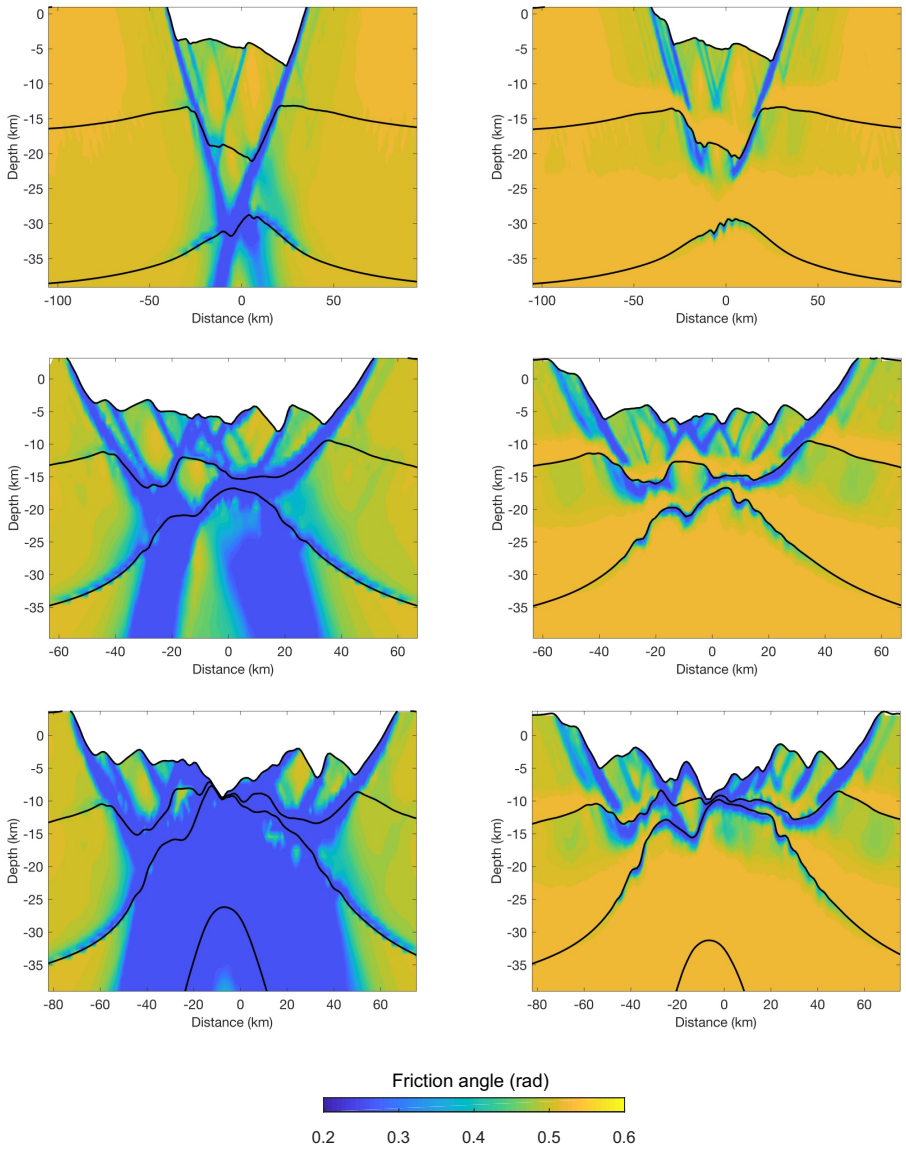

Figure 3.17: Plastic strain softening distribution: zoom of Figure 3.16. Left panel: dependent on the accumulated second strain invariant. Right panel: dependent on accumulated plastic strain.

Previous studies have made great contributions to the understanding of the role of plastic and viscous softening in geodynamical models (e.g., Frederiksen and Braun, 2001; Huismans and Beaumont, 2007, 2002, 2003). Huismans and Beaumont (2002) concluded that extension is symmetric in absence of strain softening and that may be asymmetric at a crustal or lithospheric scale by including plastic softening. This asymmetry is suppressed by high extension velocities and weak lower crusts. Frederiksen and Braun (2001) showed that the accumulated strain required to initiate viscous softening affects the deformation patterns in the lithosphere. However, plastic and viscous softening also interact with other model processes so it is important to have a better understanding of their role. In this work, I have focused on understanding the role of strain

softening on melting and small-scale convection. For this I have ran models that include a) no plastic or viscous softening, b) plastic and no viscous softening, c) plastic and viscous softening dependent on the accumulated strain and d) plastic and viscous softening dependent on the accumulated strain and temperature. These models are extended by 3 mm/yr at each side and consist of a wet quartzite upper crust, mafic granulite lower crust, dry olivine lithosphere mantle and wet olivine asthenosphere. Furthermore, the thermal boundary is fixed at the bottom of the model. Figure 3.18 compares the effective viscosity field, the streamlines and the magmatic crustal thickness of the models. The steady-state magmatic crustal thickness is taken as the constant melt production with time (Armitage, 2008). This value is expected to match the observed mid-ocean magmatic crustal thickness of different natural examples shown in Fig. 1.5 (see also Supporting information in Ros et al., 2017). The reference model (no softening, Fig. 3.18a) shows a symmetric mantle flow pattern from rifting to the sea-floor spreading. Decompressional melting starts 1 Myr before lithospheric break-up (24.4 Myr) and reaches a constant magmatic crustal thickness of 1.72 km.

The model including plastic softening (Fig. 3.18b) shows a similar but faster flow pattern, with localized faults that couple crust and mantle and upwell the mantle faster, therefore melt starts 4 Myr earlier (20.6 Myr) and produces a magmatic crustal thickness of 1.98 km at the steady-state. In this case lithospheric break-up occurs earlier than in the previous model, at 22.4 Myr. The other main difference between both models is that the one with plastic strain softening includes a weak small-scale convection pattern, while the reference one does not produce small-scale convection in the mantle.

The model that incorporates plastic and viscous strain softening promotes small scale convection before break-up of the lithosphere (Fig. 3.18c). At 14 Myr the accumulated strain at the rift axis reaches the critical strain 1 to depths of 120km, hence the factor multiplying the viscosity equation that simulates viscous softening reaches the maximum value (Fig. 3.18c) and the viscosity is reduced by 0.38. The large viscosity contrast in this asthenospheric region initiates convection cells, leading to an earlier decompressional melting (14.3 Myr) and larger amount of melt. Due to viscosity reduction the lithospheric layer starts to delaminate at the bottom. The steady-state crustal thickness is 3.15 km and lithospheric break-up occurs also earlier than in the cases without viscous softening, at 18.5 Myr.

Finally, the last model combines viscous strain softening with a temperature cut-off at $800°C$. Here, the α-factor influence is constraint to shallower levels, so convection cells are not generated before lithospheric break-up (Fig. 3.18d). Melting starts at 16 Myr and lithospheric break-up occurs at 18.9 Myr. The amount of melt generated in absence of convection is more similar

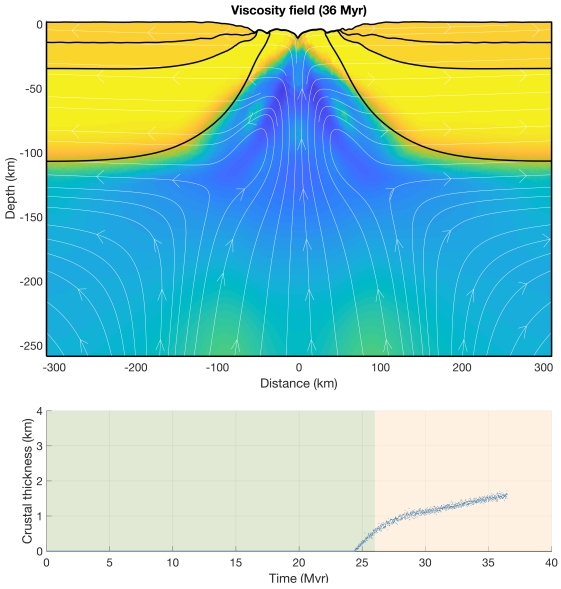

(a) Model evolution without plastic or viscous strain softening.

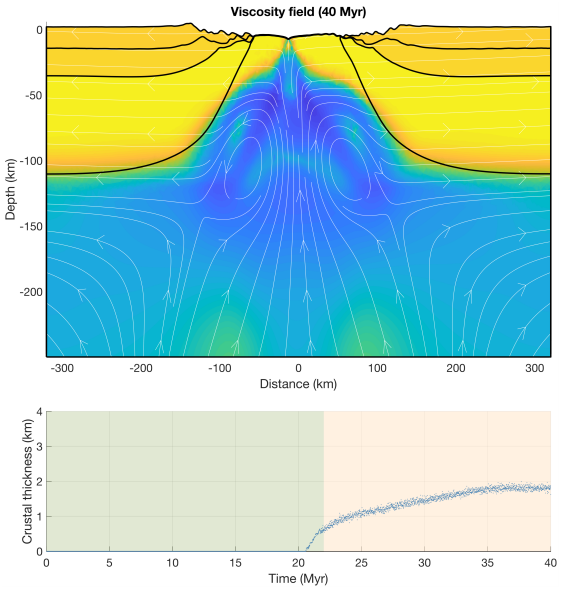

(b) Model evolution with plastic strain softening.

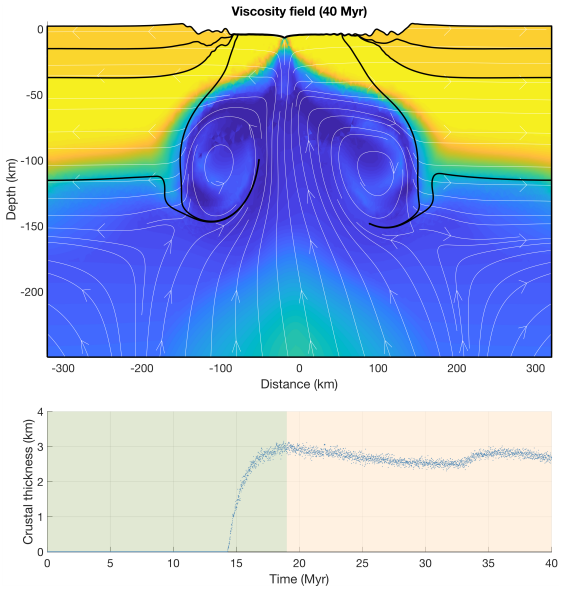

(c) Model evolution with plastic and viscous strain softening.

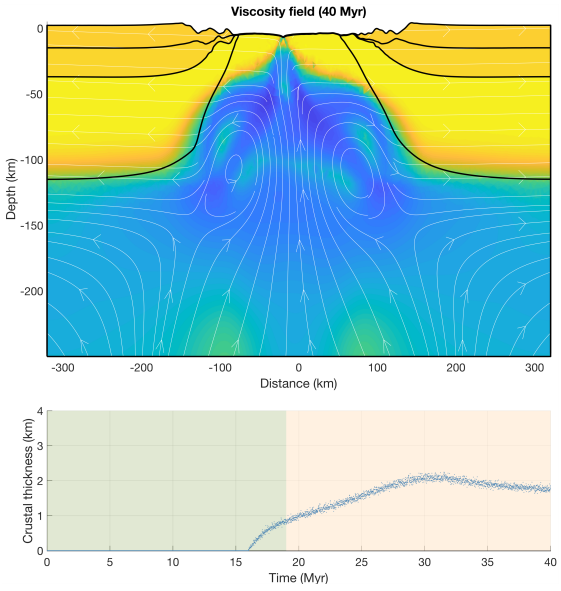

(d) Model evolution with plastic strain softening and viscous strain softening with a temperature cut-off at $800°C$.

Figure 3.18: Plastic and viscous softening effects on small scale convection (top) and melting (bottom). Top panels show viscosity field and flow pattern (streamlines). For viscosity colors refer to Fig. 3.11. Viscosity values change from $10^{18.5} Pa\,s$ (dark blues) to $10^{22.5} Pa\,s$ (light yellows). Bottom panels show syn-rift magmatic crustal thickness over green background and post-rift over orange background.

to the models without viscous softening, with a steady-state crustal thickness of 1.8 km. After lithospheric break-up the high temperature gradient creates gravitationally unstable stratification that eventually leads to convection (Korenaga and Jordan, 2004).

Though viscous softening is often included in continental rifting models (Brune et al., 2014, 2017b; Frederiksen and Braun, 2001; Huismans and Beaumont, 2003) care should be taken on the assumptions made for the ad-hoc parametrization. I have shown how two different approximations of viscous strain softening influence the mantle flow pattern through the change in the effective viscosity and, as a result, the amount of partial melting differs between the models.

3.2.3.2 **Initial weak seed**

Numerical models of continental rifting generally include an initial weak seed to localize deformation. The role of this weak seed is to center the initial deformation in the model domain (overcoming the potential influence of the lateral model boundaries) and to speed up the initial lithospheric thinning. A range of weak seeds has been used in numerical models which are either of mechanical or thermal character: fault-like, thicken crust, damage zone or thermal anomaly (e.g., Brune et al., 2012; Huismans and Beaumont, 2003; Svartman Dias et al., 2015a; Van der Pluijm and Marshak, 2005). The location of the weak seed represents the existence of pre-existing structures such as minor faults or zones with increased radiogenic production. Several authors have explored the effects of initial weak seed on the extensional rift mode and subsequent margin style (Dunbar and Sawyer, 1989; Dyksterhuis et al., 2007; Huismans and Beaumont, 2007). Dunbar and Sawyer (1989) concluded that the margin style is strongly influenced by the depth position of the initial weakness in the lithosphere, leading to symmetric narrow margins when located at the strong middle crust and to asymmetric extended margins when located at the strong mantle. On the contrary, Dyksterhuis et al. (2007) found that a single weak seed, regardless of its depth position, tends to form symmetric narrow rift modes. The study compared extension of models with coupled and decoupled rheological profiles and an embedded single weak seed. Coupled models led to a narrow basin whose width is proportional to the depth of the weak seed. In contrast, decoupled models led to two narrow basins where their width and the separation between them corresponded to the crustal and mantle brittle-ductile transition, respectively.

Previous studies have used many types of single weak seeds and depth locations. Naliboff and Buiter (2015) placed a weak seed below the Moho of presoftened material (ϕ= 10° and C=10 MPa) and size of 6 x10 km. Brune et al. (2014) upwelled the isotherm of the lithosphere-asthenosphere boundary over 5 km at the center of the model. Beaumont and Ings (2012) located a wet olivine

weak seed of 10 x 5 km with ϕ= 2° in the uppermost mantle lithosphere. Huismans and Beaumont (2011) used a weak seed below the Moho of 12 x 10 km with von Mises plastic σ_y= 10 MPa.

The numerical models include a thermal single weak seed given by a 2D Gaussian shape perturbation (x-axis width of 10 km and z-axis width of 20 km), which is introduced at the center of the model. This section provides an overview of the role of the thermal weak seed in our numerical model by testing its distribution and depth with the goal of avoiding that models initialize at the borders. I consider different thermal initialization of the models by varying the temperature (30 and 70°C) and depth position (30, 60, 90 and 120 km) of the weak seed (Fig. 3.19a). The weak seed located at 30 km can be understood as a region with high radiogenic heat production while the ones at 60, 90 and 120 km as zones influenced by thermal perturbations (Dyksterhuis et al., 2007).

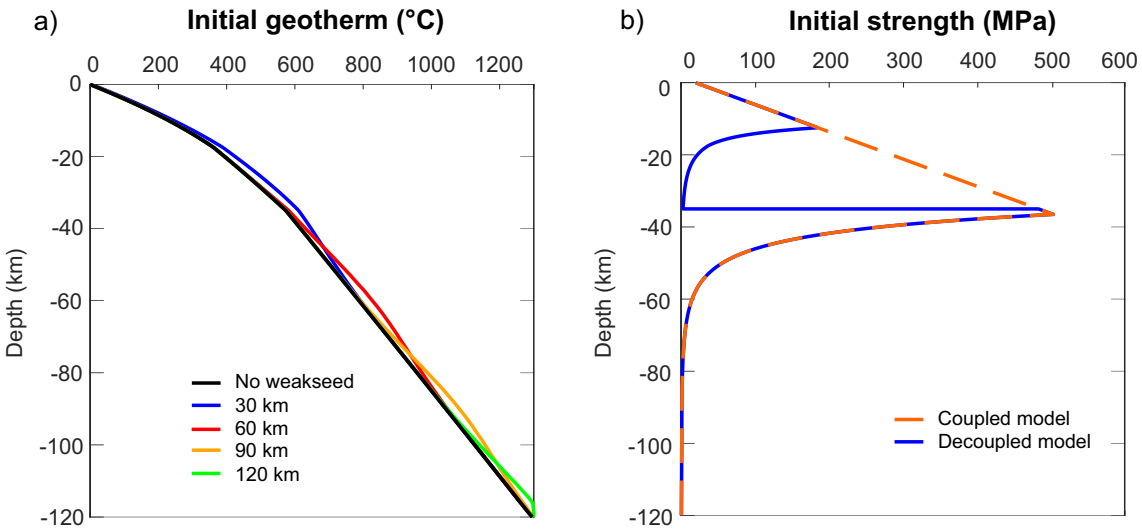

Figure 3.19: a) Initial geotherm at the model center axis for the cases with no weak seed and weak seed of 30°C at 30, 60, 90 and 120 km depth. b) Initial strength envelope of the coupled and decoupled models for a constant strain rate of 1 x $10^{-14}s^{-1}$.

Two rheological models are used: coupled crust and mantle and decoupled crust and mantle, from here on called coupled and decoupled models, respectively. These represent the end-member models tested in the thesis. Coupled models use a lower crustal rheology of mafic granulite scaled by a chosen factor $f = 15$ that strongly couples the mantle whereas decoupled models use a lower crustal rheology of wet quartzite that allows the formation of a weak ductile layer above the Moho that decouples crust and mantle (see rheological parameters in Table 3.1, and Fig. 3.19b). The scaling factor f multiplies the equation (Eq. 2.25) to strengthen or weaken the reference power law (Huismans and Beaumont, 2014). Water loading is included with a surface level of 0 km, whose numerical solver is based on the sediment loads from Andrés-Martínez (2016). Models include

plastic softening and are tested with and without viscous softening (see Section 3.2.3.1 for further details). Here we choose a cohesion of 20 MPa because the strongly coupled models failed at the surface for weaker values, since ideally crustal blocks will fall from the rift shoulders and erosion is not included in this model. Buck et al. (1999) highlighted that large vertical cliffs develop when large amounts of rock are under cohesion values of about 10 MPa. The half-extension velocity is 3 mm/yr.

Figure 3.20 shows the localization of the rift axis for a set of scenarios. Results for the coupled models are shown in the top panel. Comparison of the initial thermal weak seed for 30°C and 70°C give the same results for depth changes. Cases without viscous softening (no VS) show that depths of 30 km and 60 km localize the rift axis at the center of the model whereas deeper locations deviate it. When including the effect of viscous softening (VS) discussed in the previous section, the deepest location (120 km) deviates the rift axis toward the boundaries of the model. All models result in symmetric narrow conjugates (Fig. 3.21).

Results from the decoupled models are shown in the bottom panel of figure 3.20. In this case there is no variation in the rift axis when including viscous softening, only at depths of 120 km the rift axis delocalizes more from the model center. All models result in symmetric wide conjugates (Fig, 3.21).

Our choice for the type of initial weak seed does not promote a type of extensional mode. Our coupled models evolve as a narrow rift as suggested by Buck (1991) for lithospheres with high integrated strength and our decoupled models evolve as a wide rift. This contrasts with the result of Dyksterhuis et al. (2007) that used a single weak seed of low viscosity material and concluded that this type of weak seed promotes the development of narrow rifts independently of the initial lithospheric strength.

A minor change in the rift basins width takes place for the different cases, reaching a maximum difference of about 25 km, without affecting the main characteristics of the rifted margins. The decoupled models show a slightly larger basin width for the cases with a weak seed at 30 and 60 km, irregardless of the inclusion of viscous strain softening. I suggest that the thermal weak seeds at depths of 90 to 120 km have a higher temperature background so the model takes longer in localizing the initial deformation, but, once it is localized, the upwelling mantle expands less horizontally. For the coupled models, only the case with a 30 km depth weak seed slightly increases the basin width, irregardless of the inclusion of viscous strain softening.

Based on this parameter study, I select the weak seed of 70°C at 30 km depth for my numerical tests, since its advantage over the 30°C weak seed is that accelerates the localization of the model as well as it overcomes the model boundary effect. The preference of this type of weak seed over

others, such as a reduction the material strength, is based on the fact that the thermal weak seed diffuses with time while other types are permanently involved in the model evolution.

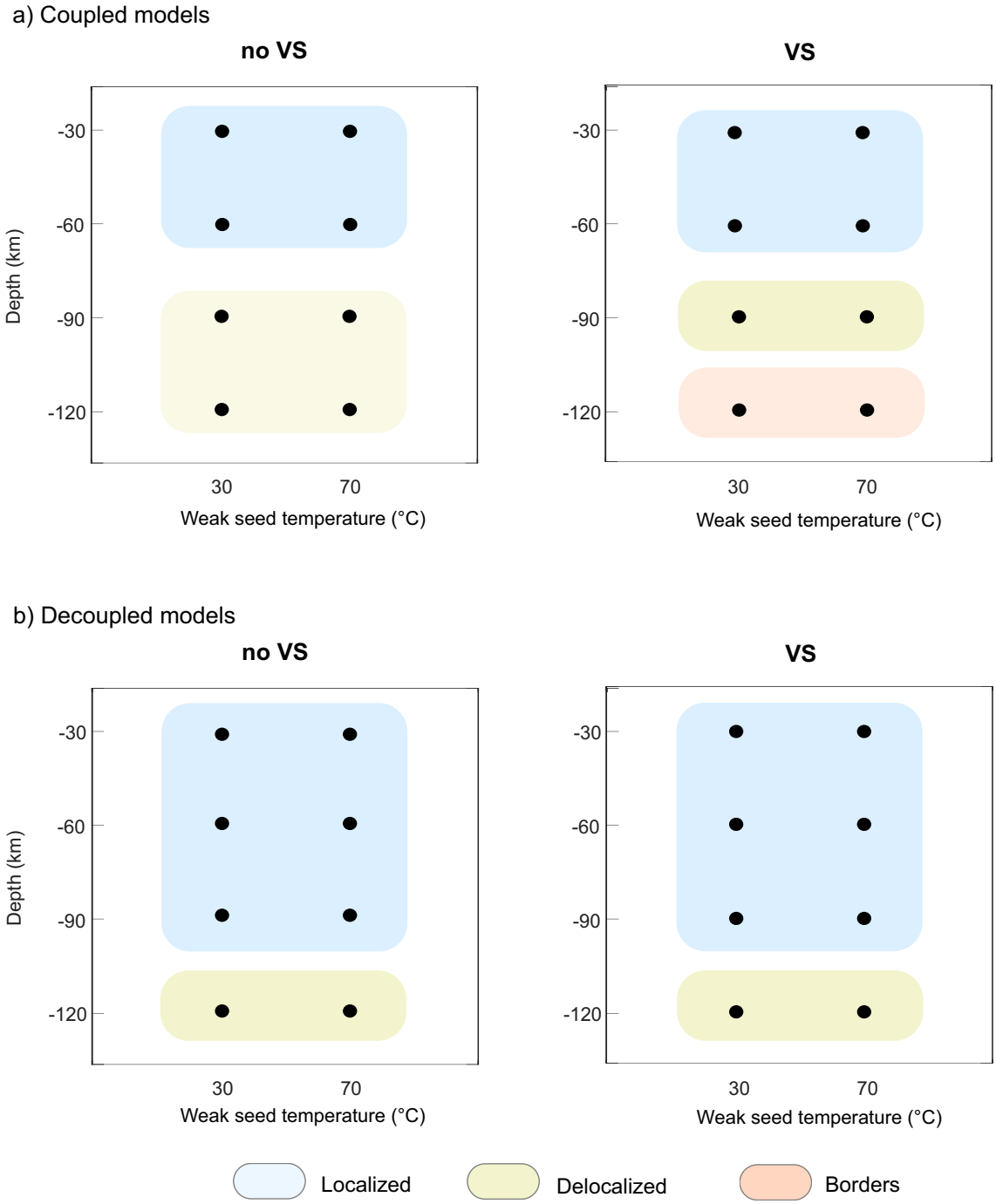

Figure 3.20: Parameter test of initial thermal weak seed (temperature and depth location) for models without and with viscous softening (VS): a) Coupled models and b) Decoupled models.

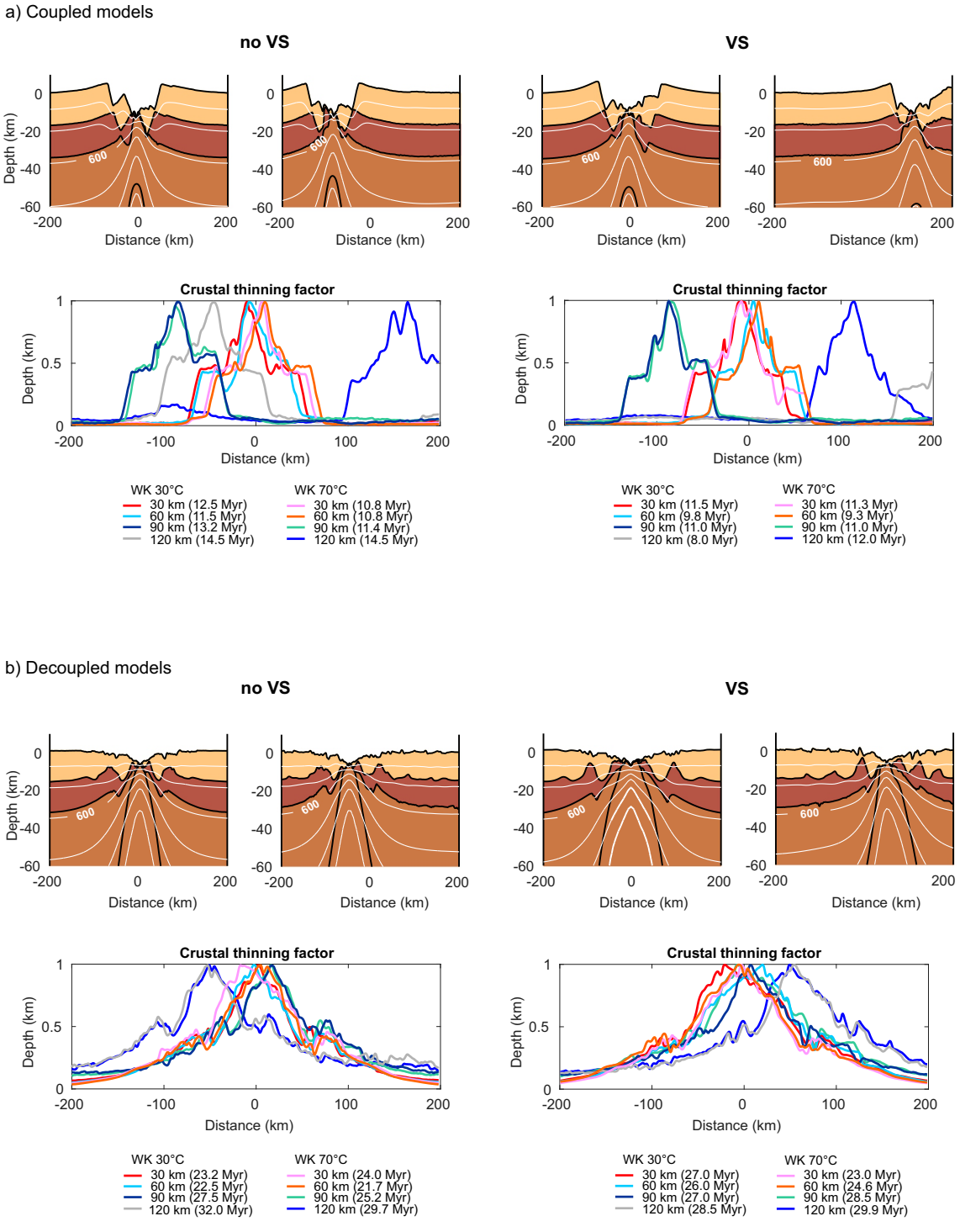

Figure 3.21: Coupled (a) and decoupled models (b) with initial thermal weak seeds (WK) at different depths. Model examples for centered and not centered rifts. Crustal thinning factors for the four group of tests: a) Coupled models without viscous softening (no VS) and with viscous softening (VS), b) Decoupled models without viscous softening (no VS) and with viscous softening (VS)

3.2.3.3 Shear heating

Shear heating is considered as a first-order strain-localization mechanism (Duretz et al., 2016; Lu et al., 2011; Regenauer-Lieb et al., 2006) . The conversion of mechanical work to heat increases the temperature of shear zones that induces strain localization (Section 2.2.2). Hartz and Podladchikov (2008) showed that shear heating may reduce the lithospheric strength by one order of magnitude. Figure 3.22 shows shear heating acting along the active shear zones of a model and the temperature difference compared to the model without shear heating. An increase of 60°C localizes at the initial weak seed and about 15-20°C along the main shear zones at 0.71 Myr after the onset of rifting. The rate of shear heating per unit of volume is an order of magnitude higher than the crustal radioactive heat production (Section 2.2.2).

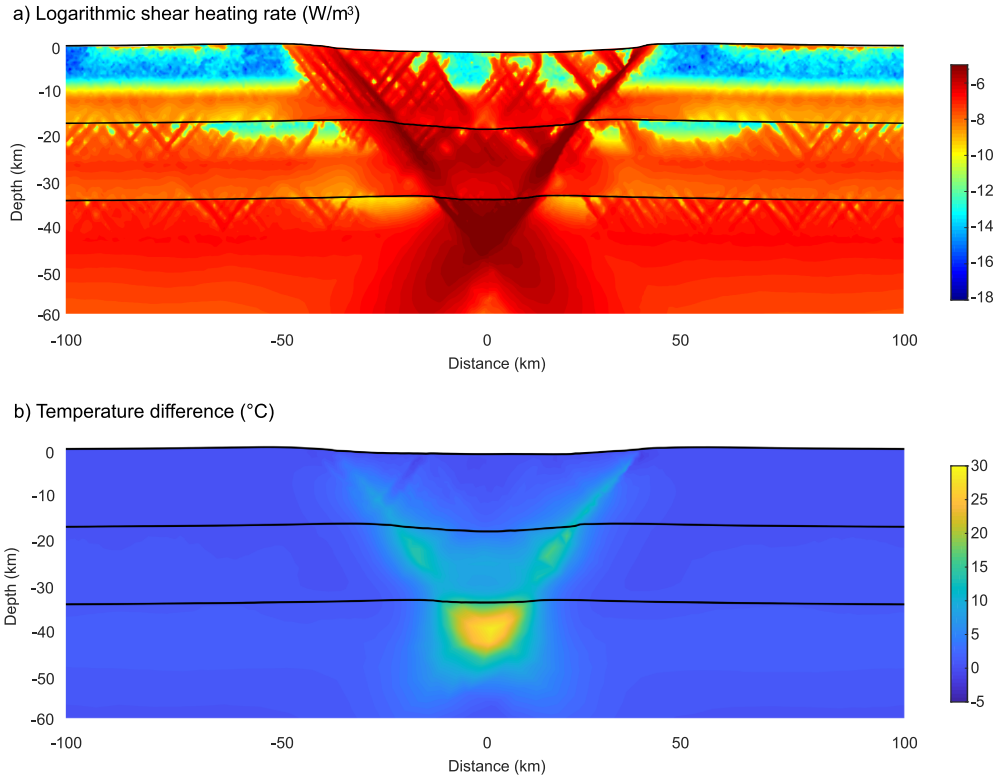

Figure 3.22: Model layers with shear heating at 0.71 Myr (upper crust, lower crust and lithosphere mantle). a) Shear heat production and b) temperature increase caused by shear heating. The highest temperature difference is reached at the weak seed, which localizes more deformation.

Shear heating contributes to increase the temperature at the base of the crust which may help the activation of the sequential faulting mode. This occurs due to the decrease in viscosity of the lower crust that allows it to flow ductile while the upper crust behaves in a brittle manner. I compare the same model without and with shear heating in Fig. 3.23 to show the effect of including this

weakening process in the final conjugate rifted margins. The model without shear heating shows two symmetric and narrow margins whereas the model with shear heating shows an asymmetric configuration with a narrow and an hyperextended wide margin. The comparison of the strain rate evolution for these two models is shown in Fig. 3.24 to observe the effect of shear heating on strain localization.

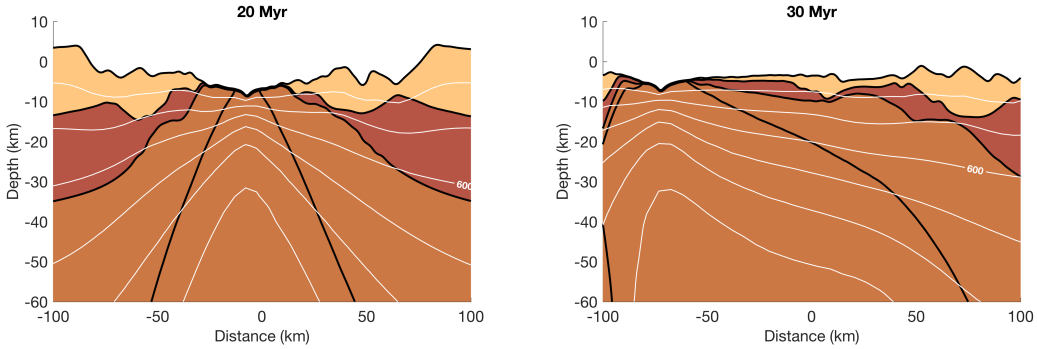

Figure 3.23: Comparison of the margins architecture for a model without (left) and with shear heating (right). The model without shear heating shows two symmetric and narrow margins whereas the model with shear heating shows an asymmetric configuration with a narrow and an hyperextended wide margin. Temperature isotherms interval of 200°C.

Figure 3.25 compares the productions of shear heat for times steps of 2, 6, 12 and 17 Myr for two end-member models with lower crustal rheologies of strong mafic granulite and weak wet quartzite, respectively. Left panel shows the evolution of the strong mafic granulite model; deformation starts with two conjugate crustal scale faults rooting in the weak seed and forming a graben (2 Myr), later is broken by more faults (6 Myr) until one active fault dominates (12 Myr) and sequential faulting mode starts developing a very wide and hyperextended margin (17 Myr). Right panel shows the evolution of the weak wet quartzite model; deformation starts in a single upper crustal fault (2 Myr), which starts rotating backwards (6 Myr) and exhuming the lower crust (12 Myr) in a core-complex extensional mode. At 17 Myr, the extensional mode has changed to wide mode distributing the deformation more uniformly over crust and mantle. The model with mafic granulite shows more production of heat respective the model with wet quartzite. These models support the results of Leloup et al. (1999) that shear heating increases with the strength of the material.

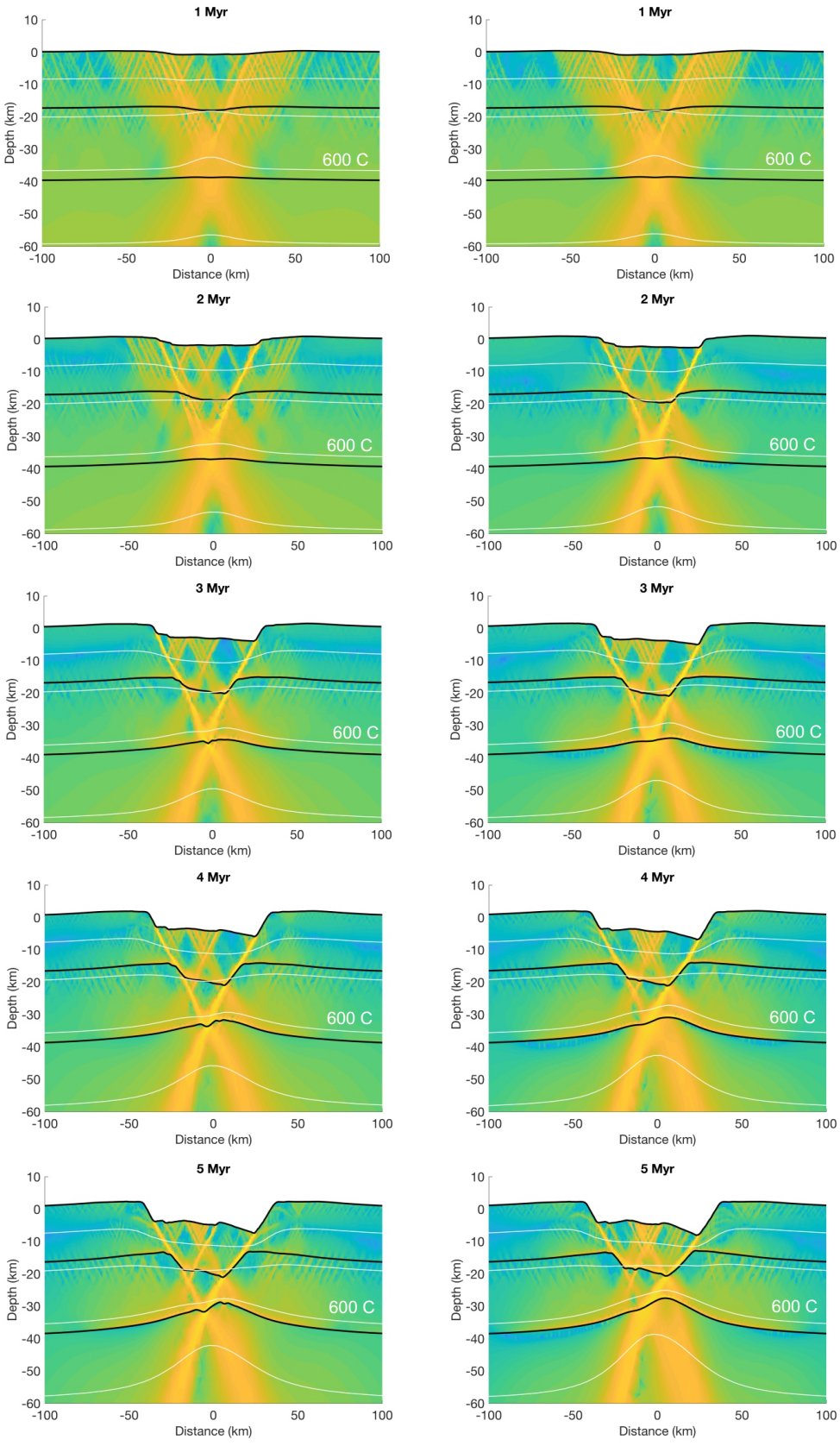
1 Myr
2 Myr
3 Myr
4 Myr
5 Myr
600 C
Depth (km)
Distance (km)
2nd invariant strain rate
-20
-18
-16
-14

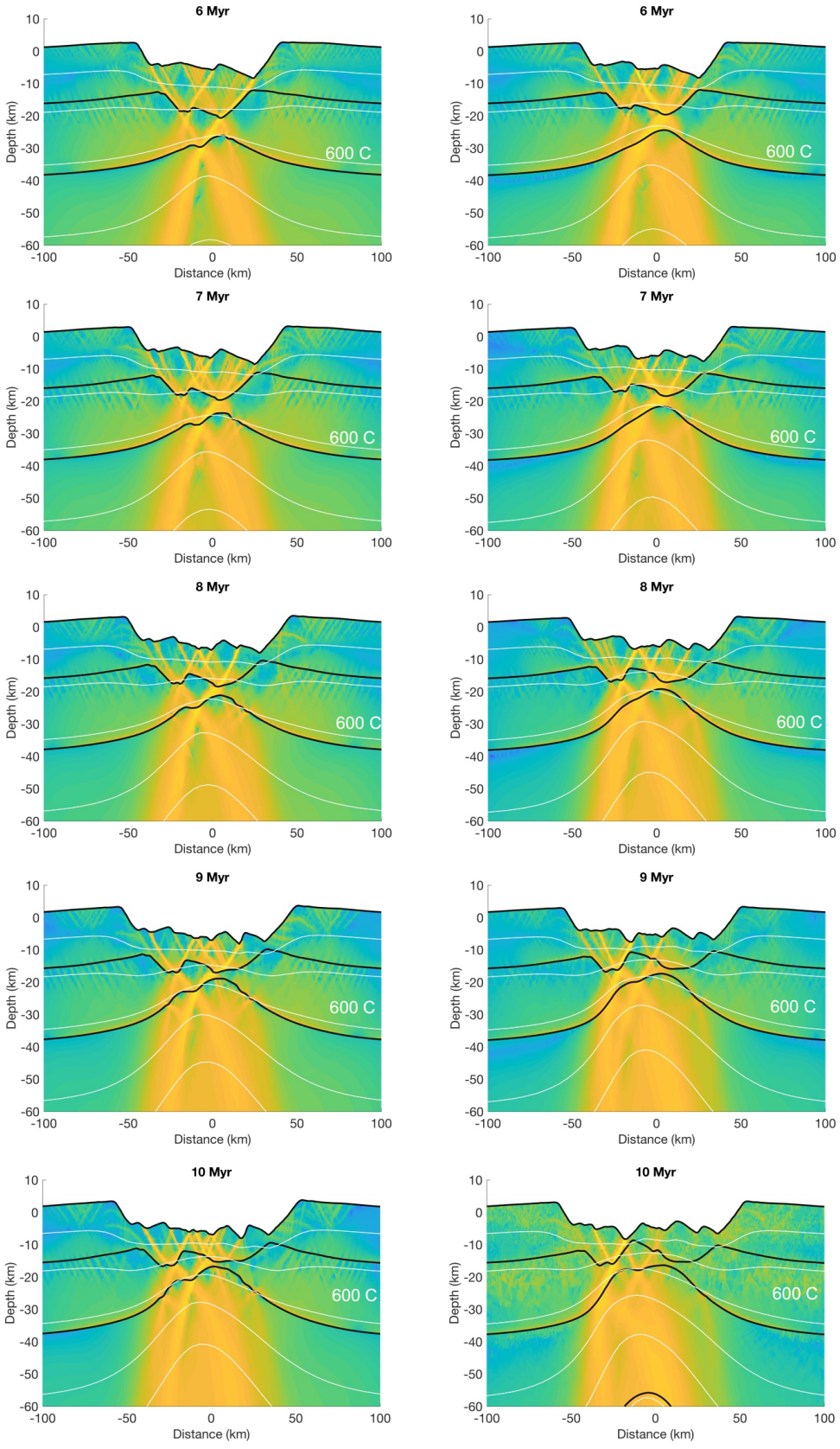
6 Myr
6 Myr
7 Myr
7 Myr
8 Myr
8 Myr
9 Myr
9 Myr
10 Myr
10 Myr
600 C
Depth (km)
Distance (km)
2nd invariant strain rate
-20
-18
-16
-14

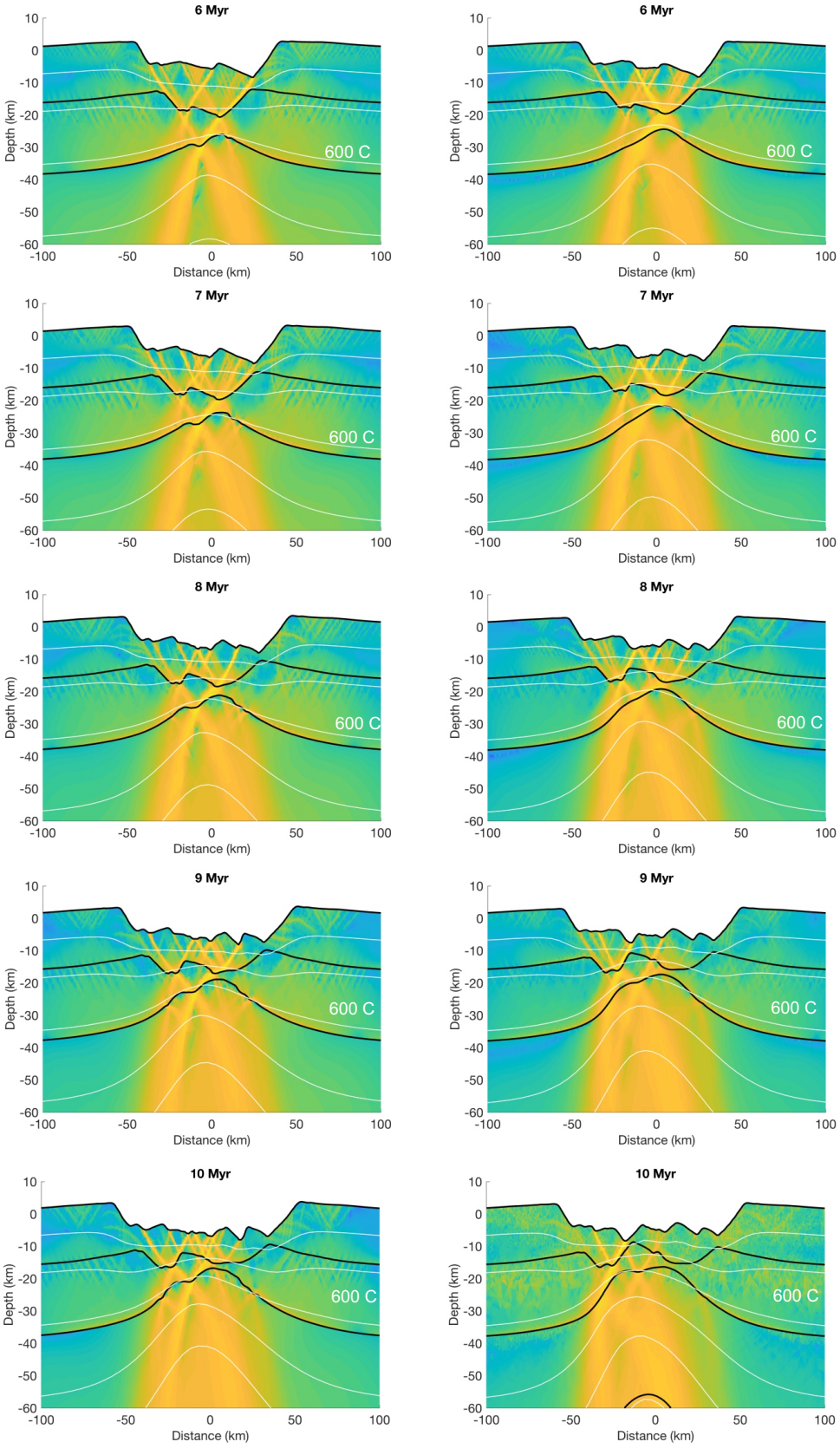
6 Myr
7 Myr
8 Myr
9 Myr
10 Myr
600 C
Depth (km)
Distance (km)
10
0
-10
-20
-30
-40
-50
-60
-100
-50
0
50
100
2nd invariant strain rate
-20
-18
-16
-14

Figure 3.24: (Previous page). Influence of shear heating on model evolution. Comparison of the 2nd invariant of the strain rate (s^{-1}) for models: without shear heating (left panel) and with shear heating (right panel). Temperature isotherms interval of 200°C.

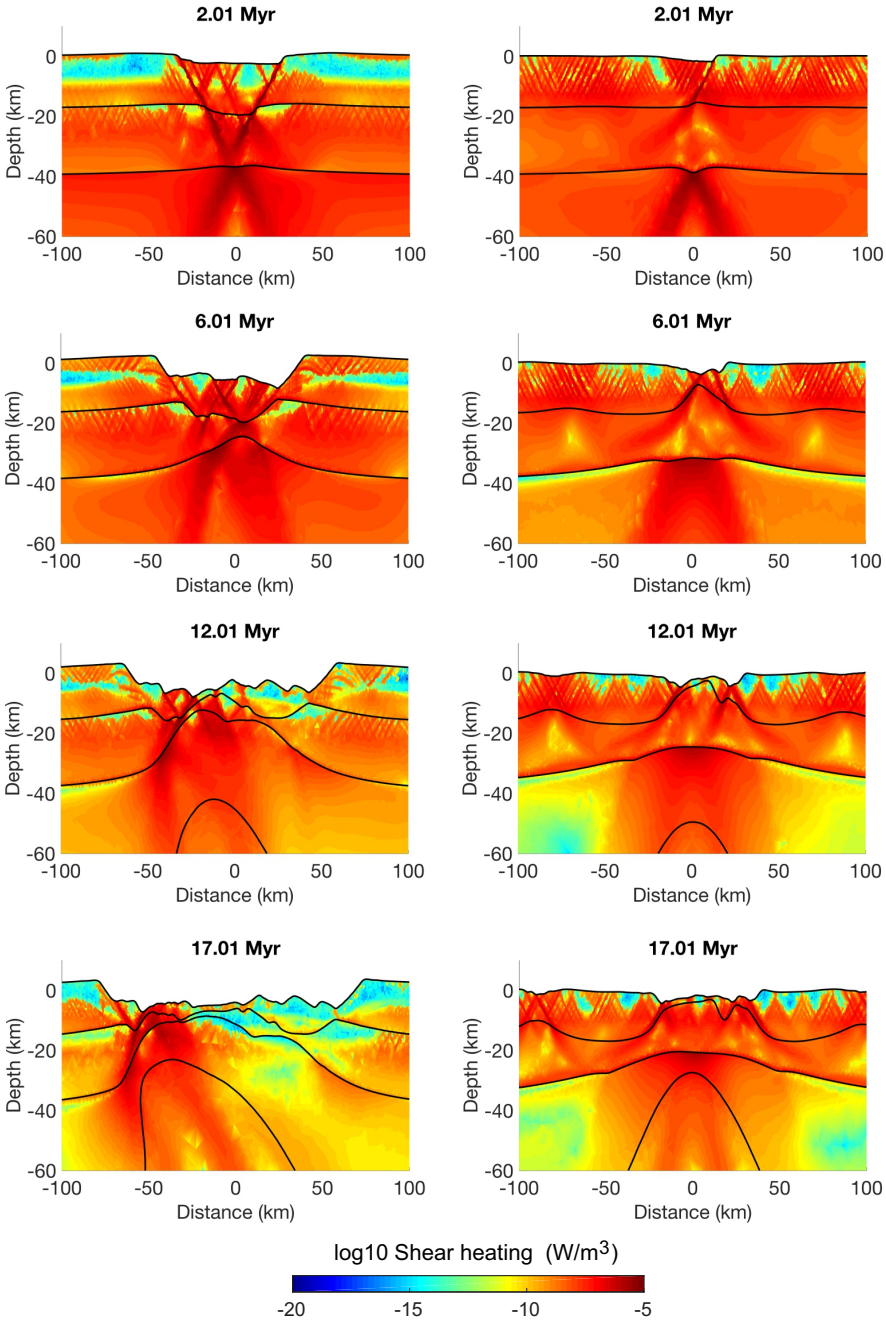

Figure 3.25: Comparison of shear heat production between two models evolution: strong lower crustal rheology (mafic granulite, left panel) and weak lower crustal rheology (wet quartzite, right panel).

3.3 Conclusions

In this chapter I present and discuss the standard model used throughout the dissertation. Based on geological observations and sensitivity tests, I model a 120 km thick lithosphere overlying an asthenosphere defined by the isotherm of $1300°C$. The strong and weak end-member models used are composed of mafic granulite and wet quartzite lower crustal rheologies, respectively. The thickness of the crust can be 35 or 40 km, with a 17.5 km thick upper crust. The initial crustal thickness implies a slight change in the Moho temperature, from $574°C$ at 35 km depth to $634°C$ at 40 km depth, that results from considering an initial thermal age of 500 Myr. The initial continental geotherm has been calculated according to the tectono-thermal age for the South Atlantic, an ideal natural laboratory to study the effects of rheology and extension velocity on the styles of rifting and post-rift margin evolution, main goals of this thesis. The composition of the mantle lithosphere and asthenosphere is based on an initial melt depletion profile. Mantle rheology changes from wet olivine with a water content of 125 ppm H/Si when the mantle is 0% depleted to dry olivine when the mantle depletion is 4%, assuming that all water has been extracted at this stage. From the bottom of the model, 400 km depth, to 130 km depth we assume the mantle has not been melted and has a depletion of 0%, corresponding to a wet olivine rheology. From 130 km depth to the base of the lithosphere, 120 km depth, melt depletion increases from 0% to 4% with a mixture rheology of wet and dry olivine that depends linearly on the degree of depletion. From the base of the lithosphere to 60 km depth, the depletion linearly increases from 4 to 10%, with a dry olivine rheology. Additionally, the standard model domain is 400 km wide and 400 km deep and includes water loading to a level of $0km$ as the developing basin subsides.

From this standard model setup, different parameters may vary its evolution. Therefore, I summarize below the main conclusions reached after the set of sensitivity tests conducted.

In order to evaluate the adequate trade-off between computational cost and mesh resolution of our test models, I have increased the standard mesh by 5 times in the lower crust and the mantle (i.e. 1 km instead of 5 km, Figure 3.11), concluding that the overall evolution of the rift and tectonic style of the resulting conjugates rifted margins are very similar (Figures 3.9, 3.10 and 3.11).

The influence of water content in the mantle has been tested in order to develop an initial compositional depleted lithosphere and fertile asthenosphere. The melt-depleted residue is more buoyant and strong than the fertile parent. This is included in the model through the temperature- and depletion dependent density and the change from wet olivine to dry olivine as the former melts. This implementation results in a more realistic estimate of syn-rift subsidence, mantle flow and uplift of the rift shoulders.

3. TESTING THE SENSITIVITY OF MARGIN DEVELOPMENT TO INPUT PARAMETERS: A GENERAL STUDY

The effect of different strain localization mechanisms on the rifting evolution and conjugate margins has been explored. The choice of our initial weak seed is based on the advantage that a thermal increase at the rift center will diffuse with time. The effect of the weak seed depth for coupled and decoupled models, including viscous strain softening and excluding it, have been tested to decide a suitable depth for all models. The results suggest the use of a weak seed of $70°C$ at 30 km depth, which anticipates the strain localization at the rift axis.

Numerous geodynamical studies have focused on the study of small-scale mantle convection in terms on temperature lateral variations and density changes related to melt retention, melt depletion and solid phase changes. Viscous strain softening is often included in these models to account for the grain-size reduction of deforming rocks in the diffusion creep regime and for lattice-preferred orientations in the dislocation creep regime. As a first order approximation, a linear increase in the pre-exponential factor is used to reduce the effective viscosity. However, at higher temperatures, a small grain size can be unstable over long time scales, leading to a grain growth recovery and a return to the dislocation creep regime. The speed of grain-size recovery scales as an Arrhenius-type process similar to the temperature dependence of diffusion creep itself. Here, I have shown the implications of temperature-dependent viscous strain softening and concluded that the temperature dependence better approximates observations from laboratory experiments while inhibiting the development of convection cells in the mantle during magma-poor syn-rift. This result is important as well for the surface heat flow obtained in the numerical models. Small scale convection affects the heat flow values at the surface (Korenaga, 2009) so artificial small scale convection would result in wrong heat flows to be compared to natural examples.

Finally, I have shown the effect of including shear heating in our numerical models and concluded that shear heating promotes asymmetric extension through the formation of a sequence of faults in time, i.e. the sequential faulting mode.

CHAPTER

4

Understanding the variability in tectonic architecture of margins: a numerical modelling study

E. Ros, M. Pérez-Gussinyé and M. Andrés-Martínez. Understanding the variability in tectonic architecture of margins: a numerical modelling study. *Ros et al., in preparation. Planned for submission to Tectonics.*

Electronic supporting information includes the movies presented in this chapter.

Author contributions:

E.R. and M.P.G. conceived the research study. **E.R.** designed and carried out the numerical modelling. M.A.M. coded the algorithm for obtaining the outputs of surface heat flow and brittle and ductile strain rates. **E.R.** produced all figures and movies. **E.R.** and M.P.G. contributed to the description and discussion of the modelling results. **E.R.** wrote the manuscript in collaboration with M.P.G.

Understanding the variability in tectonic architecture of margins: a numerical modelling study

E. Ros [1], **M. Pérez-Gussinyé** [2] **and M. Andrés-Martínez** [2]

[1]COMPASS, Department of Earth Sciences, Royal Holloway University of London, Egham TW20 0EX, UK.
[2]MARUM, Center for Marine Environmental Sciences, University of Bremen, 28334, Germany.

Key Points:

- Characterization of the lithospheric modes of extension is based on the lower crustal flow
- We discuss crustal depth dependent thinning in terms of the ratio of upper- to lower-crust thickness
- Depth dependent numerical models are compared to natural rift examples

Corresponding author: Elena Ros, Elena.Ros.2014@live.rhul.ac.uk

Abstract

Numerical models have been used to explore the role of lower crustal strength in producing different deformation modes during extension. We confirm previous studies and identify four modes of extension in the evolution of continental rifting as the lower crustal strength decreases: narrow, sequential faulting, wide and core-complex. When the initial lower crustal strength is either very strong or very weak, conjugate margins are always symmetric and deform, respectively, in narrow and core-complex/wide modes during the whole deformation. For intermediate lower crustal rheologies, there is a transition in extensional modes depending on the initial lower crustal strength: 1) an intermediate/strong strength, changes from narrow to sequential faulting mode and 2) an intermediate/weak strength results in a transition from core complex, to wide and to sequential faulting mode. Although these two types of rheologies lead to asymmetric conjugate margins, they can be distinguished by the major large faults, syn-rift uplift of the shoulders and subsidence of the basin center in the earlier case, as compared to the latter one.

We find that the deformation modes are controlled by feedbacks between thermal thinning during asthenospheric advection, strain softening on faults and shear zones, and the elastic response of the lithosphere to faulting. All these factors influence the ability of: 1) faults to localize deformation and 2) the lower crust to flow and fill in the accommodation space formed by the developing faults. The type of lower crustal flow is linked to the formation of a low viscosity channel within the deep crust, whose extent and thickness varies with the initial crustal rheology and the predominant mode of extension. This flow generally occurs at a fault-block scale, inducing small-scale crustal depth dependent thinning (DDT), except for the core complex extensional mode, where crustal DDT is of large lateral extent. We also show that: 1) low initial upper- to lower-crustal thickness ratios (UC/LC), may favor the exhumation of lower crust at the distal margins, while 2) large UC/LC may favor the disappearance of LC form the distal margin, without implying large-scale flow of the lower crust nor DDT. Moreover, we analyze the distribution of the surface heat flow with lithospheric and crustal DDT for the different modes of extension. The results highlight how the sequential faulting mode implies a migration of the heat flow peak along the developing wide margin, reaching higher values for thicker upper crusts. Finally, we compare our results for crustal DDT with natural rift examples.

1 Introduction

Four decades ago *McKenzie* [1978] introduced the uniform extension model of pure-shear for the extension of continents. This model assumes instantaneous and constant lithospheric stretching with depth to estimate the subsidence and heat flow history of the extensional basins. Despite being a good first-order approximation, it has become clear that extension may not be considered either instantaneous nor uniform with depth, the latter would be a result of the contrasting rheological properties of the lithospheric layers. Thereupon, *Royden and Keen* [1980] proposed a non-uniform extensional model where upper and lower zones of the lithosphere are decoupled by a rheological discontinuity and extend under different amounts of stretching. This model describes well the uplift of rift shoulders during extension (e.g., the East African Rift and the Red Sea) but fails to explain the observed asymmetry in some rifted margins. Shortly after, *Wernicke* [1981, 1985] proposed the model of simple-shear to explain the tectonics of the intracontinental rift of the Basin and Range Province. The model assumes that extension is accommodated along a low-angle, large-scale normal fault throughout the lithosphere, which divides the lithosphere into an upper- and a lower-plate. Each plate domain undergoes a different subsidence and heat flow history, being the upper-plate the hottest domain. *Lister et al.* [1986] applied this model to passive continental margins. The authors envisaged an upper- and lower-plate margin pair to explain the asymmetry of rifted conjugates and the development of contrasting architectures at the distal margins. However, many authors have not been able to match all observations at margins with a single model, either pure- or simple-shear. For instance, *Buck et al.* [1988] used these two end-member models to examine the topography and heat flow of the northern Red Sea area. While the simple-shear model explained the topography best, the pure shear one would better fit the heat flow. Additionally, recent seismic observations and images have not supported the existence of a single fault cutting through the entire lithosphere as suggested by *Wernicke* [1985] and *Lister et al.* [1986] [e.g., *Ranero and Pérez-Gussinyé*, 2010].

A very significant step in our understanding of rifting was done by *Buck* [1991]. He suggested rifting could be explained by the combination of three extensional modes, narrow, wide and core complex, depending on the spatial distribution of deformation and the efficiency of the lower crustal flow [Fig. 1; *Buck*, 1991]. Changes in crustal thickness during lithospheric extension produce lateral pressure gradients that can drive lower crustal flow from unextended to extended regions [*Buck*, 1991; *Ruppel*, 1995]. The rate of this flow is controlled by its effective viscosity [*Bird*, 1991], so that if the lower crust is sufficiently weak, its flow reduces the local crustal thinning [*Block and Royden*, 1990;

Bassi et al., 1993]. The narrow rift mode results when the lower crust is strong and therefore its flow towards the area of crustal stretching is limited. Thus, large lateral gradients of crustal thickness are expected. Crustal and mantle extension localizes in the thinnest and weakest area of the lithosphere, over a region narrower than 100 km. Narrow rift modes are predicted for thin crusts and relatively low heat flows. The wide rift mode results when the lower crust is weak enough to flow to the area of maximum extension and smooth the topographical contrasts of the Moho. This extending zone resists further deformation, which causes its migration to a weaker zone. Crust and mantle thin in a comparatively uniform way over a broad region. Wide rift modes are predicted for intermediate values of crustal thickness and heat flow. The core complex rift mode results when an upper crustal fault can accommodate large offsets and the lower crust is weak enough to flow towards the fault's footwall resulting in a rather flat Moho topography. Core complexes need a very weak lower crust for their formation, which can arise in conjunction with a thin brittle layer, and high heat flow [*Buck*, 1991; *Lavier et al.*, 2000; *Lavier and Buck*, 2002], a very thick postorogenic crust > 50-60 km [*Buck*, 1991; *Tirel et al.*, 2008; *Schenker et al.*, 2012], a compositionally weak lower crust [*Huet et al.*, 2011] or related to strain softening within the flowing lower crust [*Schenker et al.*, 2012]. Continental core complexes are typically related to wide rifts (e.g., in the Basin and Range Province and the Aegean region), where high-grade metamorphic rocks from the mid-lower crust are exhumed and exposed at the surface. Because of this association, *Brun* [1999] and *Tirel et al.* [2008] considered the development of core complexes as local anomalies within the wide rifts and not a separate mode of extension as suggested by *Buck* [1991].

A fourth extensional mode is the sequential faulting mode (Fig. 1), which implies the formation of sequentially younger faults towards the ocean and results in conjugate margin asymmetry. This mode was first described in seismic profiles by *Ranero and Pérez-Gussinyé* [2010] and then shown in numerical models [*Brune et al.*, 2017; *Ros et al.*, 2017]. Sequential faulting describes fault kinematics for crustal thickness of < 15-10 km, and may derive in the formation of a detachment-like structure when successive faults are spatially close (for brittle layer thickness of < 5 km), so that isostatic rebound due to slip on the most oceanward fault, listrifies the tip of the previous fault, forming a planar structure at the base of the fault blocks [*Ranero and Pérez-Gussinyé*, 2010; *Pérez-Gussinyé*, 2013]. This last phase of the evolution of sequential faulting resembles the rolling hinge model, however, it is important to note that while models based on the rolling hinge have been used to explain the most oceanward areas of some margins, where detachment-like structures have been observed [e.g., detachment-like structures in the last 30 km of Deep Galicia margin, S-reflector *Reston et al.*, 2007], the sequential faulting mode refers to a much more prolonged evolution in time and space [*Ranero and Pérez-Gussinyé*, 2010] and can generate very wide hyper-extended crust, without the need of an obvious detachment-like structure that may be observed in seismic sections [*Brune et al.*, 2014]. Sequential faulting occurs when the lower crust is strong enough to couple deformation from upper crust to mantle along a single active fault, but still weak enough to prevent rapid crustal break-up. This active fault promotes asymmetric upwelling of the mantle, which heats and weakens the fault's hangingwall allowing the development of a new fault at that location. This leads to localization of deformation into a sequence of oceanward dipping faults that generates conjugate margin asymmetry [*Ranero and Pérez-Gussinyé*, 2010; *Brune et al.*, 2014]. *Brune et al.* [2014] showed that the asymmetric uplift of the mantle elevates the temperature at the tip of the active fault generating a pocket of low viscosity at the deep lower crust. A lateral strength gradient is produced between the low viscosity pocket and the cooling mantle at the fault's footwall. These processes maintain the migration of the rift and peak heat flow progressively oceanward [*Brune et al.*, 2014; *Pérez-Gussinyé*, 2013]. Eventually, the lower crust cools and embrittles, so the low viscosity pocket vanishes and the migration of the rift pauses, leading to break-up. The resulting conjugate margins are marked by a moderate to strong asymmetry, depending on the efficiency of the low viscosity pocket. This process of margin asymmetry formation can result in a very wide area (> 100 km) of hyperextended crust (< 15-10 km thick crust) in the wide conjugate margin.

Other authors have proposed different controls on the development of asymmetry in conjugate margins, such as the presence of crustal or mantle weaknesses [*Dunbar and Sawyer*, 1989], the interaction of strain softening with the dominant/subordinate rheology [*Huismans and Beaumont*, 2002, 2003], the interval of a tectonic quiescence period [*Naliboff and Buiter*, 2015] and the extension velocity [*Huismans and Beaumont*, 2003; *Brune et al.*, 2014; *Svartman Dias et al.*, 2015]. Contrasting results have been obtained regarding the effect of extension velocity on the degree of conjugate asymmetry. *Brune et al.* [2014] tested the influence of the extension velocity on the margin asymmetry for models with a moderately strong lower crust. The study concluded that faster velocities lead to advection of isotherms to shallower levels. This results in the generation of a pocket of low viscosity within the lower crust, localized at the tip of the active fault, that can be maintained for longer time and, hence, increase conjugate asymmetry. *Huismans and Beaumont* [2003, 2009] used models with a strong lower crust, initially coupling crust and mantle, to test the sensitivity to extension velocity. The results showed more symmetric margins with increasing velocity. The

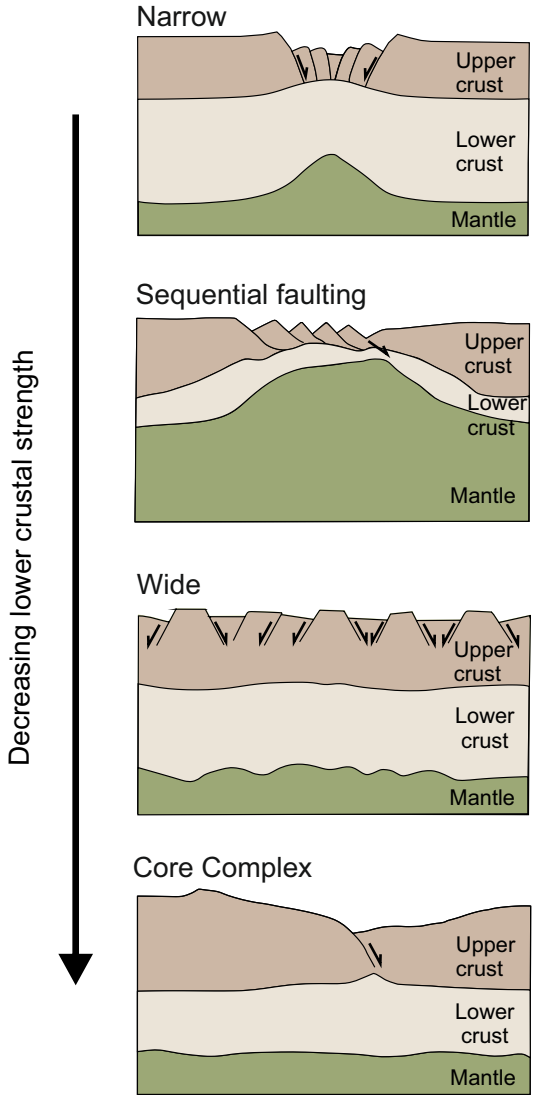

Figure 1. Cartoons of the continental lithosphere in the four modes of lithospheric extension, i.e. narrow, wide, core complex [*Buck*, 1991] and sequential faulting [*Ranero and Pérez-Gussinyé*, 2010]. Modified from [*Buck*, 1991].

explanation for this behavior is based on the fact that larger viscous stresses result from higher velocities. This leads to increased viscous coupling and more distributed and symmetric extension, which counteracts the initial asymmetry supported by the plastic strain softening. Unlike the extensional mode proposed by *Ranero and Pérez-Gussinyé* [2010] and *Brune et al.* [2014, 2017] to explain conjugate-margin asymmetry, i.e. sequential faulting, *Svartman Dias et al.* [2015] explained margin asymmetry in terms of strain hardening, lower crustal flow induced by lateral changes of crustal thickness and crustal strengthening by bending stresses within the fault area. According to this study, when lithospheric strengthening, due to bending along faults, dominates over the weakening due to thinning, new faults will form outward of the initial rift zone. This process will migrate deformation until the lower crust is thin enough.

The behavior of the lower crust is therefore a key piece in the accommodation of deformation during continental rifting. This is influenced by its composition, thermal structure, extension velocity and coupling level with regard the over- and underlying layers. Conceptual models of margin formation invoke different types of depth dependent thinning (DDT) for the deformation of the crustal layers. *Driscoll and Karner* [1998] observed large subsidence with little brittle faulting in the North Carnarvon basin and invoked flow of ductile lower crust towards the ocean beneath a mid-crust detachment to explain this observation (Fig. 2a). *Brun and Beslier* [1996], however, focused on the

observation of brittle upper crustal faults reaching the mantle at the distal West Iberia margin and hence assumed that the ductile lower crust had flowed landward of the basin center (Fig. 2b). Based on the grabbroic lower crust found in the Alpine Tethys system, the model of *Lavier and Manatschal* [2006] and *Péron-Pinvidic and Manatschal* [2009] proposed extension of a brittle lower crust overlain by a ductile middle crust, resulting in the development of downward-concave normal faults (Fig. 2c). Given the ultra-slow rate of extension at the West Iberia margin and based on numerical considerations, *Pérez-Gussinyé and Reston* [2001] deduced that, with ongoing extension, the lower crust became progressively stronger and coupled to upper crustal deformation. Hence, lower crustal deformation would have switched from ductile to brittle, and found at the toes of very thin and rotated fault blocks at the distal margin (Fig. 2d) [e.g., *Gardien et al.*, 2001]. Based on these observations and modelling, *Pérez-Gussinyé et al.* [2003] and *Ranero and Pérez-Gussinyé* [2010] suggested there was no significant depth dependent stretching between upper and lower crust and that variations in the thinning of both crustal layers occurred on a fault-block scale.

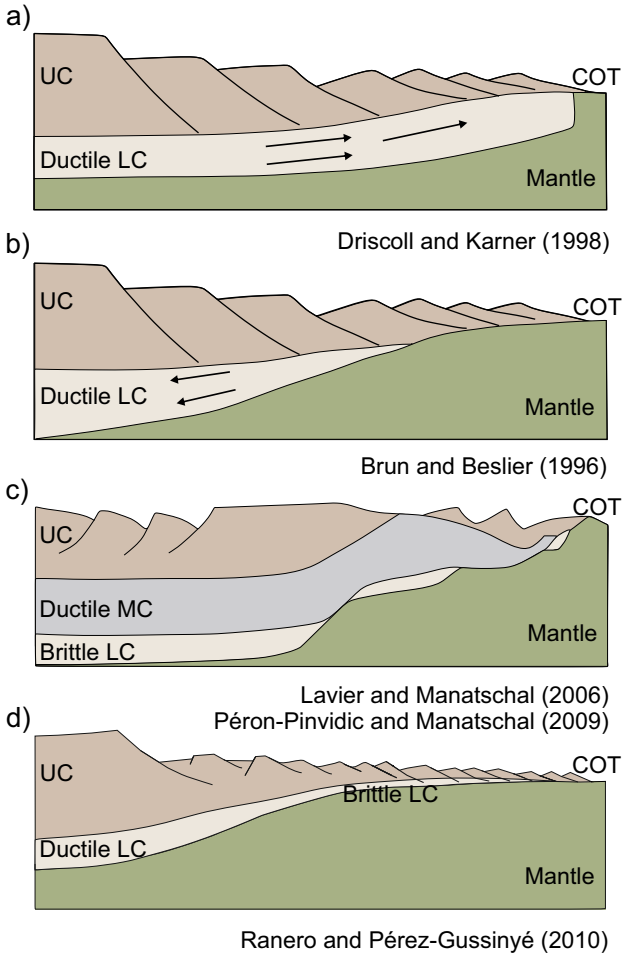

Figure 2. Conceptual models for the lower crustal flow during the formation of rifted margins. UC is upper crust, MC is middle crust and LC is lower crust. Modified after *Reston* [2007b] and *Clerc et al.* [2018].

Indications of some extent of crustal DDT seems to be present at many magma-poor margins [e.g., *Clerc et al.*, 2018]. The key is to recognize if DDT occurs over large or small spatial scales (over a distance larger than individual crustal blocks). Large-scale differential stretching implies decoupling of crust and mantle via a very weak ductile lower crust. This may result in large-distance lower crustal flow and its exhumation at the distal margin, as suggested for the Angolan margin [*Aslanian et al.*, 2009] and the Santos basin [*Evain et al.*, 2015], and also shown in numerical modelling of the central South Atlantic margins [*Huismans and Beaumont*, 2011]. Conversely, small-scale differential stretching implies that the lower crust is coupled to upper crustal fault blocks, which leads to a lower crustal excess in the faults' footwall and deficit in the hangingwall, as observed in the West Iberia margin [*Pérez-Gussinyé et al.*, 2003].

Both types of lower crustal behavior imply different distributions of lithospheric thinning, heat flow and onset, extent and composition of melting (even for the same extensional velocities) [*Ros et al.*, 2017; *Armitage et al.*, 2018].

During progressive extension, the potential of the lithosphere to localize or distribute deformation changes, resulting in transitions between the above mentioned modes of extension [*Buck*, 1991; *Hopper and Buck*, 1996; *Corti et al.*, 2003; *Brune et al.*, 2017]. These modes may be tied to distinct structural features and represent different phases of continental rifting, and its combination could explain the large variety of margin architectures observed in nature. This study aims to show how the prevalence of any of these modes during extension depends on the strength of the lower crust and extension velocity at the start of rifting and during extension. We relate the rift mode to the thickness and spatial distribution of a low viscosity channel that forms at the base of the crust in order to understand the transition from one mode of extension to another. Here we describe the tectonic evolution of a set of models and the rifted margins architecture as a combination of the wide, core complex, narrow and sequential faulting rift modes. These four modes of extension allow us to explain the variability in the architecture of magma-poor conjugate margins ranging from wide to narrow and symmetric to asymmetric, including the development of hyper-extended margins. We analyze how these different modes lead to distinct spatial and temporal distributions of DDT, between upper and lower crust and between crust and mantle. Finally we compare crustal DDT that results from the models to those observed from wide-angle data measurements at rifted margins.

2 Numerical model

We use a 2D Lagrangian numerical code that is based on the finite element solver MILAMIN [*Dabrowski et al.*, 2008] to model extension of continental lithosphere. The geodynamic code solves the equations of mass, momentum and energy for visco-elasto-plastic rheologies (see supporting information). Plastic strain softening is included to resemble the formation of faults by decreasing the initial angle of friction with accumulated strain. The friction angle changes from 30 to 15° over an accumulated strain interval of 0 to 1 (Fig. 3b). Viscous strain softening accounts for the dynamic recrystallization that takes place in the dislocation creep and reduces the size of the grain, promoting a transition to diffusion creep. We model viscous strain softening by linearly reducing the effective viscosity with a factor α (supporting information Eq. 5) as deformation accumulates (Fig. 3c). Previous studies have shown that this strain softening is limited at temperatures higher than $800°C$, which lead us to introduce a temperature cut-off in the linear decrease of the α-factor [see supporting information; *Ros et al.*, 2017].

The 2D computational domain, 400 km wide and 400 km deep, is prescribed with a free slip condition to the bottom boundary and free surface to the top boundary [*Kaus et al.*, 2010; *Andrés-Martínez et al.*, 2015]. The boundary conditions imposed on the sides are vertical free slip and horizontal velocity. The bottom boundary has horizontal free-slip and vertical velocity to preserve the law of mass conservation. We run models with a standard continental lithosphere of 120 km thick and an underlying asthenosphere. The crust is composed of a 17.5 km thick upper crust of wet quartzite and a lower crust that varies in thickness and rheology. The lower crustal rheologies used in this study are wet quartzite, wet anorthite and mafic granulite (see Table 1), with a weak, intermediate and strong strength respectively. An additional test with a very weak strength, i.e. dry quartzite, is included for comparison. We use three values for the initial crustal thickness: 30, 35 and 40 km. The effect of increasing the thickness of the crust results in an increase of the ductile thickness within the lower crust, and, hence, in the degree of decoupling between crust and mantle (Fig. 4). The models include water loading to a level of 0 km. We test velocities within the of ultra-slow spreading rates of mid-ocean ridges [*Dick et al.*, 2003], which are appropriate for magma poor margins (3, 5 and 10 mm/yr half-extension) [*Ros et al.*, 2017].

The initial geotherm increases from constant $0°C$ at the surface to $1300°C$ at the 120 km depth Lithosphere Asthenosphere Boundary (LAB). Below the LAB, the temperature is held constant with depth. Extension begins with a thermal weak seed given by a 2D Gaussian shape (x-axis width of 10 km and z-axis width of 20 km) that increases the temperature at the center of the rift, about $70°C$ at a depth of 30 km, and that dissipates with time. Table 2 shows the applied thermo-mechanical parameter values.

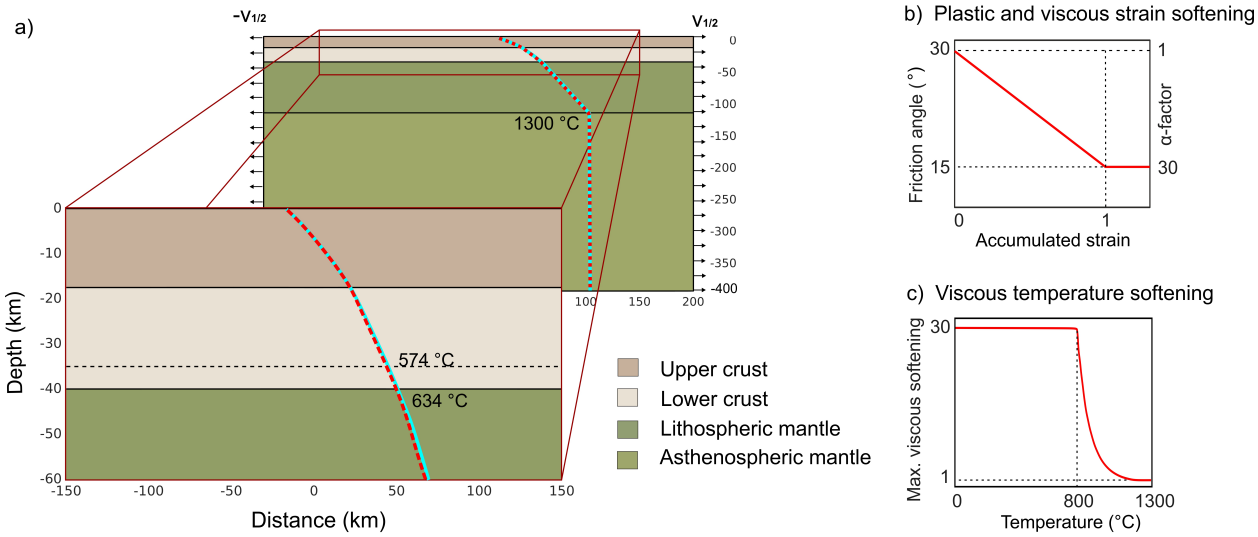

Figure 3. Numerical model setup. a) Model dimensions: 400 km width by 400 km deep. Base of upper crust at 17.5 km. Base of crust at 35 (horizontal dashed line) or 40 km (horizontal solid line) depending on the numerical experiment. Lithosphere-Asthenosphere Boundary at 120 km. Horizontal velocity boundary conditions are applied to the sides of the model, with half-extension $v_{1/2}$ values of 3, 5 and 10 mm/yr. Geotherms for cases with crustal thickness of 35 km (dashed red line) and 40 km (solid cyan line), b) Plastic and viscous strain softening and c) Temperature cut-off for the maximum viscous strain softening applied.

Lithospheric layer	**Rock type**	$\boldsymbol{log(B_{dis})}$ $(log(Pa^{-n}s^{-1}))$	$\boldsymbol{n_{dis}}$	$\boldsymbol{E_{dis}}$ $(kJmol^{-1})$	$\boldsymbol{log(B_{diff})}$ $(log(Pa^{-n}s^{-1}))$	$\boldsymbol{n_{diff}}$	$\boldsymbol{E_{diff}}$ $(kJmol^{-1})$
Upper crust	Dry quartzite	-19.57	2.4	156	0	0	0
	Wet quartzite	-28.00	4.0	223	0	0	0
Lower crust	Dry quartzite	-19.57	2.4	156	0	0	0
	Wet quartzite	-28.00	4.0	223	0	0	0
	Wet anorthite	-15.40	3.0	356	0	0	0
	Mafic granulite	-21.05	4.2	445	0	0	0
Lithospheric mantle	Dry olivine	-15.56	3.5	530	-8.65	1	375
Asthenospheric mantle	Wet olivine	-15.05	3.5	480	-8.65	1	335

Table 1. Rheological parameters. Dry quarzite [*Ranalli and Murphy*, 1987], wet quartzite [*Gleason and Tullis*, 1995], wet anorthite [*Rybacki and Dresen*, 2000], mafic granulite [*Wilks and Carter*, 1990], wet and dry olivine [*Hirth and Kohlstedt*, 2003].

Parameter	**Symbol (Units)**	**Upper crust**	**Lower crust**	**Lithospheric mantle**	**Asthenospheric mantle**
Cohesion	C (MPa)	10	10	10	10
Initial friction angle	ϕ $(°)$	30	30	30	30
Reference density	ρ (kg/m^3)	2700	2850	3300	3300
Initial depletion	F (%)	10	10	4	0
Heat capacity	Cp $(Jkg^{-1}K^{-1})$	1200	1200	1200	1200
Heat conductivity	k $(Wm^{-1}K^{-1})$	2.1	2.5	3.3	3.3
Thermal expansivity	α (μK^{-1})	24	24	30	30
Radioactive heat production	Hp (μWm^{-3})	1.3	0.2	-	-
Shear modulus	μ (GPa)	36	40	74	74

Table 2. Model parameters. The initial friction angle decreases to 15° over an accumulated strain interval of 0 to 1.

3 Results

During rifting, the spatial distribution of faulting and crustal thinning results from the complex interaction of various processes which are non-linear and feedback into each other. Here we analyze these processes, first for a very low constant extension velocity and later for higher values in order to explore the contribution of the velocity in shaping the architecture of the margin-pair.

Considering a constant extension velocity, the lower crustal strength plays a pivotal role in controlling the tectonic style of margins [e.g., *Buck*, 1991; *Huismans and Beaumont*, 2011, 2014; *Brune et al.*, 2014; *Svartman Dias et al.*, 2015; *Tetreault and Buiter*, 2017]. The rate and spatial distribution of crustal thinning depends mainly on the competition between the lower crustal flow outward from the basin, due to the extension imposed at the model sides, and the lower crustal flow towards the basin, due to the pressure low generated in the areas of local crustal thinning within the extending lithospheric section [See Fig. 2b from *Buck et al.*, 1999]. The spatial distribution of faulting depends on the ability of faults to localize extension. This ability depends on the competition between the work necessary to bend the topography around the fault due to the elastic response of the lithosphere [*Lavier and Buck*, 2002], and the work necessary to continue fault slipping. While the former work prevents further fault slip, strain softening facilitates it [*Lavier and Buck*, 2002]. The localization of deformation on faults and the offset they accommodate is also associated to the work needed to upwell the lower crust. As normal faulting occurs in the upper crust, the hagingwall and footwall move down and up, respectively. The underlying lower crust is also pulled upwards as the fault moves. The weaker the lower crust, the less work needs to be done in order for the lower crust to follow the overlying fault movement. A very weak lower crust will tend to facilitate the localization of slip on a given fault, as the lower crust can flow more easily towards the fault tip in response to slip.

3.1 Initial rift geometry and lower crustal strength

In the case our modelled lithosphere were completely viscous, the imposed flow by the mechanical boundary conditions would lead to a vertical upwelling of the ductile material and a lateral translation outwards from the basin center, similar to the flow pattern induced at mid-ocean ridges. In this section we show how different initial rheologies of the lower crust change this initial flow pattern.

The initial yield strength envelopes for the models tested in this study are depicted in Figure 4. The ductile layer of the strength envelopes is computed using the power-creep law for a strain rate of $10^{-14}s^{-1}$ and the brittle layer is estimated with the Mohr-Coulomb plasticity [*Byerlee*, 1978], which is slightly different from the Drucker-Prager plasticity used in our numerical models (see supporting information). Despite of this, the yield envelopes give an overall idea of the difference between the initial strength and coupling level of the models due to rheological changes. The initial lithospheric integrated strength is calculated for each model. The highest value is 14 TPa m, for the model with mafic granulite and 35 km crustal thickness, and the lowest value is 4.5 TPa m, for the model with wet quartzite and 40 km crustal thickness. The increase in crustal thickness decreases the coupling of the crust-mantle system [*Behn et al.*, 2002]. The degree of coupling between crust and mantle determines the strain distribution at early stages of the evolution [*Huismans and Beaumont*, 2003; *Gueydan et al.*, 2008] and hence the initial geometry of the models. We analyze the influence of the lower crustal strength on the geometry of the models at the initial stage of extension. For this we look at the vertical and lateral distribution of viscosity within the lower crust, in particular we focus on the isoviscosity contour of $10^{21} Pa\ s$ in Fig. 4. We use as examples the models extended by 3 mm/yr (models for higher velocities, 5 and 10 mm/yr, start deformation in the same mode).

For a mafic granulite rheology, the crust and mantle are coupled, and moderately coupled, in models with 35 and 40 km crustal thickness, respectively (MG models; Fig. 4b). In both models, after 3 Myr of extension, an initial graben has developed, which is the energetically most favorable fault configuration for a brittle layer extended by pure-shear [*Melosh and Williams*, 1989]. In the model with thin crust (MG 35 km; Fig. 4), the upper crustal brittle faults develop above the low viscosity zone of the lower crust, i.e. where the weak seed is located, and propagate to the brittle lithospheric mantle. This results in the downward deflection of the Moho as the symmetric graben deepens. The strong lower crust has limited flow outward from the graben because of its large viscosity. In the model with thick crust (MG 40 km; Fig. 4), the increase in crustal thickness from 35 to 40 km replaces previously strong mantle for weaker lower crust. This implies a slight decrease in the degree of coupling between crust and mantle, thereby allowing the deep lower crust to flow outward from the graben. The flow of the deep lower crust prevents the propagation of brittle upper crustal faults to the weaker lithospheric mantle, so the Moho is deflected upwards as the lower crust gets thinner. The resulting basin in the case with thin crust (35 km) has a width of ~87 km while the case with thick crust (40 km) has

a basin width of ~68 km. As the thickness of the upper brittle layer does not change from one case to the other, the width of the basin appears to be jointly controlled by the brittle part of the crust and mantle and by the strength of the lower crust. In other words, it is controlled by the effective elastic thickness (EET) of the lithosphere, as originally proposed by *Vening Meinesz* [1950], *Kusznir et al.* [1987] and *Weissel and Karner* [1989].

For a weaker rheology, wet anorthite, crust and mantle are coupled for the model with thin crust and barely coupled for the model with thick crust (AN models; Fig. 4b). The AN 35 km model starts deformation similar to the graben of the mafic granulite models. Several initial cross-conjugate faults develop above the weak zone within the lower crust (i.e. the weak seed) bounding a symmetric graben. After 3 Myr of extension, extension is localized on three active faults, where the two parallel faults on the left side of the basin are conjugate to the right side fault (AN 35 km; Fig. 4). During the first 3 Myr of extension, the lower viscosity at the very deep crust allows for a reduced lower crustal flow outward from the graben, although not enough to untighten brittle deformation between the upper crust and mantle. The resulting basin width is ~83 km while the inner graben width is ~67 km. The model with thicker crust, AN 40 km, initiates deformation in a half-graben. The increase in lower crustal thickness allows the formation of a wider low-viscosity layer (see white isoviscosity contour of $10^{21} Pa\ s$) that prevents upper crustal brittle faults connect to the shear zones of the ductile mantle. The hangingwall of the active fault bends downward while the footwall rises up assisted by the lower crustal flow. The width of the resulting asymmetric basin is ~56 km.

Models with wet quartzite completely decouple crust and mantle for the two crustal thickness (WQ models; Fig. 4b). In the WQ 35 km model, the low viscosity layer within the lower crust is laterally more distributed than in previous examples (see white isoviscosity contour of $10^{21} Pa\ s$) and allows localization of crustal faults over a broader area. This leads to the formation of two pairs of conjugate normal faults that propagate as shear zones within the lower crust and connect to the brittle lithospheric mantle faults. These faults develop two grabens with a horst centered above the weak seed. The weaker lower crustal rheology compared to the previous models allows the lower crust to effectively flow outward from the horst while the deep lower crust flows towards the center of the rift driven by the crustal thickness gradients, i.e. crustal isostasy of *Buck et al.* [1999] (see Fig. 9b). The resulting basins have widths of approximately 25 km each. The very weak lower crust of the WQ 40 km model spreads also over a large lateral width of the domain (see white isoviscosity contour of $10^{21} Pa\ s$). This would allow faults to develop over a wide area, as in the former case. However, the substitution of the top 5 km of mantle by 5 km of very weak deep lower crust results in massive lower crustal flow towards the tip of one of the central faults, allowing it to acquire a large offset. Due to the small EET of this model, the fault progressively rotates as it accommodates extension, forming a core complex that exhumes lower crust. The weak lower crust prevents the propagation of the upper crustal deformation to deeper ductile levels. The resulting basin width is ~40 km.

In summary, we observe that localization of deformation into upper crustal single faults is favoured in two opposite situations, for either very strong or very weak lower crust. Very strong lower crust allows upper crustal faults to propagate through the lower crust and connect with brittle faults in the upper mantle, creating a very coupled system. Very weak lower crust flows massively towards the center allowing one of the originally formed faults to easily accommodate slip and acquire a very large offset. Due to the small EET, this fault rotates creating a core complex-like structure and smooth topography. Conversely, in the case of very strong lower crust, rift topography is large. Wide rifts form when the lower crust is weak enough to allow various faults to develop simultaneously, but too strong to abundantly flow to any of them to generate a core complex. The further evolution of any of these systems depends on the lateral and vertical distribution of weak lower crust from this point onwards, which we discuss in the next section.

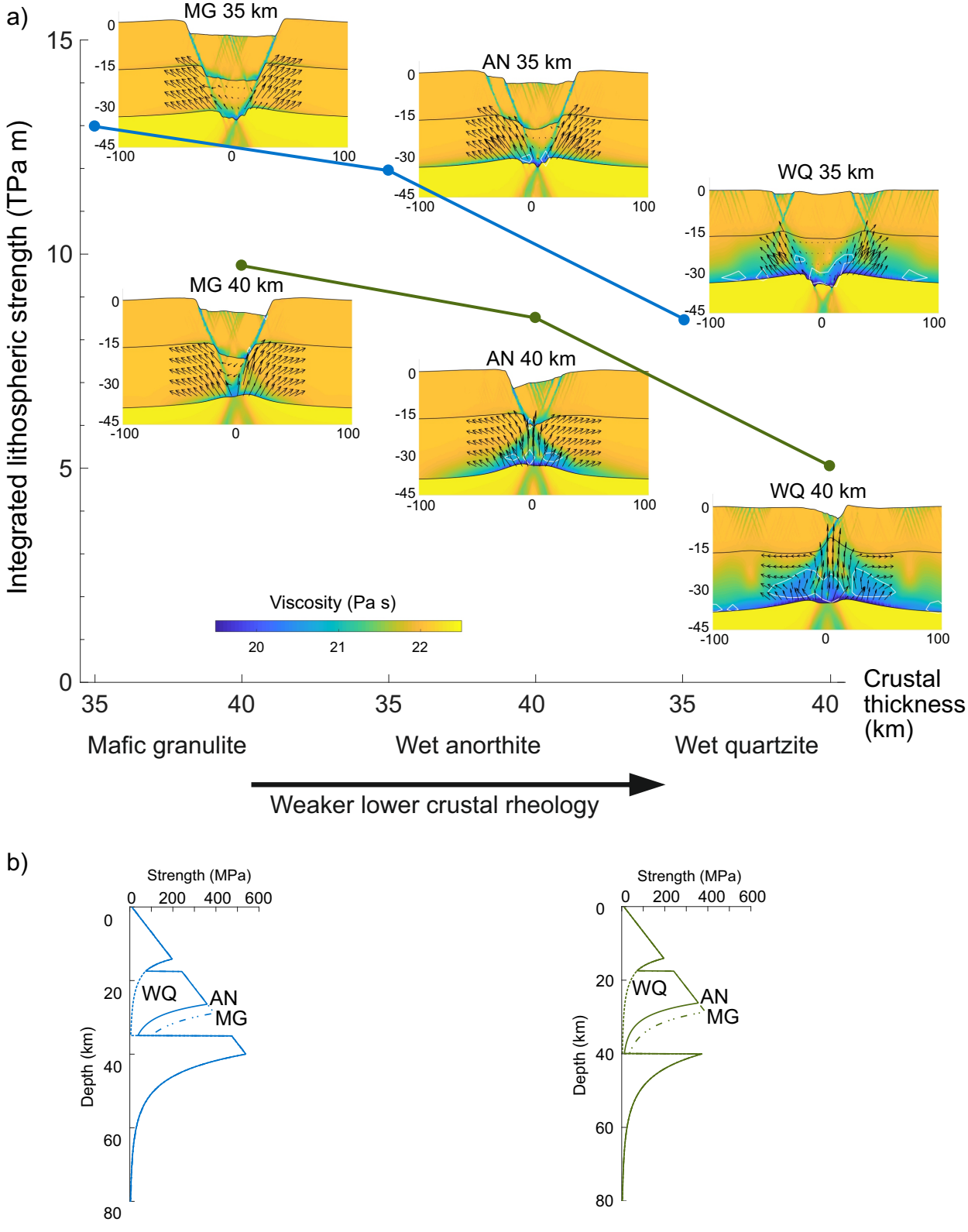

Figure 4. a) Initial integrated lithospheric strength, viscosity field and rift geometry after 3 Myr of extension for the models with lower crustal rheologies of mafic granulite (MG), wet anorthite (AN) and wet quartzite (WQ), for 35 and 40 km crustal thickness and half-extension velocity of 3 mm/yr. Depth and distance are in km. The white contour shows isoviscosity of $10^{21} Pa\,s$. Velocity arrows show the flow of the lower crust at the main active rift zone. b) Strength envelopes calculated for a strain rate of $10^{-14} s^{-1}$.

3.2 Rift development and lower crustal strength

In this section we describe the tectonic evolution of the end-member rheological models with mafic granulite and wet quartzite extended by 3 mm/yr, focusing on the behavior of the brittle and ductile lithospheric parts and how their interaction influences the lower-crust flow (see Figures 5-8 and Movies S1-S4 in supporting information).

3.2.1 Strong mafic granulite

The MG 35 km model starts localizing deformation in a narrow rift (Movie S1), where the lower-crust flow is confined by the subsiding graben (3 Myr, see also Fig. 5a and Fig. 9a). Strain is mostly localized into two faults/shear zones which dip towards the initial weak seed. Strain softening facilitates continued slip on these conjugate faults, but, with offset accumulation, the local work necessary to bend the topography becomes larger and the deformation localizes on new faults in the center of the basin, which is the weakest area as it has been thermally thinned by the upwelling mantle (4 Myr). The now weakened deep crust is capable of flowing outward from the area of maximum extension. Continued slip along faults at the basin center induces lower crustal flow towards their footwalls (5 to 8 Myr). However, outside the rift zone the lower crust retrieves the velocity pattern given by boundary conditions. The new faults disaggregate the initial graben and effectively thin the crust (Fig. 5b). The narrow mode of extension continues during most of the tectonic evolution. Final stages localize extension in an attempt of sequential faulting, where the mantle in the fault's footwall cools and behaves more brittle as it is progressively exhumed (11 Myr). Break-up is reached at 18 Myr, when brittle faults can connect from the surface to the mantle. Since brittle faults in the mantle occur in the footwall of the sequential fault array, the final break-up also occurs in the footwall of the last sequential fault. In this process the lower crust has been squeezed out of the distal margins. The resulting margins are narrow, nearly symmetric, and exhibit large shoulder uplift and strong syn-rift subsidence (Fig. 5d).

The MG 40 km model initially accommodates extension in a narrow rift (Movie S2, 1 and 2 Myr). The part of the lower crust confined by the conjugate faults flows downwards with the subsiding graben. In contrast, the deepest part of the lower crust, which is at higher temperature than in the case with 35 km crust, behaves more ductile and retains the flow enforced by the boundary conditions, i.e. flows out of the basin center. The faults bounding the graben are progressively abandoned because the work needed to bend the topography around them increases and it is easier to break new faults within the thermally weakened central graben (4 to 6 Myr, see also Fig. 6a). From 6 to 9 Myr, several faults are simultaneously active in the basin center and show contrasting dips. At 10 Myr, a dominant direction of dip is established and new faults always form at the hangingwall of previous ones, whereby the extensional mode changes to sequential faulting. The horizontal component of the lower crustal velocity is shown in Fig. 9a and c for comparison of the the narrow and sequential faulting modes. Displacement along the active fault results in asymmetric uplift of the asthenosphere towards its hangingwall (from 12 Myr in advance), thereby weakening this area and creating a low viscosity pocket at the tip of a dominant active fault (Fig. 6b). This very weak lower crust prevents faulting from mechanically breaking-up the crust. Eventually, the lower crustal pocket and the exhumed mantle in the footwall of the sequential faults cool and embrittle (23 Myr, Fig. 6c). Upper crustal brittle faults subsequently move on top of this brittle mantle area. Break-up occurs at 27 Myr soon after brittle faults can connect from surface to mantle in an area located in the footwall of the last sequential fault. The lower crust has exhumed at the distal part of both conjugate margins. The sequential faulting mode produces a wide margin with highly thinned crust and a narrow conjugate margin, which is the hangingwall of the sequential fault array, and the final tectonic configuration shows large shoulder uplift and strong syn-rift subsidence (Fig. 6d).

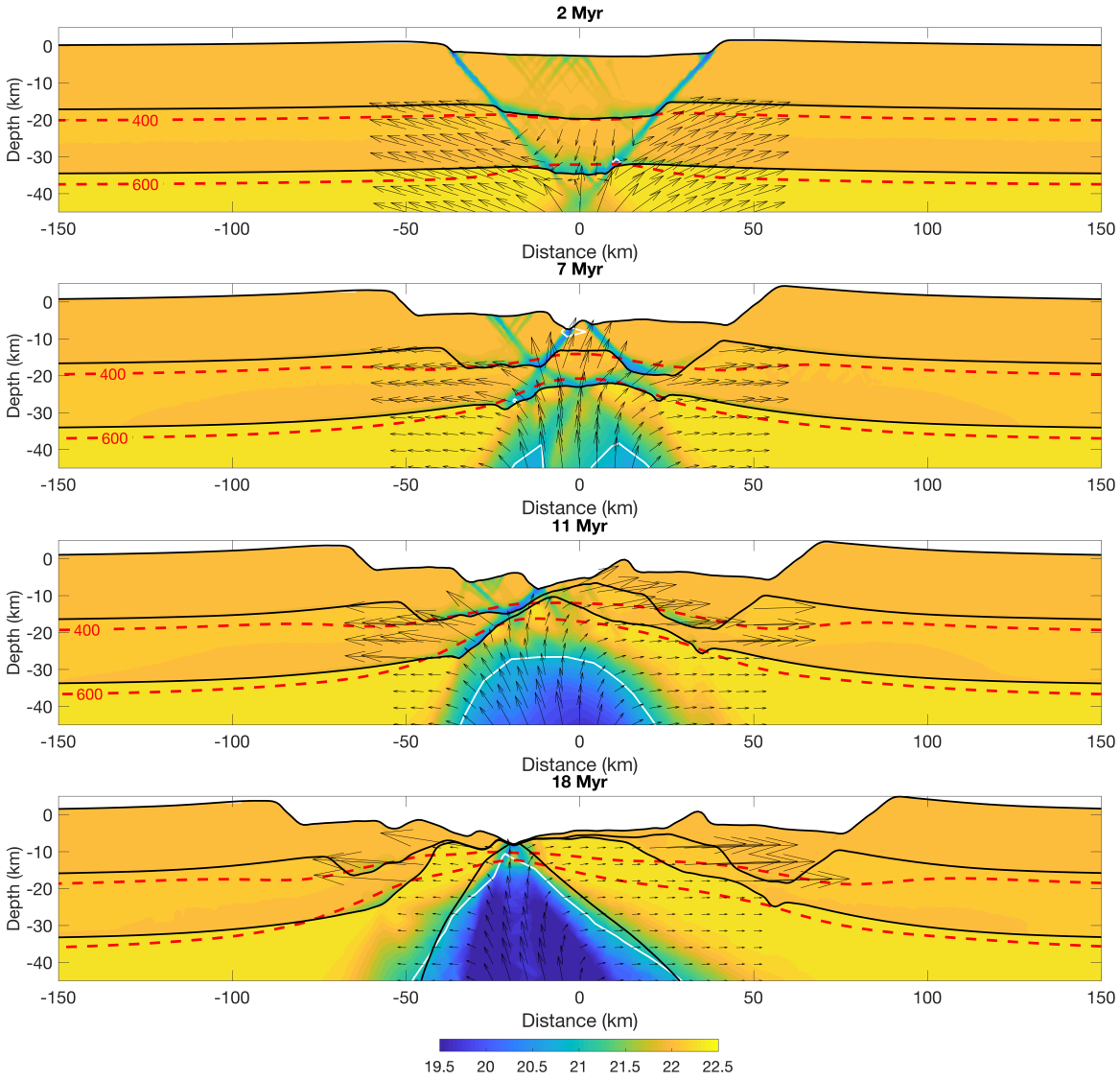

Figure 5. Evolution of the viscosity field ($Pa\,s$) of the model with mafic granulite lower crust and 35 km crustal thickness. Half-extension velocity is 3 mm/yr. The low viscosity channel ($< 10^{21} Pa\,s$) is depicted by the white contours. Isotherms of 400 and 600$^{\circ}C$ are depicted by the dashed red contours. Velocity arrows show the flow of the lower crust and mantle at the main active rift zone.

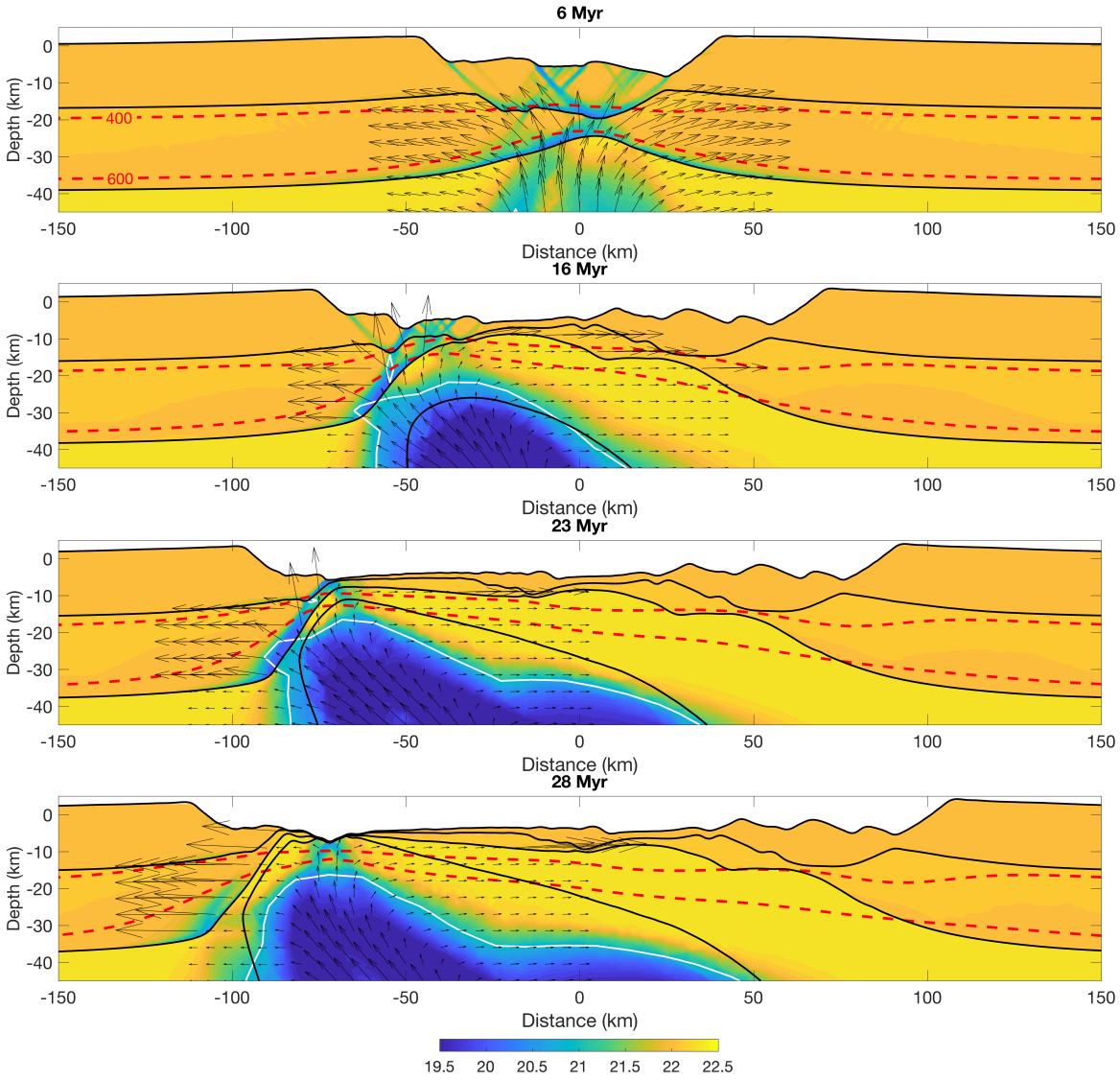

Figure 6. Evolution of the viscosity field ($Pa\,s$) of the model with mafic granulite lower crust and 40 km crustal thickness. Half-extension velocity is 3 mm/yr. The low viscosity channel ($< 10^{21} Pa\,s$) is depicted by the white contours. Isotherms of 400 and 600°C are depicted by the dashed red contours. Velocity arrows show the flow of the lower crust and mantle at the main active rift zone.

3.2.2 Weak wet quartzite

The WQ 35 km model starts rifting in wide rift mode. Brittle deformation is confined to the top part of the upper crust while the lower crustal layer behaves in a ductile manner and is bound between the brittle upper crust and mantle (Movie S3, 1 Myr). Its flow follows the imposed velocity boundaries. However, the low viscosity layer at the deep crust allows it to flow towards the center of the domain, compensating effective crustal thinning (see horizontal component of the velocity in Fig. 9b). The wide rift mode is characterized by a thin and extended low viscosity channel at the bottom of the crust (2 Myr). This results in the deformation of the upper crust by simultaneous faulting instead of two conjugate main faults dipping towards the weak seed, as previously shown for the stronger lower crustal models. Because the deformation in the upper crust is decoupled from the mantle by the weak lower crust, the two faults dipping towards the weak seed are not dominant over their antithetic faults. Hence, two grabens develop on both sides of a central horst, which is located over the weak seed (3 Myr). Below the horst, the lower crust remains practically static, while the rest of the lower crust flows towards the two grabens (3 Myr, Fig. 7a). After 4 Myr, continuous thermal thinning below the horst allows the underlying lower crust to flow outwards. Upper crustal faulting moves towards the model sides, following the outward flow of the lower crust. Simultaneous faults develop forming several mini basins (4 to 9 Myr, Fig. 7b) as predicted by the wide rift mode [*Buck*, 1991]. However, the uplift of the mantle is still centered beneath the initial horst, which weakens with time. This leads deformation to abandon the model sides and localizes on the horst (10 to 14 Myr). After 15 Myr, the model evolves to a last phase of sequential faulting mode, as the low viscosity region becomes reduced to a pocket at the tip of a dominant active fault due to cooling (18 Myr, see also Fig. 9c). Deformation moves laterally, guided by the hot and weak lower-crust flow towards the tip of the active fault. This effectively thins the crust over a wide distance. At 19 Myr, the top of the mantle beneath the footwall of the main ductile lower crustal shear zone, becomes shallow enough to behave brittle. Upper crustal deformation progressively focuses on top of this brittle upper mantle. Crustal thinning is then very effective, and lower crust flows out of the area of maximum extension (20 Myr). At 24 Myr, a well connected system of faults/shear zones tie upper crust to mantle. At this time, the deepest part of the upper crust is ductile. Break-up occurs when this ductile upper crust disappears and brittle faults cross from the surface to the mantle at 28 Myr. The locus of break-up is on the footwall of the last sequential fault. Final margins are asymmetric, do not present lower crust at their distal ends, and show low subsidence and shoulders uplift (Fig. 7d).

The low viscosities in the lower crust of the WQ 40 km model allow extension to be initially accommodated in many upper crustal faults (Movie S4, 1 Myr) while the direction of flow of the low viscosity lower crust is given by the velocity boundary conditions. After 2 Myr, one of the faults dipping towards the weak seed becomes dominant. The lower crust is weak enough to easily flow in response to slip along this fault, which in turn reinforces slip localization. Strain softening also facilitates the accumulation of slip into this initially high-angle fault that progressively rotates forming a core complex (5 Myr, Fig. 8a). This core complex rift mode is characterized by a thick low viscosity channel at the base of the crust that allows little thinning over a wide region while accommodates most deformation in a narrow zone of the upper crust. The deep crustal flow tends to distribute deformation delaying the thinning of the crust (see the horizontal velocity component in Fig. 9d). At 8 Myr, the work needed to bend the topography around the fault becomes larger than breaking new faults outward from the rift zone, which involves a progressive change to the wide rift mode (from 10 to 23 Myr, Fig. 8b). During this transition, thermal thinning is expanded to a central region of about 100 km and the low viscosity channel at the deep crust becomes thinner, changing the pattern of the lower-crust flow to a pure-shear distribution. The evolution continues in a similar manner than the case of WQ 35 km, where the wide mode switches to sequential faulting (32 Myr, Fig. 8c). In this case, the lower viscosity within the lower crust allows a long phase of sequential faulting that leads to a very wide and narrow conjugate margins. These asymmetric margins show little subsidence and shoulders uplift (51 Myr, Fig. 8d). As in the previous cases, break-up occurs when brittle faults connect surface and mantle, in the footwall of the last sequential fault..

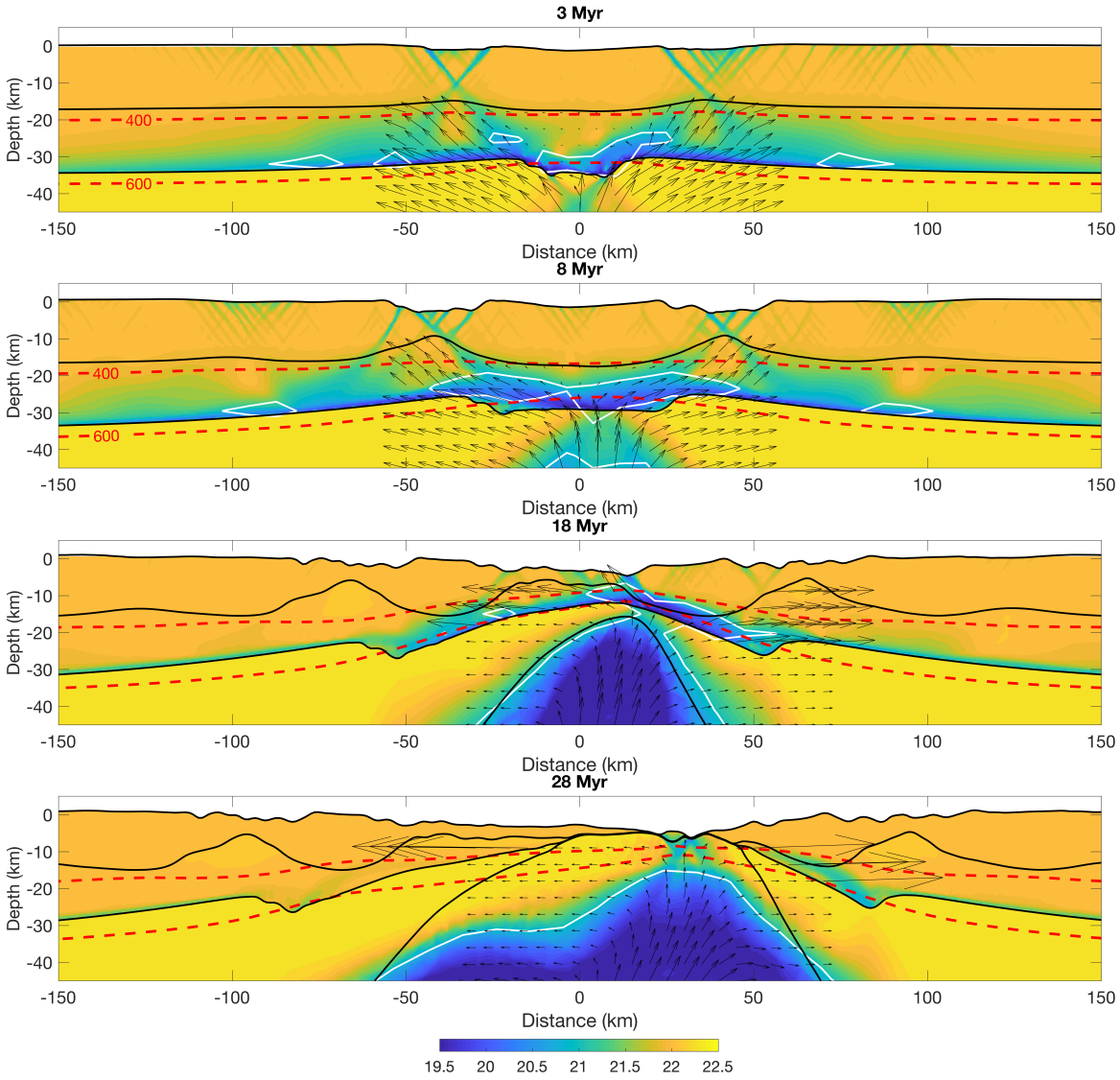

Figure 7. Evolution of the viscosity field ($Pa\,s$) of the model with wet quartzite lower crust and 35 km crustal thickness. Half-extension velocity is 3 mm/yr. The low viscosity channel ($< 10^{21} Pa\,s$) is depicted by the white contours. Isotherms of 400 and 600$^{\circ}C$ are depicted by the dashed red contours. Velocity arrows show the flow of the lower crust and mantle at the main active rift zone.

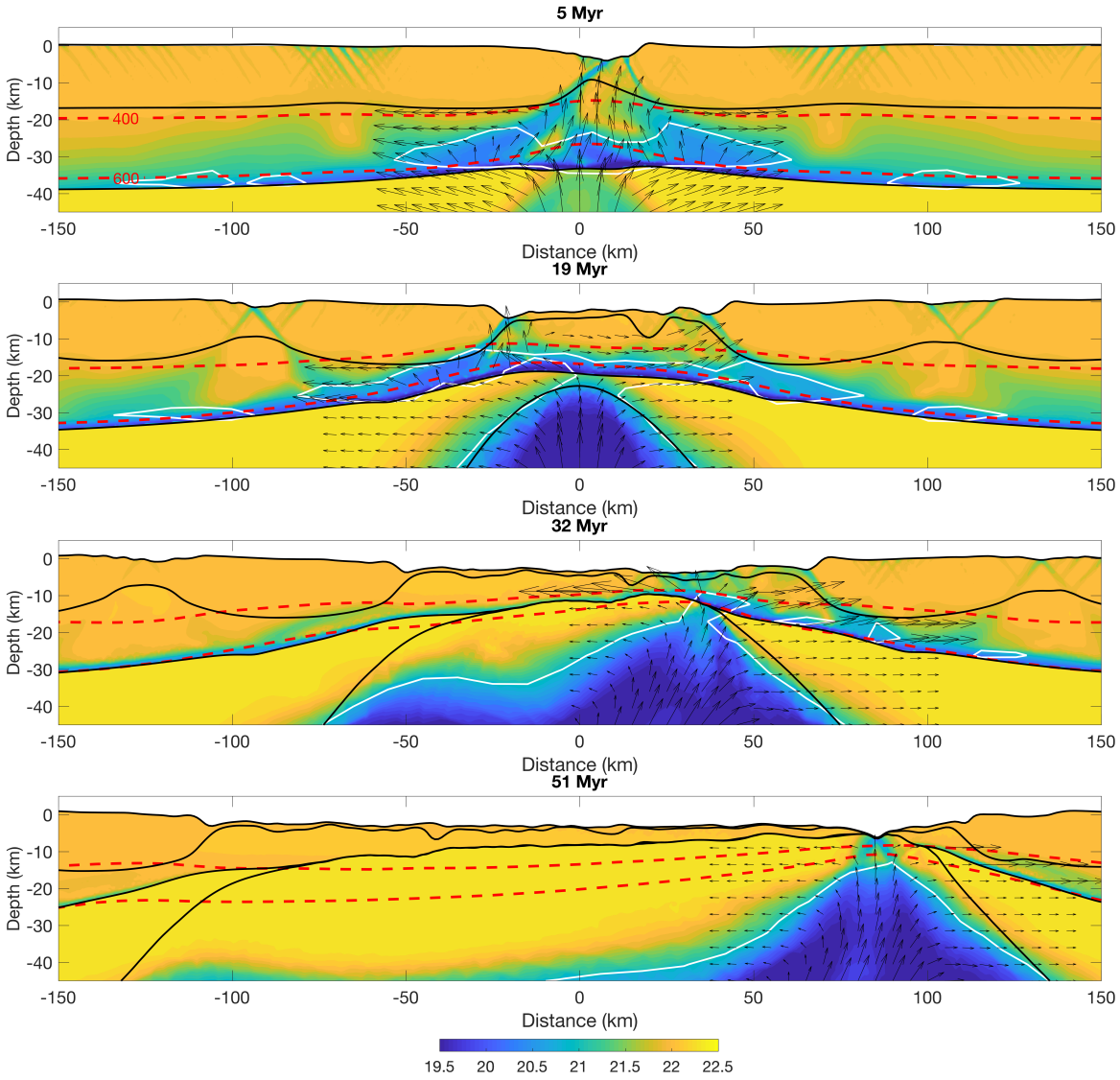

Figure 8. Evolution of the viscosity field ($Pa\,s$) of the model with wet quartzite lower crust and 40 km crustal thickness. Half-extension velocity is 3 mm/yr. The low viscosity channel ($< 10^{21} Pa\,s$) is depicted by the white contours. Isotherms of 400 and 600°C are depicted by the dashed red contours. Velocity arrows show the flow of the lower crust and mantle at the main active rift zone.

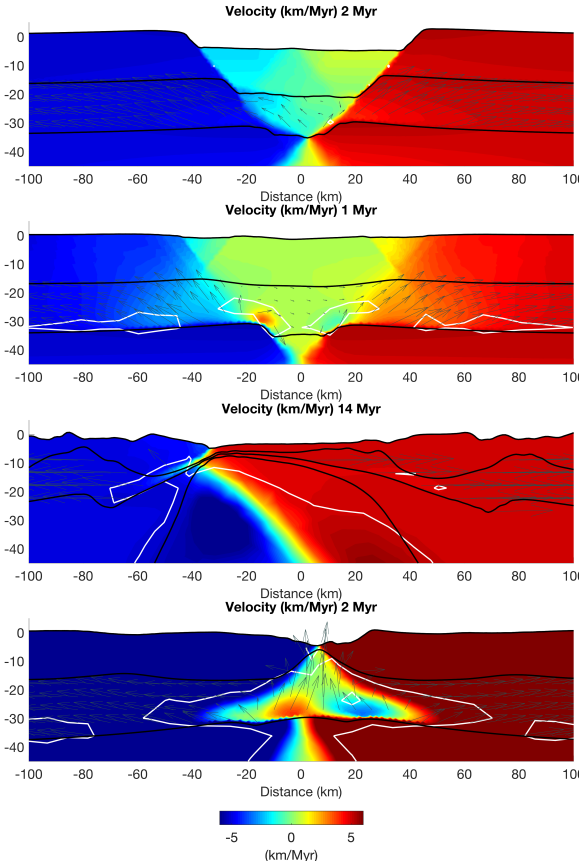

Figure 9. Horizontal component of the velocity and lower crustal flow for different modes of extension: a) narrow rift mode (model MG 35 km and 5 mm/yr half-extension), b) wide rift mode (model WQ 35 km and 5 mm/yr), c) sequential faulting rift mode (model WQ 35 km and 5 mm/yr) and d) core complex rift mode (model WQ 40 km and 10 mm/yr). The low viscosity channel ($< 10^{21} Pa\ s$) is depicted by the white contours. MG is mafic granulite and WQ is wet quartzite for the lower crust. 35 and 40 km is crustal thickness.

3.2.3 Very weak dry quartzite

We have additionally tested an extremely weak crustal rheology for the model with 40 km crustal thickness (dry quartzite, see Table 1). The evolution of the model is more similar to the results of *Huismans and Beaumont* [2014] for Type II margins, which is characterized by a continuous pure shear thinning that results in extremely wide and symmetric margins (Movie S7). In this model (5 mm/yr), the low viscosity channel within the lower crust covers a much wider lateral extent (3 Myr, Fig. 10a), enhancing the decoupling of crust and mantle, which allows the wide rift mode to dominate over most of the evolution. The inset in Fig. 10b (9 Myr) shows how this weak lower crust massively flows to the rift axis and delays effective crustal thinning. At the initial stages, deformation is accommodated by a series of core complexes that dip towards the model sides and the lower crust is completely exhumed at the basin center. As the very weak lower crust feeding the core complexes cools and becomes stronger, these faults cannot accommodate larger offsets and upper crustal deformation migrates laterally towards weaker locations at the model sides. The lower crust thins by pure shear and consequently the low viscosity channel at the crust bottom becomes thinner (25 Myr, Fig. 10c). After 35 Myr, mantle thermal thinning has debilitated the basin center and deformation focuses again within this area. Conjugate faults/shear zones connect from the surface to the mantle and, when they behave completely brittle, break-up occurs at the model center (42 Myr). The resulting margins are very wide and symmetric, with exhumed lower crust at the distal margins, very little evidence for brittle faulting and small syn-rift subsidence.

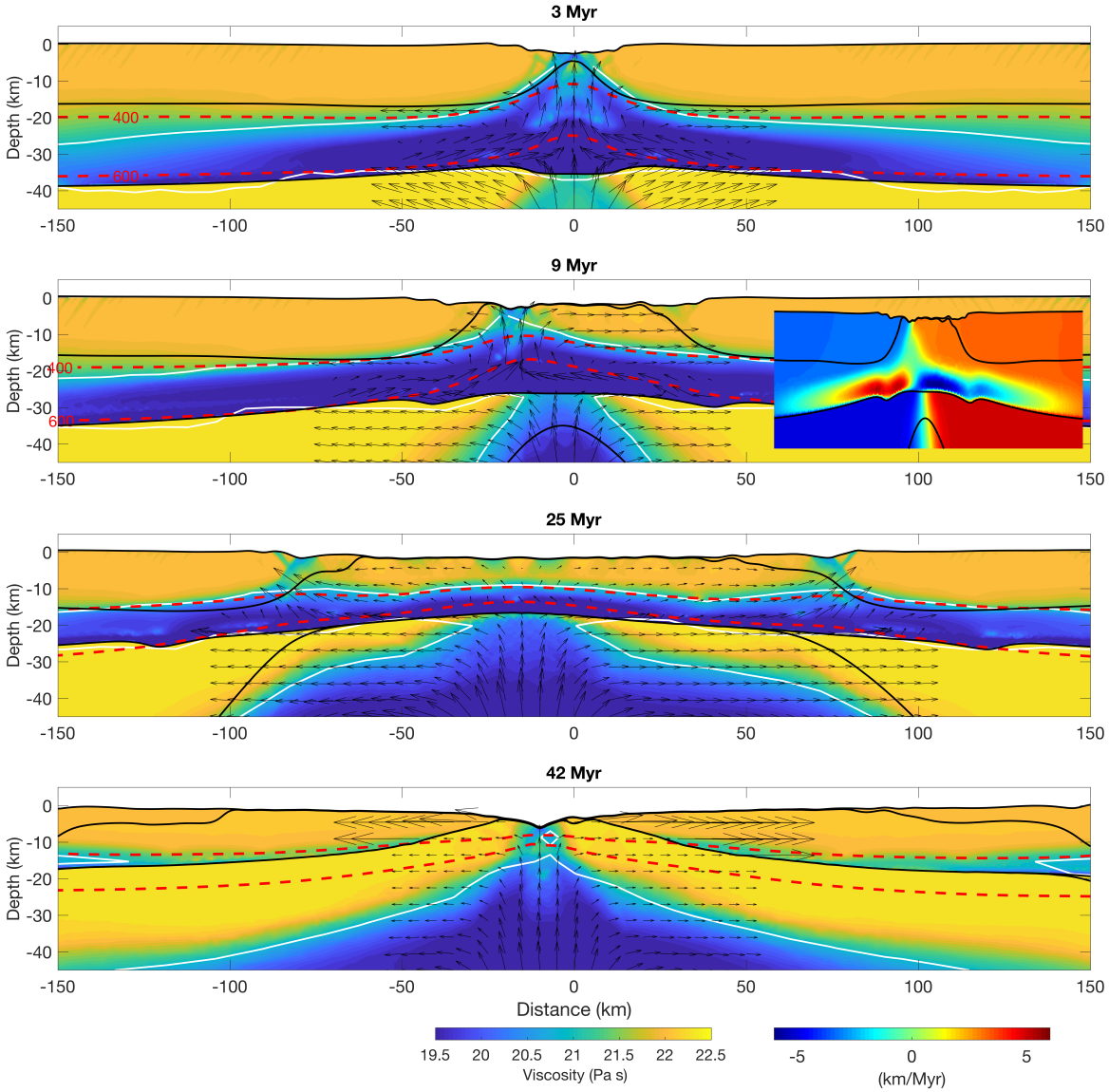

Figure 10. Evolution of the viscosity field ($Pa\,s$) of the model with very weak dry quartzite upper and lower crust and 40 km crustal thickness. Half-extension velocity is 5 mm/yr. The low viscosity channel ($< 10^{21} Pa\,s$) is depicted by the white contours. Isotherms of 400 and 600°C are depicted by the dashed red contours. Velocity arrows show the flow of the lower crust and mantle at the main active rift zone. Inset shows horizontal component of the velocity.

3.3 Influence of ultra-slow extension velocity on asymmetry

We now focus on how extension velocity modifies the evolution of deformation. In continental rifting, extension velocity plays a key role in the distribution of strain by controlling the weakening or strengthening of the lithosphere [*Kusznir and Park*, 1987; *Pérez-Gussinyé and Reston*, 2001]. On one hand, higher extension velocities involve larger background strain rates that strengthen the ductile parts of the crust and mantle and enhance initial coupling between these layers [*Buck et al.*, 1999; *Huismans and Beaumont*, 2003; *Tetreault and Buiter*, 2017]. For this higher background strain rate, the zones where strain accumulates will weaken more as strain softening depends on the accumulated strain, resulting in faster localization of deformation and accelerating break-up. On the other hand, higher extension velocities also lead to faster thermal advection [*Buck et al.*, 1999], which results in weakening. This can either result in enhanced localization of deformation and rapid break-up, or increased ductility of the crust and mantle that may delay break-up, as in the case of sequential faulting [*Brune et al.*, 2014]. The interplay between these effects modify the extensional histories we have previously described and give rise to a range of margin architectures.

Our modelling results show that the competition between the above mentioned processes, with increasing extension velocity, is closely dependent on the background rheology of the lower crust. In this section we describe the effect of changing the extension velocity for the four set-ups previously explained, i.e. models with mafic granulite and wet quartzite and crustal thickness of 35 and 40 km, where two opposite trends are observed depending on whether the lower crust is stronger or weaker.

3.3.1 Strong mafic granulite

Increasing extension velocity for the models with mafic granulite leads to narrower and symmetric margins (Fig. 11a and b). In both cases, the initial conjugate faults bounding the graben are more localized due to the higher accumulated strain and hence, strain softening. The initial crust-mantle system is still enough coupled for the faster extensional settings (5 and 10 mm/yr). The mantle upwelling and consequent thermal thinning is more rapid in these cases and keeps deformation localized at the initial narrow rift. The feedback between strain softening and thermal thinning leads to continental break-up into symmetric and narrower conjugates. This result is more noticeable for the case with a 40 km thick crust, where the slowest extension velocity (3 mm/yr) produced asymmetric margins due to the effect of strengthening in the competition of heat advection and conductive cooling, while the fastest velocity (10 mm/yr) produced symmetric margins due to dominant weakening effect of heat advection.

3.3.2 Weak wet quartzite

The effect of increasing the extension velocity differs for the wet quartzite models with 35 and 40 km thick crust. For the WQ 35 km models, faster extension velocities result in more asymmetric margins (Fig. 11c). The initial system is more decoupled for higher velocities, with the generation of a thicker and more distributed low viscosity layer at the deep crust, which allows more lower crustal flow. Fast strain softening and thermal weakening override the initial increase in coupling due to the higher ductile stresses. Faster thermal thinning with increasing extension velocity implies that heat advection is more effective, hence, the low viscosity pocket within the lower crust that promotes sequential faulting lasts longer because the isotherms are kept at shallower levels. The resulting conjugate-margin asymmetry becomes more pronounced as the wide margin becomes wider [*Brune et al.*, 2014]. Therefore, the effect of increasing the velocity for a weaker lower crust is the opposite to previous stronger models. Faster velocities promote the development of a wider margin and hence a larger degree of asymmetry.

In contrast, for the WQ 40 km models, faster extension velocities results in narrower, but still asymmetric, margins. The initial stages are characterized by the development of a core complex and distributed deformation also to either sides of the rift. With increasing velocity, the low viscosity channel within the lower crust becomes thicker and wider. In the case of the highest velocity, this channel is as thick as the whole lower crust and results in a larger flow of lower crust towards the developing core complex. This leads to lower crustal exhumation soon after the start of extension. The difference between the three velocity cases relates to the relative time of the onset of sequential faulting. As the velocity increases, sequential faulting starts over a previously thinner crust due to the effect of thermal thinning and strain softening. As a consequence, the phase of sequential faulting lasts shorter for higher velocities, since crustal breakup is reached sooner. Therefore, although the low viscosity pocket for these models is thicker for faster velocities, as in the case of WQ 35 km, the crustal thickness by the time that sequential faulting starts (32 Myr for the model extended by 3 mm/yr, 18 Myr for 5 mm/yr and 6 Myr for 10 mm/yr), counteracts the widening of the margin.

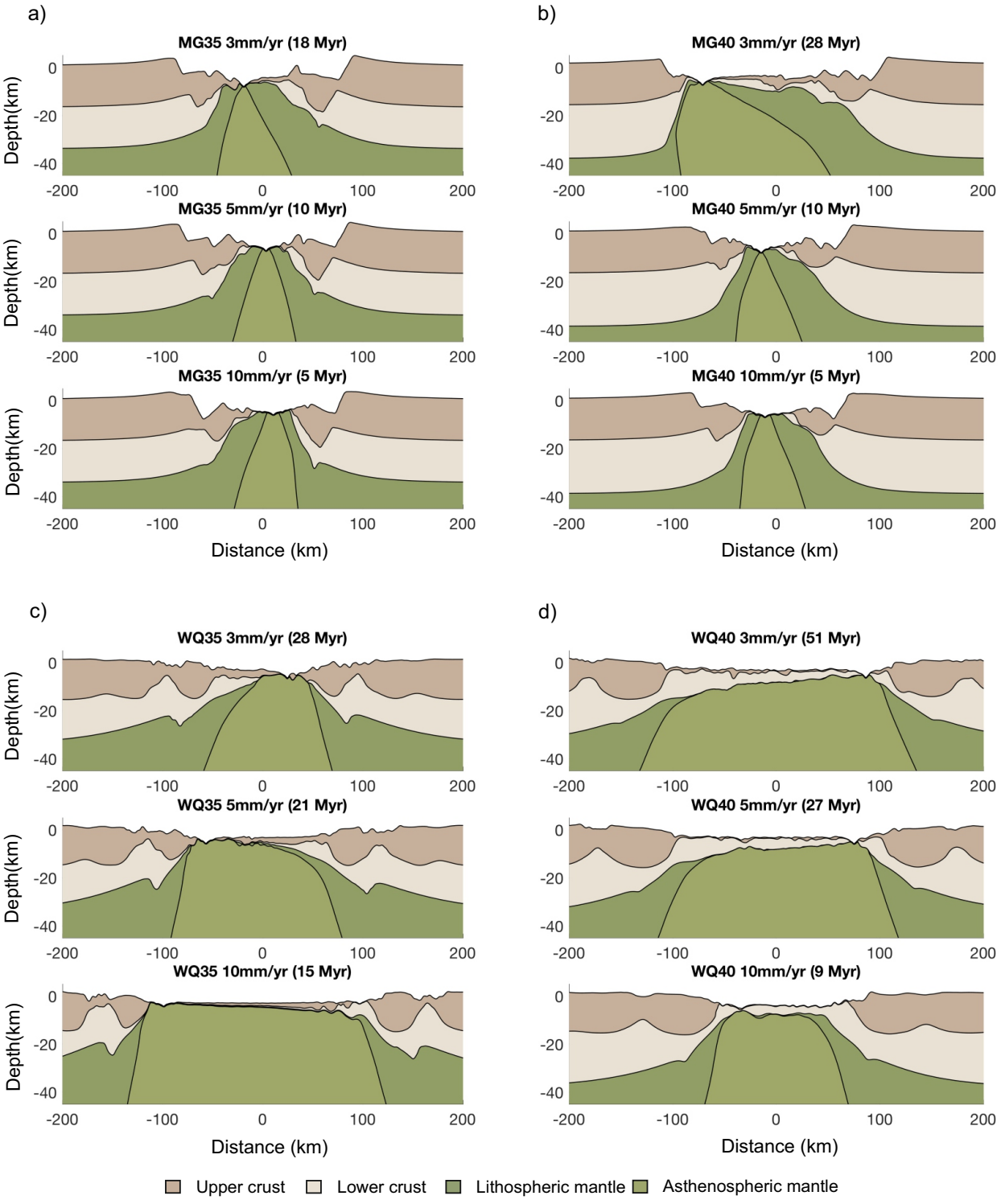

Figure 11. Final stage of the tested models for the extension velocities of 3, 5 and 10 mm/yr. MG is mafic granulite and WQ is wet quartzite for the lower crustal rheology. 35 and 40 indicate km of crustal thickness.

The two different trends arise as a consequence of the proportion of brittle to ductile crust by the time sequential faulting starts (Fig. 12). Models with 40 km crustal thickness have thicker brittle crust which counteracts the effect

of the low viscosity pocket in the ductile crust. This is due to a more distributed thermal thinning during previous extension as a consequence of the larger shear zone developed above the Moho. This shear zone results from strain softening and lower crustal strength.

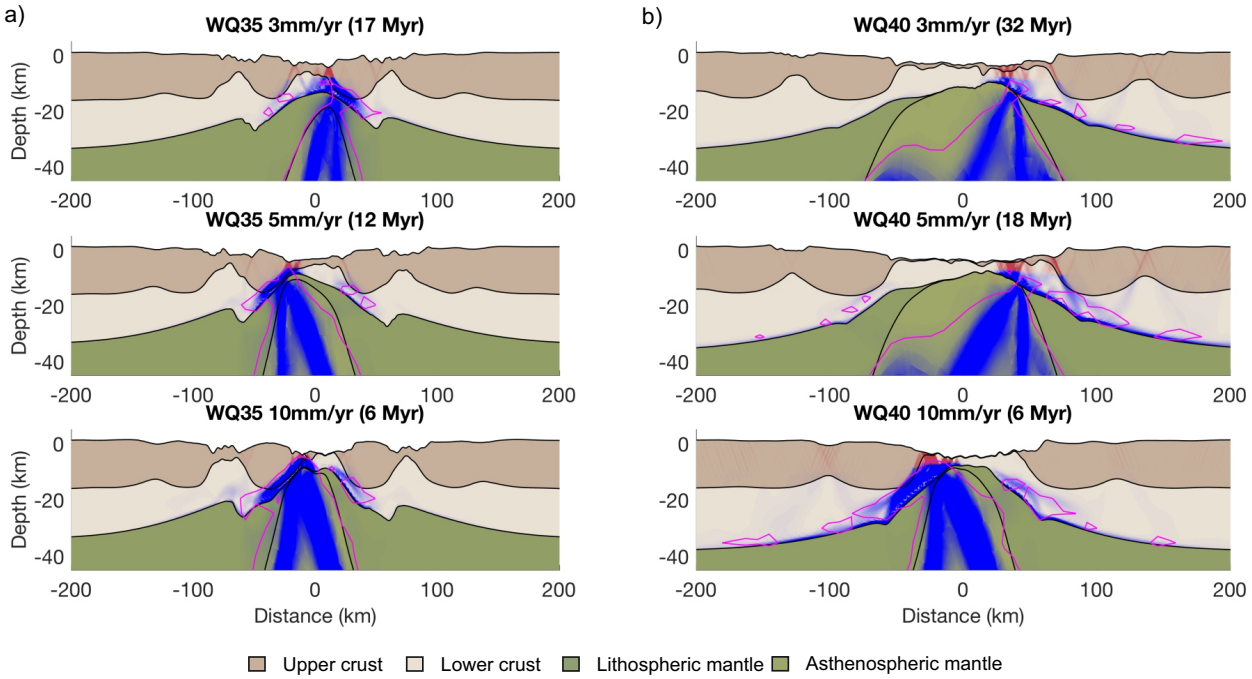

Figure 12. Models with wet quartzite lower crust by the start of sequential faulting. a) models with 35 thick-crust. b) models with 40 thick-crust. Half-extension velocities are 3, 5 and 10 mm/yr from top to bottom. Upper crustal thickness is 17.5 km. Red and blue colors show plastic and viscous strain rate (s^{-1}), respectively. The low viscosity channel ($< 10^{21} Pa\ s$) is depicted by the pink contours.

3.4 Influence of upper and lower crustal thickness ratio on lower crust exhumation

We have seen in previous sections how the lower crust is either exhumed or removed at the distal margins. In this section we analyze the reasons underlying the different behaviors by looking at how lower crustal exhumation depends on the ratio of the thickness of the upper and the lower crust H_{UC}/H_{LC}. We have tested values of H_{UC}/H_{LC} between 0.33 and 2 and Fig.14 shows how the exhumation of the lower crust depends on this ratio.

We first describe the results of the models shown in previous sections. In previous models, the upper crust is always 17.5 km thick and the lower crustal thickness varies between 17.5 and 22.5 km, for a total crustal thickness of 35 km and 40 km, respectively. The evolution of these models shows that for a ratio $H_{UC}/H_{LC} = 1$ (models with 35 km total crustal thickness), none of the models shows exhumation of the lower crust for any lower crustal rheology and extension velocity (Fig. 11a and c). However, for a ratio $H_{UC}/H_{LC} = 0.78$ (models with 40 km total crustal thickness), exhumation of the lower crust is promoted with decreasing lower crustal viscosity (Figs. 11b and d). For the strong mafic granulite models, only a very short phase of lower crustal exhumation occurs followed by crustal break-up. However, for the weak wet quartzite, lower-crust exhumation is observed over larger extensions. For the models with weak rheology, the amount of exhumed lower crust increases with extension velocity. The cause is that faster velocities lead to a less viscous rheology over a more extended region at the deep crust, which is more prone to flow and allow the formation of core complexes (comparison of low viscosity channel at 1 Myr in Fig. 13).

We test new models by varying the initial crustal thickness (30, 35 and 40 km) and the upper crustal thickness (10, 15 and 20 km) to extend the parameter space of the upper-lower crustal thickness ratio H_{UC}/H_{LC} . The models consist of a lower crustal rheology of intermediate strength, i.e. wet anorthite, and are extended by 5 and 10 mm/yr velocities.

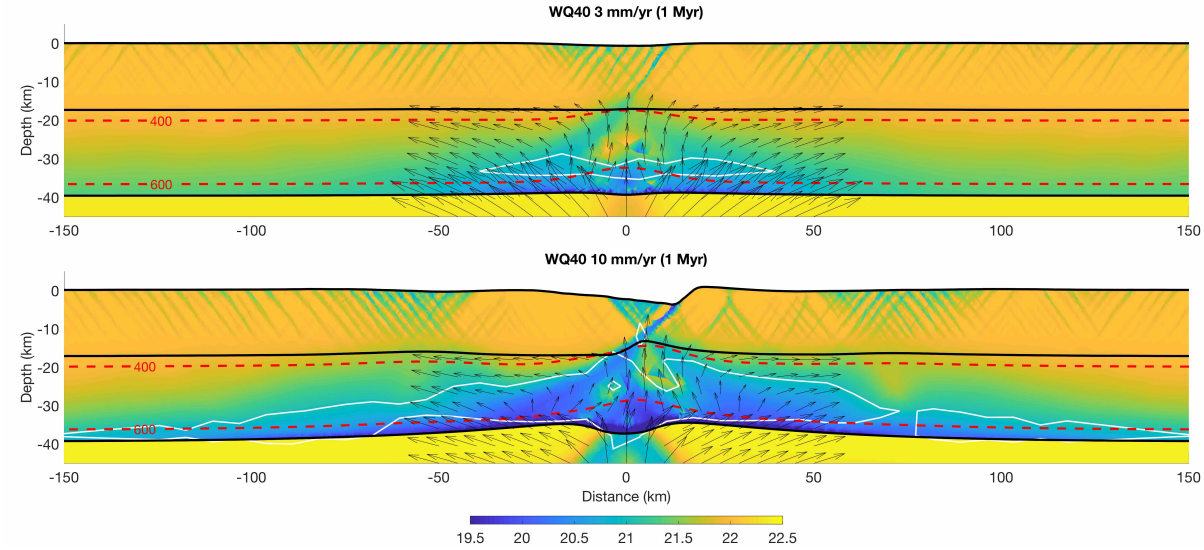

Figure 13. Viscosity field ($Pa\,s$) of two numerical models with wet quartzite lower crust and 40 km thick crust after 1 Myr of extension. Top: model with 3 mm/yr half-extension velocity. Bottom: model with 10 mm/yr half-extension velocity. The low viscosity channel ($< 10^{21} Pa\,s$) is depicted by the white contours. Isotherms of 400 and 600°C are depicted by the dashed red contours. Velocity arrows show the flow of the lower crust and mantle at the main active rift zone.

Figure 14 shows the ratio H_{UC}/H_{LC} for the different thickness combinations. We explore the role of H_{UC}/H_{LC} as a control for lower crustal exhumation.

For values of H_{UC}/H_{LC} between 0.3 and 0.5, the lower crust is at least twice as thick as the upper crust, facilitating the exhumation of the lower crust. The case with initial crust of 40 km and upper crust of 10 km ($H_{UC}/H_{LC} = 0.33$, 5 mm/yr) localizes deformation in a graben at early stages (see Movie S5 in supporting information). After 4 Myr of extension, an initially high-angle fault in the middle of the graben becomes progressively listric as the weak lower crust flows towards its tip. This fault exhumes lower crust and, short after (5.4 Myr), a new fault develops on its hanging wall which continues to exhume lower crust. Subsequently, an array of sequential faults develops on the exhumed and cooled lower crust, which behaves brittle on its shallower part. The few final sequential faults break into the future conjugate margin, bringing upper crust in the last stages of rifting. The resulting wide margin exposes a wide area of lower crust at the sea-floor (about 50 km) and the distal part includes upper crust which has been cut from the narrow margin side (Fig. 14b).

For values of H_{UC}/H_{LC} between 0.5 and 1, the lower crust is still thicker than the upper crust but the difference diminishes. In this transitional zone (Fig. 14), the extension velocity controls whether or not the lower crust is exhumed. For the wet anorthite rheology we are using, faster velocities (10 mm/yr) translate to more ductile behavior, which facilitates the flow of the lower crust and its prolonged extension, resulting in exhumation.

Finally, values of H_{UC}/H_{LC} equal or greater than 1 means that the upper crustal thickness is thicker than the lower crust and prevents the exhumation of the latter. In these models the lower crust flows out of the basin before the upper crust ruptures. For example, the model with initial crust of 35 km thick and upper crust of 20 km ($H_{UC}/H_{LC} = 1.33$, 10 mm/yr) (see Movie S5 in supporting information), starts also deformation in a graben, but the evolution differs from the previous example. In this case, an initial graben accommodates deformation. As the strong graben subsides, its base drives the lower crust downwards. The lower crust is squeezed between the upwelling mantle and the downwelling graben and it flows away from the extending region. At 2 Myr, the thickness of the lower crust below the graben is already less than 5 km. New faults cutting through the graben thin more the lower-crust layer until the upper crust and mantle couple. As a result, the lower crust is missing in the distal part of the rifted margins (Fig. 14a).

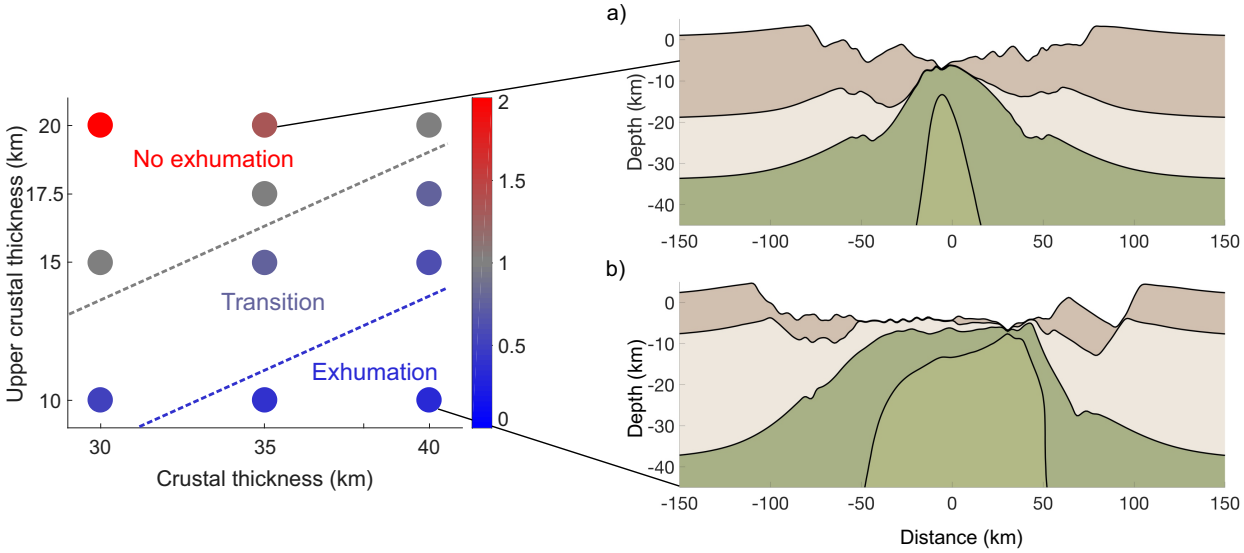

Figure 14. Parameter test of initial upper-lower crustal thickness ratio H_{UC}/H_{LC} and its effect on lower crustal exhumation. Results from models with wet anorthite lower crust, extended by 5 and 10 mm/yr. a) H_{UC}/H_{LC} = 1.33 , model with crustal thickness of 35 km and upper crust of 20 km (10 mm/yr) . b) H_{UC}/H_{LC} = 0.33 , model with crustal thickness of 40 km and upper crust of 10 km (5 mm/yr).

3.5 Lithospheric depth dependent thinning and heat flow history

The thermal evolution undergone by natural rifted margins is difficult to constraint. Present heat flow measurements are key in the understanding the thermal structure of continental margins. However, the amount of heat flow observations from margins is still scarce and other type of data, such as the subsidence history, are used to predict heat flow by applying kinematic and thermal models [*Watts*, 2012]. The temporal evolution of heat flow strongly depends on lithospheric thinning. Therefore, this section focuses on analyzing the surface heat flow evolution during different modes of lithospheric extension, i.e. narrow, wide, core complex and sequential faulting. At the beginning of rifting, all models start with surface heat flow of 54 mW/m^2, except above the thermal weak seed where the heat flow reaches a maximum value of 81 mW/m^2. In order to relate the surface heat flow distribution to the lithospheric thinning, we calculate the thinning factor γ of different lithospheric layers, where $\gamma = 1 - \frac{1}{\beta}$ and β is the stretching factor [*McKenzie*, 1978] defined as the ratio of initial to final thickness.

Firstly, we compare the evolution of two models that after break up show symmetric conjugate margins. An initially coupled model that deforms as a narrow rift mode and an initially decoupled model that deforms as a succession of core complex and wide modes (Movie S6 and S7 in supporting information). Movie S6 shows in the top panel the heat flow history and the thinning factors for the crust and lithospheric mantle for a model with mafic granulite lower crust, 35 km thick crust with 17 km of upper crust, extended by 5 mm/yr. This model evolves as a narrow rift mode until break-up (bottom panel). The model starts with the development of a graben and two heat flow peaks occurring above the graben border faults (2 Myr). Slip along the new faults dismembering the graben thin the crust and increase the heat flow as a result of the upwelling mantle below (5 Myr). As crustal thinning continues, a basin forms in the center of the domain where heat flow increases until reaching its maximum before break-up (7 Myr). On average, most areas of the margins have undergone heat flows of about 100 mW/m^2, with some peaks of 200 mW/m^2 over active faults, while the margins sectors in the most distal parts, close to the break-up area, have undergone values of about 400 mW/m^2.

Movie S7 shows the evolution of a model with dry quartzite in both crustal layers (the weakest rheology tested in this study), 40 km of crustal thickness and upper crust of 17 km, for an extension velocity of 5 mm/yr. The initial lower crust is very weak and it is exhumed in a core complex mode by localized faults, until around 16-20 Myr. This generates high heat-flow peaks of about 200 mW/m^2 localized in the area of the active core complexes, while the rest of the thinned crust sustains heat flows of around 100 mW/m^2, even when the entire lithospheric mantle has been

thinned after 13 Myr. This means that, in the area of the core complexes, a significant proportion of the heat is brought up by advection of the lower crust. After 20 Myr, the weak lower crust feeding the core complexes exhausts due to its exhumation and consequent cooling. Upper crustal deformation by faulting moves to both sides of the area affected by core complex activity, while this central area thins in pure shear. This model evolves into a wide rift mode of deformation, which thins the crust very little and in a distributed way over a wide area (25 Myr). After 34 Myr, the center of the basin has been significantly weakened by thermal thinning and deformation returns to this zone. Thus, the crust effectively thins and breaks, leading to an increase of heat flow to 400 mW/m^2 at the very distal margin domains. The proximal margins, where upper crust is still present and have not been affected by core complexes, have undergone a practically constant heat flow of 100 mW/m^2 (see snapshot at break-up 41 Myr: from 100 km to more than 200 km, and from -100 km to less than -200 km). In contrast, the intermediate domains, where core complexes were active, have experienced peak heat flows of 200 mW/m^2 in the first 20 Myr of extension (see snapshot at break-up 41 Myr: from 50 km to 100 km, and from -100 km to -150 km).

Figure 15 compares the surface heat flow for a maximum crustal thinning of 70 % for the narrow (5 Myr) and wide (31 Myr) rifting models. Our results support first-order estimates from *Hopper and Buck* [1996] who showed that, for the narrow rift mode, the heat flow away from the active rift remains constant while an increase is produced inside the active rift zone. In our narrow rift model (Fig. 15a), we can observe this localized heat flow anomaly that increases as crustal thinning continues and that is higher above the deep high angle faults. For the wide rift mode, *Hopper and Buck* [1996] showed that this increase in heat flow does not occur, instead, it has a more uniform distribution over the broad active zone. Our wide rift model (Fig. 15b) also shows this distribution, with local highs above the active faults. We observe as well how the narrow rift model, that results from extension of coupled lithospheric layers, shows similar thinning distribution of crust and mantle while the wide rift model, which arise from decoupled lithospheric layers, let the mantle to thin faster than the crust at the center of the extending region.

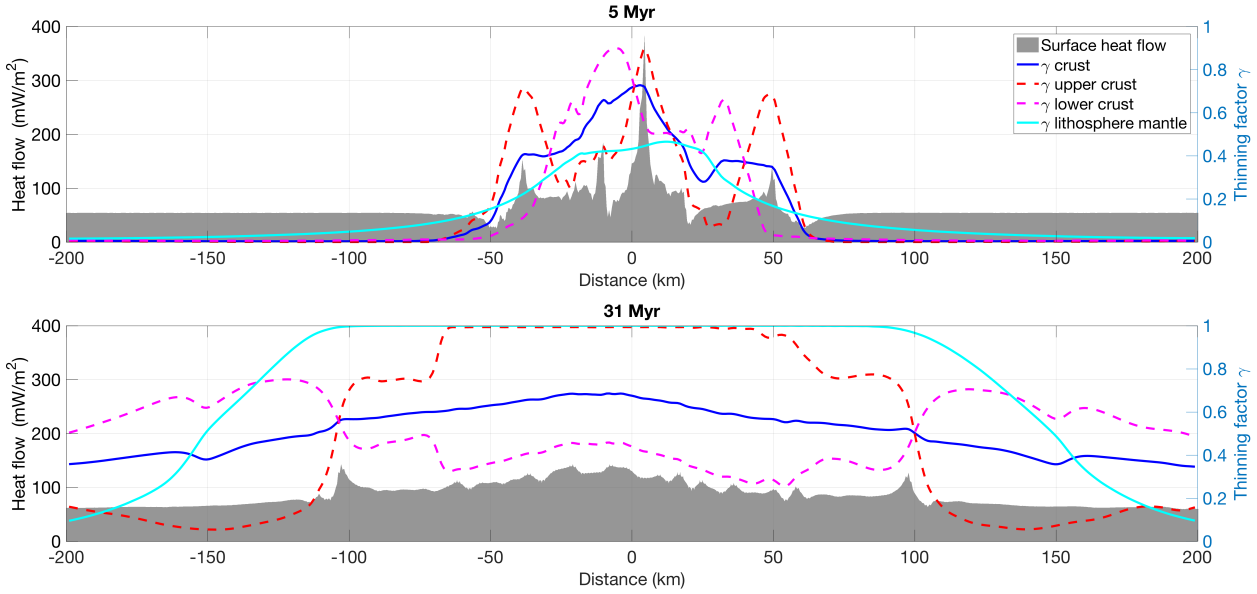

Figure 15. Comparison of the surface heat flow and thinning factors (γ) distribution for symmetric extension of models undergoing narrow rift mode (top panel) and core complex and wide rift mode (bottom panel). Crustal thinning is of 70% in both models. Top: model with mafic granulite lower crust, 35 km thick crust with 17 km of upper crust, extended by 5 mm/yr. Bottom: model with dry quartzite in both crustal layers, 40 km of thick crust with 17 km of upper crust, extended by 5 mm/yr.

Secondly, we compare three asymmetric models that present a long phase of the sequential faulting mode, where the proportions of upper and lower crust differ between them (Movie S8, S9 and S10 in supporting information). The first model has a lower crust of mafic granulite, crust of 40 km and upper crust of 17 km, and it is extended by 3 mm/yr (Movie S8). The model starts in a narrow rift mode and changes to sequential faulting mode after 9 Myr, when the

mantle has thinned about 45 % and the crust 75 %. The sequence of faults thins progressively the crust and upwells the asthenosphere towards the tip of the active fault. This mode involves an increase in temperature at the fault's tip that it is reflected on the surface heat flow. A migrating heat flow peak of values between 300 and 500 mW/m^2 has gone through the final wide margin for an extension of 100 km (see snapshot at 27 Myr: from -40 to 60 km) over a period of 15 Myr. In this case, the upper- and lower-crust thinning distribution have been similar during the whole evolution (Fig. 16a). After the asthenosphere reaches the surface, deformation jumps to the narrow margin producing an allochton of continental crust (from 28 to 37 Myr).

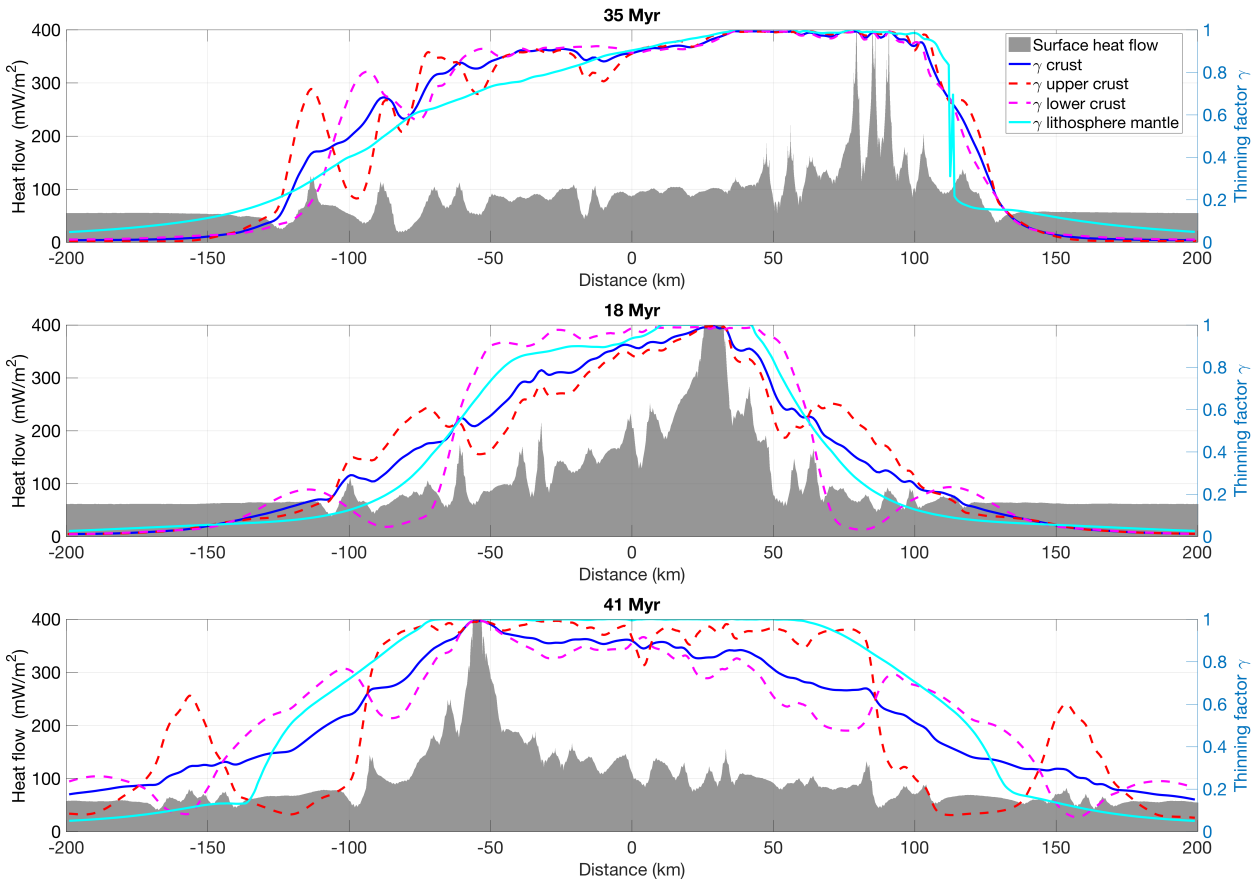

Figure 16. Comparison of the surface heat flow and thinning factors (γ) distribution for asymmetric extension of models undergoing sequential faulting rift mode. Crustal thinning is about 70-75% in the three models. Top: model with mafic granulite lower crust, 40 km thick crust with 17 km of upper crust, extended by 3 mm/yr. Middle: model with wet anorthite lower crust, 33 km thick crust with 22 km of upper crust, extended by 4 mm/yr. Bottom: model with wet quartzite lower crust, 40 km of thick crust with 16 km of upper crust, extended by 3 mm/yr.

The second model has a weak lower crust of wet anorthite, a crust of 33 km and upper crust of 22 km, with an extension velocity of 4 mm/yr (Movie S9). The lower crust flows outward from the basin center at the early stages of the narrow rift mode, before sequential faulting starts at 12 Myr. The mantle has been thinned to 90 % and the crust 70 % below the basin center by the start of sequential faulting. Therefore, the asymmetric upwelling of the asthenosphere towards the active fault takes only 5 Myr to reach the surface. The heat flow peak migrates for an extension of 40 km, heating up the thin crust of the wide margin (see snapshot at 18 Myr: from -15 to 25 km) with values between 400 and 500 mW/m^2. In this case, the lower-crust thinning distribution has been larger than upper-crust thinning until the

complete removal of the lower crust (Fig. 16b), which is strongly related to the relative initial thickness of both crustal layers, since the lower crust was initially half the thickness of the upper crust.

The last model uses a very weak lower crust with wet quartzite, a crust of 40 km and upper crust of 16 km, and 3 mm/yr of extension velocity (Movie S10). From initial core complex mode, the model evolves to wide rift mode at 10 Myr and later to sequential faulting mode, at 24 Myr. The upper crust has been practically thinned and the sequence of faults develop mostly on brittle lower crust. Lithospheric mantle thinning is of 100 % below the basin while crustal thinning has reached a maximum of 75 %. As the rift center migrates during this extensional mode, the heat flow peak moves with the rift center with values between 200 and 300 mW/m^2. An extension of 100 km in the distal part of the wide margin (from -50 to 50 km in the snapshot at 41 Myr) has undergone larger values of heat flow for a period of 16 Myr. In this case, the upper-crust thinning distribution has been higher than the lower-crust thinning (Fig. 16c).

Figure 16 compares the surface heat flow at the time of break-up for the three models showing a phase of sequential faulting. The values reached by the heat flow peak during sequential faulting differ between the three models. By the time sequential faulting starts, crustal thinning is very similar for the three cases, with values between 70 and 75 %, however, mantle thinning changes from 45 % for the first model, to 90 and 100 % for the second and third model. Given the mantle thinning factors below the basin, one would expect a higher heat flow due to the proximity of the asthenosphere. However, we observe that the main change is related to upper crustal thinning. Upper-crust thinning is lower in the second model, which contains higher radioactive production, and results in a higher value of the heat flow peak (400 to 500 mW/m^2) (Fig. 16b). In contrast, upper-crust thinning is higher in the third model, with very low radioactive production and this results in a lower value of the heat flow peak (200 to 300 mW/m^2) (Fig. 16c). Finally, the first model shows intermediate values of 300 to 500 mW/m^2 as it still conserves a thin upper crustal layer (Fig. 16a).

3.6 Crustal depth dependent stretching

In this section we investigate the ratio of upper- to lower-crust thickness UC/LC across the thinning lithosphere for different modes of extension. Distinct distribution of crustal depth dependent stretching, DDS, and crustal stretching factor, β_c, result depending on the lower crustal strength. First, we compare the two end-member models of previous section that result in symmetric margins: the coupled model that evolves as a narrow rift (mafic granulite lower crust, 35 km thick crust with 17 km of upper crust, extended by 5 mm/yr) and the decoupled model that evolves as a core complex and wide rift (dry quartzite in both crustal layers, 40 km of thickness and upper crust of 17 km, for an extension velocity of 5 mm/yr).

For the coupled model, rifting evolves in narrow mode (Movie S6, middle panel). At the initial stages of extension, two main border faults form and exhume LC in their footwalls, creating an excess of LC in these areas and a deficit below the central graben they enclose (2 Myr). As faults accumulate slip, the relative deficits of LC and UC are enhanced (3 Myr). With increasing extension, border faults become abandoned and deformation focuses on the thermally weakened central graben (4 Myr). A new major fault forms exhuming lower crust in its footwall, which results in crustal thinning. The LC moves outwards following the flow prescribed by the boundary conditions. Further deficit of LC is generated in the basin center, specially in the hangingwall of the main fault (i.e. left of 0 km at 5 Myr). Deformation finally moves to the footwall of this fault, where the mantle has been cooled and is brittle (6 Myr), and, hence, deformation is very localized at the basin center ($\beta_c > 10$). Here two faults form at the edge of each future margin. These faults continue to slip and exhume LC in their footwalls until final break-up occurs and the mantle is exposed at the surface. The final pattern of UC/LC shows LC excesses and deficits at a fault-block scale, which can be trace back to the main faults.

For the decoupled model, rifting shows a completely different evolution for the crustal DDS (Movie S7, middle panel). Here deformation localizes in a series of core complexes that exhume lower crust at the basin center. This occurs until around 20 Myr ($\beta_c = 2$ at the center of the basin) and results in a very broad area of LC excess with very little topography. On both sides of this area, a deficit of lower crust occurs where the upper crust is still thick. Deformation continues for 14 Myr by pure shear of the lower crust and faulting of the upper crust at the sides of the exhumed lower crust. At $\beta_c = 4$ (34 Myr), the center of the basin has been thermally weakened and deformation focuses there again. Two main basinward dipping faults dominate the deformation and lead to break-up. The final pattern of UC and LC distribution shows a large central area characterized by excess of LC and basin sides with deficit of LC. This excess of LC cannot be traced to any recognizable fault-block scale, as core complexes have had different dip directions and successively cut each other.

The main difference between both models is provided by the flow of the lower crust. For the coupled model, this flow is limited and mostly behaves following the upper-crust faulting (Fig. 17a). For the decoupled model, this flow is massive towards the basin center and it is associated to the activity of several core complexes. Therefore, the coupled model shows a variation in UC/LC at a fault-block scale while the decoupled model shows a great change in UC/LC over large distances (Fig. 17b).

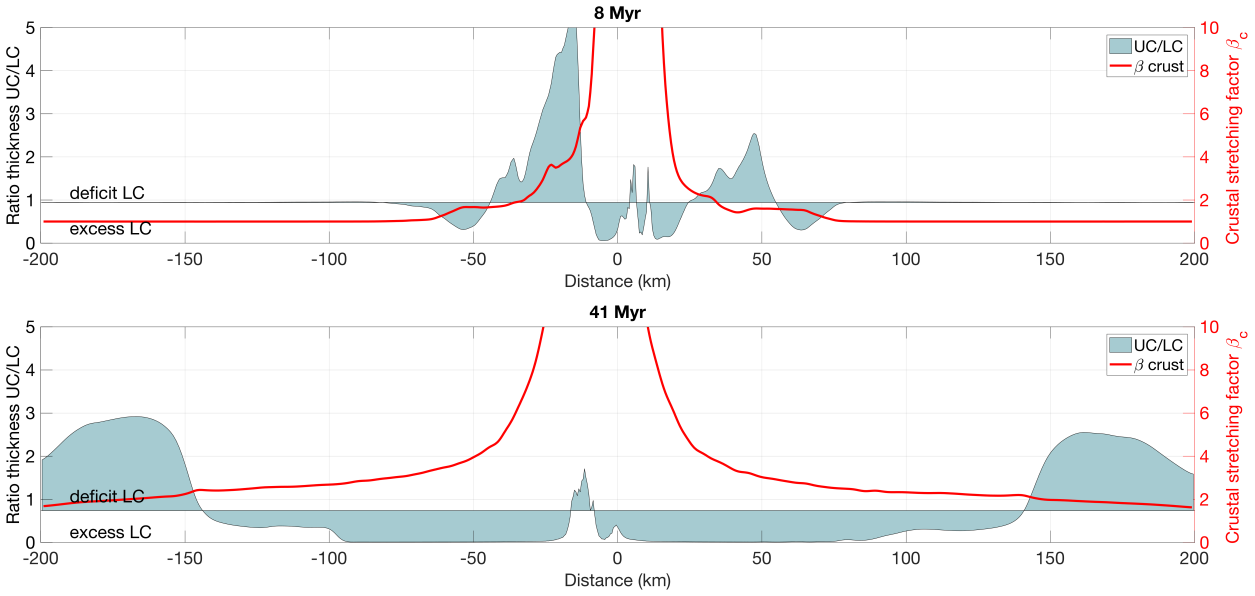

Figure 17. Comparison of the ratio UC/LC and crustal stretching factor (β_c) distribution for symmetric models at the time of break-up, which have evolve as narrow rift mode (top panel) and core complex and wide rift mode (bottom panel). Top: model with mafic granulite lower crust, 35 km thick crust with 17 km of upper crust, extended by 5 mm/yr. Bottom: model with dry quartzite in both crustal layers, 40 km of thick crust with 17 km of upper crust, extended by 5 mm/yr.

We analyze below the ratio UC/LC for the three asymmetric models described in the previous section where sequential faulting mode takes place. The first model has a mafic granulite lower crust, with 40 km crustal thickness, 17 km thick upper crust and 3 mm/yr half-extension (Movie S8, middle panel). At early stages this model behaves in a similar manner to the previous coupled model in terms of UC/LC, showing excess of LC in the footwalls and deficits in the hangingwalls. However, the weaker deep lower crust in this model allows a rift mode switch from the initial narrow to sequential faulting for a value of $\beta_c = 6$ (6 to 9 Myr). At the time of break-up, the observed variations in the excess/deficit of LC are at the scale of fault blocks (Fig. 18a). Here, the upper and lower crust have thinned by similar amounts during most of the rifting period.

The following model has a wet anorthite lower crust, 33 km crustal thickness, 22 km thick upper crust and 4 mm/yr half-extension (Movie S9, middle panel). In this model, the lower crustal layer is very thin (11 km of thickness). Hence, when the lower crust flows towards the footwalls of the major faults (1 to 6 Myr), a large deficit of LC occurs below the basin since the lower crust is rapidly consumed. Sequential faulting starts when $\beta_c = 6$ (12 Myr) and the lower crust has been completely removed from the active region. Figure 18b shows the ratio UC/LC at the time of break-up (18 Myr), the LC deficit below the basin could be interpreted as a consequence of a massive lower crustal flow from the basin center to the sides, along distances of $\sim$ 150 km. However, what has happened is that the lower crust has been excised from the basin center at early stages by following upper crustal faulting. This means that also this model has undergone a fault-block scale lower crustal flow.

The last model has a wet quartzite lower crust, 40 km crustal thickness, 17 km thick upper crust and it is extended by 3 mm/yr (Movie S10, middle panel). This model evolves similarly to the previous decoupled model but, since the lower crust here is less weak, the initial phase of core complex rift mode is shorter (until 12 Myr, with a β_c increasing

from 1 to 1.5) and deformation moves outward from the basin center earlier (~ 17 Myr, where $\beta_c = 2$ at the center of the basin). This wide rift mode leads to an extending region characterized by excess of LC because of the effective flow towards the footwall of the active faults (21 Myr), resulting in a value of $\beta_c = 3$ in the basin center. Sequential faulting starts at about 30 Myr for a $\beta_c \sim 7$ over previously exhumed lower crust. In this case, the final pattern of UC/LC (Fig. 18c) shows a wide margin with large distances of LC excess, where exhumed lower crust is found at the distal domain, and few peaks of LC deficit, here and in the proximal domains.

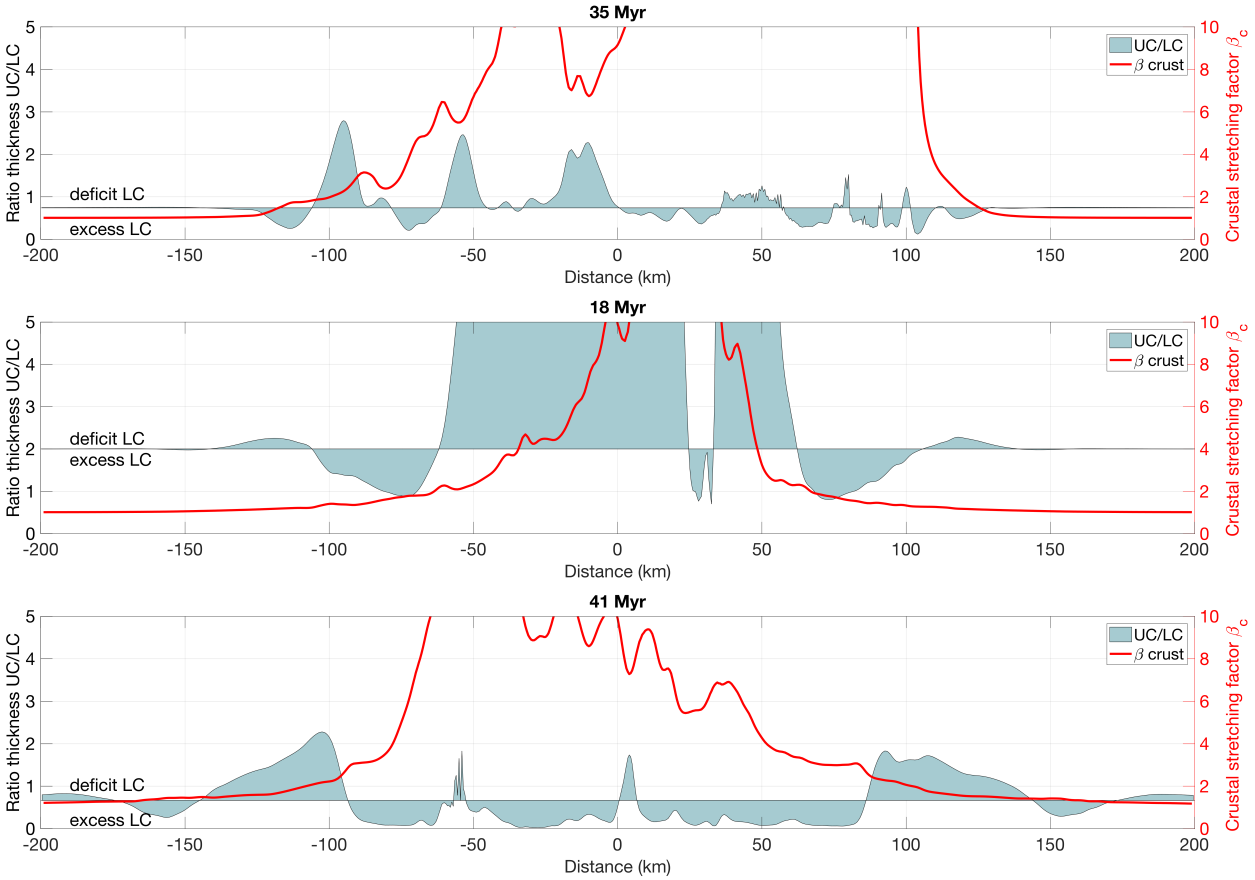

Figure 18. Comparison of the ratio UC/LC and crustal stretching factor (β_c) distribution for asymmetric models at the time of break-up, which have undergone a phase of sequential faulting. Top: model with mafic granulite lower crust, 40 km thick crust with 17 km of upper crust, extended by 3 mm/yr. Middle: model with wet anorthite lower crust, 33 km thick crust with 22 km of upper crust, extended by 4 mm/yr. Bottom: model with wet quartzite lower crust, 40 km of thick crust with 16 km of upper crust, extended by 3 mm/yr.

4 Discussion

4.1 Initial rift geometry

We have shown how the lower crustal strength influences the initial geometry of the rifts through the degree of coupling in the crust-mantle system (Fig. 4). From our results we find that for a strong and intermediate strength (MG 35 km, MG 40 km, AN 35 km and AN 40 km), the coupling of crust and mantle results in an initial narrow rift, characterized by graben or half-graben structures. For a weaker strength (WQ 35 km), the decoupling of crust and

mantle leads to an initial wide rift, with the formation of two grabens and a horst. And for an even weaker strength (WQ 40 km) a core-complex is developed, assisted by the low strength of both deep crust and mantle. We observe a similar change in the initial pattern than *Buiter et al.* [2008], where their Figure 6 shows how decreasing the viscosity of the lower crust changes the geometry from graben to half-graben. Also, we observe that the initial geometries of our wet quartzite models are in agreement with the results from *Whitney et al.* [2013, their Figure 11b]. For their set of thermal and rheological parameters with a 60 km thick crust, the study shows how the increase in crustal thickness from 50 to 55 km changes initial deformation from multiple upper-crust normal faults and homogeneously distributed deformation of the lower crust (wide rift mode), to a strong deformation in the upper crust and localized flow in the lower crust (core complex rift mode). The core complexes in our models do not show a flat Moho topography, often suggested in the formation of a continental core complex. *Block and Royden* [1990] previously showed two patterns of extension where a either flat or domed Moho could result, depending on whether the flow of the lower crust or the upper mantle was compensating the lithospheric extension. *Schenker et al.* [2012] further supported these bimodal results. In our models, lithospheric extension in a core complex mode is partly supported by the flow of the weak lower crust and the upwelling mantle, which deflects the Moho upwards.

Increasing the crustal thickness from 35 to 40 km replaces initially strong mantle for weaker lower crust, which implies larger decoupling of crust and mantle given by both weaker deep lower crust and weaker uppermost mantle. This induces a change in the initial geometrical pattern of the models. For instance, increasing the crustal thickness in the case of wet quartzite lower crust results in less work needed for the lower crust to flow towards the fault tip in response to slip, assisted by both weak deep lower crust and uppermost mantle. This observation correlates well with the conclusions of *Gueydan et al.* [2008], who related the change from narrow to wide rift mode to a decrease in the uppermost mantle strength, and *Tirel et al.* [2008], who showed a change from wide to core complex mode by also decreasing the strength of the uppermost mantle.

The thermal weak seed used in our models to localize deformation at the early stages tends to form two main conjugate faults rooting above the weak seed, although this faulting pattern is also modified by the rheology. In the case of wet quartzite and 35 km thick-crust, the use of a weak seed given by a triangular-shape elevation of the $1300°C$ isotherm [*Brune et al.*, 2014, 2017] would distribute more the upper crustal deformation, forming several horsts and grabens instead of only one horst and two grabens (as it occurs in our model forced by our choice of weak seed). Localization of deformation occurs faster with our type of weak seed but, as it diffuses with time, it does not affect the overall results.

The variations in extension velocity and lower crustal strength resulted in different modes of deformation, subsidence pattern, margin width and conjugate asymmetry. We analyzed these results and related them to the strength of the lithosphere. For this we looked at the extent and thickness of the low viscosity areas in the deep crust and followed their evolution with time. Numerical modelling studies have previously shown that the viscosity of the lower crust is a key control on the evolution of continental rifting [*Pérez-Gussinyé and Reston*, 2001; *Brune et al.*, 2014; *Huismans and Beaumont*, 2011, 2014], which depends on the lower crustal temperature, composition and extension velocity. We have found that the threshold viscosity for the distinct types of low viscosity channels characterizing the extensional modes in our models is $10^{21} Pa\ s$ (Fig. 19). The following section summarizes the main characteristics found for each mode of extension.

4.2 What determines a mode of extension?

We have obtained an initial narrow rift mode for strong and intermediate lower crustal strengths (models MG 35 km, MG 40 km, AN 35 km and AN 40 km). Here, the lower crust had limited flow outward from the forming basin because of its large viscosity, which resulted in its confinement within a graben or half-graben structure that localized initial deformation. Thicker crusts (40 km) and intermediate rheologies (AN) allowed the deepest part of the lower crust to flow outward from the basin center, although still coupling upper crustal and mantle brittle deformation, and which is reflected in the upwards deflection of the Moho below the basin center. Figure 19 shows how the large viscosity of the lower crust involved in the narrow rift mode results in a very small and localized low viscosity channel at the deep crust (isoviscosity contour $< 10^{21} Pa\ s$).

In this narrow mode, the localization of deformation into one or two single crustal-scale faults was favored by the strong lower crust, coupling upper crust and mantle deformation, and strain softening. Models that started deformation as a narrow rift mode and changed to another mode at low velocities (i.e. MG 40 km and AN 40 km for 3 mm/yr), evolved only as a narrow mode for higher velocities (5 and 10 mm/yr). This was caused by the enhanced coupling

between upper crust and mantle and the continuous localized deformation from the feedback between faster strain softening and thermal thinning. This narrow mode localizes surface heat flow at the basin center, where only major faults show higher peaks of heat flow. Larger values of heat flow occur close to the break-up area, where the most distal parts of the symmetric margins emerge.

Our models underwent sequential faulting mode when the lower crust was strong enough to couple deformation from upper crust to mantle but still weak enough to prevent faults reach the mantle and produce rapid crustal break-up. Models with strong and intermediate lower crustal strength showed a phase of sequential faulting only for thicker crusts (MG 40 km and AN 40 km) and low velocity (3 mm/yr). In these cases, the sequence of active faults was sustained by a deep lower crust weak enough to develop a low viscosity pocket in the hangingwall of the active fault (isoviscosity contour $< 10^{21} Pa\ s$ in Fig. 19) and a slow velocity that favoured the strengthening of the mantle at the fault's footwall. Models with weak lower crustal strength showed a phase of sequential faulting, either shorter or longer, for both crustal thickness (WQ 35 km and WQ 40 km) and all extension velocities (3, 5 and 10 mm/yr). At some point in the evolution of these models, the lower crust behaved in a manner that was able to develop a pocket of low viscosity within the active fault's hangingwall connecting upper crust and mantle deformation. The size of this pocket was larger for faster velocities because heat advection is more effective. The sequential faulting mode is characterized by lower crustal flow on a fault-block scale since the lower crust within the low viscosity pocket flows towards the tip of the active fault.

In this sequential faulting mode, localization of upper crustal deformation is along a single active fault that connects to the mantle in a semi-coupled way. This mode involves an asymmetric upwelling of the mantle towards the fault's tip, which increases its temperature and hence its is reflected on the surface heat flow. We have shown in our results that, owing to the array of faults that develop sequentially in time, the rift and the heat flow migrates progressively oceanward. As a consequence, the thermal history differs for the different sectors of the resulting wide margin, which have strong implications for hydrocarbon maturation [*Pérez-Gussinyé*, 2013].

The wide rift mode occurred in the models with weak lower crust (WQ 35 km and WQ 40 km), for all extension velocities, and in the case with very weak lower crust (DQ 40 km). The lower crust was able to effectively flow outward from the zone of maximum extension while the deep lower crust was temporarily able to flow towards the center of the rift, driven by crustal isostasy. In the case of WQ 35 km, the initial wide rift mode resulted in an upper crustal configuration of two grabens and a horst. This deformation later distributed towards the model sides following the lower crustal flow. In the cases of WQ 40 km and DQ 40 km, the wide rift occurred as an intermediate mode in the evolution. During this mode, the work needed for the lower crustal flow to allow the formation of faults was less than the work needed to bend the topography around the faults, therefore resulting in simultaneous faulting. For higher velocities, these models also showed a phase of wide rift mode, although for a shorter period.

In this wide mode, a decoupling level between crust and mantle is given by the low strength of the lower crust, which generates a thin and extended low viscosity layer (isoviscosity contour $< 10^{21} Pa\ s$ in Fig. 19). This results in a more uniform distribution of surface heat flow over the broad active zone, where only local peaks occur above the simultaneous faults.

Finally, the core complex mode occurred at the initial stage of models with the weakest lower crustal strength (WQ 40 km and DQ 40 km). The very weak lower crust easily flowed towards the tip of a major high-angle fault in response to slip. The small EET and the strain softening reinforced the accumulation of slip and the fault progressively rotated forming a core complex that exhumed lower crust. The deep crustal flow tended to distribute deformation delaying the thinning of the crust. Also, the very weak lower crust prevented the propagation of upper crustal deformation into deeper ductile levels. Our models confirm the results of *Huet et al.* [2011] in which a core complex formed even in relatively cold crust. We suggest that this is likely to occur as long as the lower crust is enough weak to massively flow towards the tip of the developing fault.

In this core complex mode, a thick low viscosity channel is formed at the base of the crust that allows little thinning over a wide region while accommodates most deformation in a narrow zone of the upper crust (isoviscosity contour $< 10^{21} Pa\ s$ in Fig. 19). In the case of higher extension velocities, this channel thickens and results in a larger flow of lower crust towards the developing core complex, leading to wider exposures of exhumed lower crust. During the core complex mode, the localized heat flow above the faults shows lower peaks respect to the background surface heat flow and in comparison to the narrow rift mode. This is due to the delayed thermal thinning and the faster upper crustal thinning, which implies less radioactive production.

Brun and Beslier [1996] proposed that the core complex mode is merely a type of wide mode with the formation of metamorphic core complexes at the early stages of extension. Our results suggest that both approximations could be valid, since our tests undergone a core complex mode only at the start of rifting and the characteristic low viscosity channel is very similar between both wide and core complex modes. But it could also be considered as an additional mode of extension due to the difference regarding the thickened part of the channel that supports the exhumation of the ductile lower crust.

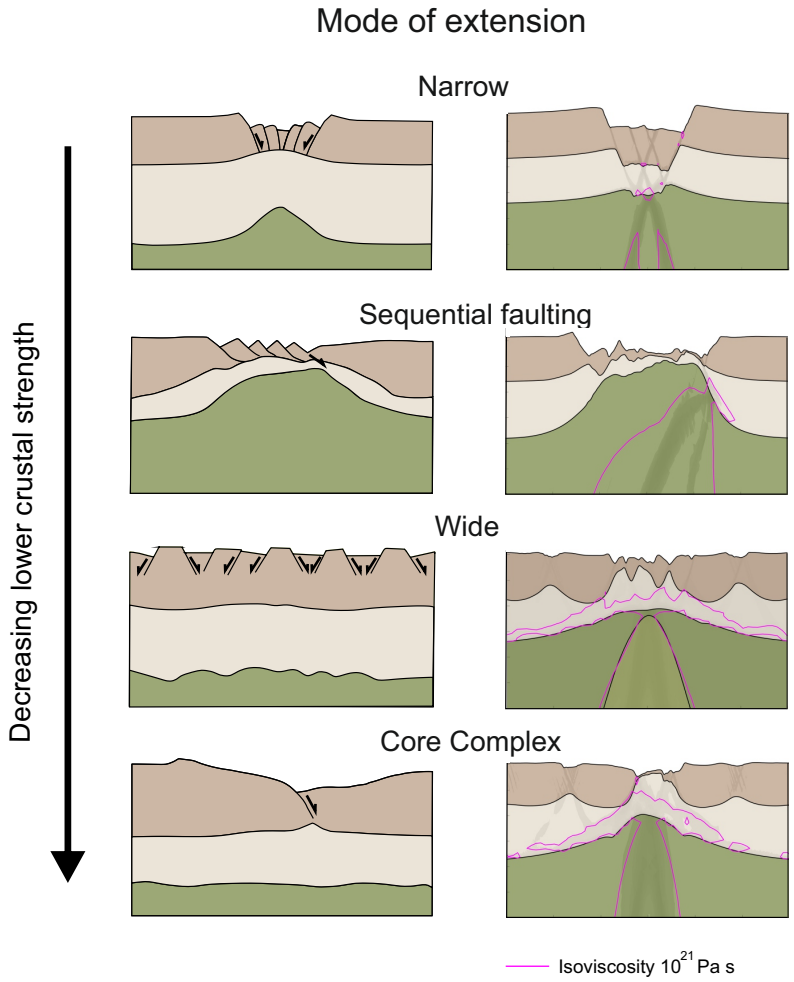

Figure 19. Modes of extension, from top to bottom, narrow, sequential faulting, wide and core complex. Link between the spatial distribution and thickness of the low viscosity channel within the lower crust (pink isoviscosity contour $< 10^{21} Pa\ s$) and the mode of extension. The change in the lower crustal strength promotes transitions between the different modes of extension.

4.3 Transitions between modes of extension

The models described in this study show how the initial thickness and behavior of the crust changes with ongoing extension, mostly depending on thermal thinning, strain softening and the elastic response of the lithosphere. This induces transitions between the extensional modes that depends on the difference between the work needed to keep deformation within the active area and the work needed to deform the unextended close areas [*Hopper and Buck*, 1996]. Our model results show two types of transitions between modes. The first type is a transition from strong to intermediate crustal strength that results in a change from narrow to sequential faulting mode. Here, the initial strong lower crust behaves mostly brittle and highly couples crust and mantle. The strong lower crust and strain softening facilitate localization of deformation into faults bounding a graben, i.e. as a narrow rift mode. With ongoing

extension, the work needed to bend the topography around the faults increases, and thermal thinning weakens the central graben which makes it easier to break new faults there. Also, the thermally weakened deep lower crust behaves now more ductile and decouples more the crust and mantle, however, it is still able to develop a low viscosity pocket that significantly couples upper-crust and mantle deformation. In this type of evolution, the initial coupling between crust and mantle slightly decreases with time, mostly induced by the very localized thermal thinning of the deeper and weaker lower crust.

The second type of transition occurs from very weak to intermediate crustal strength. Here, the very weak initial lower crust easily flows in response to slip along a main developing fault, which in turn reinforces slip localization. Accumulation of slip by strain softening and small EET results in the rotation of the fault, forming a core complex. When the fault has accommodated large offset, the work needed to bend the topography around the fault becomes larger than breaking new faults towards the model sides. Also, as the lower crust is exhumed within the core complex, it cools and embrittles. This, together with ongoing crustal thinning, leads to a reduced amount of very weak lower crust at the bottom, which distributes deformation over a wider area and involves a progressive change to the wide rift mode. As extension continues, crustal thinning is more pronounced and the upper crustal part cools. Hence, the region of weak lower crust becomes reduced to a pocket at the tip of a dominant active fault, switching the wide rift mode to sequential faulting mode. Thus, in this type of evolution, there is a progressive coupling of the upper-crust and mantle deformation that leads to a transition from core complex, to wide and eventually to the sequential faulting mode, which is largely supported by crustal thinning and cooling of the exhumed lower crust.

In summary, we observe four modes of extension. Three of them may appear from the start of rifting, narrow, wide and core complex, depending on the initial lower crustal rheology. The fourth mode, sequential faulting, which is responsible for the final asymmetry of the margins, only appears as the rheological lithospheric structures changes during rifting.

4.4 Depth dependent thinning

We have shown how the presence of a weak lower crust is key in the migration of deformation. The lateral flow of lower crust allows for the emergence of crustal DDT. We have previously discussed crustal DDT for a series of models in terms of the changes of the ratio of upper- to lower-crust thickness UC/LC. Here we summarize the main remarks for the lithospheric and crustal DDT of different modes of extension and compare them to the conceptual models of crustal DDT introduced in Figure 2.

We note that in the narrow rift mode there is faster thinning of the crust than of the mantle, and that crustal thinning is more localized at the basin center while mantle thinning is more distributed. Crustal DDT shows excess of LC at the faults' footwalls and deficit of LC at the hangingwalls. Therefore, the final pattern of UC/LC shows crustal DDT at a fault-block scale. In contrast, the wide rift mode shows higher mantle thinning than crustal thinning. Here, crustal thinning is very distributed while mantle thinning is more pronounced below the center of the model (i.e. over a similar area width than in the narrow mode). Although this mode is characterized by a weak deep lower crust that allows for lower crustal flow and distribution of deformation over a broad region, the overall pattern of UC/LC is dominated by the excesses and deficits of LC on a fault-block scale. The sequential faulting mode has always followed other modes of extension. Thus, the type of lithospheric and crustal DDT at the start of sequential faulting has been different for the distinct models. We have discussed before the implications of these differences in the final pattern of UC/LC, and we observe that sequential faulting always leads to a fault-block scale crustal flow. However, this final pattern will be masked in cases where the lower crust has been previously exhumed or removed, i.e. prior lower crustal flow has occurred oceanward or landward in a larger scale. In the core complex mode, mantle thinning is greater than crustal thinning, which is more distributed. Crustal DDT shows excess of LC in the footwall of the developing core complex and deficit in the hangingwall. The formation of consecutive core complexes hence leads to large-scale lower crustal flow towards the extending basin center. This results in a pattern of UC/LC characterized by excess of LC at the basin center and deficit of LC on both sides of this area.

In view of the results, an important conclusion from this study is that crustal DDT is linked to the initial proportion of upper- to lower-crust thickness UC/LC and the type of coupling between both layers, where the exhumation of lower crust is favoured by the presence of a lower crust thicker than the upper crust. The evaluated modes of extension show different lithospheric and crustal DDT. We observe an increasing lower crustal flow from the narrow to the sequential faulting mode, and from this to the wide rift mode. However, the flow in these modes occurs at a scale of fault blocks, resulting in crustal DDT at a small-scale. In contrast, the core complex rift mode involves a large-scale crustal DDT,

where the lower crust massively flows towards the rift axis and results in its exhumation. According to our results, we suggest that the core complex mode is the only mode that undergo a large-scale crustal DDT, which drives large amounts of lower crust to the rift axis. Hence, these lower crustal rocks would be found on the distal part of the final margins, reminding of the model of *Driscoll and Karner* [1998] that proposed a large-scale flow of the lower crust towards the ocean for the North Carnarvon basin (Figure 2a). We observe a lower crustal flow at a fault-block scale for the others modes, as proposed by *Pérez-Gussinyé et al.* [2003] for the Galicia Interior basin (Figure 2d). However, we do not observe in any mode a large-scale flow towards the sides of the domain, as indicated by the model of *Brun and Beslier* [1996], where a lanward lower crust flow was advocated. Instead, we observe cases where there is a small flow outward from the basin, as in the wide rift mode, and if the thickness of the lower crust is much smaller than the one of the upper crust, it can result in its complete consummation.

Despite the existence of many crustal-scale profiles along magma-poor conjugates, there is a little understanding on the crustal DDT responsible for the final crustal structures. We will later compare our numerical model results with natural rift examples in an attempt to gain insight into the crustal processes that dominate the mechanisms of extension of different margins worldwide.

4.5 Comparison with natural rift examples

Our numerical experiments show that the small- or large-scale of the lower crustal flow is highly dependent on the lower crustal strength. The ratio of upper- to lower-crust thickness UC/LC helps to understand the mechanisms of extension. Here we present a series of natural rift examples and compare the ratio UC/LC and crustal stretching factor β_c to our modelling results. Based on this comparison, we propose an extension mechanism for the lower crust of the natural margins. We use velocity models from the northern, central and southern Atlantic and the South China Basin, and assume that the upper and lower velocity layers correlate well with the upper and lower petrological crustal layers.

A first observation regarding this comparison is the generally shorter crustal taper that occurs in our models with respect to the natural margins. We attribute this to the initial weak seed used in the models in order to localize deformation. This weak seed favours rapid localization of deformation towards the center of the model domain, which leads to more localized thinning and hence abrupt crustal taper. A second observation is that our models have neither post-rift subsidence nor sediments. The top basement topography would change with both processes.

4.5.1 Robustness of velocity models

The geophysical characterization of magma-poor rifted margins is typically based on wide-angle seismic techniques that determine P wave velocities. This technique allows to characterize sub-surface lithologies. The continental upper crust is commonly associated to seismic P wave velocities between 5.7 and 6.4 km/s, while the continental lower crust is associated to velocities between 6.3 y 7.0 km/s [*Christensen and Mooney*, 1995; *Minshull*, 2009]. The Moho discontinuity is commonly associated to a strong velocity step from lower crustal velocities to a velocity of $\sim$ 8 km/s. The association of these velocities to crustal layers has been commonly used to interpret the nature of the crust and the amount of differential stretching between crustal layers at continental margins. However, there is an inherent uncertainty in these interpretations as the changes in P wave velocities that crustal and mantle rocks experience with changing temperature, pressure and hydration conditions during rifting is not yet fully understood. For example, *Reston* [2007a] has suggested that lower crustal rocks could acquire upper crustal velocities when they are brought to shallower levels during extension. Additionally, different acquisition configurations in terms of ocean bottom seismometers (OBS) spacing, as well as approaches to model the data, make it difficult to exactly compare the resulting velocity models.

In wide-angle seismic acquisition, a spacing of the OBS below 20 km has been generally accepted to sample well the deep crustal structure across rifted margins [*Minshull*, 2009]. However, in recent times a much closer spacing has been used [e.g., *Pichot et al.*, 2014; *Sallarès et al.*, 2011]. Methods to model wide-angle data can be divided into two main categories, inversion and forward methods. Within these broad categories, many differences exist as to the quality, lateral and depth resolution of the results, depending on seismometer spacing and the use of coincident multichannel seismic data (MCS) for wide-angle data modelling. Also, differences exist on whether the latter data are only used to model the sediments and top basement or are additionally used to model intra-basement reflectors. Lately, joint inversion of closely spaced wide-angle and MCS data appears to give the highest spatial resolution [e.g., *Pichot et al.*, 2014; *Sallarès et al.*, 2011, Sallarès personal communication]. These latter type of modelling shows velocity variations which are easily related to deformation observed in MCS profiles, and allow to properly image the

intricate relationship between upper and lower crustal deformation. This would be the type of modelling which one would ideally have at hand to compare P wave velocity models and our numerical models results. Unfortunately, many models present a smoothed out picture of velocity layers within the crust, making comparisons to numerical models difficult. Nevertheless, here we attempt to compare the UC/LC ratio observed from wide-angle data, and that obtained from our numerical models, to constrain the mode of deformation at several rifted margins of the world.

Seismic profile (region)	Year	Profile length (km)	Stations: OBS/OBH/LS	Method used	Other data and methods used	Instrument spacing (km)
ISE-17 (GIB)	1997	190	7 OBH	Forward	MCS	22.5
SMART1 (NS)	2001	490	19 OBS	Forward/Gravity	MCS	20-40
MIRROR-01 (M)	2011	400	28 OBS/15 LS	Forward/Gravity/Synthetic	MCS/Grav/ Mag/Bathy	9
SB02 (SSPS)	2010-2011	>1000	55-60 OBS/24 LS	Inversion	MCS/ Grav/ Mag	
SCS PR1+PR2 (SCSB)	2011	1000	50 OBS	Joint inversion*	Nearby seismic reflection profiles	18

Table 3. Acquisition parameters for the seismic profiles presented in this study. Regions are GIB for Galicia Interior Basin, NS for Nova-Scotia, M for Morocco, SSPS for Santos Basin-Sao Paulo Plateau System and SCSB for South China Sea Basin. Stations types are OBS for Ocean Bottom Seismic, OBH for Ocean Bottom Hydrophone and LS for Land Station. Methods are MCS for Multichannel seismic, Grav for Gravimetry, Mag for Magnetic and Bathy for Bathymetry. Modified from *Biari et al.* [2017]. *Method of *Korenaga et al.* [2000] combining refraction and reflection travel times.

4.5.2 Galicia Interior Basin

The Galicia Interior Basin is an abandoned rift located at the magma-poor margin off West Iberia. It has been studied by *Pérez-Gussinyé et al.* [2003] based on a multichannel seismic (MCS) prestack depth-migrated section with coincident wide-angle seismic velocity model along the profile ISE-17. On the east and west sides of the basin, the continental crust has a thickness of 24 and 21 km, respectively. This thickness reaches values of about 6 to 8 km at the center of the basin, showing an asymmetric structure. The onshore crust is assumed to be 32 km thick [*Córdoba et al.*, 1988]. The velocity model is shown in Figure 20a, with the UC/LC ratio and crustal stretching factor β_c. The east flank shows little faulting on the top basement and smooth thinning towards the basin. In contrast, west from the 130 km, the top basement shows large eastward dipping faults. Both rift flanks show $\beta_c < 2$, which implies little extension, while the center of the basin shows $\beta_c < 4-6$. *Pérez-Gussinyé et al.* [2003] interpreted that lower crustal rocks initially behaved in a ductile manner, because faults in the rift flanks appear only within the upper crust. In the center of the basin, faults appear to reach the lower crust and exhume it at their footwalls, suggesting that lower crustal rocks had cooled and moved to the brittle deformation regime. In contrast to the conceptual models that suggested the occurrence of a large-scale lower crustal flow outward from the basin center, *Pérez-Gussinyé et al.* [2003] proposed the alternative scenario where only small-scale flow occurred. This conclusion was based on the observation of local excesses and deficits of lower crust at the footwalls and hanginwalls of faults.

We compare the profile ISE-17 with the numerical model of wet anorthite lower crust, crustal thickness of 40 km and 3 mm/yr of extension at 13 Myr (Figure 20b). Both models, the wide-angle and the numerically modelled section, show a decrease in the fault block size towards the basin center, with similar values of $\beta_c = 4-6$. The ratio UC/LC is constant on the rift flanks, which agrees with the low variation observed in the velocity model. This is interpreted as an evidence that large-scale displacement of the lower crust did not happen, either landward or oceanward, which is corroborated by the previous evolution of the numerical model. Variations of the UC/LC ratio appear in the basin center and reflect the small-scale flow of the lower crust as it fills the gaps of the sequence of active faults, without the need for invoking flow at a larger scale.

4.5.3 Nova Scotia-Morocco margins

The Nova Scotia Margin lies between a magma-poor province to the north and a magma-dominated province to the south. In order to explore the along-strike variability, three wide-angle refraction seismic lines were acquired in 2001 (the SMART survey). We investigate only Line 1 [*Funck et al.*, 2004], since the southern Lines 2 and 3 are located in a more magma-dominated environment.

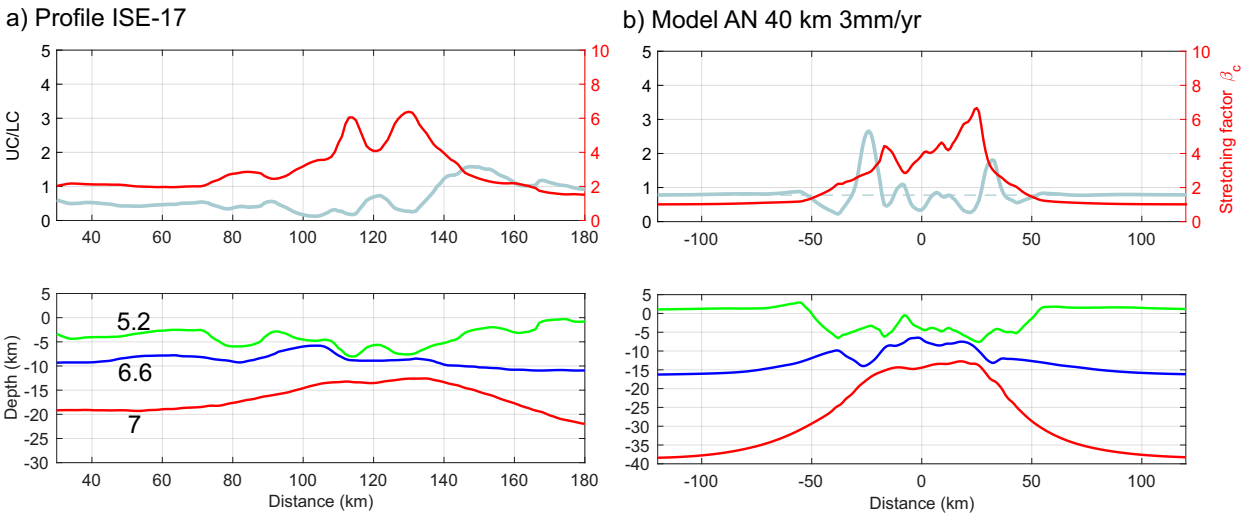

Figure 20. Thickness ratio UC/LC, crustal stretching factor β_c and crustal velocity structure (velocity contours are used to define the top basement (green), base of upper crust (blue) and Moho (red)): a) across the Galicia Interior Basin [Seismic profile ISE-17, *Pérez-Gussinyé et al.*, 2003] and b) across the numerical model with wet anorthite rheology for the lower crust, 40 km crustal thickness, 17.5 km upper crustal thickness and half-extension of 3 mm/yr, after 13 Myr of extension.

Figures 21a and 22a show, respectively, the UC/LC ratio, crustal stretching factor β_c and velocity models for the conjugate margins of northern Nova Scotia and Morocco. The Nova Scotia profile SMART1 [*Funck et al.*, 2004] and the Moroccan profile MIRROR-01 [*Biari et al.*, 2015] from wide-angle seismic experiments have an onshore continental crust 36 km thick. Both margins show three crustal layers, with upper, middle and lower crust. For consistency with our numerical models that use two crustal layers, we consider the middle crust to be part of the upper crust and choose the isovelocity contour of 6.5 km/s for the intracrustal boundary, in agreement with the velocity characterization of lower crustal materials [*Christensen and Mooney*, 1995]. It is important to note that the lack of reported M-series magnetic anomaly lineations at the seaward ends of both margins hinders the identification of this limit. A smoother crustal thinning is observed in the Nova Scotia margin, with a change from 36 to 3 km over 230 km, while the Morocco margin changes from 36 to 9 km over 170 km [*Biari et al.*, 2015]. The UC/LC ratio appears quite uniform, with local excesses and deficits of LC coinciding with upper crustal faults, as the LC top boundary is flat.

The numerical model shown in Figs. 21b and 22b is compatible with the conjugates of SMART1 and MIRROR-01 in terms of both crustal DDS and margin width. This model uses a weak lower crust of wet anorthite, initial crustal thickness of 40 km and 5 mm/yr of extension. We identify similar tilted fault blocks in the continental slope of SMART1 and our model. However, the top basement of the MI-01 is smoother than our modelling result. Perhaps the upper crust in our model should be weaker to reproduce better the observed topography. In MI-01 the crustal resolution is not enough to show crustal break-up at the seaward limit, which makes difficult to compare the distal crustal DDS with our numerical model. In spite of that, we obtain a similar uniform UC/LC ratio in our models . This is indicative of a small-scale lower crustal flow outward from the basin center at the late stages, perhaps driven by the increasing thermal thinning with further extension. Our numerical model evolution bears certain similarities with the conceptual model proposed by *Maillard et al.* [2006] (Fig. 23b) whereby the Nova Scotia and Morocco margins are the lower- and upper-plate, respectively, that result from the development of a lithospheric-scale shear zone dipping towards the Morocco margin. However, this idealized model indeed shows a more complicated pattern of non-uniform extension, as suggested by *Reston* [2009]. In our numerical model, after the first 4 Myr of extension localized in a narrow rift, sequential faulting starts by developing a sequence of active crustal-scale shear zones that pinches out the lower crust, in other words, the lower crust flows outward from the rift zone (Fig. 23a). Following the removal of the lower crust, deformation jumps into the hangingwall and crustal break up occurs, where mantle is exposed at the surface. It is important to note that in our model the asymmetry between both margins is not the result of a lithospheric-scale shear zone, but the result of the emergence of a sequential fault array towards the end of rifting [*Ranero and Pérez-Gussinyé*, 2010; *Brune et al.*, 2014].

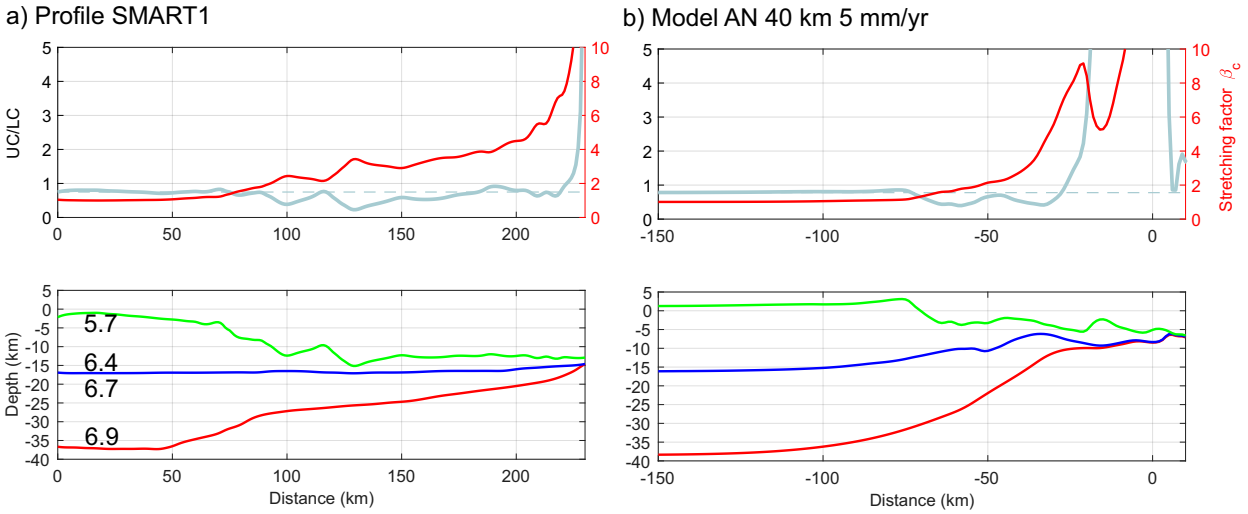

Figure 21. Thickness ratio UC/LC, crustal stretching factor β_c and crustal velocity structure (velocity contours are used to define the top basement (green), base of upper crust (blue) and Moho (red)): a) across the Nova Scotia margin [Seismic profile SMART1, *Funck et al.*, 2004] and b) across the numerical model with wet anorthite rheology for the lower crust, 40 km crustal thickness, 17.5 km upper crustal thickness and half-extension of 5 mm/yr, at crustal break-up.

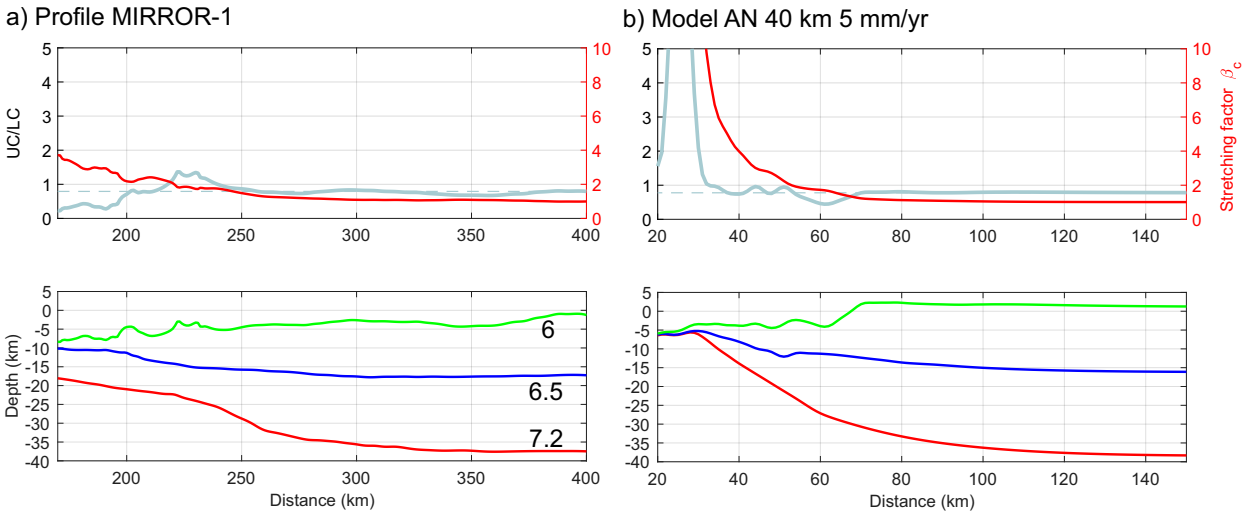

Figure 22. Thickness ratio UC/LC, crustal stretching factor β_c and crustal velocity structure (velocity contours are used to define the top basement (green), base of upper crust (blue) and Moho (red)): a) across the Morrocan margin [Seismic profile MIRROR-01, *Biari et al.*, 2015] and b) across the numerical model with wet anorthite rheology for the lower crust, 40 km crustal thickness, 17.5 km upper crustal thickness and half-extension of 5 mm/yr, at crustal break-up.

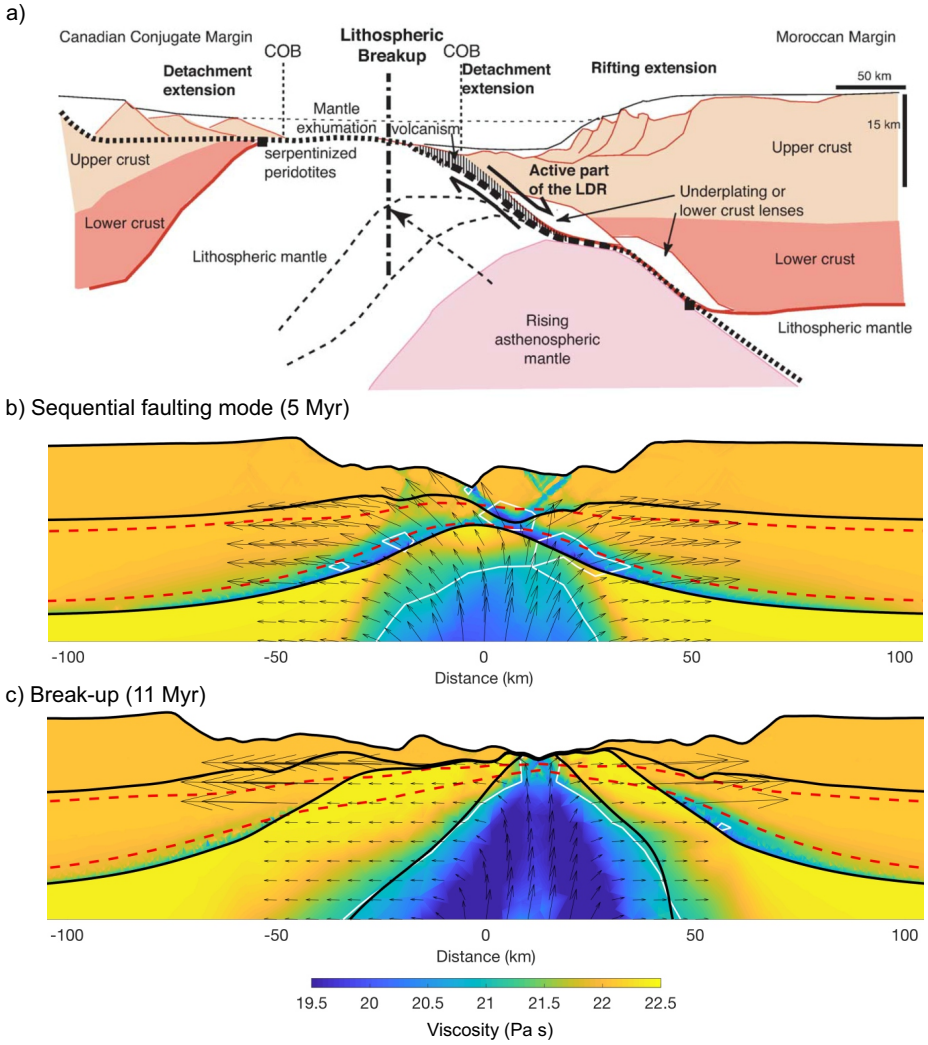

Figure 23. a) Model of the conjugate margins of Morocco and Nova Scotia at a pre-rupture stage from *Maillard et al.* [2006]. b) Numerical model with wet anorthite, 40 km thick-crust and 5 mm/yr during the sequential faulting mode. c) Break-up of the numerical model in (b).

4.5.4 Santos Basin-Sao Paulo Plateau System

The SanBa experiment imaged the deep crustal structure of the Santos Basin-Sao Paulo Plateau System (SSPS) [*Evain et al.*, 2015]. The velocity model of profile SB02, based on wide-angle seismic data, is shown in Fig. 24a. The thickness of the onshore continental crust is about 40 km, with a thickness for the upper crust of 23 km and the lower crust of 19 km. The necking zone (from -90 to 30 km, their domain N) is characterized by the Moho rising to about 23 km and the basement deepening to 10 km, which results in an upper-crust thinning of 10 km. *Evain et al.* [2015] noted that the exact position of the upper-lower crustal boundary should be taken as uncertain. In spite of that, they suggested that the upper crustal thickness strongly decreases while showing an increase in the velocity, and that this can be due to either its removal (exhumation of the lower crust) or a thickening of the sedimentary cover. In contrast, the lower crust maintains the same velocity as its thickness decreases. This margin shows an excess of LC along its whole distance (Fig. 24a). *Evain et al.* [2015] proposed that the lower crust could be exhumed between -30 to 640 km (their domains A, B, B' and C) in order to explain the observed high crustal velocities. The profile shows a wide margin with a gentle crustal thinning from the platform to the seaward end. This suggests the relevance of ductile lower crustal deformation during extension.

We discuss the results of a numerical model that presents similar characteristics to this profile (Fig. 24b). The model uses a weak rheology for the lower crust (i.e. wet quartzite), initial crustal thickness of 42 km and extension velocity of 5 mm/yr. This model was previously used in *Ros et al.* [2017] to compare the tectonic style of the SSPS margin and predict its type of oceanization. The resulting margin is about half width the margin of Santos, which has been suggested to result from a failed spreading center localized between the northern Pelotas Basin and the southern Santos Basin [*Moulin et al.*, 2013; *Gomes et al.*, 2002; *Mohriak*, 2001], and which cannot be reproduced in our 2-D models. In spite of that, we observe a similar gentle slope for the Moho, about 18 km over a distance of 150 km (from -250 to -150 km), while the SBO2 profile shows a decrease of about 19 km over a distance of 100 km. Both margins show an excess of LC within the hyperextended crust, that in the case of our model results in exhumation of the lower crust at the distal domain. Considering the results of previous Section 3.4, this can be related to the lower initial ratio UC/LC used in the model (UC/LC=0.71)in comparison to the one of the seismic profile (UC/LC = 1.2). Our model was initially decoupled with a lower crust flowing toward the rift axis during the initial stages, allowing the formation of core complexes that exhumed it. By analogy to this model, we suggest that an oceanward large-scale flow of lower crust occurred also during the formation of the Santos margin, which can explain the observed ratio UC/LC in the distal margin. This type of depth dependant stretching mechanism remind us of the model proposed by *Driscoll and Karner* [1998]. However, it is worth to note that the LC flow is not a result of late LC flow towards the basin center, but occurs during the early stages of core-complex deformation.

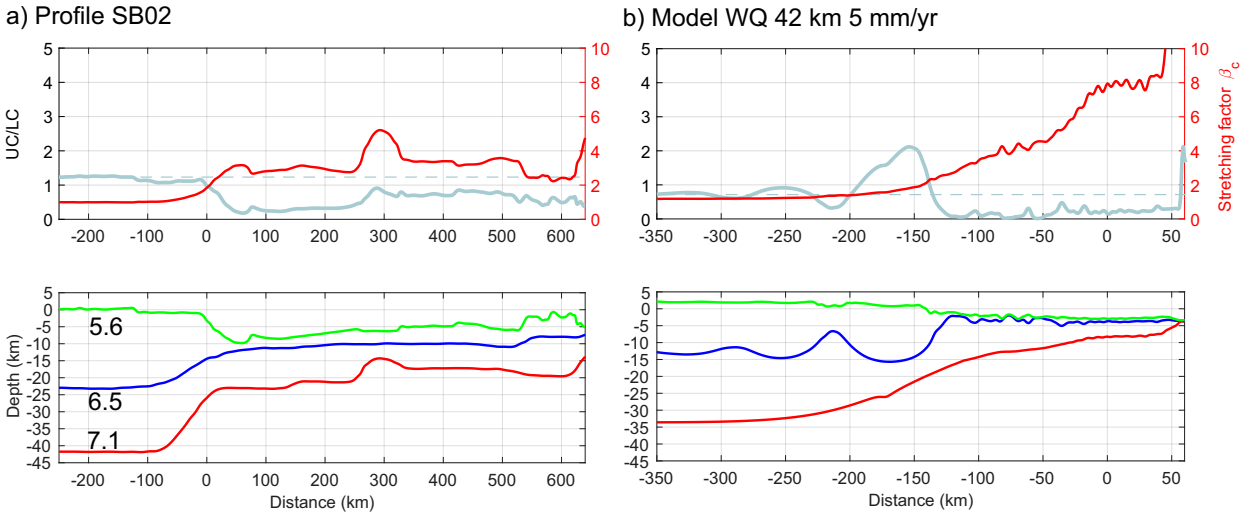

Figure 24. Thickness ratio UC/LC, crustal stretching factor β_c and crustal velocity structure (velocity contours are used to define the top basement (green), base of upper crust (blue) and Moho (red)): a) across the Santos Basin-Sao Paulo Plateau System [Seismic profile SB02, *Evain et al.*, 2015] and b) across the numerical model with wet quartzite rheology for the lower crust, 42 km crustal thickness, 17.5 km upper crustal thickness and half-extension of 5 mm/yr, at crustal break-up.

4.5.5 South China Sea Basin

The upper and lower crustal structure of the SW South China Sea has been documented by *Pichot et al.* [2014]. The 1000-km-long profile was divided into two parts, the northern PR1 profile of 740 km and the southern PR2 profile of 458 km [*Pichot et al.*, 2014, their Fig.4b]. The simplified velocity structure along the continental crust of these two margins and the calculated UC/LC ratio and crustal stretching factor β_c are shown in Figs. 25a and 26a, for the two conjugate lines PR1 and PR2 respectively. The unextended continental crust is 32 km thick [*Chen et al.*, 2010; *Pichot et al.*, 2014]. The study shows how extension across both margins is distributed on small- (15-30 km) and large-scale (45-90 km) subsurface structures where tilting of the velocity isocontours at the upper crust can be related to the upper crustal faults. Large-scale tilted fault blocks were found in seismic reflection profiles of the vicinity, which are consistent with the presence of large-scale normal faults bounding lateral velocity variations identified in the SCS profile. The large-scale faults appear to root at the uppermost lower crust, thereby affecting the velocity contours at this

level. However, the deep lower crust appears to have been undisturbed by overlying faulting, as the Moho is practically flat. Hence the deep lower crust must have been rather weak and ductile during deformation.

We compare these conjugates to the model with very weak dry quartzite crustal rheology, which results in very wide symmetric margins (Figs. 25b and 26b). The crust of the SCS profiles is much thinner than in our models, but we observe a similar pattern for crustal DDS. We observe a smooth thinning of the Moho while the upper-lower crustal boundary is greatly affected by the crustal faults that root in this level, as in the velocity model profiles. The ratio UC/LC in our numerical model clearly shows this behavior in the proximal margins, while the distal margins show an excess of lower crust due to its large-scale flow towards the basin center (where exhumed lower crust is found). Lower crust does not appear to be exhumed in the wide-angle line modelled by *Pichot et al.* [2014]. We would need a weaker crust to cause a wide margin such as the South China Sea, however, in our models, such a weak lower crust always becomes exhumed during the core complex phase at the start of rifting. We can think of various ways our models and wide-angle data could fit, but at the moment, they are speculations. The first one is that lower crust is actually exhumed, but its P wave velocity is much lower when it is at shallow depths and lower temperatures, so that wide-angle data are not able to distinguish where LC exhumation occurs. A second possibility is that a different weak seed for the initialization of our models may naturally lead to more distributed deformation over a wide area, without the need of having such a weak lower crust. And thirdly, the lower crust may have been of intermediate strength, but ongoing magmatic underplating during latter stages of rifting may have weaken it, allowing it to flow, while upper crustal faulting may still be important and enhanced by overlying sedimentation [*Olive et al.*, 2014; *Andrés-Martínez*, 2016].

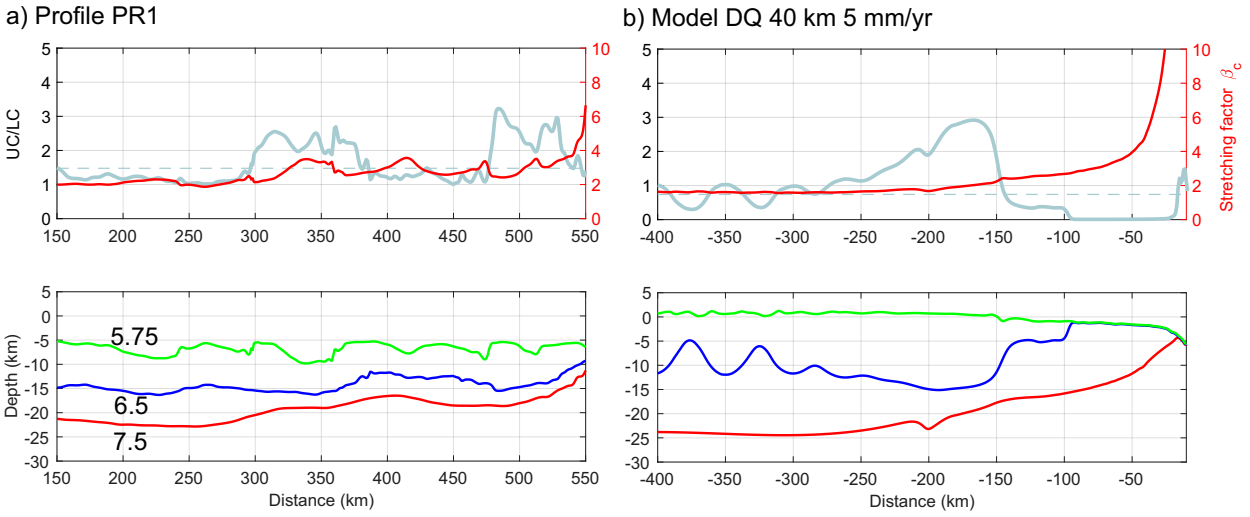

Figure 25. Thickness ratio UC/LC, crustal stretching factor β_c and crustal velocity structure (velocity contours are used to define the top basement (green), base of upper crust (blue) and Moho (red)): a) across the SW South China Sea [Seismic profile PR1, *Pichot et al.*, 2014] and b) across the numerical model with dry quartzite rheology for both crustal layers, 40 km crustal thickness, 17 km upper crustal thickness and half-extension of 5 mm/yr, at crustal break-up.

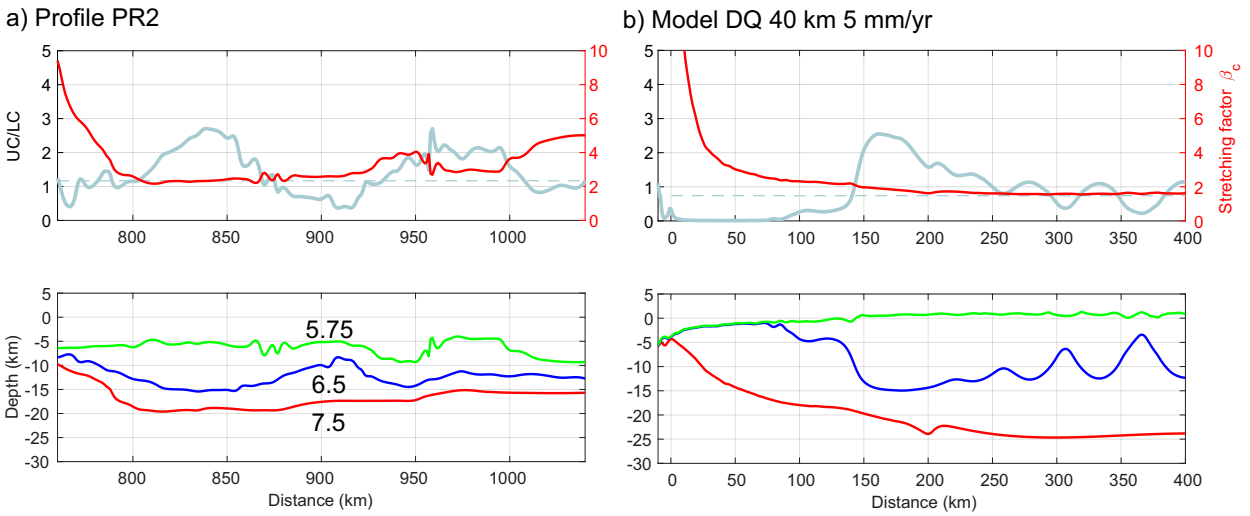

Figure 26. a-b) Crustal velocity structure across the SW South China Sea [Seismic profile PR2, *Pichot et al.*, 2014]. Velocity contours are used to define the top basement (green), base of upper crust (blue) and Moho (red) for comparison with the numerical model (c-d). c-d) Numerical model with dry quartzite rheology for both crustal layers, 40 km crustal thickness, 17 km upper crustal thickness and half-extension of 5 mm/yr, at crustal break-up.

5 Conclusions

We have investigated the formation of magma-poor margins with geodynamic numerical models by varying key parameters such as the initial crustal thickness, lower crustal rheology and extension velocity. Our results reproduce the variability in tectonic style observed in natural examples of rifted margins. We identify four modes of extension in the evolution of continental rifting, which are dominated by the strength of the lower crust. From strong to weak lower crustal strength, the modes of extension are narrow, sequential faulting, wide and core complex [*Buck*, 1991; *Ranero and Pérez-Gussinyé*, 2010]. We looked at the role of the lower crustal flow in localizing deformation. For a strong lower crust, the restricted lower crustal flow leads to a narrow mode of extension. For an intermediate lower crust, there is enough flow within a small pocket in the hangingwall of the active dominant fault that produces sequential faulting mode. For a weak lower crust, the flow is enough to distribute deformation over a broad region and lead to a wide mode. And for very weak lower crust, a massive flow results towards the tip of the fault, which is able to accumulate long offset and promote extension as a core complex mode. Additionally, we observe two types of transition between these modes depending on the variations of the lower crustal strength with ongoing extension: 1) from strong to intermediate crustal strength, which results in a transition from narrow to sequential faulting mode and 2) from very weak to intermediate crustal strength, which results in a transition from core complex, to wide and to sequential faulting mode.

Our models show that localization of upper crustal brittle deformation into single or more faults depends on whether the topography around the fault can bend in response to slip, which in turn depends on the EET, strain softening and the ability of the lower crust to flow and fill the accommodation space. The latter is related to the formation of a low viscosity channel above the crust-mantle boundary, i.e. Moho, which extent limits the distance over which deformation can be transferred between both layers. The threshold viscosity that defines the thickness and extent of this low viscosity channel it in our models is the isocontour $10^{21} Pa\,s$. The type of low viscosity channel can be used as a guide for determining the mode of extension: 1) the narrow mode is characterized by a very small and localized low viscosity area, 2) the sequential faulting mode by a low viscosity pocket in the hangingwall of the active fault, 3) the wide mode by a thin and extended low viscosity layer, and 4) the core complex mode by a very thick and distributed layer.

In addition, we find that the resulting margin asymmetry is a consequence of the interplay between extension velocity and lower crustal strength. Two trends arise from increasing extension velocity in our models: 1) change from asymmetric to symmetric margins for a strong and a very weak lower crustal rheology and 2) change from asymmetric

conjugates with a relatively wide margin to asymmetric conjugates but a wider margin, which occurs for a relatively weak lower crust. These changes are induced by the different proportions of brittle to ductile behavior of the lower crust.

We also evaluated the DDT of the crust and lithosphere in our numerical experiments and compared them to natural rift examples. Lithospheric DDT is present in all our models, where the amount of crustal and mantle thinning varies for the different modes of extension. Through our study we observe that only the core complex mode leads to large-scale crustal DDT, where exhumation of the lower crust can be found at the distal rifted margins. We find that an increasing lower crustal flow occurs from the narrow to the sequential faulting mode, and from this to the wide rift mode. However, this flow occurs at a fault-block scale, leading to small-scale crustal DDT. Additionally, the initial proportion of upper- to lower-crust thickness and the type of coupling between both layers may influence the final pattern of crustal DDT. We base that on the observation that the exhumation of lower crust is favoured by the presence of a lower crust thicker than the upper crust, however this does not imply that a large-scale lower crustal flow has occurred during the formation of the margin. Therefore, we suggest that the presence of exhumed lower crust at the distal margins can be produced either by a large-scale crustal DDT as the one observed in the core complex mode of extension or by an initial lower crustal layer much thicker than the upper crust, without implying an abundant lower crustal flow.

From the comparison of our numerical model results and the natural rift examples, we infer that some margins could have undergone a large-scale oceanward flow of the lower crust, promoted by the presence of a weak lower crust and resulting in its exhumation at the distal margin (e.g., the SB02 profile in the Santos basin). This result could be compared to the conceptual model of *Driscoll and Karner* [1998]. However, crustal DDT during continental rifting generally occurs at a small-scale, as previously suggested by *Pérez-Gussinyé et al.* [2003] for the Galicia Interior basin. We do not observe any example of large-scale lower crustal flow toward the land, as proposed by *Brun and Beslier* [1996].

Another remarkable conclusion is related to the mode of extension and heat flow distribution. The narrow and wide rift modes show similar values of surface heat flow but in a localized or distributed region, respectively. The sequential faulting mode implies the migration of the heat flow peak along the developing wide margin, where higher values are reached in models with thicker upper crusts, due to the larger content in radioactive elements. Finally, the core complex mode localizes large heat flow values above the developing core complex.

References

Andrés-Martínez, M. (2016), Rifted margin architecture and the interplay between mantle, crustal and surface processes from geodynamic numerical experiments, Ph.D. thesis, Royal Holloway, University of London.

Andrés-Martínez, M., J. P. Morgan, M. Pérez-Gussinyé, and L. Rüpke (2015), A new free-surface stabilization algorithm for geodynamical modelling: Theory and numerical tests, *Physics of the Earth and Planetary Interiors*, *246*, 41–51.

Armitage, J. J., K. D. Petersen, and M. Pérez-Gussinyé (2018), The role of crustal strength in controlling magmatism and melt chemistry during rifting and breakup, *Geochemistry, Geophysics, Geosystems*.

Aslanian, D., M. Moulin, J.-L. Olivet, P. Unternehr, L. Matias, F. Bache, M. Rabineau, H. Nouzé, F. Klingelheofer, I. Contrucci, et al. (2009), Brazilian and african passive margins of the central segment of the south atlantic ocean: Kinematic constraints, *Tectonophysics*, *468*(1-4), 98–112.

Bassi, G., C. E. Keen, and P. Potter (1993), Contrasting styles of rifting: Models and examples from the eastern canadian margin, *Tectonics*, *12*(3), 639–655.

Behn, M. D., J. Lin, and M. T. Zuber (2002), A continuum mechanics model for normal faulting using a strain-rate softening rheology: Implications for thermal and rheological controls on continental and oceanic rifting, *Earth and Planetary Science Letters*, *202*(3-4), 725–740.

Biari, Y., F. Klingelhoefer, M. Sahabi, D. Aslanian, P. Schnurle, K. Berglar, M. Moulin, K. Mehdi, D. Graindorge, M. Evain, et al. (2015), Deep crustal structure of the north-west african margin from combined wide-angle and reflection seismic data (mirror seismic survey), *Tectonophysics*, *656*, 154–174.

Biari, Y., F. Klingelhoefer, M. Sahabi, T. Funck, M. Benabdellouahed, M. Schnabel, C. Reichert, M.-A. Gutscher, A. Bronner, and J. Austin (2017), Opening of the central atlantic ocean: Implications for geometric rifting and asymmetric initial seafloor spreading after continental breakup, *Tectonics*.

Bird, P. (1991), Lateral extrusion of lower crust from under high topography in the isostatic limit, *Journal of Geophysical Research: Solid Earth*, *96*(B6), 10,275–10,286.

Block, L., and L. H. Royden (1990), Core complex geometries and regional scale flow in the lower crust, *Tectonics*, *9*(4), 557–567.

Brun, J. (1999), Narrow rifts versus wide rifts: inferences for the mechanics of rifting from laboratory experiments, *Philosophical Transactions-Royal Society of London Series A Mathematical Physical and Engineering Sciences*, pp. 695–709.

Brun, J., and M. Beslier (1996), Mantle exhumation at passive margins, *Earth and Planetary Science Letters*, *142*(1-2), 161–173.

Brune, S., C. Heine, M. Pérez-Gussinyé, and S. V. Sobolev (2014), Rift migration explains continental margin asymmetry and crustal hyper-extension, *Nature Communications*, *5*.

Brune, S., C. Heine, P. D. Clift, and M. Pérez-Gussinyé (2017), Rifted margin architecture and crustal rheology: reviewing iberia-newfoundland, central south atlantic, and south china sea, *Marine and Petroleum Geology*, *79*, 257–281.

Buck, W. R. (1991), Modes of continental lithospheric extension, *Journal of Geophysical Research*, *96*(B12), 20,161–20,178.

Buck, W. R., F. Martinez, M. S. Steckler, and J. R. Cochran (1988), Thermal consequences of lithospheric extension: pure and simple, *Tectonics*, *7*(2), 213–234.

Buck, W. R., L. L. Lavier, and A. N. Poliakov (1999), How to make a rift wide, *PHILOSOPHICAL TRANSACTIONS-ROYAL SOCIETY OF LONDON SERIES A MATHEMATICAL PHYSICAL AND ENGINEERING SCIENCES*, pp. 671–689.

Buiter, S. J., R. S. Huismans, and C. Beaumont (2008), Dissipation analysis as a guide to mode selection during crustal extension and implications for the styles of sedimentary basins, *Journal of Geophysical Research: Solid Earth*, *113*(B6).

Byerlee, J. (1978), Friction of rocks, in *Rock friction and earthquake prediction*, pp. 615–626, Springer.

Chen, Y., F. Niu, R. Liu, Z. Huang, H. Tkalčić, L. Sun, and W. Chan (2010), Crustal structure beneath china from receiver function analysis, *Journal of Geophysical Research: Solid Earth*, *115*(B3).

Christensen, N. I., and W. D. Mooney (1995), Seismic velocity structure and composition of the continental crust: A global view, *Journal of Geophysical Research: Solid Earth*, *100*(B6), 9761–9788.

Clerc, C., J.-C. Ringenbach, L. Jolivet, and J.-F. Ballard (2018), Rifted margins: Ductile deformation, boudinage, continentward-dipping normal faults and the role of the weak lower crust, *Gondwana Research*, *53*, 20–40.

Córdoba, D., E. Banda, and J. Ansorge (1988), P-wave velocity-depth distribution in the hercynian crust of northwest spain, *Physics of the earth and planetary interiors*, *51*(1-3), 235–248.

Corti, G., M. Bonini, S. Conticelli, F. Innocenti, P. Manetti, and D. Sokoutis (2003), Analogue modelling of continental extension: a review focused on the relations between the patterns of deformation and the presence of magma, *Earth-Science Reviews*, *63*(3), 169–247.

Dabrowski, M., M. Krotkiewski, and D. Schmid (2008), Milamin: Matlab-based finite element method solver for large problems, *Geochemistry, Geophysics, Geosystems*, *9*(4).

Dick, H. J., J. Lin, and H. Schouten (2003), An ultraslow-spreading class of ocean ridge, *Nature*, *426*(6965), 405.

Driscoll, N. W., and G. D. Karner (1998), Lower crustal extension across the northern carnarvon basin, australia: Evidence for an eastward dipping detachment, *Journal of Geophysical Research: Solid Earth*, *103*(B3), 4975–4991.

Dunbar, J. A., and D. S. Sawyer (1989), How preexisting weaknesses control the style of continental breakup, *Journal of Geophysical Research: Solid Earth*, *94*(B6), 7278–7292.

Evain, M., A. Afilhado, C. Rigoti, A. Loureiro, D. Alves, F. Klingelhoefer, P. Schnurle, A. Feld, R. Fuck, J. Soares, et al. (2015), Deep structure of the santos basin-são paulo plateau system, se brazil, *Journal of Geophysical Research: Solid Earth*, *120*(8), 5401–5431.

Funck, T., H. R. Jackson, K. E. Louden, S. A. Dehler, and Y. Wu (2004), Crustal structure of the northern nova scotia rifted continental margin (eastern canada), *Journal of Geophysical Research: Solid Earth*, *109*(B9).

Gardien, V., G. Poupeau, B. Muceku, R. Hébert, G. Beaudoin, and E. Labrin (2001), The evolution of amphibolites from site 1067, odp leg 173 (iberia abyssal plain): Jurassic rifting to the pyrenean compression, *Geological Society, London, Special Publications*, *187*(1), 191–208.

Gleason, G. C., and J. Tullis (1995), A flow law for dislocation creep of quartz aggregates determined with the molten salt cell, *Tectonophysics*, *247*(1), 1–23.

Gomes, P. O., J. Parry, and W. Martins (2002), The outer high of the santos basin, southern são paulo plateau, brazil: tectonic setting, relation to volcanic events and some comments on hydrocarbon potential, in *AAPG Hedberg Conference,âĂŸHydrocarbon Habitat of Volcanic Rifted Passive Margins*, pp. 8–11.

Gueydan, F., C. Morency, and J.-P. Brun (2008), Continental rifting as a function of lithosphere mantle strength, *Tectonophysics*, *460*(1-4), 83–93.

Hirth, G., and D. Kohlstedt (2003), Rheology of the upper mantle and the mantle wedge: A view from the experimentalists, *Inside the subduction Factory*, pp. 83–105.

Hopper, J. R., and W. R. Buck (1996), and passive margin formation, *Journal of Geophysical Research*, *101*(B9), 20–175.

Huet, B., L. Le Pourhiet, L. Labrousse, E. Burov, and L. Jolivet (2011), Formation of metamorphic core complex in inherited wedges: A thermomechanical modelling study, *Earth and Planetary Science Letters*, *309*(3-4), 249–257.

Huismans, R., and C. Beaumont (2009), Structural style of formation of passive margins, insights from dynamical modelling, *Trabajos de geología*, *29*(29).

Huismans, R., and C. Beaumont (2011), Depth-dependent extension, two-stage breakup and cratonic underplating at rifted margins, *Nature*, *473*(7345), 74.

Huismans, R. S., and C. Beaumont (2002), Asymmetric lithospheric extension: The role of frictional plastic strain softening inferred from numerical experiments, *Geology*, *30*(3), 211–214.

Huismans, R. S., and C. Beaumont (2003), Symmetric and asymmetric lithospheric extension: Relative effects of frictional-plastic and viscous strain softening, *Journal of Geophysical Research: Solid Earth*, *108*(B10).

Huismans, R. S., and C. Beaumont (2014), Rifted continental margins: The case for depth-dependent extension, *Earth and Planetary Science Letters*, *407*, 148–162.

Kaus, B. J., H. Mühlhaus, and D. A. May (2010), A stabilization algorithm for geodynamic numerical simulations with a free surface, *Physics of the Earth and Planetary Interiors*, *181*(1), 12–20.

Korenaga, J., W. Holbrook, G. Kent, P. Kelemen, R. Detrick, H.-C. Larsen, J. Hopper, and T. Dahl-Jensen (2000), Crustal structure of the southeast greenland margin from joint refraction and reflection seismic tomography, *Journal of Geophysical Research: Solid Earth*, *105*(B9), 21,591–21,614.

Kusznir, N., and R. Park (1987), The extensional strength of the continental lithosphere: its dependence on geothermal gradient, and crustal composition and thickness, *Geological Society, London, Special Publications*, *28*(1), 35–52.

Kusznir, N., G. Karner, and S. Egan (1987), Geometric, thermal and isostatic consequences of detachments in continental lithosphere extension and basin formation.

Lavier, L. L., and W. R. Buck (2002), Half graben versus large-offset low-angle normal fault: Importance of keeping cool during normal faulting, *Journal of Geophysical Research: Solid Earth*, *107*(B6).

Lavier, L. L., and G. Manatschal (2006), A mechanism to thin the continental lithosphere at magma-poor margins, *Nature*, *440*(7082), 324–328.

Lavier, L. L., W. R. Buck, and A. N. Poliakov (2000), Factors controlling normal fault offset in an ideal brittle layer, *Journal of Geophysical Research: Solid Earth*, *105*(B10), 23,431–23,442.

Lister, G., M. Etheridge, and P. Symonds (1986), Detachment faulting and the evolution of passive continental margins, *Geology*, *14*(3), 246–250.

Maillard, A., J. Malod, E. Thiébot, F. Klingelhoefer, and J.-P. Réhault (2006), Imaging a lithospheric detachment at the continent–ocean crustal transition off morocco, *Earth and Planetary Science Letters*, *241*(3-4), 686–698.

McKenzie, D. (1978), Some remarks on the development of sedimentary basins, *Earth and Planetary science letters*, *40*(1), 25–32.

Melosh, H., and C. Williams (1989), Mechanics of graben formation in crustal rocks: A finite element analysis, *Journal of Geophysical Research: Solid Earth*, *94*(B10), 13,961–13,973.

Minshull, T. A. (2009), Geophysical characterisation of the ocean–continent transition at magma-poor rifted margins, *Comptes Rendus Geoscience*, *341*(5), 382–393.

Mohriak, W. U. (2001), South atlantic ocean salt tectonics, volcanic centers, fracture zones and their relationship with the origin and evolution of the south atlantic ocean: Geophysical evidence in the brazilian and west african margins., in *7th International Congress of the Brazilian Geophysical Society*.

Moulin, M., D. Aslanian, M. Rabineau, M. Patriat, and L. Matias (2013), Kinematic keys of the santos–namibe basins, *Geological Society, London, Special Publications*, *369*(1), 91–107.

Naliboff, J., and S. J. Buiter (2015), Rift reactivation and migration during multiphase extension, *Earth and Planetary Science Letters*, *421*, 58–67.

Olive, J.-A., M. D. Behn, and L. C. Malatesta (2014), Modes of extensional faulting controlled by surface processes, *Geophysical Research Letters*, *41*(19), 6725–6733.

Pérez-Gussinyé, M. (2013), A tectonic model for hyperextension at magma-poor rifted margins: an example from the west iberia–newfoundland conjugate margins, *Geological Society, London, Special Publications*, *369*(1), 403–427.

Pérez-Gussinyé, M., and T. J. Reston (2001), Rheological evolution during extension at nonvolcanic rifted margins: onset of serpentinization and development of detachments leading to continental breakup, *Journal of Geophysical Research: Solid Earth*, *106*(B3), 3961–3975.

Pérez-Gussinyé, M., C. Ranero, T. J. Reston, and D. Sawyer (2003), Mechanisms of extension at nonvolcanic margins: Evidence from the galicia interior basin, west of iberia, *Journal of Geophysical Research: Solid Earth*, *108*(B5).

Péron-Pinvidic, G., and G. Manatschal (2009), The final rifting evolution at deep magma-poor passive margins from iberia-newfoundland: a new point of view, *International Journal of Earth Sciences*, *98*(7), 1581–1597.

Pichot, T., M. Delescluse, N. Chamot-Rooke, M. Pubellier, Y. Qiu, F. Meresse, G. Sun, D. Savva, K. Wong, L. Watremez, et al. (2014), Deep crustal structure of the conjugate margins of the sw south china sea from wide-angle refraction seismic data, *Marine and Petroleum Geology*, *58*, 627–643.

Ranalli, G., and D. C. Murphy (1987), Rheological stratification of the lithosphere, *Tectonophysics*, *132*(4), 281–295.

Ranero, C. R., and M. Pérez-Gussinyé (2010), Sequential faulting explains the asymmetry and extension discrepancy of conjugate margins, *Nature*, *468*(7321), 294.

Reston, T. (2007a), Extension discrepancy at north atlantic nonvolcanic rifted margins: Depth-dependent stretching or unrecognized faulting?, *Geology*, *35*(4), 367–370.

Reston, T. (2009), The structure, evolution and symmetry of the magma-poor rifted margins of the north and central atlantic: a synthesis, *Tectonophysics*, *468*(1-4), 6–27.

Reston, T. J. (2007b), The formation of non-volcanic rifted margins by the progressive extension of the lithosphere: the example of the west iberian margin, *Geological Society, London, Special Publications*, *282*(1), 77–110.

Reston, T. J., T. Leythäuser, G. Booth-Rea, D. Sawyer, D. Klaeschen, and C. Long (2007), Movement along a low-angle normal fault: The s reflector west of spain, *Geochemistry, Geophysics, Geosystems*, *8*(6).

Ros, E., M. Pérez-Gussinyé, M. Araújo, M. Thoaldo Romeiro, M. Andrés-Martínez, and J. P. Morgan (2017), Lower crustal strength controls on melting and serpentinization at magma-poor margins: Potential implications for the south atlantic, *Geochemistry, Geophysics, Geosystems*.

Royden, L., and C. Keen (1980), Rifting process and thermal evolution of the continental margin of eastern canada determined from subsidence curves, *Earth and Planetary Science Letters*, *51*(2), 343–361.

Ruppel, C. (1995), Extensional processes in continental lithosphere, *Journal of Geophysical Research: Solid Earth*, *100*(B12), 24,187–24,215.

Rybacki, E., and G. Dresen (2000), Dislocation and diffusion creep of synthetic anorthite aggregates, *Journal of Geophysical Research: Solid Earth*, *105*(B11), 26,017–26,036.

Sallarès, V., A. Gailler, M.-A. Gutscher, D. Graindorge, R. Bartolomé, E. Gracia, J. Diaz, J. J. Dañobeitia, and N. Zitellini (2011), Seismic evidence for the presence of jurassic oceanic crust in the central gulf of cadiz (sw iberian margin), *Earth and Planetary Science Letters*, *311*(1-2), 112–123.

Schenker, F., T. Gerya, and J.-P. Burg (2012), Bimodal behavior of extended continental lithosphere: Modeling insight and application to thermal history of migmatitic core complexes, *Tectonophysics*, *579*, 88–103.

Svartman Dias, A. E., L. L. Lavier, and N. W. Hayman (2015), Conjugate rifted margins width and asymmetry: The interplay between lithospheric strength and thermomechanical processes, *Journal of Geophysical Research: Solid Earth*, *120*(12), 8672–8700.

Tetreault, J., and S. Buiter (2017), The influence of extension rate and crustal rheology on the evolution of passive margins from rifting to break-up, *Tectonophysics*.

Tirel, C., J.-P. Brun, and E. Burov (2008), Dynamics and structural development of metamorphic core complexes, *Journal of Geophysical Research: Solid Earth*, *113*(B4).

Vening Meinesz, F. (1950), Les graben africains, résultat de compression ou de tension dans la croûte terrestre, *Bull. Inst. R. Colon. Belge*, *21*, 539–552.

Watts, A. (2012), Models for the evolution of passive margins, in *Regional Geology and Tectonics: Phanerozoic Rift Systems and Sedimentary Basins*, pp. 32–57, Elsevier.

Weissel, J. K., and G. D. Karner (1989), Flexural uplift of rift flanks due to mechanical unloading of the lithosphere during extension, *Journal of Geophysical Research: Solid Earth*, *94*(B10), 13,919–13,950.

Wernicke, B. (1981), Low-angle normal faults in the basin and range province: nappe tectonics in an extending orogen, *Nature*, *291*(5817), 645.

Wernicke, B. (1985), Uniform-sense normal simple shear of the continental lithosphere, *Canadian Journal of Earth Sciences*, *22*(1), 108–125.

Whitney, D. L., C. Teyssier, P. Rey, and W. R. Buck (2013), Continental and oceanic core complexes, *Bulletin*, *125*(3-4), 273–298.

Wilks, K. R., and N. L. Carter (1990), Rheology of some continental lower crustal rocks, *Tectonophysics*, *182*(1-2), 57–77.

Supporting Information for

"Understanding the variability in tectonic architecture of margins: a numerical modelling study"

E. Ros[1], M. Pérez-Gussinyé[2]and M. Andrés-Martínez[2]

[1]COMPASS, Department of Earth Sciences, Royal Holloway University of London, Egham TW20 0EX, UK.

[2]MARUM, Center for Marine Environmental Sciences, University of Bremen, 28334, Germany.

Contents

Additional Supporting Information (Files uploaded separately)

Movie S1. Evolution of the numerical model with mafic granulite lower crust, 35 km crustal thickness, 17.5 km upper crustal thickness and 3 mm/yr half-extension velocity.

Movie S2. Evolution of the numerical model with mafic granulite lower crust, 40 km crustal thickness, 17.5 km upper crustal thickness and 3 mm/yr half-extension velocity.

Movie S3. Evolution of the numerical model with wet quartzite lower crust, 35 km crustal thickness, 17.5 km upper crustal thickness and 3 mm/yr half-extension velocity.

Movie S4. Evolution of the numerical model with wet quartzite lower crust, 40 km crustal thickness, 17.5 km upper crustal thickness and 3 mm/yr half-extension velocity.

Movie S5. Comparison of the numerical models with wet anorthite lower crust, 35 km crustal thickness, 20 km upper crustal thickness and 10 mm/yr half-extension and with wet anorthite lower crust, 40 km crustal thickness, 10 km upper crustal thickness and 5 mm/yr half-extension.

Movie S6. Evolution of the numerical model with mafic granulite lower crust, 35 km crustal thickness, 17 km upper crustal thickness and 5 mm/yr half-extension velocity.

Corresponding author: E. Ros, Elena.Ros.2014@live.rhul.ac.uk

Movie S7. Evolution of the numerical model with dry quartzite upper and lower crusts, 40 km crustal thickness, 17 km upper crustal thickness and 3 mm/yr half-extension velocity.

Movie S8. Evolution of the numerical model with mafic granulite lower crust, 40 km crustal thickness, 17 km upper crustal thickness and 3 mm/yr half-extension velocity.

Movie S9. Evolution of the numerical model with wet anorthite lower crust, 33 km crustal thickness, 22 km upper crustal thickness and 4 mm/yr half-extension velocity.

Movie S10. Evolution of the numerical model with wet quartzite lower crust, 40 km crustal thickness, 16 km upper crustal thickness and 3 mm/yr half-extension velocity.

Introduction

The supplementary information provides a further description of our 2D numerical model and initial rheological profile. We include 10 supporting movies that show the evolution of the numerical models referenced in the main manuscript.

1 Numerical model

The thermomechanical numerical models solve the conservation equations of mass, momentum and energy for an incompressible Stokes flow, respectively

$$\frac{\partial v_i}{\partial x_i} = 0 \tag{1}$$

$$\frac{\partial \sigma_{ij}}{\partial x_j} + \rho g_i = 0 \tag{2}$$

$$\rho C_p \frac{DT}{Dt} = -\frac{\partial q_i}{\partial x_i} + H + H_s \tag{3}$$

where v_i are the velocity components, σ_{ij} is the Cauchy stress tensor, g_i is the gravitational acceleration, x_i are the spatial coordinates, ρ is the density, C_p is the heat capacity at constant pressure, T is the temperature, DT/Dt is the Lagrangian time derivative of temperature, $\frac{\partial q_i}{\partial x_i}$ is the partial derivative of heat flux $q_i = -\kappa \frac{\partial T}{\partial x_i}$ and κ is the thermal conductivity, H is the volumetric radioactive heat production and H_s is the heat dissipation from the non-elastic deformation, i.e. shear heating. Shear heating H_s increases the temperature within shear zones, thus reducing the strength of the shear zone compared to that of the surrounding rocks. Hence, this weakening process is important for the localization of shear zones (Ranalli and Murphy, 1987; Lu et al., 2011).

2 Rheological laws

We assume a visco-elasto-plastic behavior. For stresses below the yield surface, we use a power-law flow based on laboratory experiments, and the effective viscosity, limited by dislocation and diffusion creep, is given by the general equation

$$\eta = A^{\frac{-1}{n}} \dot{\varepsilon}_{II}^{\frac{1-n}{2n}} d^{m/n} \, fH_2O^{-r/n} \, exp\left(\frac{Q+PV}{nRT}\right) \tag{4}$$

where $\dot{\varepsilon_{II}}$ is the 2nd invariant of the deviatoric strain rate tensor, A is the pre-exponential factor, d is the grain size, m is the grain-size exponent, fH_2O is the water fugacity, r is the water fugacity exponent, Q is the activation energy, P is the pressure, V is the activation volume , R is the universal gas constant and T is the temperature. The pre-exponential factor A includes the conversion from uniaxial and triaxial laboratory experimental data into the invariant state.

Plastic deformation takes place when the Drucker-Prager yield surface is reached

$$\sigma_y = \sigma_{II} = Psin\phi + Ccos\phi \tag{5}$$

where P is pressure, ϕ is angle of internal friction, C is cohesion and σ_{II} is 2nd invariant of the deviatoric stress tensor.

3 Strain softening

Plastic strain softening is commonly included in numerical models to simulate cohesion and friction angle weakening at faults, which is achieved by defining a parametrical function of some type of finite strain. Here, we fix the cohesion value to 10 MPa and define the friction angle ϕ as a function of the accumulated second strain invariant ϵ_{IIh}

$$\phi = (\epsilon_{IIh} - \epsilon_{IIh_1}) \frac{\phi_2 - \phi_1}{\epsilon_{IIh_2} - \epsilon_{IIh_1}} + \phi_1 \tag{6}$$

where ϕ_1 is the initial friction angle, ϕ_2 is the softened friction angle, and $\epsilon_{IIh2} - \epsilon_{IIh1}$ is the strain interval where plastic strain softening takes place. We set ϕ_1=30°, ϕ_2=15°, ϵ_{IIh1}=0 and ϵ_{IIh2}=1. The accumulated strain tensor ϵ_{IIh} is calculated from the deformation gradient (Andrés-Martínez, 2016).

Shear zones develop in the viscous domain when the accumulated strain leads to dynamic recrystallization causing a reduction in the grain-size. The consequent change from dislocation to diffusion creep will be temporary due to the fast grain growth occurring in diffusion creep. To incorporate viscous strain softening in our model we take into

account that significant softening by grain size reduction will localize in shear zones if grain growth is inhibited (De Bresser et al., 2001), and that mantle strain softening, via dislocation-accommodated grain boundary sliding, decreases with temperature, being very limited at temperatures higher than 800°C (Précigout and Gueydan, 2009). Therefore, we introduce a strain- and temperature-dependent factor α in the viscosity equation (Eq. 4), which multiplies the pre-exponential factor A and that reduces the effective viscosity as deformation accumulates. The dependence of the α-factor on the accumulated strain is given by

$$\alpha(T) = (\epsilon_{IIh} - \epsilon_{IIh_1}) \frac{\alpha_2(T) - \alpha_1}{\epsilon_{IIh_2} - \epsilon_{IIh_1}} + \alpha_1 \tag{7}$$

where α_2 is temperature-dependent, with a value of 30 between 0°C and 800°C followed by an exponential decrease from α_2=30 at 800°C to α_2=1 at 1200°C; α_1 = 1, ϵ_{IIh1}=0 and ϵ_{IIh2}=1. In the viscosity equation (Eq. 4), α is raised to the inverse of n, meaning that a value of α= 30 corresponds to a change in viscosity of about 0.4 compared to the undeformed rock.

4 Rheological profile

The composition of the mantle lithosphere and asthenosphere is based on an initial melt depletion profile. Mantle rheology changes from wet olivine with a water content of 125 ppm H/Si (Hirth and Kohlstedt, 1996; Rüpke et al., 2006) when the mantle is 0% depleted to dry olivine when the mantle depletion is 4%, assuming that all water has been extracted at this stage (Morgan, 1997). From the bottom of the model, 400 km depth, to 130 km depth we assume the mantle has not been melted and has a depletion of 0 %, corresponding to a wet olivine rheology. From 130 km depth to the base of the lithosphere, 120 km depth, melt depletion increases from 0% to 4% with a mixture rheology of wet and dry olivine that depends linearly on the degree of depletion. From the base of the lithosphere to 60 km depth, the depletion linearly increases from 4 to 10%, with a dry olivine rheology.

The reference densities for upper crust, lower crust and mantle are 2700 kg m^{-3}, 2850 kg m^{-3} and 3300 kg m^{-3}, respectively. The density changes with temperature and with amount of depletion. Following the Boussinesq approximation (Ranalli, 1995), density is expressed as $\rho = \rho_0(1 - \alpha(T - T_0) - \beta F)$, where ρ is the density, α is the thermal expansivity, β is a factor that parametrizes the influence of melt extraction on density and is equal to 0.044 (Armitage et al., 2013), F is the melt depletion, ρ_0 is the reference density and T_0 is the reference temperature.

Supporting movies captions

Movie S1. Evolution of the numerical model with mafic granulite lower crust, 35 km crustal thickness, 17.5 km upper crust and 3 mm/yr half-extension velocity. Isotherms of 400 and 600°C are depicted by the dashed red contours. Top: Red and blue colors show plastic and viscous strain rate (s^{-1}), respectively. Bottom: Viscosity field and low

viscosity channel depicted by the white contours ($< 10^{21} Pas$). Velocity arrows show the flow of the lower crust and mantle at the main active rift zone.

Movie S2. Evolution of the numerical model with mafic granulite lower crust, 40 km crustal thickness, 17.5 km upper crust and 3 mm/yr half-extension velocity. Isotherms of 400 and 600°C are depicted by the dashed red contours. Top: Red and blue colors show plastic and viscous strain rate (s^{-1}), respectively. Bottom: Viscosity field and low viscosity channel depicted by the white contours ($< 10^{21} Pas$). Velocity arrows show the flow of the lower crust and mantle at the main active rift zone.

Movie S3. Evolution of the numerical model with wet quartzite lower crust, 35 km crustal thickness, 17.5 km upper crust and 3 mm/yr half-extension velocity. Isotherms of 400 and 600°C are depicted by the dashed red contours. Top: Red and blue colors show plastic and viscous strain rate (s^{-1}), respectively. Bottom: Viscosity field and low viscosity channel depicted by the white contours ($< 10^{21} Pas$). Velocity arrows show the flow of the lower crust and mantle at the main active rift zone.

Movie S4. Evolution of the numerical model with wet quartzite lower crust, 40 km crustal thickness, 17.5 km upper crust and 3 mm/yr half-extension velocity. Isotherms of 400 and 600°C are depicted by the dashed red contours. Top: Red and blue colors show plastic and viscous strain rate (s^{-1}), respectively. Bottom: Viscosity field and low viscosity channel depicted by the white contours ($< 10^{21} Pas$). Velocity arrows show the flow of the lower crust and mantle at the main active rift zone.

Movie S5. Viscosity field of two numerical models with wet anorthite lower crust. Top: model with 35 km crustal thickness, 20 km upper crust and 10 mm/yr half-extension velocity. Bottom: model with 40 km crustal thickness, 10 km upper crust and 5 mm/yr half-extension velocity. Isotherms of 400 and 600°C are depicted by the dashed red contours. Viscosity field and low viscosity channel depicted by the white contours ($< 10^{21} Pas$).

Movie S6. Evolution of the numerical model with mafic granulite lower crust, 35 km crustal thickness, 17 km upper crust and 5 mm/yr half-extension velocity. Top: surface heat flow and thinning factors (γ) for the crust and lithospheric mantle. Middle: ratio of upper- to lower-crust thickness UC/LC and crustal stretching factor β_c. Bottom: Red and blue colors show plastic and viscous strain rate (s^{-1}), respectively. Isotherms of 400 and 600°C are depicted by the dashed red contours. Velocity arrows show the flow of the lower crust and mantle at the main active rift zone.

Movie S7. Evolution of the numerical model with dry quartzite in both crustal layers, 40 km crustal thickness, 17 km upper crust and 5 mm/yr half-extension velocity. Top: surface heat flow and thinning factors (γ) for the crust and lithospheric mantle. Middle: ratio of upper- to lower-crust thickness UC/LC and crustal stretching factor β_c. Bottom: Red and blue colors show plastic and viscous strain rate (s^{-1}), respectively. Isotherms of 400 and 600°C are depicted by the dashed red contours. Velocity arrows show the flow of the lower crust and mantle at the main active rift zone.

Movie S8. Evolution of the numerical model with mafic granulite lower crust, 40 km crustal thickness, 17 km upper crust and 3 mm/yr half-extension velocity. Top: surface heat flow and thinning factors (γ) for the crust and lithospheric mantle. Middle: ratio of upper- to lower-crust thickness UC/LC and crustal stretching factor β_c. Bottom: Red and blue colors show plastic and viscous strain rate (s^{-1}), respectively. Isotherms of 400 and 600°C are depicted by the dashed red contours. Velocity arrows show the flow of the lower crust and mantle at the main active rift zone.

Movie S9. Evolution of the numerical model with wet anorthite lower crust, 33 km crustal thickness, 22 km upper crust and 4 mm/yr half-extension velocity. Top: surface heat flow and thinning factors (γ) for the crust and lithospheric mantle. Middle: ratio of upper- to lower-crust thickness UC/LC and crustal stretching factor β_c. Bottom: Red and blue colors show plastic and viscous strain rate (s^{-1}), respectively. Isotherms of 400 and 600°C are depicted by the dashed red contours. Velocity arrows show the flow of the lower crust and mantle at the main active rift zone.

Movie S10. Evolution of the numerical model with wet quartzite lower crust, 40 km crustal thickness, 16 km upper crust and 3 mm/yr half-extension velocity. Top: surface heat flow and thinning factors (γ) for the crust and lithospheric mantle. Middle: ratio of upper- to lower-crust thickness UC/LC and crustal stretching factor β_c. Bottom: Red and blue colors show plastic and viscous strain rate (s^{-1}), respectively. Isotherms of 400 and 600°C are depicted by the dashed red contours. Velocity arrows show the flow of the lower crust and mantle at the main active rift zone.

References

Andrés-Martínez, M. (2016). Rifted margin architecture and the interplay between mantle, crustal and surface processes from geodynamic numerical experiments. PhD thesis, Royal Holloway, University of London.

Armitage, J. J., Jaupart, C., Fourel, L., and Allen, P. A. (2013). The instability of continental passive margins and its effect on continental topography and heat flow. Journal of Geophysical Research: Solid Earth, 118, 1817-1836.

De Bresser, J., Ter Heege, J., and Spiers, C. (2001). Grain size reduction by dynamic recrystallization: Can it result in major rheological weakening?. International Journal of Earth Sciences, 90(1), 28-45.

Hirth, G., and Kohlstedt, D. L. (1996). Water in the oceanic upper mantle: Implications for rheology, melt extraction and the evolution of the lithosphere. Earth and Planetary Science Letters, 144(1-2), 93-108.

Lu, G., Kaus, B. J., and Zhao, L. (2011). Thermal localization as a potential mechanism to rift cratons. Physics of the Earth and Planetary Interiors, 186(3), 125-137.

Morgan, J. P. (1997). The generation of a compositional lithosphere by mid-ocean ridge melting and its effect on subsequent off-axis hotspot upwelling and melting. Earth and Planetary Science Letters, 146(1-2), 213-232.

Précigout , J., and Gueydan, F. (2009). Mantle weakening and strain localization: Implications for the long-term strength of the continental lithosphere. Geology, 37(2), 147-150.

Ranalli, G., and Murphy, D. C. (1987). Rheological stratification of the lithosphere. Tectonophysics, 132(4), 281-295.

Ranalli, G. (1995). Rheology of the earth. the Netherlands: Springer Science and Business Media.

Rüpke, L., Phipps Morgan, J., and Eaby Dixon, J. (2006). Implications of subduction rehydration for earth's deep water cycle. In S. D. Jacobsen and S. Van Der Lee (Eds.), Earth's deep water cycle (pp. 263-276). Washington, DC: American Geophysical Union.

CHAPTER

5

Lower crustal strength controls on melting and serpentinization at magma-poor margins: potential implications for the South Atlantic

Citation:

Ros, E., Pérez-Gussinyé, M., Araújo, M., Thoaldo Romeiro, M., Andrés-Martínez, M., and Morgan, J. P. (2017). Lower crustal strength controls on melting and serpentinization at magma-poor margins: potential implications for the South Atlantic. Geochemistry, Geophysics, Geosystems, 18, 4538–4557. https://doi.org/10.1002/2017GC007212

Electronic supporting information includes the movies presented in this chapter.

Author contributions:

The manuscript draft, models design and discussion of results and conclusions was a joint effort by **E.R.** and M.P.G. The seismic lines in Figure 2 were interpreted by M.T.R and M.A., and discussed in Section 2.1 and Section 3.1 by **E.R.**, M.P.G. and M.A. The serpentinization numerical code was further developed by **E.R.** after M.A.M. and M.P.G. The melting and underplating numerical codes were developed by **E.R.** under the supervision of M.P.G. and J.P.M. The analisis of results and preparation of figures and movies (excluding Figure 2), both in the manuscript and in the supporting information, was done by **E.R.** All authors read the manuscript and contributed to the final version. The submission of the manuscript and review of comments from the journal editor and reviewers was done by **E.R.** with the supervision of M.P.G.

AGU PUBLICATIONS

Geochemistry, Geophysics, Geosystems

RESEARCH ARTICLE
10.1002/2017GC007212

Key Points:
- Lower crustal strength controls the onset and amount of melting and serpentinization during 'ultra-slow' continental rifting
- Strong lower crust favors a continent-ocean transition with exhumed and serpentinized mantle, underlain by frozen magma
- Weak lower crust favors a magmatic dominated COT, perhaps underlain by serpentinites

Supporting Information:
- Supporting Information S1
- Movie S1
- Movie S2
- Movie S3
- Movie S4
- Movie S5

Correspondence to:
E. Ros,
Elena.Ros.2014@live.rhul.ac.uk

Citation:
Ros, E., Pérez-Gussinyé, M., Araújo, M., Thoaldo Romeiro, M., Andrés-Martínez, M., & Morgan, J. P. (2017). Lower crustal strength controls on melting and serpentinization at magma-poor margins: potential implications for the South Atlantic. *Geochemistry, Geophysics, Geosystems*, *18*. https://doi.org/10.1002/2017GC007212

Received 31 AUG 2017
Accepted 14 NOV 2017
Accepted article online 2 DEC 2017

Lower Crustal Strength Controls on Melting and Serpentinization at Magma-Poor Margins: Potential Implications for the South Atlantic

Elena Ros[1], Marta Pérez-Gussinyé[2], Mario Araújo[3], Marco Thoaldo Romeiro[3], Miguel Andrés-Martínez[2], and Jason P. Morgan[1]

[1]COMPASS, Department of Earth Sciences, Royal Holloway University of London, Egham, UK, [2]MARUM – Center for Marine Environmental Sciences, University of Bremen, Germany, [3]Petrobras R&D Center, Horácio Macedo Avenue, 950, Rio de Janeiro, Brazil

Abstract Rifted continental margins may present a predominantly magmatic continent-ocean transition (COT), or one characterized by large exposures of serpentinized mantle. In this study we use numerical modeling to show the importance of the lower crustal strength in controlling the amount and onset of melting and serpentinization during rifting. We propose that the relative timing between both events controls the nature of the COT. Numerical experiments for half-extension velocities $<=$10 mm/yr suggest there is a genetic link between margin tectonic style and COT nature that strongly depends on the lower crustal strength. Our results imply that very slow extension velocities ($<$ 5 mm/yr) and a strong lower crust lead to margins characterized by large oceanward dipping faults, strong syn-rift subsidence and abrupt crustal tapering beneath the continental shelf. These margins can be either narrow symmetric or asymmetric and present a COT with exhumed serpentinized mantle underlain by some magmatic products. In contrast, a weak lower crust promotes margins with a gentle crustal tapering, small faults dipping both ocean- and landward and small syn-rift subsidence. Their COT is predominantly magmatic at any ultra-slow extension velocity and perhaps underlain by some serpentinized mantle. These margins can also be either symmetric or asymmetric. Our models predict that magmatic underplating mostly underlies the wide margin at weak asymmetric conjugates, whereas the wide margin is mainly underlain by serpentinized mantle at strong asymmetric margins. Based on this conceptual template, we propose different natures for the COTs in the South Atlantic.

1. Introduction

In the last decades, a number of studies have shown that while some extensional margins follow the classical model of crustal and lithospheric break-up immediately followed by magmatic oceanic accretion (e.g., the Woodlark Basin; Taylor et al., 1999), others, the so-called magma-poor margins, exhibit large exposures of serpentinized mantle at a wide continent-ocean transition (COT). This transition is located between the oceanward end of the thinned continental crust and the first occurrence of magmatic oceanic crust. The West Iberia-Newfoundland conjugates and the ancient Tethys margins now exposed in the Alps have become archetypes for this margin style. In the former numerous drillings and geophysical surveys have been carried out, while the latter have been the focus of numerous field geology studies (e.g., Bayrakci et al., 2016; Boillot et al., 1987; Groupe-Galice, 1979; Lavier & Manatschal, 2006; Lemoine et al., 1986; Manatschal, 2004; Manatschal & Müntener., 2009; Masini et al., 2012; Mohn et al., 2010, 2012; Müntener et al., 2000; ODP Leg 173 Shipboard Scientific Party, 1998; Péron-Pinvidic et al., 2007; Reston et al., 1996; Sawyer et al., 1994; Tucholke & Sibuet, 2007; Tucholke et al., 2007; Welford et al., 2010; Whitmarsh & Miles, 1995; Whitmarsh et al., 1996, 1998). Whether or not the COT of margins consists of exhumed serpentinized mantle is relevant, among other reasons, because these areas may host intense serpentinite-based hydrothermal activity during continental break-up (Beard & Hopkinson, 2000; Klein et al., 2015). This involves production of hydrogen and methane at low temperature ranges that are within the limits of chemolithotropic life (Klein et al., 2015; Schrenk et al., 2013; Skelton et al., 2005), and the storage of water and element transfer from the mantle (e.g., Si, Mg, Ca), which may significantly impact magma-poor sedimentary environments (Pinto et al., 2017).

Typically, rifted margins were classified according to syn-rift magmatism. Magma-poor margins were thought to show scarce magmatism and exposed mantle at the COT, while magma-rich margins were characterized by an excess of magmatism. These two types of margins were considered to constitute end-members of a margin spectrum exhibiting variable degree of magmatism (e.g., Sawyer et al., 2007). Recent literature, however, classify many margins that do not show excess magmatism as magma-poor, i.e., place them toward one end of the margin spectrum. Some of these margins are the Gulf of Aden margin (Autin et al., 2010), the Goban Spur margin (Sibuet & Tucholke, 2013), the south Australian margin (Direen et al., 2007) and the South Atlantic Angola-Campos rift system and Santos and Espirito Santo basins (Pinto et al., 2017; Unternehr et al., 2010; Zalán et al., 2011; see also references to other margins in Reston, 2009). By analogy to the West Iberia-Newfoundland magma-poor conjugates, many of these margins have been interpreted to also have a COT consisting of exhumed and serpentinized mantle (e.g., Direen et al., 2013; Osmundsen & Ebbing, 2008; Peron-Pinvidic et al., 2017). However, drilling and detailed wide-angle seismic data at these COTs is still lacking to confirm this generalized interpretation (see also Eagles et al., 2015). The detailed nature of the COT at these margins may consist of exhumed mantle as in the archetypical West Iberia-Newfoundland margins, or of mainly magmatic products, perhaps underlain by serpentinized mantle, not yet forming a typical magmatic oceanic crust (see Figures 2a and 2b from Sawyer et al., 2007). Additionally, it is not clear whether exhumed mantle COTs also contain some 'hidden' magmatic products. For example, in the Iberia Abyssal plain sector of the West Iberia margin where the observational data set is one of the most complete up to date, the exhumed mantle may be underlain by a 2 km thick magmatic layer; an interpretation that also fits the geophysical data (Minshull, 2009; Russell & Whitmarsh, 2003; Sibuet et al., 2007). What appears to be clear is that magma-poor margins tend to extend at very slow velocities, within the realm of ultra-slow spreading velocities in oceanic ridges ($\leq$ 10 mm/yr half extension), where magmatism tends to be scarce.

Over the last decade, numerical modeling studies have become increasingly prevalent to understand the geodynamical processes involved in continental rifting (Beaumont & Ings, 2012; Nagel & Buck, 2004; Naliboff & Buiter, 2015). In particular, many authors have explored the relationship between the lower crustal strength and the tectonic evolution of margins with the goal of explaining the observed variability in the crustal asymmetry, faulting patterns and margin width (Bassi, 1995; Brune et al., 2017; Buck, 1991; Hopper & Buck, 1996; Huismans & Beaumont, 2014; Pérez-Gussinyé & Reston, 2001; Sharples et al., 2015; Svartman Dias et al., 2015; Wijns et al., 2005). These studies suggest that, for a strong lower crust, upper crustal deformation by faulting is highly coupled to mantle deformation by shear zones within the lower crust. These produce very effective crustal thinning, resulting in narrow symmetric margins characterized by large oceanward dipping faults that produce strong syn-rift subsidence (narrow rift mode, Buck, 1991; Type I, Huismans & Beaumont, 2011). However, for a weak lower crust, the deformation is distributed over a wide area, leading to the formation of wide symmetric margins, with small offset faults dipping both landward and oceanward and small syn-rift subsidence (wide rift mode, Buck, 1991; Type II, Huismans & Beaumont, 2011). For a lower crust of intermediate strength, the lower crust is strong enough to allow localization in a single active fault, although still weak enough to prevent rapid crustal break-up by faulting. In this case, localization of deformation in a single large fault leads to asymmetric uplift of the mantle, heating and weakening the hangingwall of the large active fault, where the next fault will form. This leads to the emergence of an oceanward younging and dipping fault array which is sequential in time, and which generates a marked margin asymmetry (Brune et al., 2014, 2017; Ranero & Pérez-Gussinyé, 2010). In this study we use numerical modeling to analyze whether these extensional modes (i.e., narrow, wide and sequential faulting) can also be related to COT types. We distinguish between COTs where serpentinized mantle is dominant at the top basement and COTs that are predominantly magmatic.

In particular, our contribution focuses on the role of lower crustal strength in determining the rate of mantle upwelling versus the rate of crustal embrittlement. This, in turn, controls the relative timing of the onsets of melting and serpentinization during extension and, hence, the nature and extent of the COT (Minshull et al., 2001; Pérez-Gussinyé & Reston, 2001; Pérez-Gussinyé et al., 2006). The concept that the relative timings of melting and serpentinization may control the nature of the COT is based on the notion that serpentinized mantle may act as a barrier for melt migration. In this work we assume that once melts are generated, they quickly move to the area of maximum extension beneath the crust (Gudmundsson, 1990, 2011). When this

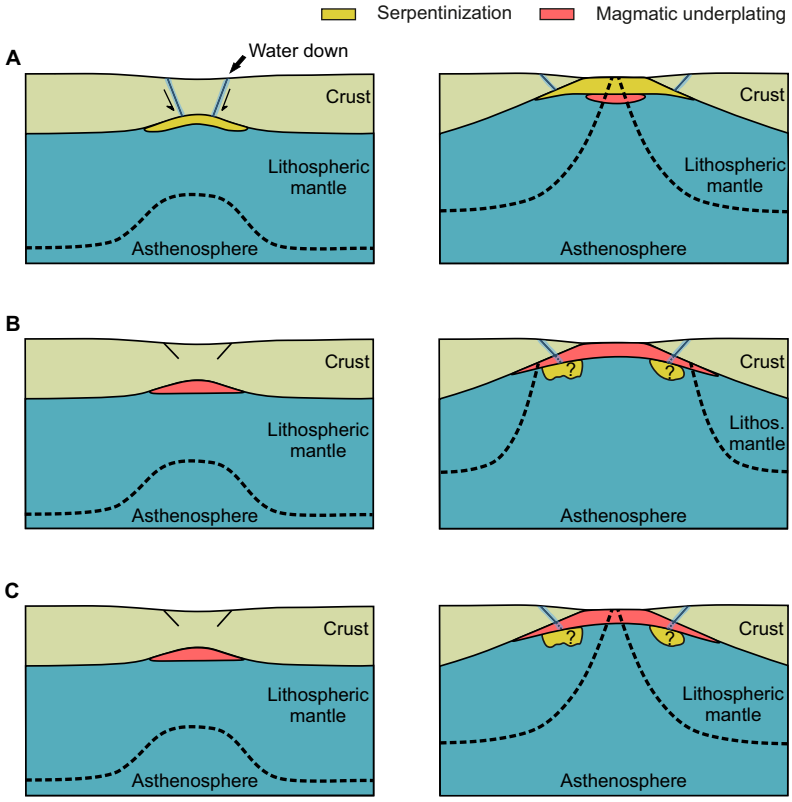

Figure 1. Cartoons showing three break-up styles of magma-poor continental rifting. (a) Brittle lower crust allows the formation of crustal-scale faults that act as conduits for the water, which reaches the mantle and serpentinize it before melting starts. The crust breaks-up before the lithosphere mantle and the resulting COT shows exhumed and serpentinized mantle, underlain by magmatic underplating. (b) Ductile lower crust inhibits the formation of crustal-scale faults until later in rifting history, hence melting starts before serpentinization. The mantle lithosphere breaks-up before the crust, resulting in a magmatic dominated COT, perhaps underlain by serpentinized mantle. (c) Ductile lower crust inhibits the formation of crustal-scale faults until later in rifting history. The crust breaks-up before the lithosphere mantle and a magmatic dominated COT results, below which may be serpentinites. No exposed mantle is observed in cases B and C, regardless of the relative timing between the crust and lithosphere mantle rupture.

area has been already occupied by serpentinized mantle, two factors may hinder the ascent of melt to upper levels within the crust and/or their extrusion (Figure 1a). First, serpentinized mantle may act as an 'impermeable' barrier to melt transport by porous flow. We base this assumption on the fact that, in subduction zones, serpentinites have been proposed to be impermeable in the direction perpendicular to shearing at the subducting plate interface (Katayama et al., 2009; Kawano et al., 2011). This suggests that, in extensional environments, a layer of serpentinized mantle may also act as a barrier to vertical melt migration. Second, if melt is intruding by diking in the brittle regime, then nondilatant brittle deformation of serpentinite (Escartin et al., 1997) may act as an additional stress barrier that the dike has to overcome. Alternatively, other magma/serpentine interactions could lead to serpentinites being a natural barrier to dike propagation. For example, if the hot dike magma induces rapid devolatilization of serpentine at the serpentine contact, this large pulse of volatiles could induce fracture along the serpentinized mantle interface that favors the dike propagating alongside, rather than into the region of serpentinized mantle. Furthermore, serpentine devolatilization is strongly endothermic, thus favoring more rapid dike cooling/freezing. All these scenarios do not exclude the possibility that melt eventually intrudes the serpentinite layer, but rather stress that the presence of serpentinite can hinder the intrusion of melt through serpentine to reach the top basement. Hence, when serpentinization has occurred prior to melting, the COT could tend to appear as mainly serpentinized mantle at the surface, with melts being mostly underplated or intruded into the serpentinite layer, and only a small volume of extruded melt products (Figure 1a).

The necessary conditions for mantle to be exhumed at the COT have been considered in previous studies of numerical modeling. Some authors concluded that mantle is exhumed at the COT when crustal break-up occurs before lithospheric break-up (e.g., Type 1 margins; Huismans & Beaumont, 2011; Figure 1a). However, these models do not include the generation of magma nor of serpentinization during continental rifting, which is crucial for understanding the nature of the COT. We show that in extensional margins where melting begins relatively early in the rifting process, irrespective of whether the lithosphere (Figure 1b) or the crust 'breaks' first (Figure 1c), melt ascends to underplate the crust prior to serpentinization, thus moving regions of potential serpentinization to deeper and hotter levels in the mantle, where serpentinization is less likely. Hence, these margins should be characterized by more magmatism and much less serpentinization, generating an abrupt transition to magmatic oceanic crust with no exposed mantle (Figures 1b and 1c).

In this work, we include melting and the serpentinization of the mantle in numerical models to assess the amount, timing and distribution of melts and serpentinized mantle during continental rifting. Our models suggest that extension at ultra-slow velocities does not necessarily lead to mantle exhumation at the COT of magma-poor margins and that mantle exhumation is strongly dependent on lower crustal strength. Additionally, we use numerical modeling as a further tool to help interpret and understand the processes leading to COT formation. We qualitatively compare the tectonic style of our model results to 3 interpreted seismic profiles in the central South Atlantic segment (Figure 2). We are not aiming to reproduce all the features of the South Atlantic margins to validate our model results, but instead to use both numerical and seismic profiles for comparison between the first order characteristic of the margins tectonic styles, including margins widths, faulting patterns, and crustal deformation, in order to make predictions on the nature of the COTs along the profiles. Definite observations are still lacking concerning the nature of the COT in this margin sector due to the relative lack of wide-angle seismic data and drilling. To date, only a refraction survey in the Santos basin has been published (Evain et al., 2015); this shows a magmatic COT. Below we will briefly summarize the tectonic structure of the margins in our study area and the different interpretations that have been given to the COTs at these margins in previous studies.

2. Study Area

Opening of the central South Atlantic segment propagated northward from the Rio Grande Fracture Zone to the Ascension Fracture Zone (Blaich et al., 2011; Eagles, 2007; Pérez-Díaz & Eagles, 2014) and lasted about 30 Myr, from the Late Jurassic/Early Cretaceous to the Aptian (Heine et al., 2013). The study area encompasses three representative conjugate margins: Camamu/South Gabon, Campos/North Kwanza and North Santos/South Kwanza (Figure 2). There is still some debate on the timing and location of break-up because it occurred during the Cretaceous Magnetic Quiet period (Bird & Hall, 2016). The location and extent of the continent-ocean transition (COT) is also debated because the present interpretations are based only on multichannel seismic data, except for the section we use in the Santos basin.

Figure 2 shows the landward limit of the oceanic crust (LaLOC) from Heine et al. (2013). This limit separates homogenous oceanic crust from an area that could include some transitional crust between the continental and oceanic domains. In the two southern sectors of our study area, the LaLOC is at most 30–40 km oceanward from the COB defined by Blaich et al. (2011) while in the northern area is almost coincident. This difference arises partly because the LaLOC allows the inclusion of transitional crust and the COB by Blaich et al. (2010, 2011) represents the oceanward limit of the continental crust. The LaLOC in Figure 2 is used to give a picture of the first-order variation of the margin width in the whole study area. However, we use more regional studies in the areas of the seismic sections for our seismic interpretations, e.g., Blaich et al. (2011) and Lentini et al. (2010) in the two southern sectors, and Blaich et al. (2010) in the northern sector. Despite these various interpretations on the continental margin width, they all exhibit a very marked change in polarity from North to South (Figure 2d). The Brazilian and African margins exhibit opposite tendencies, with the former increasing in width toward the South and the latter decreasing. Below, we briefly describe interpretations of seismic lines in these key sectors, which show a change in the style of extension from the Camamu/Gabon sector, where the margins developed close to the San Francisco craton, to the Campos/North Kwanza and North Santos/South Kwanza sectors, where the margins developed close to the Ribeira fold belt.

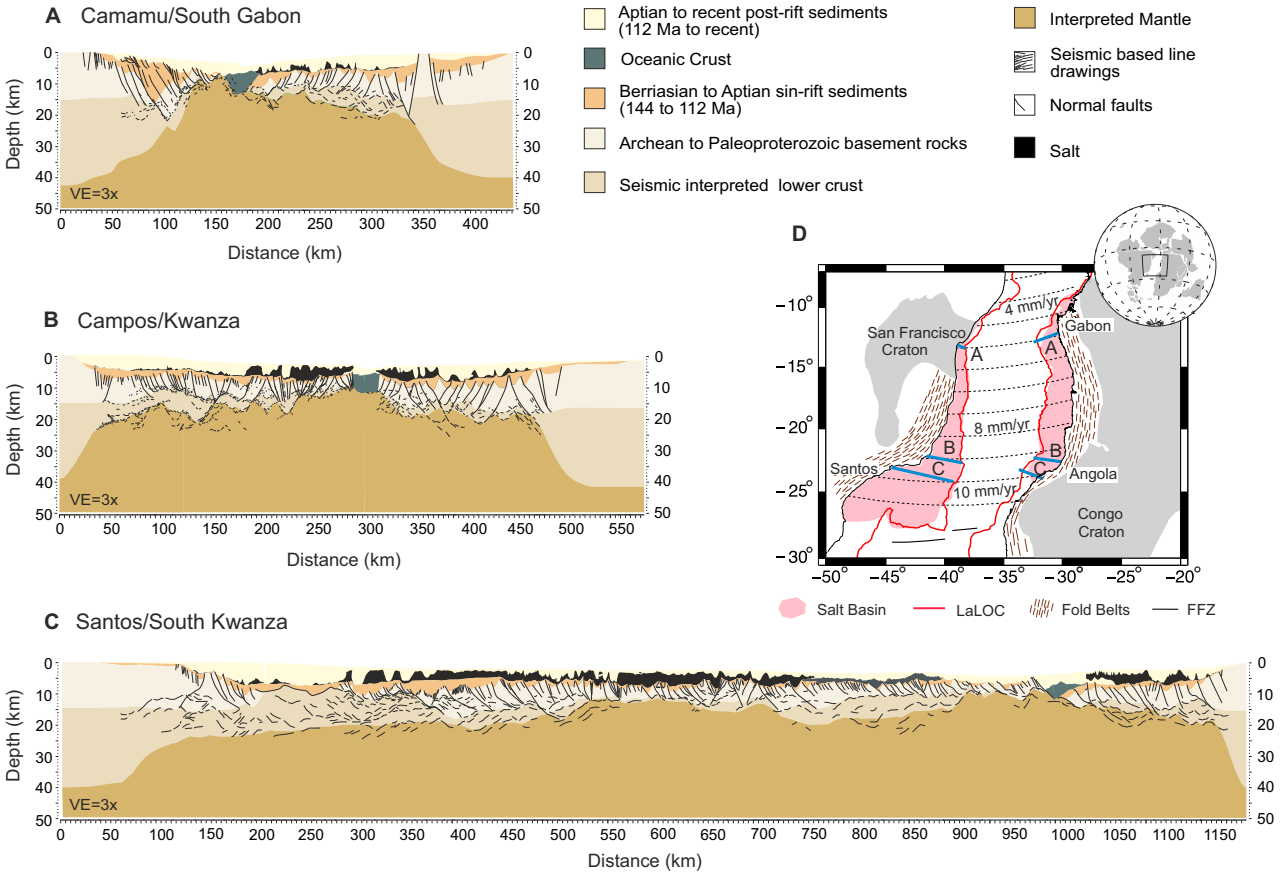

Figure 2. Geological interpretation of central South Atlantic conjugate margins. (a) Interpretation of seismic line in Camamu/South Gabon. Asymmetric narrow-wide margin configuration, with the Brazilian margin thinning abruptly over $<$ 100 km and the African conjugate gradually thinning over 200 km. Note large faults dip mostly oceanward and exhibit large syn-riftt subsidence. (b) Interpretation of seismic line in Campos/North Kwanza. Symmetric wide domains with a $\sim$ 500 km conjugate width. Note small faults, dipping ocean- and landward, exhibiting small syn-rift subsidence. (c) Interpretation of seismic line in North Santos/South Kwanza. Asymmetric margins with a 950 km margin width in North Santos and a 200 km width in South Kwanza. Note small faults, dipping ocean- and landward, and small syn-rift subsidence. Crustal thicknesses offshore were constrained by 2-D gravity modeling and onshore by receiver function and tomographic maps of Assumpção et al. (2013). In the specific case of the Santos Basin, the interpretation was also supported by the wide-angle refraction seismic of Evain et al. (2015). (d) Plate reconstruction of the South Atlantic (Africa is kept fixed) (adapted from Heine et al., 2013) with the locations of the interpreted seismic sections. The LaLOC is the landward limit of the oceanic crust from Heine et al. (2013). From North to South the degree of asymmetry and the full-extension velocity increases. The rheology changes from craton to fold belt as we move southward. FFZ is Florianópolis Fracture Zone from Pérez-Díaz and Eagles (2014). V.E. Vertical Exaggeration.

2.1. Interpretation of Seismic Lines

The locations of the interpreted seismic lines of the South Atlantic central segment used in this study are shown in Figure 2. The corresponding seismic lines are proprietary data of ION-GXT and have been already published (Blaich et al., 2010; Ferreira et al., 2009; Kumar et al., 2013; Zalan et al., 2011). Any interpretation of multichannel seismic data is a subjective process, especially when the seismic image is not sharp, as is sometimes the case under some areas in the salt basins of the Campos and Santos. In this study we present interpretations of the first-order characteristics that define margin tectonic style where there is more agreement. These include the width of the continental margin, the asymmetry of the conjugates, the fault associated subsidence and the faulting pattern. We describe the latter based on the offset, dip direction and spatial distribution of faults. For example, we examine whether the shelf break exhibits large faults with accompanying abrupt syn-rift subsidence, or whether along the hyperextended sector of the seismic sections, where crustal thickness is less than 15 km, faults dip predominantly in one direction or randomly. These first-order faulting patterns are typically well recognized in seismic sections. Crustal thicknesses

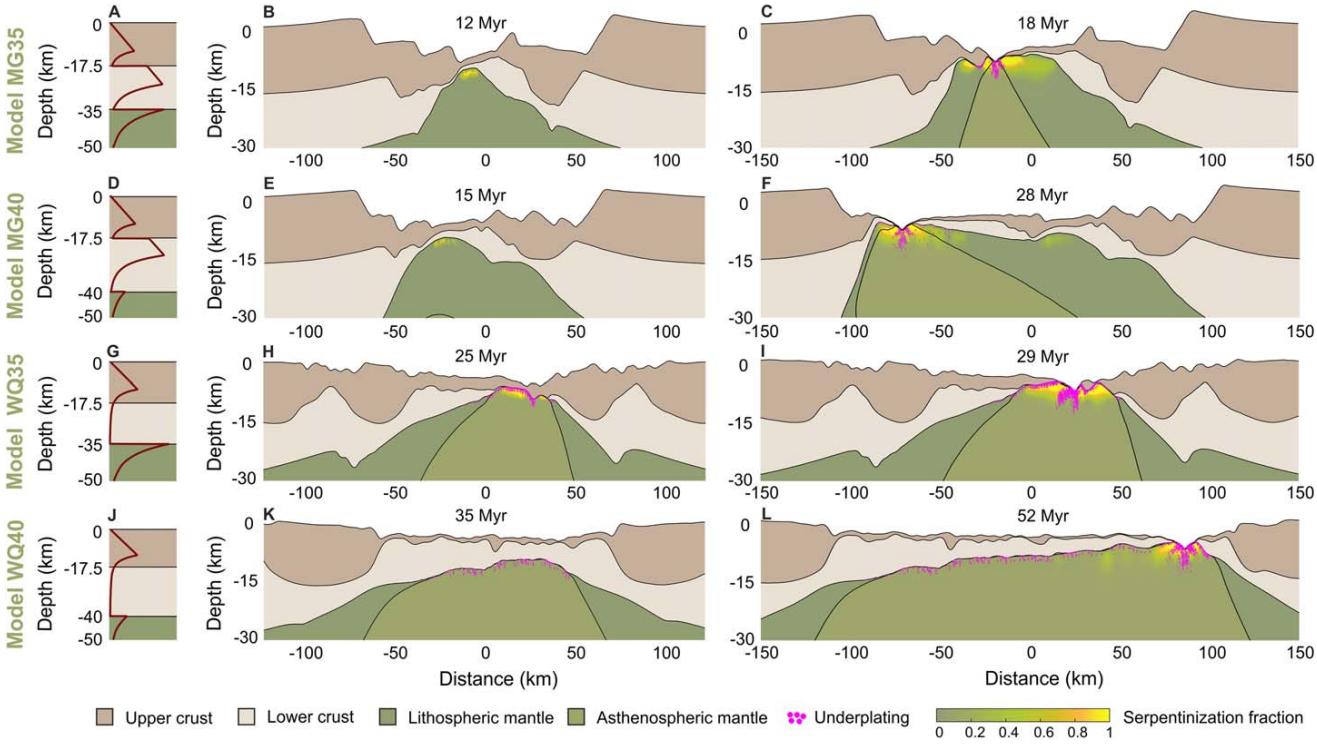

Figure 3. Initial strength envelope (A, D, G, J), intermediate snapshot (B, E, H, K) and break-up snapshot (C, F, I, L) of the MG35, MG40, WQ35 and WQ40 numerical models, respectively. Lower crusts are of mafic granulite (MG) or wet quartzite (WQ) and crustal thicknesses are thin (35) or thick (40). Snapshots show rheological layers, serpentinization with a color scale and underplating in pink color (see Legend). Note that the snapshots show the most representative times for each model. A movie with the evolution of each model can be found in the supporting information.

offshore were constrained by 2-D gravity modeling and onshore by receiver function and tomographic maps of Assumpção et al. (2013). In the specific case of the Santos Basin, the interpretation is also supported by wide-angle refraction data of Evain et al. (2015). We qualitatively compare these interpreted first-order margin characteristics with those observed in numerical models to make predictions about the COT nature along the interpreted sections.

Our interpretations in the Santos-South Kwanza and Campos-Kwanza lines are very similar to those published by Kumar et al. (2013; their Figures 5 and 9). In the Camamu-Gabon sector our interpretation is in accord with that published by Blaich et al. (2011; their Figure 3). Although we could have simply used the previous interpretations from the literature, we felt the need to provide an integrated view of the conjugated margins in terms of asymmetry, thinning profile, margin width and faulting pattern. Such integrated view was only possible by revisiting the seismic lines, which is shown below.

At basin scale the seismic lines show significant differences in the pattern of faulting distribution and depocentre depths. We assume that the present day crustal thicknesses estimated onshore are unthinned continental crusts. Therefore, we define the length of the margins from the unthinned continental crust to the COB. In the North, the Camamu/Southern Gabon margin pair is asymmetric, with the short conjugate margin on the Brazilian side and long one on the Gabon side (Figure 2a). Here the proximal zones are subdivided into large blocks, bounded by faults with offsets between 7 and 8 km (Araújo et al., 2015). These faults control deep depocentres, probably related to a stage of large syn-tectonic subsidence. Faults dip mainly oceanward on both margins. Another important characteristic is the crustal thinning of the crust, changing from a 40 km thickness to 10 km within a short distance (20 km) on the Brazilian side. In the Gabon side, crustal thinning is much smoother, so that the margin is much wider than on the Brazilian side. This configuration defines a marked asymmetry with a total length of 430 km. Our interpretation is quite similar to that recorded by Blaich et al. (2011). The occurrence of strong asymmetry, accompanied by oceanward dipping faults exhibiting large offsets, suggests deformation of an intermediate lower crustal strength

by sequential faulting mode, leading to the formation of a wide hyper-extended margin and a narrow conjugate (Brune et al., 2014, 2017; Ranero & Pérez-Gussinyé, 2010).

Southward, the conjugate margin pair of the Campos/Kwanza basins developed on the Neoproterozoic Ribeira/Kaoko Mobile Belt that extends over more than 500 km (Figure 2b). In terms of length, this sector is much wider, reaching a maximum length of 560 km. In both margins there are segments of typically hyper-extended crust (thickness $<$ 10 km). These widths are $\sim$ 250 km in the Campos basin and 140 km in Kwanza basin. Faults dip both landward and basinward, only in the distal parts of the margins do they systematically dip oceanward. These faults show small offsets (2.5 km), defining depocentres of similar depth values. This large width of the conjugate margins, in combination with smooth crustal thinning profile and the absence of large fault offsets suggest deformation in wide rift mode or Type II margins (Buck, 1991; Huismans & Beaumont, 2011), with a predominance of ductile deformation during extension.

To the South, the margins of North Santos/South Kwanza show thinning that is extremely large and asymmetric between the conjugate margins (Figure 2c). The Northern section of the Santos Basin also developed on the Ribeira/Kaoko fold belt but in a region with crust thicker than 40 km. Here the main characteristic is a very wide margin in the Brazilian side- over $\sim$ 800 km- while the conjugate South Kwanza margin is much shorter ($\sim$ 200 km). The gentle crustal thinning profile from the Brazilian platform to the hyperextended sector, the presence of divergent horst and grabens, with typically small offsets, and the large width of the conjugate margin all suggest the importance of ductile lower crustal deformation during extension. Note that the opening of this margin sector evolves with a 3-D structural heterogeneity and that the profile we show is oblique to the average opening direction, such that the Brazilian margin width in the extension direction may be 30% shorter.

2.2. Previous Interpretations of the COT in Our Study Area

The nature of the COT in our study area has been a topic of much debate in the recent years. Along the Camamu and Espirito Santo margins, Blaich et al. (2010, 2011) interpret the COT to be rotated fault blocks and wedge-shaped syn-rift sediments, where the thinned continental crust could be likely intruded by mafic material. Peron-Pinvidic et al. (2017) interpret the COTs of the Gabon and Kwanza as exhumed mantle which can be variously serpentinized. Mohriak et al. (2012) characterize the Espirito Santos-Kwanza margins with a magmatic COT. Unternehr et al. (2010) apply the conceptual model of Lavier and Manatschal (2006) to the seismic profiles of Campos and Angola in order to interpret the COT as exhumed mantle. This interpretation is also made by Zalán et al. (2011), who state that a serpentinized exhumed mantle transition can be mapped from Espirito Santo to Santos basins. However, Mohriak et al. (2008), Aslanian et al. (2009) and Kumar et al. (2013) suggest that extension in this area may have been partly accomplished by volcanic extrusions and intrusions and do not find evidence of exhumed mantle (except maybe along the Florianopolis fracture zone). Finally, wide-angle seismic data indicate an abrupt transition to normal oceanic crust in the Santos Basin (Evain et al., 2015).

3. Methods

We model extension of a rheologically layered visco-elasto-plastic lithosphere using a 2-D numerical code based on the Finite Element Method MILAMIN solvers (Dabrowski et al., 2008). The code uses a Lagrangian formulation to solve the conservation equations of mass, momentum and energy for an incompressible Stokes flow (see supporting information; Lu et al., 2011). Strain softening is included in the plastic and viscous deformation to localize deformation into shear bands that mimic faults in nature (see supporting information; Bos & Spiers, 2002; Buck & Lavier, 2001; Buck & Poliakov, 1998; De Bresser et al., 2001; Huismans & Beaumont, 2002; Lavier et al., 1999; Malvern, 1969; Précigout & Gueydan, 2009).

Decompression melting occurs where the mantle temperature exceeds the dry solidus (see supporting information Figures S1A and S1B). Melt generation is calculated at each time step based on the formulation of Morgan (2001), and the total amount of melt is located at the base of the crust forming a dike (Ito et al., 1996, see Figure 3 and section "Melt productivity and emplacement" in supporting information; Lavecchia et al., 2017; Schmeling, 2010; Simon et al., 2009). The production of melt depletes the mantle source and decreases its density (see section "Thermal and rheological profiles" in supporting information; Armitage et al., 2013). We assume that no melt is retained in the mantle and that after 4% of depletion the mantle

source has removed all the water, leading to a change in rheology from wet to dry olivine. This dehydration effect on the rheology will strength the mantle source.

In nature, as melt is produced, it ascends and either underplates, intrudes the crust or is extruded (Cannat et al., 2009). Underplating and intrusion can occur in the form of dikes and sills (Mathieu et al., 2008). For our numerical models we choose to accumulate all the melt produced at each time step in a column with a width equal to the full spreading velocity multiplied by the model time step, and a vertical thickness equal to the volume of produced melt divided by the width. We refer to the vertical thickness of the melt column as the magmatic crustal thickness by its analogy to the magmatic crustal thickness that would be produced in an oceanic ridge (Dick et al., 2003). Because the melt is placed at each time step in a new column, we refer to this column as dike. At each time step the new `dike` is positioned below the Moho in the location of maximum extension. The increasing number of dikes during rifting accumulates beneath the Moho and form what we call magmatic underplating (Thybo & Artemieva, 2013).

We allow serpentinization to occur when three conditions are met: the crust is entirely brittle, faults are active and the mantle is within the temperature range for serpentinization (~100 - 450°C). The first two criteria assume that the main conduits of water to serpentinize the mantle are active crustal-scale faults, as described in Pérez-Gussinyé and Reston (2001) and Bayrakci et al. (2016). The rate and extent of serpentinization is calculated with a dependence on temperature given by experimental data (Emmanuel & Berkowitz, 2006; see supporting information Figure S1C). The transformation of olivine into serpentinites releases heat to the surrounding rock as $Q=-H\frac{\partial \rho_m}{\partial t}$ where ρ_m is the mass of forsterite per unit volume, t is the time and H is the heat reaction per unit mass of forsterite. In study we assume a temperature raise $300^{\circ}C$ for complete serpentinization. The viscosity of the serpentinized mantle decreases with the raise in temperature, which in turn reduces its ductile strength, and the density is the same as the mantle density. Since our numerical code is incompressible, we neglect the volume increase that results from serpentinization. This effect would promote strain localization along serpentinized fault planes (Iyer, 2007), which may help the formation of detachment faults. To define which faults are active we use a parameter that estimates how large the strain rate is within the fault in comparison to the maximum and minimum strain rates in the model domain. The exact definition of this parameter and how it influences our estimations of serpentinization is described below.

In nature, the production of serpentinized mantle depends on many factors, including the permeability and porosity of the active faults that control the access of water to the mantle (Emmanuel & Berkowitz, 2006; Macdonald & Fyfe, 1985). The numerical threshold that defines active faults cutting through the crust is subject of discussion. Here, we consider active the faults with larger strain rates than a threshold value $\dot{\varepsilon}_{th}$, which is calculated from the maximum and minimum strain rates ($\dot{\varepsilon}_{\max}$ and $\dot{\varepsilon}_{\min}$) along the model domain $\dot{\varepsilon}_{th}=f\cdot(\dot{\varepsilon}_{\max}-\dot{\varepsilon}_{\min})+\dot{\varepsilon}_{\min}$, where f is an arbitrary factor ranging from 0 to 1. We ran sensitivity tests to the f factor by varying its value from 0.001 to 0.5 (corresponding to the 0.1% and the 50% of the strain rate variation, respectively) with crustal thickness of 35 km, half-extension velocity of 3 mm/yr and two different lower crustal rheologies: mafic granulite and wet quartzite (supporting information Figure S2). The models with a larger f resulted in a slight delay of the onset of serpentinization (~ 0.1 to 0.4 Myr, for mafic granulite and wet quartzite, respectively) and less amount of serpentinized mantle. The difference in the parameter influences mainly the depth at which water is simulated to reach the mantle, and therefore the depth of the serpentinized zone, which changes about 5 km. Consequently, the degree of serpentinization is also affected, obtaining larger zones of 100% serpentinized mantle for the lower parameter. From wide-angle seismic refraction studies in the Iberia Abyssal Plain, highly serpentinized mantle up to 100% has been estimated in the COT, which decreases with depth (Chian et al., 1999), consistent with results from ODP drilling (Sawyer et al., 1994). Despite the small differences, the general outcomes for the nature and composition of the COTs hold after varying this numerical threshold within a reasonable range (supporting information Figure S2). The threshold parameter value assumed for this study is 0.15. Although this modeling parameter is not well constrained, we consider that our assumption for crust-cutting active faults better approximates the locations for generation of serpentinization in comparison to the condition with a merely brittle crust.

3.1. Model Setup

The 2-D model domain is 400 km wide by 400 km deep. The boundary conditions prescribed at the lateral and bottom boundaries are tangential free slip, with half-extension rate at the sides and full-extension rate

at the bottom to preserve the conservation of mass. This approach upwells the asthenospheric bottom as pure shear. Free surface is applied to the top boundary (Andrés-Martínez et al., 2015; Kaus et al., 2010). We run model simulations by applying different half-extension velocities within the ultra-slow range (3, 5 and 10 mm/yr), as Heine et al. (2013) suggested for this area (Figure 2d), to explore the implications of increasing the velocity on the COT nature.

Table S1 shows the rheological parameters used for modeling (Gleason & Tullis, 1995; Hirth & Kohlstedt, 2003; Ranalli & Murphy, 1987; Wilks & Carter, 1990): a wet olivine asthenosphere, dry olivine lithospheric mantle and wet quartzite upper crust (see section "Thermal and rheological profiles" in supporting information; Currie & Hyndman, 2006; Hirth & Kohlstedt, 1996; Morgan, 1997; Ranalli, 1995; Rüpke et al., 2006). To make simple and comparable simulations, we only change the strength of the lower crust between two rheologies: strong mafic granulite and weak wet quartzite. These rheologies are not meant to simulate the real composition of the lower crust, but rather are used as end-member strengths for the lower crust. When comparing to our study area, it must be kept in mind that, presently, there is not enough data on the onshore lithospheric structure that could give us detailed information on the rheology at the time of rifting. So we make informed guesses and compare the tectonic style observed in our seismic lines with the model results of the end-member rheologies. In the North of our study area, the rifting developed close to or at the San Francisco craton, so we assume that the lower crustal rheology was likely to be strong there. Continent-wide tomography results and high Te underneath the San Francisco craton indicate a thicker and colder lithosphere under this area (Feng et al., 2007; Pérez-Gussinyé et al., 2007, 2009). The lower crust and lithosphere under cratons is conventionally assumed to be strong (see strength envelopes in Burov, 2011), thus we compare our profile to the strong-end member case, mafic-granulite.

Toward the South, the rift develops on top of the Ribeira-Kaoko fold belt, the rocks are much younger and dominantly composed by gneisses and metasedimentary rocks metamorphosed from upper greenschist to amphibolite and few regions with granulites (Heilbron et al., 2008). The gentle continental slope and crustal tapering, in combination with the large width of these margins indicates that the lower crust must have been weak during rifting. This weakness may have been in part the result of the thermal influence of the Tristan da Cunha Plume during the onset of rifting (136 Ma). We use our weak end-member rheology to compare with the tectocnic style in this area. In addition, we change lower crustal strength by increasing crustal thickness from 35 km to 40 km, which are the crustal thicknesses observed in our study area (Assumpcão et al., 2013).

4. Results

Based on the relative onsets of serpentinization and melting, we describe the type of COT that would be expected for the weak and strong end-member strengths and various extensional velocities, i.e., 3, 5 and 10 mm/yr, used in this study. Similar to previous numerical models, our results show margin tectonic styles ranging from narrow to wide and from symmetric to asymmetric style as the lower crustal strength changes (Figure 3; e.g., Bassi et al., 1993; Brune et al., 2017; Buiter et al., 2008; Dunbar & Sawyer, 1989; Huismans & Beaumont, 2014; Naliboff & Buiter, 2015; Svartman Dias et al., 2015; Tetreault & Buiter, 2017). We decrease the lower crustal strength by changing the lower crustal rheology from strong mafic granulite to weak wet quartzite and by varying the crustal thickness from 35 to 40 km. For a given crustal thickness, the strong lower crust model always leads to narrower margins than the weak case (Figure 3), as already described in numerous publications (e.g., Bassi, 1991; Buck, 1991; Huismans & Beaumont, 2011). For any given lower crustal rheology, the conjugate margins become more asymmetric as the crustal thickness increases (Figure 3). Below we describe how the lower crustal strength affects the tectonic style and the production and timing of melting and serpentinization in our model runs of 3 mm/yr half-extension velocity (Figure 3).

For the strongest and thinnest lower crust case (Model MG35; Figures 3a–3c and supporting information Movie S1), the low thermal gradients that prevail during rifting result in strong localization of the deformation into large fault offsets, causing effective crustal thinning and embrittlement of the lower crust. At 11 Myr crustal faults that reach the mantle and act as conduits for water, allow serpentinization to start beneath ~3–4 km thick crust, where the mantle is at temperatures suitable for serpentinization (Figure 3b and supporting information Movie S1). At this time the thermal gradient is still too low for the mantle to melt (Figures 3b and 4a). The narrow extensional mode (as described by Buck, 1991) dominates rifting and

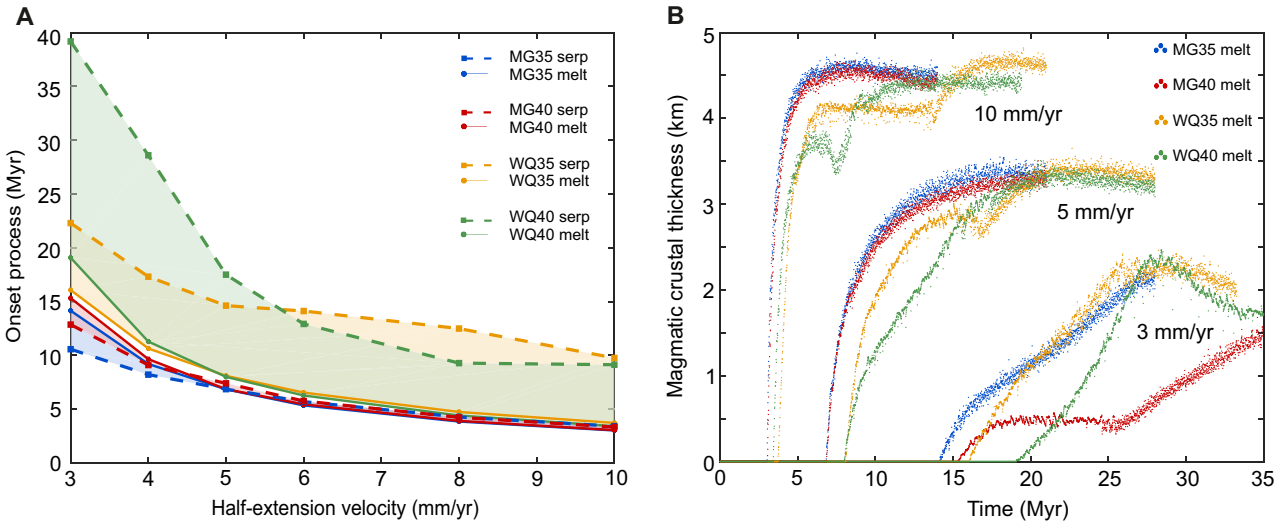

Figure 4. Numerical model results for the onset of melting and serpentinization and for the predicted magmatic crustal thickness. Models with mafic granulite lower crust are shown in blue and red colors for the 35 and 40 km thickness cases, respectively. Models with wet quartzite lower crust are shown in yellow and green colors for the 35 and 40 km thickness cases, respectively. (a) Melting and serpentinization onsets during the evolution of the numerical models, where models with half-extension velocities of 4, 6 and 8 mm/yr have been included to refine the transition between velocities. Solid and dashed lines link the onsets of melting and serpentinization, respectively, for the same lower crustal rheology and different extension velocities. (b) Predicted magmatic crustal thickness evolution over time.

leads to symmetric narrow conjugate margins. An earlier onset of serpentinization than that of melting results in a COT dominated by exhumed serpentinized lithospheric mantle at the seafloor, underplated by a thin magmatic layer (Figure 3c).

An increase in the lower crustal thickness implies a weakening at the bottom of the crust, so that the level of crust-mantle coupling decreases in comparison to the previous case (see strength envelopes in Figures 3a and 3d). This promotes a switch from the initial narrow deformation mode to a sequential faulting mode after 10 Myr of extension (Model MG40, Figures 3e and 3f; supporting information Movie S2). The latter mode occurs where deformation localizes in a single active fault and the lower crust is weak enough to flow to the fault tip. This inhibits crustal break-up by faulting and promotes the generation of a sequence of active faults that laterally migrate the rift center and dip oceanward, resulting in asymmetric conjugate margins (see Brune et al., 2014; Ranero & Pérez-Gussinyé, 2010). As sequential faulting progresses, serpentinization starts before melting (at 13 Myr; Figure 3e and supporting information Movie S2). Serpentinization does not occur as a consequence of the water moving down through the main active oceanward fault because the ductile lower crust flow does not allow the fault to reach the mantle. Instead, serpentinization is generated as the water downflows through the much less prominent faults dipping landward. These are located in the immediate footwall of the active fault, where the crust is thinner than 4 km (Figure 3e and supporting information Movie S2). We observe in our tests that serpentinization occurs in the footwall of the main active fault, which differs from the interpretation of Bayrakci et al. (2016) who suggested that, during the sequential faulting mode in the Deep Galicia margin, antithetic faults to the main active fault developed and acted as water conduits, which would explain the apparent focus of serpentinization underneath the hanging walls of normal faults in the margin. However, the sequential faulting mode is characterized by the development of a lower crustal flow that partly decouples crust and mantle at the tip of the fault, heating up this zone and inhibiting the formation of faults, in the hanging wall, that reach the mantle (Brune et al., 2014). Pinto et al. (2015) highlighted the difficulty in determining the pathways for the seawater migration into the mantle and proposed two options: through synthetic and antithetic normal faults in the hanging wall of a detachment fault or along the detachment itself, showing a more serpentinized footwall. Both types of water down flow would, however, produce very similar serpentinization profiles. Eventually, conductive cooling embrittles the lower crust and allows crustal break-up to occur ~9 Myr later than in the previous case with a thinner crust. The spatial extent of serpentinization beneath the thinned crust is much larger in the wide margin (20–30 km) than in the narrow one. Very little underplated magma is observed

beneath the crust on both margin sides (< 0.5 km; Figures 3f and 4b and supporting information Movie S2). The COT is characterized by exhumed serpentinized mantle at the seafloor, intruded and underplated by very little amounts of frozen magma (< 1.5 km; Figures 3f and 4b).

For the weakest and thinnest lower crust (Model WQ35, Figures 3g–3i), the increased degree of crust-mantle decoupling compared to the two previous cases, results in distributed faulting over a wide zone, with uniform crustal and lithosphere mantle thinning (i.e., wide rift mode, Buck, 1991) (from 0 to 11 Myr; Movie S3). The weak lower crustal flow inhibits the formation of crustal-scale faults, which delays the onset of serpentinization to 23 Myr, i.e., 6 Myr after the onset of melting (Figures 3h and 4a; supporting information Movie S3). Break-up leads to conjugate margins that are mostly symmetric, where the slightly wider margin results from a last stage of sequential faulting, as shown in Movie S3. Mantle serpentinization starts after melting, therefore the serpentinized zone is generated beneath the already frozen magma underplating the crust. We consider the COT to be a magma-dominated domain where magma products can be found at the sea-floor, and may be underlain by serpentinized mantle (Figure 3i).

For the same weak rheology and thicker lower crust (Model WQ40; Figures 3j–3l) extension starts in core complex mode (Buck, 1991; Tirel et al., 2008), localizing deformation in upper crustal detachment faults, whereas the lower crust and lithosphere mantle accommodates deformation over a wide region (from 0 to 12 Myr; Movie S4). As extension continues, the deformation changes to wide mode until 32 Myr. Later cooling kicks in leading to localization of deformation where the crust is the thickest, as the cooled mantle in the thinned region is stronger (e.g., Bassi et al., 1993), and switches to sequential faulting mode at 34 Myr. Melting starts at 19 Myr whereas serpentinization starts 21 Myr after melting (Figure 4a and supporting information Movie S4). Sequential faulting in the last stages of extension leads to the formation of two asymmetric margins, where the hyper-extended wide margin is underplated by magma along much of its length ~150 km (Figure 3l). This contrasts with the asymmetric model of a strong lower crust (Figure 3f) in which the wide margin is underplated by serpentinized mantle (compare Figures 3e and 3f with Figures 3k and 3l). The COT is magma dominated, with magmatic products at the seafloor, perhaps underlain by some serpentinized mantle (Figure 3l).

To obtain extremely wide and symmetric margins (e.g., Type II from Huismans & Beaumont, 2011 and Brune et al., 2017), we have to decrease the upper and lower crustal strengths from that in our standard models (see supporting information Figure S3 and Table S1 for rheological parameters). This very weak crustal model starts with a high degree of crust-mantle decoupling, which promotes distributed faulting in a wide mode that dominates the rift evolution and eventually leads to symmetric wide conjugate margins underplated by magma and a magmatic dominated COT.

When extension velocity is higher (5 and 10 mm/yr) all cases undergo melting prior to serpentinization, independently of the lower crustal rheology (Figure 4a and supporting information Figure S4). This is because higher velocities result in faster mantle uplift, which allows melting to start before serpentinization. At 5 mm/yr and for strong lower crusts, serpentinization takes place short after melting (< 1 Myr) due to the rapid embrittlement of the crust, most likely resulting in a narrow COT with both exhumed serpentinized mantle and magmatic products. For weak lower crusts, serpentinization occurs much later than melting in all cases, suggesting that for weak rheologies COTs will be dominated by magma without exhumation of lithospheric mantle for any ultra-slow extension velocity.

5. Discussion

5.1. Dependence of Melting on Lower Crustal Strength

It is well known that during oceanic spreading and continental rifting melting mainly depends on mantle temperature, composition and extension velocity (Armitage et al., 2009; Bown & White, 1995; Jokat et al., 2003; Morgan, 1987; Sotin & Parmentier, 1989; White et al., 2001). Figure 4a shows the dependence of mantle melting on lower crustal strength for ultra-slow extension velocities (≤ 10 mm/yr half-extension) which predominate in magma-poor environments. This dependence is most obvious for the cases with the lowest velocities tested here, 3 and 4 mm/yr, and determines the nature and extent of the COT. For 3 mm/yr, the strong and thin mafic granulite lower crust melting starts at 14 Myr, whereas for the thick and weak wet quartzite it starts at 19 Myr (Figures 4a and 4b and supporting information Movie S5). Despite being

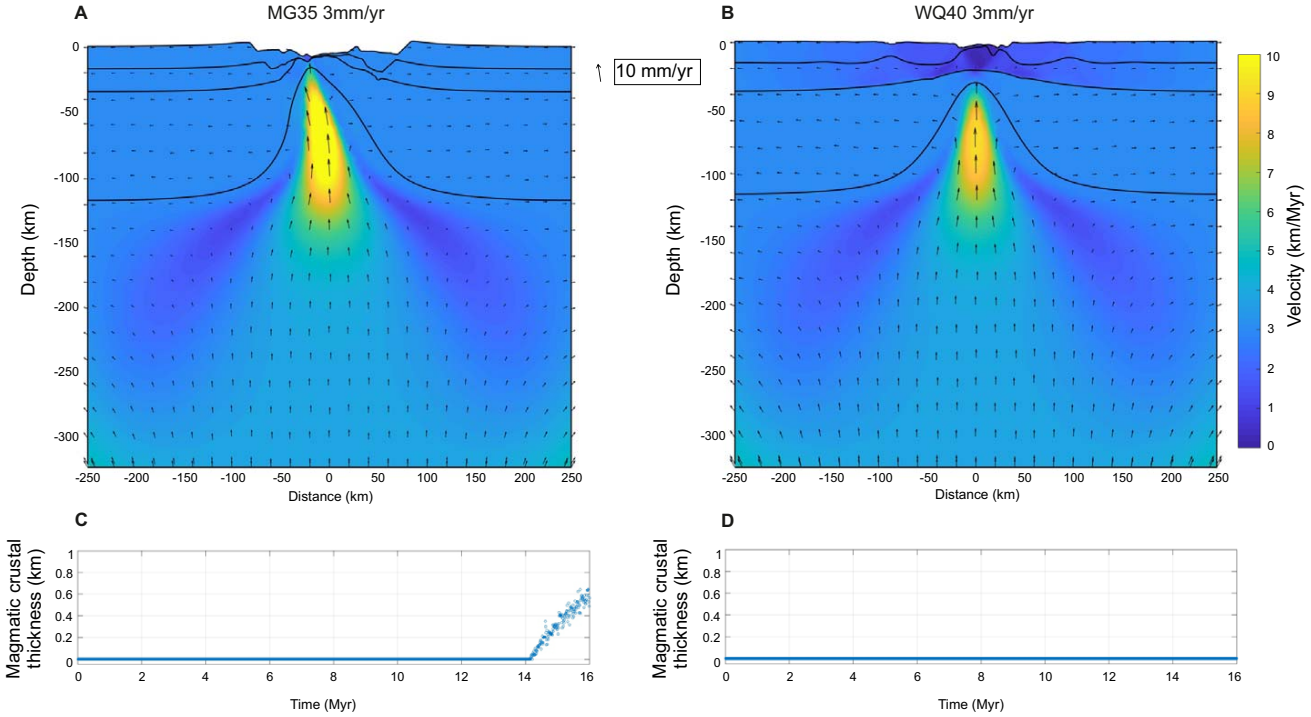

Figure 5. Velocity flow snapshot at 16 Myr after the onset of extension for the 3 mm/yr half-extension models: (a) MG35, mafic granulite lower crust and 35 km crustal thickness and (b) WQ40, wet quartzite lower crust and 40 km crustal thickness. Predicted magmatic crustal thickness from the onset of extension to 16 Myr after, for the 3 mm/yr half-extension models: (c) MG35 and (d) WQ40.

extended with the same velocity, the weak lower crust leads to a larger crust-mantle decoupling and slower uplift of the mantle than the strong lower crust model, which delays the onset of melting (Figure 5).

The dependence of predicted magmatic crustal thickness on crustal rheology over time is shown in Figure 4b. We have calculated the magmatic crustal thickness by assuming that all magma produced at each time step is accommodated in a dike beneath the Moho (see supporting information). For each velocity group, the onset of melting occurs earlier for strong lower crustal rheologies (mafic granulite) and it is delayed for larger decoupling between crust and mantle, which occurs with increasing crustal thickness or decreasing crustal strength (wet quartzite). For 3 mm/yr, the magmatic crustal thickness varies between 1 and 2 km depending on the crustal strength, whereas higher velocities of 5 and 10 mm/yr lead to magmatic thicknesses of 3.5 and 4.5 km respectively, regardless of the crustal rheology.

5.2. Linking Margin Tectonic Style and COT Nature

Our results suggest that margins where ductile processes dominate deformation are likely to be characterized by magma-dominated COTs with little to no serpentinized mantle, regardless of the extension velocity. This type of margin can be recognized by their large width, gentle continental slope and crustal tapering, small offset faults that dip both land- and oceanward and are indicative for the long periods on wide rifting mode, and little syn-rift subsidence (Figure 6). The delay between the onset of melting and that of serpentinization tends to be larger for wider margins (Figure 4a), indicating that the likelihood to find any serpentinized mantle in between magmatic products decreases as the margin width increases. The degree of symmetry is not symptomatic of the type of COT. However, asymmetric margins will be characterized by a thin layer of melt underplated mostly underneath the wide margin (Figure 6d), while at symmetric conjugate margins the level of magmatic underplating under both sides is similar (Figure 6c).

Margins characterized by strong crust, which leads to more brittle dominated deformation processes, show the onset of serpentinization prior to melting for very slow velocities ($<$ 5 mm/yr half-extension; Figure 4a). These margins are likely to be associated with a COT consisting of exhumed and serpentinized mantle

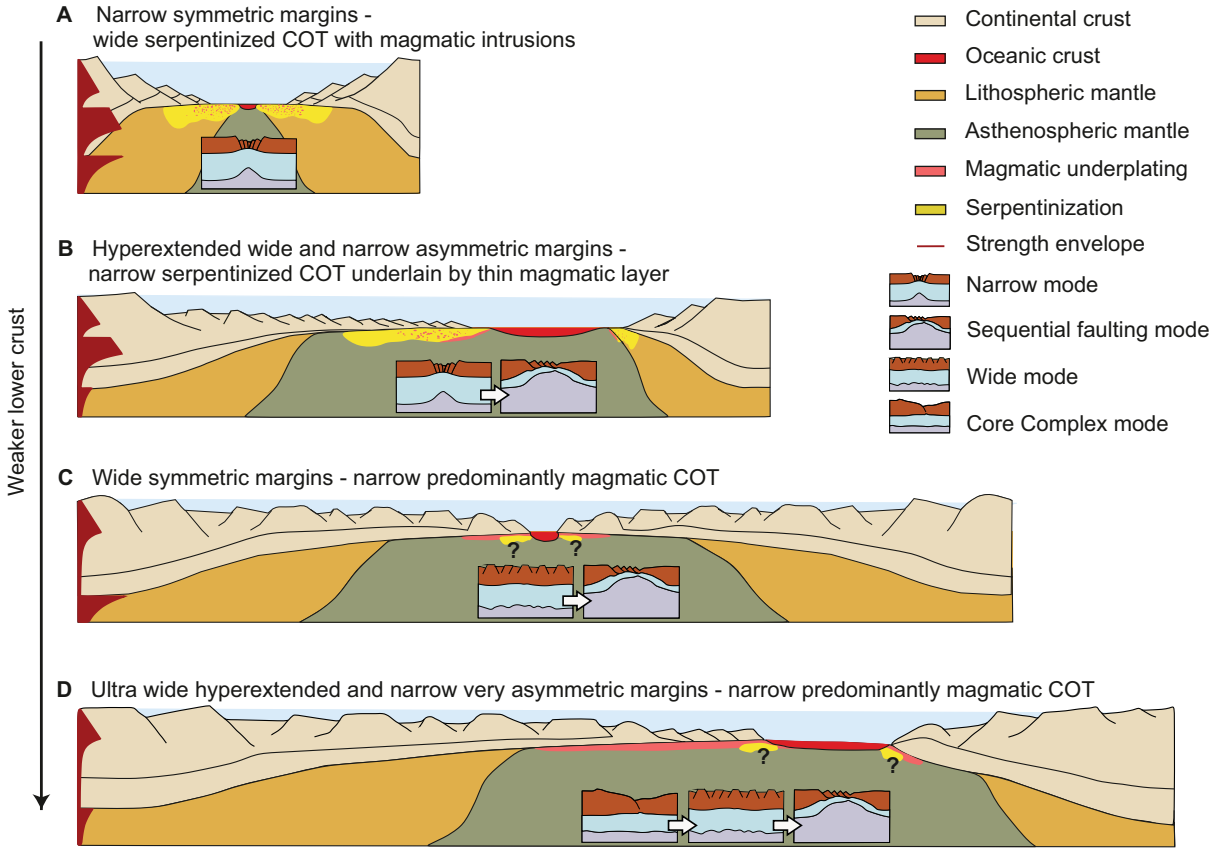

Figure 6. Conceptual model showing the genetic link between tectonic style and COT nature at magma-poor conjugate margins. Cartoons show break-up stage of the models extended by 3 mm/yr. Lower crustal strength ranges from strong (top plot a) to very weak (bottom panel D); (a)Mafic granulite and thin lower crust. (b) Mafic granulite and thick lower crust. (c) Wet quartzite and thin lower crust. (d) Wet quartzite and thick lower crust. Boxes show the mode evolution for each of the tectonic styles.

underplated by a thin layer of melt (Figures 6a and 6b). These margins can be recognized by large fault offsets ($>$ 5 km) defining the shelf break, abrupt crustal thinning, mainly oceanward dipping faults and large syn-rift subsidence. Symmetric margins tend to be narrow because large brittle faults are very effective at thinning the crust and causing quick break-up. Asymmetric margins are formed by tapping into deep levels of weak lower crust which prevents such rapid break-up by faulting and so become typically wider than symmetric ones. The onset of serpentinization occurs later for asymmetric than symmetric margins. Additionally, serpentinization under the thinned crust in asymmetric margins is mainly localized underneath the thinned crust of the wide margin, while it is more uniformly distributed underneath symmetric margins. The time gap between onset of serpentinization and that of melting is smaller for asymmetric margins (Figure 4a). Thus, the exhumed mantle at the COT probably presents more evidence of magmatism and may be narrower for asymmetric than for symmetric margins (Figures 6a and 6b).

In summary, we suggest that in order to understand margin evolution it will be useful to distinguish between margin sections that have gone through extensional modes of core-complex, wide, and narrow modes, since these have characteristic heat-flow and subsidence histories. This, in combination with rift migration accomplished by sequential faulting can explain the degree of asymmetry observed in conjugate margins (Figure 6). Our results support the idea that the development of a hyperextended crust is not necessarily related to the exhumation of lithospheric mantle, as described by Lau et al. (2015) for the East Orphan Basin, Cowie et al. (2017) for the Angolan margin and Evain et al. (2015) for the Santos Basin. Margins that undergo a prolonged phase of wide rifting tend to show a magmatic dominated COT, while those that undergo a dominant narrow extension phase, whether or not in combination with sequential faulting,

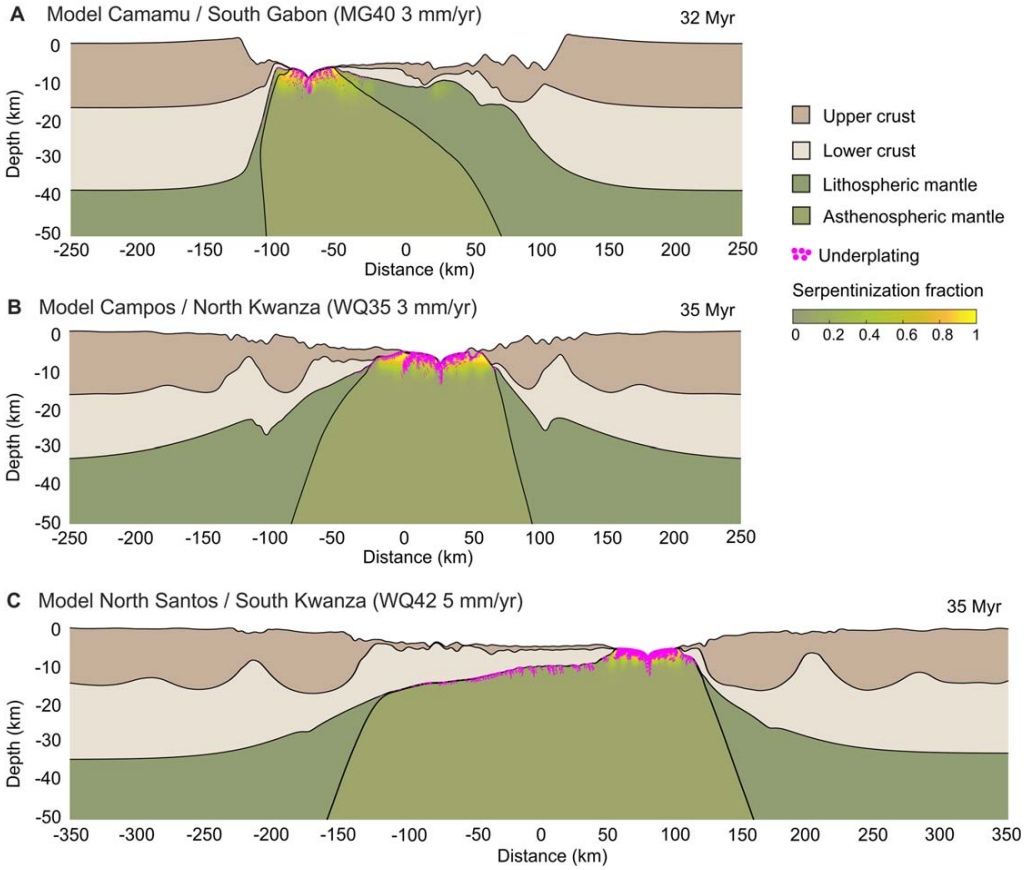

Figure 7. Compilation of the best-fit numerical models reproducing the main characteristics for the three seismic lines of the central South Atlantic segment. (a) Camamu/Gabon model (MG40: Mafic granulite, 40 km crustal thickness and 3 mm/yr extension). (b) Campos/North Kwanza model (WQ35: Wet quartzite, 35 km crustal thickness and 3 mm/yr extension). (c) North Santos/South Kwanza model (WQ42: Wet quartzite, 42 km crustal thickness and 5 mm/yr extension).

and those which extended very slowly ($<$ 5 mm/yr) tend to exhibit a COT consisting of exhumed serpentinized mantle (Figure 6).

5.3. Implications for the Central South Atlantic COTs

As we move southward along our study area, the conjugate margin-pair widths increase, while the continental slope and crustal tapering become gentler, indicating an increasing importance of ductile crustal deformation processes (Figure 2a). This suggests that the original lithosphere in which these margins developed was weaker to the South. The reason for a progressive weakening may either be a change in the lithology and amount of fluids of the lower crust, a thermal weakening in the South associated with the "Tristan da Cunha" plume that is linked to Paraná flood basalts, or a change in the lithospheric strength from the São Francisco craton in the North to the warmer and thinner Ribeira/Kaoko fold belts to the South. In this study we have chosen to reproduce the change in strength by changing only the crustal composition and thickness, as this gives us a good indication of margin tectonic style and COT nature with varying strength.

We have chosen three modeled sections to correlate the main characteristics of the transects shown in our study area (Figures 2 and 7). The Camamu/Gabon interpreted line shows an asymmetric structure with large, oceanward-dipping faults, abrupt crustal tapering, and large syn-rift subsidence, indicative for rifting in a strong crust (Figure 2a). We compare this line to the model with mafic granulite and 40 km crustal thickness extended by 3 mm/yr half-extension velocity (Heine et al., 2013). The initial conditions result in asymmetric conjugate margins with lateral dimensions and patterns of crustal thinning similar to those of the

observed section (Figures 2a and 7a). We suggest that the thinnest crust (< 3–4 km thick) along this conjugate margin transect may be underlain by serpentinized mantle with little magmatism. Serpentinized mantle is more likely to be found underneath the hyper-extended crust of the wide margin (the Gabon side) and the COT may present a narrow zone of exhumed serpentinized mantle (in comparison to the ~200 km of West Iberia, Minshull et al., 2014), with underplated magmatic products. This interpretation agrees with that of Clerc et al. (2017) for the Gabon COT, where their study suggests that it may consist of either be exhumed mantle or proto-oceanic crust, and that of Caixeta et al. (2009) for the Camamu basin who propose the occurrence of mantle exhumation at the COT, based on seismic, gravimetric and magnetometric data.

The model with weak wet quartzite lower crust, 35 km of crustal thickness and half-extension velocity of 3 mm/yr, is compared to the observations of the Campos/North Kwanza conjugate margins (Figures 2b and 7b). The geoseismic transect shows fairly symmetric conjugate margins, a moderate crustal tapering, small fault offsets dipping both land- and oceanward and little syn-rift subsidence, characteristics that are well reproduced by our model. The distal margins in our model show a break-up of the lithosphere mantle prior to upper-crustal break-up, as the Type II models of Huismans and Beaumont (2011, 2014), and the resulting COT is dominated by magma with an abrupt transition to oceanic crust. This interpretation for the COT is similar to the interpretation of the northern Angolan margin from Cowie et al. (2017), who suggested that it is a mix of hyperextended crust and magmatic material in basis of gravity modeling.

Along the North Santos/South Kwanza section the extension velocity is higher than to the North with approximately 5 mm/yr half-extension (Heine et al., 2013). We compare the section in this area (Figure 2c) to a model with wet quartzite lower crust, 42 km crustal thickness and 5 mm/yr (Figure 7c). This model results in a tectonic style quite similar to the case with 40 km crust, wet quartzite lower crust and 3 mm/yr (Figures 3j–3l and supporting information Movie S4). We chose to increase by 2km the input parameter of crustal thickness because the margins that resulted with 40 km were much narrower than those with 3 mm/yr, as the higher velocity led to a quicker localization and break-up. The 42 km crustal thickness is in the range of the onshore estimates for this area (Assumpção et al., 2013). The model results in a hyperextended margin that is 433 km wide and a 272 km wide conjugate, both margins thin from 42 to ~4.5 km. The wide hyperextended margin is slightly narrower than the observed in Santos; we follow other authors and suggest that the very large width of these margins results from a failed spreading center localized between the northern Pelotas Basin and the southern Santos Basin that cannot be reproduced in our 2-D models (Gomes et al., 2002; Mohriak, 2001; Moulin et al., 2013). Our model shows a very weak margin that goes through the extensional modes of core-complex, wide margin and finally rift migration accomplished by sequential faulting, as the lithospheric layers progressively cool and couple. Rifting lasts for a very long period of about 35 Myr, and it is characterized by very little syn-rift subsidence, perhaps providing the necessary conditions for the formation of a large salt basin. Faults are small, mostly dipping ocean- and landward, excluding those areas affected by the sequential faulting phase at the end of rifting. The Santos Basin in our model is underplated along most of its length by melt, while underplating is much less ubiquitous in the conjugate margin (Figure 7c). The COT is predominantly magmatic and the transition to standard oceanic crust is fairly abrupt. Although our result for the COT contrasts with the interpretation from Zalán et al. (2011), who suggested the exhumation of mantle based on the interpretation of multi-channel seismic lines, it coincides with the interpretations from Kumar et al. (2013), Aslanian et al. (2009) and Mohriak et al. (2008), who used the same type of data, and from Evain et al. (2015), who used multichannel and additional wide-angle seismic data to differentiate between various types of COT.

6. Conclusions

The above numerical models have shown different implications for the linkage between tectonic style and COT type of magma-poor conjugate rifted margins. During continental extension, a feedback between the rheology of the lower crust and the extension velocity strongly controls the onset of melting and serpentinization. The more decoupled the crust-mantle system, the greater the delay between the onsets of melting and serpentinization. This delay decreases with increasing extension velocity. Models with slow extension velocity (3 mm/yr) and strong mafic granulite lower crust show serpentinization prior to melting. We suggest that these models will present a COT characterized by exhumed and serpentinized mantle. In contrast, models

with weaker wet quartzite lower crust undergo an earlier onset of melting than serpentinization at all velocities tested here (3, 5 and 10 mm/yr half-extension), suggesting that a magmatically dominated COT would result.

The tectonic style of conjugate rifted margins (pattern of symmetry/asymmetry, margin width, pattern of faulting and subsidence) is strongly influenced by the strength of the lower crust, which confirms the results of previous studies (e.g., Brune et al., 2017; Tetreault & Buiter, 2017). Margin tectonic style can be explained by a combination of core-complex, wide and narrow rifting mode, as suggested by Buck (1991), combined with a fourth extensional mode, rift migration accomplished by sequential faulting (Brune et al., 2014, 2017; Ranero & Pérez-Gussinyé, 2010), which accounts for the observed degree of asymmetry.

The COT nature is linked to the tectonic style through the modes of extension that continental lithosphere undergoes, which in turn depend on the strength of lower crust and extension velocity. Strong lower crust leads to a development of large faults (offsets $> \sim 5$ km) mainly dipping oceanward, abrupt crustal thinning, large syn-rift subsidence and the onset of serpentinization prior to melting, which results in a COT consisting of exhumed and serpentinized mantle. Weaker rheologies decrease the degree of coupling between crust and mantle promoting the generation of small faults (offsets < 5 km) that dip both ocean- and landward, and that induce smooth crustal thinning and minor syn-rift subsidence. This type of deformation delays the onset of serpentinization more than it slows mantle upwelling and melting, so that melting starts before serpentinization at any velocity within the ultra-slow range, and leading to a more magmatic COT.

Our results predict a COT dominated by exhumed serpentinized mantle for strong lower crustal rheologies and slow velocities in the central South Atlantic segment (i.e., Camamu-Gabon conjugate margins) and a more magmatic COT with a rather abrupt transition to oceanic crust for weaker lower crustal rheologies and/or higher extension velocities (i.e., Campos-Kwanza and North Santos-South Kwanza conjugate margins). Therefore, our results show that magma-poor margins can exhibit COTs which lack exhumed and serpentinized mantle at their COT.

Acknowledgments
The authors thank COMPASS for the funding support. Elena Ros is grateful to Albert de Montserrat for his valuable discussions on the topic. We also thank S. Buiter, T. Minshull and L. Lavier for their valuable revisions which helped to improve the paper. The MCS data used in this study are proprietary data from ION-GXT. The data have been published before in several publications indicated in the text.

References

Andrés-Martínez, M., Morgan, J. P., Pérez-Gussinyé, M., & Rüpke, L. (2015). A new free-surface stabilization algorithm for geodynamical modelling: Theory and numerical tests. *Physics of the Earth and Planetary Interiors*, *246*, 41–51.

Araújo, M. N. C., Pérez-Gussinyé, M., & Romeiro, M. A. T. (2015). *A influência da taxa de deformaçao e reologia no estilo estrutural do rifte sul-Atlântico*. Paper presented at 9th International Symposium on Tectonics, Brazilian Geological Society, Salvador, Brazil.

Armitage, J. J., Henstock, T. J., Minshull, T. A., & Hopper, J. R. (2009). Lithospheric controls on melt production during continental breakup at slow rates of extension: Application to the North Atlantic. *Geochemistry, Geophysics, Geosystems*, *10*, Q06018. https://doi.org/10.1029/2009GC002404

Armitage, J. J., Jaupart, C., Fourel, L., & Allen, P. A. (2013). The instability of continental passive margins and its effect on continental topography and heat flow. *Journal of Geophysical Research: Solid Earth*, *118*, 1817–1836. https://doi.org/10.1002/jgrb.50097

Aslanian, D., Moulin, M., Olivet, J. L., Unternehr, P., Matias, L., Bache, F., . . . Labails, C. (2009). Brazilian and African passive margins of the Central Segment of the South Atlantic Ocean: Kinematic constraints. *Tectonophysics*, *468*(1), 98–112.

Assumpção, M., Bianchi, M., Julià, J., Dias, F. L., França, G. S., Nascimento, R., . . . Lopes, A. E. (2013). Crustal thickness map of Brazil: Data compilation and main features. *Journal of South American Earth Sciences*, *43*, 74–85.

Autin, J., Leroy, S., Beslier, M. O., D'acremont, E., Razin, P., Ribodetti, A., . . . Al Toubi, K. (2010). Continental break-up history of a deep magma-poor margin based on seismic reflection data (northeastern Gulf of Aden margin, offshore Oman). *Geophysical Journal International*, *180*(2), 501–519.

Bassi, G. (1991). Factors controlling the style of continental rifting: Insights from numerical modelling. *Earth and Planetary Science Letters*, *105*(4), 430–452.

Bassi, G. (1995). Relative importance of strain rate and rheology for the mode of continental extension. *Geophysical Journal International*, *122*(1), 195–210.

Bassi, G., Keen, C. E., & Potter, P. (1993). Contrasting styles of rifting: Models and examples from the eastern Canadian margin. *Tectonics*, *12*(3), 639–655.

Bayrakci, G., Minshull, T. A., Sawyer, D. S., Reston, T. J., Klaeschen, D., Papenberg, C., & Perez-Gussinye, M. (2016). Fault-controlled hydration of the upper mantle during continental rifting. *Nature Geoscience*, *9*(5), 384–388.

Beard, J. S., & Hopkinson, L. (2000). A fossil, serpentinization-related hydrothermal vent, Ocean Drilling Program Leg 173, Site 1068 (Iberia Abyssal Plain): Some aspects of mineral and fluid chemistry. *Journal of Geophysical Research*, *105*(B7), 16527–16539.

Beaumont, C., & Ings, S. J. (2012). Effect of depleted continental lithosphere counterflow and inherited crustal weakness on rifting of the continental lithosphere: General results. *Journal of Geophysical Research*, *117*, B08407. https://doi.org/10.1029/2012JB009203

Bird, D. E., & Hall, S. A. (2016). Early seafloor spreading in the South Atlantic: New evidence for M-series magnetochrons north of the Rio Grande Fracture Zone. *Geophysical Journal International*, *206*(2), 835–844.

Blaich, O. A., Faleide, J. I., & Tsikalas, F. (2011). Crustal breakup and continent-ocean transition at South Atlantic conjugate margins. *Journal of Geophysical Research*, *116*, B01402. https://doi.org/10.1029/2010JB007686

Blaich, O. A., Faleide, J. I., Tsikalas, F., Lilletveit, R., Chiossi, D., Brockbank, P., & Cobbold, P. (2010). January). Structural architecture and nature of the continent-ocean transitional domain at the Camamu and Almada Basins (NE Brazil) within a conjugate margin setting. In *Geological Society, London, Petroleum geology conference series* (Vol. 7, No. 1, pp. 867–883). London, UK: Geological Society of London.

Boillot, G., Winterer, E. L., Meyer, A. W., et al. (1987). In *Proceedings of the Ocean Drilling Program, initial reports* (Vol. 103). College Station, TX: Ocean Drilling Program. https://doi.org/10.2973/odp.proc.ir.103.1987

Bos, B., & Spiers, C. J. (2002). Frictional-viscous flow of phyllosilicate-bearing fault rock: Microphysical model and implications for crustal strength profiles. *Journal of Geophysical Research*, *107*(B2), 2028. https://doi.org/10.1029/2001JB000301
Bown, J. W., & White, R. S. (1995). Effect of finite extension rate on melt generation at rifted continental margins. *Journal of Geophysical Research*, *100*(B9), 18011–18029.
Brune, S., Heine, C., Clift, P. D., & Pérez-Gussinyé, M. (2017). Rifted margin architecture and crustal rheology: Reviewing Iberia-Newfoundland, Central South Atlantic, and South China Sea. *Marine and Petroleum Geology*, *79*, 257–281.
Brune, S., Heine, C., Pérez-Gussinyé, M., & Sobolev, S. V. (2014). Rift migration explains continental margin asymmetry and crustal hyper-extension. *Nature Communications*, *5*.
Buck, W. R. (1991). Modes of continental lithospheric extension. *Journal of Geophysical Research*, *96*(B12), 20161–20178.
Buck, W. R., & Lavier, L. L. (2001). A tale of two kinds of normal fault: The importance of strain weakening in fault development. *Geological Society, Special Publications*, *187*(1), 289–303.
Buck, W. R., & Poliakov, A. N. (1998). Abyssal hills formed by stretching oceanic lithosphere. *Nature*, *392*(6673), 272–275.
Buiter, S. J., Huismans, R. S., & Beaumont, C. (2008). Dissipation analysis as a guide to mode selection during crustal extension and implications for the styles of sedimentary basins. *Journal of Geophysical Research*, *113*, B06406. https://doi.org/10.1029/2007JB005272
Burov, E. B. (2011). Rheology and strength of the lithosphere. *Marine and Petroleum Geology*, *28*(8), 1402–1443.
Caixeta, J. M., Ferreira, T. S., Lima, F. D., Francisco, C., & Dias, A. (2009). APPG International Conference & Exhibition (15–18 November 2009, Rio de Janeiro, Brazil), Diachronous rift system along Bahia State coast: An example of extended crust and mantle exhumation in the South Atlantic Ocean. AAPG Search and Discovery Article #90100.
Cannat, M., Manatschal, G., Sauter, D., & Peron-Pinvidic, G. (2009). Assessing the conditions of continental breakup at magma-poor rifted margins: What can we learn from slow spreading mid-ocean ridges? *Comptes Rendus Geoscience*, *341*(5), 406–427.
Chian, D. P., Louden, K. E., Minshull, T. A., & Whitmarsh, R. B. (1999). Deep structure of the ocean-continent transition in the southern Iberia Abyssal Plain from seismic refraction profiles: Ocean Drilling Program (Legs 149 and 173) transect. *Journal of Geophysical Research*, 104(B4), 7443–7462.
Clerc, C., Ringenbach, J. C., Jolivet, L., & Ballard, J. F. (2017). Rifted margins: Ductile deformation, boudinage, continentward-dipping normal faults and the role of the weak lower crust. *Gondwana Research*. https://doi.org/10.1016/j.gr.2017.04.030, in press.
Cowie, L., Angelo, R. M., Kusznir, N., Manatschal, G., & Horn, B. (2017). Structure of the ocean–continent transition, location of the continent–ocean boundary and magmatic type of the northern Angolan margin from integrated quantitative analysis of deep seismic reflection and gravity anomaly data. *Geological Society, Special Publications*, *438*(1), 159–176.
Currie, C. A., & Hyndman, R. D. (2006). The thermal structure of subduction zone back arcs. *Journal of Geophysical Research*, *111*, B08404. https://doi.org/10.1029/2005JB004024
Dabrowski, M., Krotkiewski, M., & Schmid, D. W. (2008). MILAMIN: MATLAB-based finite element method solver for large problems. *Geochemistry, Geophysics, Geosystems*, *9*, Q04030. https://doi.org/10.1029/2007GC001719
De Bresser, J., Ter Heege, J., & Spiers, C. (2001). Grain size reduction by dynamic recrystallization: Can it result in major rheological weakening?. *International Journal of Earth Sciences*, *90*(1), 28–45.
Dick, H. J., Lin, J., & Schouten, H. (2003). An ultraslow-spreading class of ocean ridge. *Nature*, *426*(6965), 405–412.
Direen, N. G., Borissova, I., Stagg, H. M. J., Colwell, J. B., & Symonds, P. A. (2007). Nature of the continent–ocean transition zone along the southern Australian continental margin: A comparison of the Naturaliste Plateau, SW Australia, and the central Great Australian Bight sectors. *Geological Society, Special Publications*, *282*(1), 239–263.
Direen, N. G., Stagg, H. M., Symonds, P. A., & Norton, I. O. (2013). Variations in rift symmetry: Cautionary examples from the Southern Rift System (Australia–Antarctica). *Geological Society, Special Publications*, *369*(1), 453–475.
Dunbar, J. A., & Sawyer, D. S. (1989). How preexisting weaknesses control the style of continental breakup. *Journal of Geophysical Research*, *94*(B6), 7278–7292.
Eagles, G. (2007). New angles on South Atlantic opening. *Geophysical Journal International*, *168*(1), 353–361.
Eagles, G., Pérez-Díaz, L., & Scarselli, N. (2015). Getting over continent ocean boundaries. *Earth-Science Reviews*, *151*, 244–265.
Emmanuel, S., & Berkowitz, B. (2006). Suppression and stimulation of seafloor hydrothermal convection by exothermic mineral hydration. *Earth and Planetary Science Letters*, *243*(3), 657–668.
Escartin, J., Hirth, G., & Evans, B. (1997). Effects of serpentinization on the lithospheric strength and the style of normal faulting at slow-spreading ridges. *Earth and Planetary Science Letters*, *151*(3–4), 181–189.
Evain, M., Afilhado, A., Rigoti, C., Loureiro, A., Alves, D., Klingelhoefer, F., . . . Lima, M. V. (2015). Deep structure of the Santos Basin-São Paulo Plateau System, SE Brazil. *Journal of Geophysical Research: Solid Earth*, *120*, 5401–5431. https://doi.org/10.1002/2014JB011561
Feng, M., Van der Lee, S., & Assumpção, M. (2007). Upper mantle structure of South America from joint inversion of waveforms and fundamental mode group velocities of Rayleigh waves. *Journal of Geophysical Research*, *112*, B04312. https://doi.org/10.1029/2006JB004449
Ferreira, T. S., Caixeta, J. M., & Lima, F. D. (2009). Controle do embasamento no rifteamento das bacias de Camamu e Almada. *Boletim De Geociências Da Petrobras, Rio De Janeiro*, *17*(1), 69–88.
Gleason, G. C., & Tullis, J. (1995). A flow law for dislocation creep of quartz aggregates determined with the molten salt cell. *Tectonophysics*, *247*(1), 1–23.
Gomes, P. O., Parry, J., & Martins, W. (2002). September). The outer high of the Santos Basin, southern Sao Paulo Plateau, Brazil: Tectonic setting, relation to volcanic events and some comments on hydrocarbon potential. In *AAPG Hedberg Conference on hydrocarbon habitat of volcanic rifted passive margins* (pp. 8–11). American Association of Petroleum Gelogists.
Groupe Galice (1979). The continental margin off Galicia and Portugal: Acoustical stratigraphy, dredge stratigraphy, and structural evolution, *Initial Reports Deep Sea Drilling Project*, *47*(Part 2), 633–662.
Gudmundsson, A. (1990). Emplacement of dikes, sills and crustal magma chambers at divergent plate boundaries. *Tectonophysics*, *176*(3–4), 257–275.
Gudmundsson, A. (2011). Deflection of dykes into sills at discontinuities and magma-chamber formation. *Tectonophysics*, *500*(1), 50–64.
Heilbron, M., Valeriano, C. M., Tassinari, C. C. G., Almeida, J., Tupinambá, M., Siga, O., & Trouw, R. (2008). Correlation of Neoproterozoic terranes between the Ribeira Belt, SE Brazil and its African counterpart: Comparative tectonic evolution and open questions. *Geological Society, Special Publications*, *294*(1), 211–237.
Heine, C., Zoethout, J., & Müller, R. D. (2013). Kinematics of the South Atlantic rift. *Solid Earth*, *4*(2), 215–253.
Hirth, G., & Kohlstedt, D. (2003). Rheology of the upper mantle and the mantle wedge: A view from the experimentalists. In J. Eiler (Ed.), *Inside the Subduction Factory* (pp. 83–105). Washington, DC: American Geophysical Union.
Hirth, G., & Kohlstedt, D. L. (1996). Water in the oceanic upper mantle: Implications for rheology, melt extraction and the evolution of the lithosphere. *Earth and Planetary Science Letters*, *144*(1–2), 93–108.

Hopper, J. R., & Buck, W. R. (1996). and passive margin formation. *Journal of Geophysical Research*, *101*(B9), 20–175.
Huismans, R., & Beaumont, C. (2011). Depth-dependent extension, two-stage breakup and cratonic underplating at rifted margins. *Nature*, *473*(7345), 74–78.
Huismans, R. S., & Beaumont, C. (2002). Asymmetric lithospheric extension: The role of frictional plastic strain softening inferred from numerical experiments. *Geology*, *30*(3), 211–214.
Huismans, R. S., & Beaumont, C. (2014). Rifted continental margins: The case for depth-dependent extension. *Earth and Planetary Science Letters*, *407*, 148–162.
Ito, G., Lin, J., & Gable, C. W. (1996). Dynamics of mantle flow and melting at a ridge-centered hotspot: Iceland and the Mid-Atlantic Ridge. *Earth and Planetary Science Letters*, *144*(1–2), 53–74.
Iyer, K. (2007). *Mechanisms of serpentinization and some geochemical effects* (Doctoral dissertation). Oslo, Norway: University of Oslo.
Jokat, W., Ritzmann, O., Schmidt-Aursch, M. C., Drachev, S., Gauger, S., & Snow, J. (2003). Geophysical evidence for reduced melt production on the Arctic ultraslow Gakkel mid-ocean ridge. *Nature*, *423*(6943), 962–965.
Katayama, I., Hirauchi, K. I., Michibayashi, K., & Ando, J. I. (2009). Trench-parallel anisotropy produced by serpentine deformation in the hydrated mantle wedge. *Nature*, *461*(7267), 1114–1117.
Kaus, B. J., Mühlhaus, H., & May, D. A. (2010). A stabilization algorithm for geodynamic numerical simulations with a free surface. *Physics of the Earth and Planetary Interiors*, *181*(1), 12–20.
Kawano, S., Katayama, I., & Okazaki, K. (2011). Permeability anisotropy of serpentinite and fluid pathways in a subduction zone. *Geology*, *39*(10), 939–942.
Klein, F., Humphris, S. E., Guo, W., Schubotz, F., Schwarzenbach, E. M., & Orsi, W. D. (2015). Fluid mixing and the deep biosphere of a fossil Lost City-type hydrothermal system at the Iberia Margin. *Proceedings of the National Academy of Sciences United States of America*, *112*(39), 12036–12041.
Kumar, N., Danforth, A., Nuttall, P., Helwig, J., Bird, D. E., & Venkatraman, S. (2013). From oceanic crust to exhumed mantle: A 40 year (1970–2010) perspective on the nature of crust under the Santos Basin, SE Brazil. *Geological Society, Special Publications*, *369*(1), 147–165.
Lau, K. H., Watremez, L., Louden, K. E., & Nedimović, M. R. (2015). Structure of thinned continental crust across the Orphan Basin from a dense wide-angle seismic profile and gravity data. *Geophysical Journal International*, *202*(3), 1969–1992.
Lavecchia, A., Thieulot, C., Beekman, F., Cloetingh, S., & Clark, S. (2017). Lithosphere erosion and continental breakup: Interaction of extension, plume upwelling and melting. *Earth and Planetary Science Letters*, *467*, 89–98.
Lavier, L. L., Buck, W. R., & Poliakov, A. N. (1999). Self-consistent rolling-hinge model for the evolution of large-offset low-angle normal faults. *Geology*, *27*(12), 1127–1130.
Lavier, L. L., & Manatschal, G. (2006). A mechanism to thin the continental lithosphere at magma-poor margins. *Nature*, *440*(7082), 324–328.
Lemoine, M., Bas, T., Arnaud-Vanneau, A., Arnaud, H., Dumont, T., Gidon, M., . . . Tricart, P. (1986). The continental margin of the Mesozoic Tethys in the Western Alps. *Marine and Petroleum Geology*, *3*(3), 179–199.
Lentini, M. R., Fraser, S. I., Sumner, H. S., & Davies, R. J. (2010). Geodynamics of the central South Atlantic conjugate margins: Implications for hydrocarbon potential. *Petroleum Geoscience*, *16*(3), 217–229.
Lu, G., Kaus, B. J., & Zhao, L. (2011). Thermal localization as a potential mechanism to rift cratons. *Physics of the Earth and Planetary Interiors*, *186*(3), 125–137.
Macdonald, A. H., & Fyfe, W. S. (1985). Rate of serpentinization in seafloor environments. *Tectonophysics*, *116*(1–2), 123–135.
Malvern, L. E. (1969). *Introduction to the mechanics of a continuous medium* (monograph).
Manatschal, G. (2004). New models for evolution of magma-poor rifted margins based on a review of data and concepts from West Iberia and the Alps. *International Journal of Earth Sciences*, *93*(3), 432–466.
Manatschal, G., & Müntener, O. (2009). A type sequence across an ancient magma-poor ocean-continent transition: The example of the western Alpine Tethys ophiolites. *Tectonophysics*, *473*, 4–19.
Masini, E., Manatschal, G., & Mohn, G. (2012b). The Alpine Tethys rifted margins: Reconciling old and new ideas to understand the stratigraphic architecture of magma-poor rifted margins. *Sedimentology*, *60*(1), 174–196.
Mathieu, L., De Vries, B. V. W., Holohan, E. P., & Troll, V. R. (2008). Dykes, cups, saucers and sills: Analogue experiments on magma intrusion into brittle rocks. *Earth and Planetary Science Letters*, *271*(1), 1–13.
Minshull, T. A. (2009). Geophysical characterisation of the ocean–continent transition at magma-poor rifted margins. *Comptes Rendus Geoscience*, *341*(5), 382–393.
Minshull, T. A., Dean, S. M., White, R. S., & Whitmarsh, R. B. (2001). Anomalous melt production after continental break-up in the southern Iberia Abyssal Plain. *Geological Society, Special Publications*, *187*(1), 537–550.
Minshull, T. A., Dean, S. M., & Whitmarsh, R. B. (2014). The peridotite ridge province in the southern Iberia Abyssal Plain: Seismic constraints revisited. *Journal of Geophysical Research: Solid Earth*, *119*, 1580–1598. https://doi.org/10.1002/2014JB011011
Mohn, G., Manatschal, G., Beltrando, M., Masini, E., & Kusznir, N. (2012). Necking of continental crust in magma-poor rifted margins: Evidence from the fossil Alpine Tethys margins. *Tectonics*, *31*, TC1012. https://doi.org/10.1029/2011TC002961
Mohn, G., Manatschal, G., Müntener, O., Beltrando, M., & Masini, E. (2010). Unravelling the interaction between tectonic and sedimentary processes during lithospheric thinning in the Alpine Tethys margins. *International Journal of Earth Sciences*, *99*(1), 75–101.
Mohriak, W., Nemčok, M., & Enciso, G. (2008). South Atlantic divergent margin evolution: Rift-border uplift and salt tectonics in the basins of SE Brazil. *Geological Society, Special Publications*, *294*(1), 365–398.
Mohriak, W. U. (2001, October). South Atlantic ocean salt tectonics, volcanic centers, fracture zones and their relationship with the origin and evolution of the South Atlantic Ocean: Geophysical evidence in the Brazilian and West African Margins. In *7th International Congress of the Brazilian Geophysical Society*.
Mohriak, W. U., Szatmari, P., & Anjos, S. (2012). Salt: Geology and tectonics of selected Brazilian basins in their global context. *Geological Society, Special Publications*, *363*(1), 131–158.
Morgan, J. P. (1987). Melt migration beneath mid-ocean spreading centers. *Geophysical Research Letters*, *14*(12), 1238–1241.
Morgan, J. P. (1997). The generation of a compositional lithosphere by mid-ocean ridge melting and its effect on subsequent off-axis hotspot upwelling and melting. *Earth and Planetary Science Letters*, *146*(1–2), 213–232.
Morgan, J. P. (2001). Thermodynamics of pressure release melting of a veined plum pudding mantle. *Geochemistry, Geophysics, Geosystems*, *2*(4), 1001. https://doi.org/10.1029/2000GC000049
Moulin, M., Aslanian, D., Rabineau, M., Patriat, M., & Matias, L. (2013). Kinematic keys of the Santos–Namibe basins. *Geological Society, Special Publications*, *369*(1), 91–107.
Müntener, O., Hermann, J., & Trommsdorff, V. (2000). Cooling history and exhumation of lower-crustal granulite and upper mantle (Malenco, Eastern Central Alps). *Journal of Petrology*, *41*(2), 175–200.

Nagel, T. J., & Buck, W. R. (2004). Symmetric alternative to asymmetric rifting models. *Geology*, *32*(11), 937–940.
Naliboff, J., & Buiter, S. J. (2015). Rift reactivation and migration during multiphase extension. *Earth and Planetary Science Letters*, *421*, 58–67.
ODP Leg 173 Shipboard Scientific Party (1998). Drilling reveals transition from continental breakup to early magmatic crust. *Eos, Transactions American Geophysical Union*, *79*(173), 180–181.
Osmundsen, P. T., & Ebbing, J. (2008). Styles of extension offshore mid-Norway and implications for mechanisms of crustal thinning at passive margins. *Tectonics*, *27*, TC6016. https://doi.org/10.1029/2007TC002242
Pérez-Díaz, L., & Eagles, G. (2014). Constraining South Atlantic growth with seafloor spreading data. *Tectonics*, *33*, 1848–1873. https://doi.org/10.1002/2014TC003644
Pérez-Gussinyé, M., Lowry, A. R., & Watts, A. B. (2007). Effective elastic thickness of South America and its implications for intracontinental deformation. *Geochemistry, Geophysics, Geosystems*, *8*, Q05009. https://doi.org/10.1029/2006GC001511
Pérez-Gussinyé, M., Metois, M., Fernández, M., Vergés, J., Fullea, J., & Lowry, A. R. (2009). Effective elastic thickness of Africa and its relationship to other proxies for lithospheric structure and surface tectonics. *Earth and Planetary Science Letters*, *287*(1), 152–167.
Pérez-Gussinyé, M., Morgan, J. P., Reston, T. J., & Ranero, C. R. (2006). The rift to drift transition at non-volcanic margins: Insights from numerical modelling. *Earth and Planetary Science Letters*, *244*(1), 458–473.
Pérez-Gussinyé, M., & Reston, T. J. (2001). Rheological evolution during extension at nonvolcanic rifted margins: Onset of serpentinization and development of detachments leading to continental breakup. *Journal of Geophysical Research*, *106*(B3), 3961–3975.
Peron-Pinvidic, G., Manatschal, G., Masini, E., Sutra, E., Flament, J. M., Haupert, I., & Unternehr, P. (2017). Unravelling the along-strike variability of the Angola–Gabon rifted margin: A mapping approach. *Geological Society, Special Publications*, *438*(1), 49–76.
Péron-Pinvidic, G., Manatschal, G., Minshull, T. A., & Sawyer, D. S. (2007). Tectonosedimentary evolution of the deep Iberia-Newfoundland margins: Evidence for a complex breakup history. *Tectonics*, *26*, TC2011. https://doi.org/10.1029/2006TC001970
Pinto, V. H. G., Manatschal, G., Karpoff, A. M., Ulrich, M., & Viana, A. R. (2017). Seawater storage and element transfer associated with mantle serpentinization in magma-poor rifted margins: A quantitative approach. *Earth and Planetary Science Letters*, *459*, 227–237.
Pinto, V. H. G., Manatschal, G., Karpoff, A. M., & Viana, A. (2015). Tracing mantle-reacted fluids in magma-poor rifted margins: The example of Alpine Tethyan rifted margins. *Geochemistry, Geophysics, Geosystems*, *16*, 3271–3308. https://doi.org/10.1002/2015GC005830
Précigout, J., & Gueydan, F. (2009). Mantle weakening and strain localization: Implications for the long-term strength of the continental lithosphere. *Geology*, *37*(2), 147–150.
Ranalli, G. (1995). *Rheology of the earth*. the Netherlands: Springer Science and Business Media.
Ranalli, G., & Murphy, D. C. (1987). Rheological stratification of the lithosphere. *Tectonophysics*, *132*(4), 281–295.
Ranero, C. R., & Pérez-Gussinyé, M. (2010). Sequential faulting explains the asymmetry and extension discrepancy of conjugate margins. *Nature*, *468*(7321), 294–299.
Reston, T. J. (2009). The structure, evolution and symmetry of the magma-poor rifted margins of the North and Central Atlantic: A synthesis. *Tectonophysics*, *468*(1), 6–27.
Reston, T. J., Krawczyk, C. M., & Klaeschen, D. (1996). The S reflector west of Galicia (Spain): Evidence from prestack depth migration for detachment faulting during continental breakup. *Journal of Geophysical Research*, *101*(B4), 8075–8091.
Rüpke, L., Phipps Morgan, J., & Eaby Dixon, J. (2006). Implications of subduction rehydration for earth's deep water cycle. In S. D. Jacobsen & S. Van Der Lee (Eds.), *Earth's deep water cycle* (pp. 263–276). Washington, DC: American Geophysical Union.
Russell, S. M., & Whitmarsh, R. B. (2003). Magmatism at the west Iberia non-volcanic rifted continental margin: Evidence from analyses of magnetic anomalies. *Geophysical Journal International*, *154*(3), 706–730.
Sawyer, D. S., Whitmarsh, R. B., Klaus, A., et al. (1994). In *Proceedings of Ocean Drilling Program, initial reports* (Vol. 149). College Station, TX: Ocean Drilling Program. https://doi.org/10.2973/odp.proc.ir.149.1994
Sawyer, D. S., Coffin, M. F., Reston, T. J., Stock, J. M., & Hopper, J. R. (2007). COBBOOM: The continental breakup and birth of oceans mission. *Scientific Drilling*, *5*, 13–25.
Schmeling, H. (2010). Dynamic models of continental rifting with melt generation. *Tectonophysics*, *480*(1), 33–47.
Schrenk, M. O., Brazelton, W. J., & Lang, S. Q. (2013). Serpentinization, carbon, and deep life. *Reviews in Mineralogy and Geochemistry*, *75*(1), 575–606.
Sharples, W., Moresi, L. N., Jadamec, M. A., & Revote, J. (2015). Styles of rifting and fault spacing in numerical models of crustal extension. *Journal of Geophysical Research: Solid Earth*, *120*, 4379–4404. https://doi.org/10.1002/2014JB011813
Sibuet, J. C., Srivastava, S., & Manatschal, G. (2007). Exhumed mantle-forming transitional crust in the Newfoundland-Iberia rift and associated magnetic anomalies. *Journal of Geophysical Research*, *112*, B06105. https://doi.org/10.1029/2005JB003856
Sibuet, J. C., & Tucholke, B. E. (2013). The geodynamic province of transitional lithosphere adjacent to magma-poor continental margins. *Geological Society, Special Publications*, *369*(1), 429–452.
Simon, K., Huismans, R. S., & Beaumont, C. (2009). Dynamical modelling of lithospheric extension and small-scale convection: Implications for magmatism during the formation of volcanic rifted margins. *Geophysical Journal International*, *176*(1), 327–350.
Skelton, A., Whitmarsh, R., Arghe, F., Crill, P., & Koyi, H. (2005). Constraining the rate and extent of mantle serpentinization from seismic and petrological data: Implications for chemosynthesis and tectonic processes. *Geofluids*, *5*(3), 153–164.
Sotin, C., & Parmentier, E. M. (1989). Dynamical consequences of compositional and thermal density stratification beneath spreading centers. *Geophysical Research Letters*, *16*(8), 835–838.
Svartman Dias, A. E., Lavier, L. L., & Hayman, N. W. (2015). Conjugate rifted margins width and asymmetry: The interplay between lithospheric strength and thermomechanical processes. *Journal of Geophysical Research: Solid Earth*, *120*, 8672–8700. https://doi.org/10.1002/2015JB012074
Taylor, B., Goodliffe, A. M., & Martinez, F. (1999). How continents break up: Insights from Papua New Guinea. *Journal of Geophysical Research*, *104*(B4), 7497–7512.
Tetreault, J. L., & Buiter, S. J. H. (2017). The influence of extension rate and crustal rheology on the evolution of passive margins from rifting to break-up. *Tectonophysics*.
Thybo, H., & Artemieva, I. M. (2013). Moho and magmatic underplating in continental lithosphere. *Tectonophysics*, *609*, 605–619.
Tirel, C., Brun, J. P., & Burov, E. (2008). Dynamics and structural development of metamorphic core complexes. *Journal of Geophysical Research*, *113*, B04403. https://doi.org/10.1029/2005JB003694
Tucholke, B. E., Sawyer, D. S., & Sibuet, J. C. (2007). Breakup of the Newfoundland–Iberia rift. *Geological Society, Special Publications*, *282*(1), 9–46.
Tucholke, B. E., & Sibuet, J. C. (2007). Leg 210 synthesis: Tectonic, magmatic, and sedimentary evolution of the Newfoundland-Iberia rift. In *Proceedings of the Ocean Drilling Program, scientific results* (Vol. 210, pp. 1–56). College Station, TX: Ocean Drilling Program.
Unternehr, P., Péron-Pinvidic, G., Manatschal, G., & Sutra, E. (2010). Hyper-extended crust in the South Atlantic: In search of a model. *Petroleum Geoscience*, *16*(3), 207–215.

Welford, J. K., Hall, J., Sibuet, J. C., & Srivastava, S. P. (2010). Structure across the northeastern margin of Flemish Cap, offshore Newfoundland from Erable multichannel seismic reflection profiles: Evidence for a transtensional rifting environment. *Geophysical Journal International*, *183*(2), 572–586.

White, R. S., Minshull, T. A., Bickle, M. J., & Robinson, C. J. (2001). Melt generation at very slow-spreading oceanic ridges: Constraints from geochemical and geophysical data. *Journal of Petrology*, *42*(6), 1171–1196.

Whitmarsh, R. B., Beslier, M.-O., Wallace, P. J., et al. (1998). In *Proceedings of Ocean Drilling Program, initial reports* (Vol. 173). College Station, TX: Ocean Drilling Program. https://doi.org/10.2973/odp.proc.ir.173.1998

Whitmarsh, R. B., & Miles, P. R. (1995). Models of the development of the West Iberia rifted continental margin at 40° 30′ N deduced from surface and deep-tow magnetic anomalies. *Journal of Geophysical Research*, *100*(B3), 3789–3806.

Whitmarsh, R. B., White, R. S., Horsefield, S. J., Sibuet, J. C., Recq, M., & Louvel, V. (1996). The ocean-continent boundary off the western continental margin of Iberia: Crustal structure west of Galicia Bank. *Journal of Geophysical Research*, *101*(B12), 28291–28314.

Wijns, C., Weinberg, R., Gessner, K., & Moresi, L. (2005). Mode of crustal extension determined by rheological layering. *Earth and Planetary Science Letters*, *236*(1), 120–134.

Wilks, K. R., & Carter, N. L. (1990). Rheology of some continental lower crustal rocks. *Tectonophysics*, *182*(1–2), 57–77.

Zalán, P. V., Severino, M. D. C. G., Rigoti, C. A., Magnavita, L. P., Oliveira, J. A. B., & Vianna, A. R. (2011). An entirely new 3D-view of the crustal and mantle structure of a South Atlantic passive margin–Santos, Campos and Espírito Santo Basins, Brazil. In *AAPG annual conference and Exhibition* (pp. 10–13). Tulsa, OK: American association of Petroleum Geologists.

Geochemistry, Geophysics, Geosystems

Supporting Information for

Lower crustal strength controls on melting and serpentinization at magma-poor margins: potential implications for the South Atlantic

Elena Ros[1], Marta Pérez-Gussinyé[2], Mario Araújo[3], Marco Thoaldo Romeiro[3], Miguel Andrés-Martínez[2], Jason P. Morgan[1]

[1]COMPASS, Department of Earth Sciences, Royal Holloway University of London, Egham UK.

[2]MARUM – Center for Marine Environmental Sciences, University of Bremen, Germany.

[3]Petrobras R&D Center, Horácio Macedo Avenue, Rio de Janeiro-RJ, Brazil.

Contents of this file

Additional Supporting Information (Files uploaded separately)

Movie S1. Evolution of the numerical model with mafic granulite lower crust, 35 km crustal thickness and 3 mm/yr half-extension velocity.
Movie S2. Evolution of the numerical model with mafic granulite lower crust, 40 km crustal thickness and 3 mm/yr half-extension velocity.
Movie S3. Evolution of the numerical model wet quartzite lower crust, 35 km crustal thickness and 3 mm/yr half-extension velocity.
Movie S4. Evolution of the numerical model wet quartzite lower crust, 40 km crustal thickness and 3 mm/yr half-extension velocity.
Movie S5. Comparison of the numerical models evolution MG35 and WQ40 (3 mm/yr half-extension).

Introduction

The supplementary information provides a further description of our 2D numerical model and initial rheological and thermal conditions. We provide 4 supporting figures illustrating the modelling of melting and serpentinization and examples of additional numerical models. We also include 5 supporting movies that show the evolution of the numerical models at 3 mm/yr half-extension velocity.

Text S1. Numerical model

The thermo-mechanical numerical models solve the conservation equations of mass, momentum and energy for an incompressible Stokes flow, respectively

$$\frac{\partial v_i}{\partial x_i} = 0 \quad . (1)$$

$$\frac{\partial \sigma_{ij}}{\partial x_j} + \rho g_i = 0 \quad . (2)$$

$$\rho C_p \frac{DT}{Dt} = \kappa \frac{\partial^2 T}{\partial x_i^2} + H + H_s \quad . (3)$$

where v_i are the velocity components, σ_{ij} is the Cauchy stress tensor, g_i is the gravitational acceleration, x_i are the spatial coordinates, ρ is the density, C_p is the heat capacity at constant pressure, T is the temperature, $\frac{DT}{dt}$ is the Lagrangian time derivative of temperature, κ is the thermal conductivity, H is the volumetric radioactive heat production and H_s is the heat dissipation form the non-elastic deformation, i.e. shear heating. Shear heating H_s increases the temperature within shear zones, thus reducing the strength of the shear zone compared to that of the surrounding rocks. Hence, this weakening process is important for the localization of shear zones (Ranalli & Murphy, 1987; Lu et al., 2011).

Text S2. Rheological laws

We assume a visco-elasto-plastic behavior with the additive decomposition of the deviatoric strain into

$$\dot{\varepsilon}'_{ij} = \dot{\varepsilon}'^{visc}_{ij} + \dot{\varepsilon}'^{el}_{ij} + \dot{\varepsilon}'^{pl}_{ij} = \frac{\sigma'_{ij}}{2\eta} + \frac{1}{2\mu}\frac{D\sigma'_{ij}}{Dt} + \dot{\gamma}\frac{\partial G}{\partial \sigma'_{ij}} \quad . (4)$$

where $\dot{\varepsilon}'_{ij}$ is the deviatoric strain rate tensor, η is the viscosity, $\sigma'_{ij}$is the deviatoric stress tensor, μ is the elastic shear modulus, $\frac{D\sigma'_{ij}}{Dt}$ is the Lagrangian time derivative of stress, $\dot{\gamma}$ is the plastic multiplier and G is the plastic potential function. We adopt a non-associative, Prandtl-Reuss flow law, where the second invariant of the stress is taken as the plastic potential function.
Viscosity is limited by dislocation and diffusion creep. The viscosity in the model is defined by the general equation

$$\eta = A^{-1/n}\ d^{m/n}\ f_{H_2O}^{-r/n}\ \dot{\varepsilon}_{II}^{(1-n)/2n}\ exp\left(\frac{Q+PV}{nRT}\right) \quad . (5)$$

where A is the pre-exponential factor, d and m are the grain size and its exponent, f_{H_2O} is the water content with its exponent r (Hirth & Kohlstedt, 2003), $\dot{\varepsilon}_{II}$ is the second invariant of the deviatoric strain rate tensor, E is the activation energy, P is the pressure, V is the activation volume, n is the power-law exponent, R is the gas constant and T is the temperature. The pre-exponential factor A includes the conversion from uniaxial and triaxial laboratory experimental data into the invariant state.
Plastic deformation takes place when the Drucker-Prager yield surface is reached

$$\sigma_y = Psin\phi + Ccos\phi \quad . (6)$$

where P is pressure, ϕ is the angle of internal friction and C is the cohesion.

Text S3. Thermal and rheological profiles

The initial geotherm increases from constant 0°C at the surface to 1300°C at the 120 km depth Lithosphere-Asthenosphere Boundary (LAB). Below the LAB, the temperature is held constant with depth. A thermal perturbation of 70°C with a 2D Gaussian shape (x-axis width of 10 km and z-axis width of 20 km) is introduced at the center of the model at 30 km depth to localize the initial deformation. This thermal perturbation dissipates with time.

The composition of the mantle lithosphere and asthenosphere is based on an initial melt depletion profile. Mantle rheology changes from wet olivine with a water content of 125 ppm H/Si (Hirth & Kohlstedt, 1996; Rüpke et al., 2006) when the mantle is 0% depleted to dry olivine when the mantle depletion is 4%, assuming that all water has been extracted at this stage (Morgan, 1997). From the bottom of the model, 400 km depth, to 160 km depth we assume the mantle has not been melted and has a depletion of 0 %, corresponding to a wet olivine rheology. From 160 km depth to the base of the lithosphere, 120 km depth, melt depletion increases from 0% to 4% with a mixture rheology of wet and dry olivine that depends linearly on the degree of depletion.

From the base of the lithosphere to 60 km depth, the depletion linearly increases from 4 to 10%, with a dry olivine rheology. As melting occurs in our model the increasing depletion affects the mantle rheology and its density. The reference densities for upper crust, lower crust and mantle are 2700 kg m^{-3}, 2850 kg m^{-3} and 3300 kg m^{-3}, respectively. The density changes with temperature and with amount of depletion. Following the Boussinesq approximation (Ranalli, 1995), density is expressed as $\rho = \rho_o(1 - \alpha(T - T_o) - \beta F)$, where ρ is the density, α is the thermal expansivity, β is a factor that parametrizes the influence of melt extraction on density and is equal to 0.044 (Armitage et al., 2013), F is the melt depletion, ρ_o is the reference density and T_o is the reference temperature.

Parameter	Symbol (Units)	Wet quartzite	Dry quartzite	Mafic granulite	Dry olivine	Wet olivine
Dislocation pre-exponential factor	$\log(A_{dis})$ ($\log(Pa^{-n}s^{-1})$)	-28.00	-19.57	-21.05	-15.56	-15.05
Dislocation exponent	n_{dis}	4.0	2.4	4.2	3.5	3.5
Dislocation activation energy	E_{dis} ($KJ\ mol^{-1}$)	223	156	445	530	480
Diffusion pre-exponential factor	$\log(A_{dif})$ ($\log(Pa^{-n}s^{-1})$)	-	-	-	-8.65	-8.65
Diffusion exponent	n_{dif}	-	-	-	1	1
Diffusion activation energy	E_{dif} ($kJ\ mol^{-1}$)	-	-	-	375	335
Grain size	d (mm)	-	-	-	6	6
Grain size exponent	m	-	-	-	3	3
Reference density	ρ (kg/m^3)	2700 (2850)	2850	2850	3300	3300
Heat capacity	Cp $(J\ kg^{-1}\ K^{-1})$	1200	1200	1200	1200	1200
Heat conductivity	k $(W\ m^{-1}\ K^{-1})$	2.1 (2.5)	2.5	2.5	3.3	3.3
Thermal expansivity	α (μK^{-1})	24	24	24	30	30
Radioactive heat production	H_p $(\mu W m^{-3})$	1.3 (0.2)	0.2	0.2	-	-
Shear modulus	μ (GPa)	36 (40)	40	40	74	74

Table S1. Flow law references: wet quartzite (Gleason & Tullis, 1995), dry quartzite (Ranalli & Murphy, 1987), mafic granulite (Wilks & Carter, 1990), dry and wet olivine (Hirth & Kohlstedt, 2003). We use a grain size of 6 mm (Brune et al., 2014). The rheology of wet quartzite is used in both upper and lower crusts and are indicated in brackets for the latter. Thermal parameters from Currie & Hyndman (2006).

Text S4. Strain softening

In nature, fault planes or gouges represent mechanical discontinuities along which rock strength decreases. A reduction in the cohesion (Buck & Lavier, 2001) or in the angle of friction (Bos & Spiers, 2002) are two possible causes for rocks weakening. Both cohesion loss and friction angle reduction imply that faults are typically weaker than the surrounding undamaged rock and susceptible to strain localization. Plastic strain softening is commonly included in numerical models to simulate cohesion and friction angle weakening at faults, which is achieved by defining a parametrical function of some type of finite strain (Huismans & Beaumont, 2002; Buck & Poliakov, 1998; Lavier et al., 1999). Here, we fix the cohesion value to 10 MPa and define the friction angle ϕ as a function of the accumulated second strain invariant ε_{IIh}

$$\phi = \left(\varepsilon_{IIh} - \varepsilon_{IIh_1}\right)\frac{\phi_2 - \phi_1}{\varepsilon_{IIh_2} - \varepsilon_{IIh_1}} + \phi_1 \quad . (7)$$

where ϕ_1 is the initial friction angle, ϕ_2 is the softened friction angle, and $\varepsilon_{IIh_2} - \varepsilon_{IIh_1}$ is the strain interval where plastic strain softening takes place. We set $\phi_1 = 30$, $\phi_2 = 15$, $\varepsilon_{IIh_1} = 0$ and $\varepsilon_{IIh_2} - \varepsilon_{IIh_1} = 1$. The accumulated strain tensor ε_{IIh} is calculated from the deformation gradient (*Malvern*, 1969).

Shear zones develop in the viscous domain when the accumulated strain leads to dynamic recrystallization causing a reduction in the grain-size. The consequent change from dislocation to diffusion creep will be temporary due to the fast grain growth occurring in diffusion creep. To incorporate viscous strain softening in our model we take into account that significant softening by grain size reduction will localize in shear zones if grain growth is inhibited (De Bresser et al., 2001), and that mantle strain softening, via dislocation-accommodated grain boundary sliding, decreases with temperature, being very limited at temperatures higher than 800 °C (Précigout & Gueydan, 2009). Therefore, we introduce a strain- and temperature-dependent factor α in the viscosity equation (Eq. 6) that reduces the effective viscosity as deformation accumulates. The dependence of the α-factor on the accumulated strain is given by

$$\alpha = \left(\varepsilon_{IIh} - \varepsilon_{IIh_1}\right)\frac{\alpha_2(T) - \alpha_1}{\varepsilon_{IIh_2} - \varepsilon_{IIh_1}} + \alpha_1 \quad . (8)$$

where α_2 is temperature-dependent, with a value of 30 between 0°C and 800°C followed by an exponential decrease from $\alpha_2 = 30$ at 800°C to $\alpha_2 = 1$ at 1200°C; α_1 = 1, $\varepsilon_{IIh_1} = 0$ and $\varepsilon_{IIh_2} = 1$. In the viscosity equation (Eq. 5), α is raised to the inverse of n, meaning that a value of α = 30 corresponds to a change in viscosity of about 0.4 compared to the undeformed rock.

Text S5. Melt productivity and emplacement

The mantle dehydrates as it melts, but the contribution of wet melting is negligible compared to dry melting (Hirth & Kohlstedt, 1996). Therefore, we only consider dry melting of a homogeneous fertile peridotite mantle. Fractional melting occurs when the mantle temperature exceeds the pressure- and depletion-dependent solidus temperature (Fig. S1A and B). Consequently, the temperature reduces as the latent heat is absorbed until the mantle geotherm equals the solidus temperature. The solidus temperature is updated after melting through its dependence on the mantle depletion (Eq. 9). The amount of melt generated at each time step is calculated based on the formulation of Morgan (2001). The dry solidus temperature is given by

$$\mathrm{T_s} = \mathrm{T_{s0}} + \frac{\partial \mathrm{T_s}}{\partial \mathrm{P}}\mathrm{P} + \frac{\partial \mathrm{T_s}}{\partial \mathrm{F}}\mathrm{F} \quad . (9)$$

where $T_{s0} = 1081°C$ is the solidus temperature at the surface, $\frac{\partial T_s}{\partial P} = 32 \cdot 10^{-9}$ °C /Pa is the solidus-pressure dependence, P is the pressure, $\frac{\partial T_s}{\partial F} = 350$ °C is the solidus-depletion dependence and F is melt depletion.

During each (Lagrangian) time step a melting node is advected to a new location, and the melt productivity during the time step is given by

$$\Delta F = \frac{\Delta T}{\frac{L}{C_p} + \frac{\partial T_s}{\partial F}} \quad . (10)$$

where L is latent heat of melting, $\frac{L}{C_p} = 550$ °C and ΔT is the difference between the end-position rock and solidus temperatures.

Previous studies of melting include the effect of melt retention in the density and the viscosity equations (e.g. Simon et al., 2009; Schmeling, 2010; Lavecchia et al., 2017). For example, Simon et al. (2009) uses a maximum value of 1% for the melt retained in the mantle source; although it can have a slight impact on the density, they showed how the impact on the viscosity equation is countered by the dehydration strengthening, which we include in our model. Also, some melt formulations (e.g. Simon et al., 2009; Schmeling, 2010; Lavecchia et al., 2017) have melting in the damp regime, which produces a very small amount of extra melting. We consider that our melt parametrization is comparable to theirs. Perhaps relatively sooner and larger melts would be produced by the effect of including melting in the damp regime, but this would not affect our main results.

Schemling (2010) extract all melt after 2% and emplace it in a melt layer on the top of the model following a bell shaped rate function. In our case, as we assume that all melt is moved upwards in a dike, to the area of maximum extension, our final 'underplating layer' is totally different from their 'volcanics surface', since we are looking at different goals. Finally, they include solidification of ascended melt, this together with the Darcy's flow are good implementations for future work. Finally, at the emplacement level, Lavecchia et al. (2017) add the effect of melt presence in the decrease of strength by predicting a drop in the plastic yield strength with a loss of cohesion and in viscosity. They also include melt solidification and heat released by moving melts. The novel incorporation of the melt presence in the decrease of plastic yield strength is interesting but we assume that all melt generated in our model at each time step is instantaneously advected below the Moho and solidified in a dike, so we skip these intermediate migrating steps from the melt source to the emplacement level and subsequent solidification impact. Although our melt emplacement formulation is ad-hoc, it is a valid first order approximation based on the studies of melt migration paths as explained previously.

During each time step, the total amount of melt is emplaced beneath the Moho forming a column, which we call dike. The thickness of the dike is calculated following Ito et al. (1996): the degree of melt at nodal positions is weighted by the corresponding nodal area and integrated over the total area of melt, the resulting amount of melt is divided by a distance D equivalent to the product of the full-spreading velocity v_{full} and the time increment dt: $D = v_{full} \cdot dt$, whose result gives the thickness of the dike or equivalent predicted magmatic crust. In nature, part of the melt freezes on its way to the surface (Cannat et al., 2009), whereby this estimation provides an upper limit to the magmatic crustal thickness.

Each dike is decomposed as a combination of tracers that move with the nodal velocity field of the mantle. These tracers are modeled as semi-transparent circles with radius scaled by the time step

amount of melt. The increasing number of dike tracers during the evolution of the rift leads to zones where their accumulation shows more opacity and represents the higher density of underplated magmatic material. A more realistic melt emplacement would require of compressible formulation which is out of the scope of this paper. Note that the magmatic crustal thickness is the thickness of the dike produced at each time step and it not related to the thickness of the underplating.

We have run several models with extension velocities in the slow, intermediate and fast spreading regime (Fig. S5) to calculate the magmatic crustal thickness variation as a function of the extension velocity (Fig. S6). The predicted magmatic crustal thicknesses are in agreement with mid-ocean ridges seismic crust observations, as shown in Fig. S6 (Bown & White, 1995; Dick et al, 2003). Dick et al. (2003) uses two models for the oceanic crustal thickness, the buoyant and the passive mantle flow models (Phipps Morgan et al., 1987; Sotin & Parmentier, 1989). The formation of oceanic crust by melt extraction decreases the density of the melt mantle source which upwells below the spreading center. This creates a compositional buoyancy that impacts on the upwelling rate, mantle flow pattern and hence enhances crustal thickness in comparison to the thickness result from only passive plate spreading. The mantle viscosity strongly controls the dominance of the buoyancy force: for 10^{22} Pa s , passive spreading dominates and the oceanic crustal thickness depends on spreading rate, whereas for 10^{19} Pa s, compositional buoyancy dominates and the crustal thickness is almost independent on spreading rate. Our models show a behavior similar to passive upwelling for slow velocities and to buoyant upwelling for higher velocities. The reason can be that higher velocities promote the production of larger amounts of melt and hence more compositional buoyancy that dominates over passive upwelling. Our steady-state thickness of about 5-6 km for full-extension velocities higher than 20 mm/yr, which is the upper-limit of the ultra-slow regime, agrees with Cannat et al. (2009) who stated 'Most ridges receive enough magma to build a magmatic crust that is 6 km thick on average'.

Supporting figures

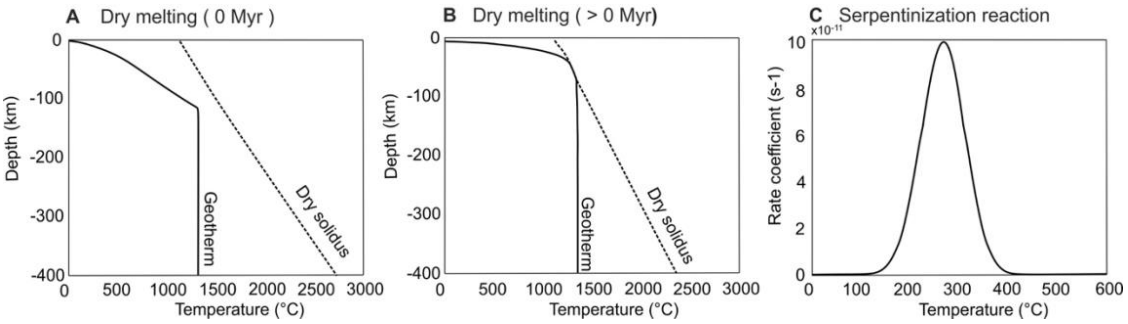

Figure S1. Model for decompressional melting and rate of serpentinization during continental rifting. (a) Initial geotherm and dry solidus. (b) Melting starts when the geotherm crosses the solidus and consequently the temperature is reduced as the latent heat is absorbed and the temperature equals the solidus temperature. The solidus temperature is updated after melting through its dependence on the mantle depletion. (c) Serpentinization rate dependence on temperature calculated with a dependence on temperature given by experimental data (Emmanuel and Berkowitz, 2006).

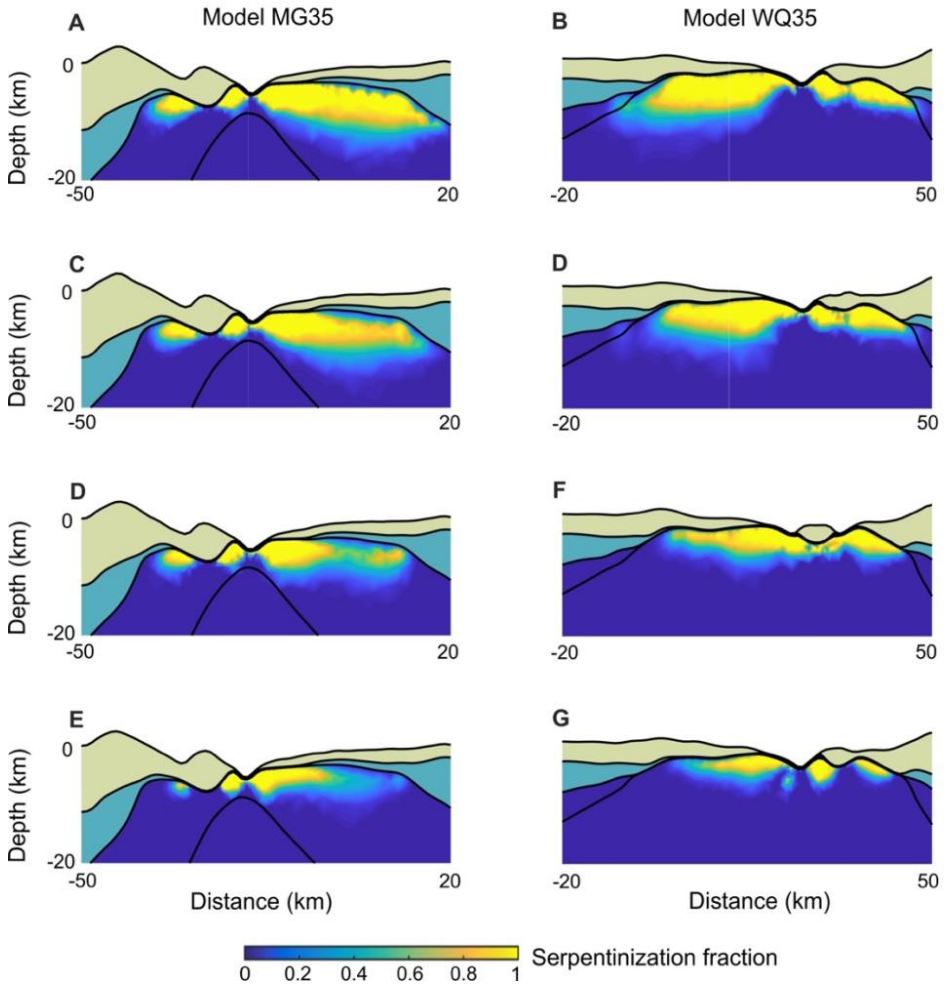

Figure S2. Numerical models testing the sensitivity of the amount of serpentinization on the parameter ***f*** that defines active faults that allow water downflow (see 'Serpentinization: sensitivity tests' in Supplementary information). Left panel: models with mafic granulite lower crust, 35 km crustal thickness and 3 mm/yr half-extension velocity. The value of the active fault parameter ***f*** is: (a) 0.1%, (c) 1 %, (d) 10 % to (e) 50%. Right panel: models with wet quartzite lower crust, 35 km thickness and 3 mm/yr half-extension velocity. The value of the active fault parameter ***f*** is: (b) 0.1%, (d) 1 %, (f) 10 % to (g) 50%. As the parameter increases the resulting serpentinized zone slightly decreases in amount and depth.

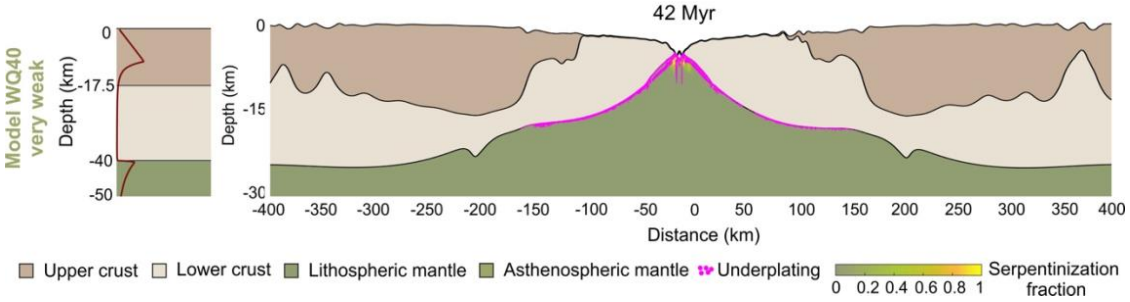

Figure S3. Numerical model with very weak quartzite upper crust and lower crust after break-up (see Table 1 for rheological parameters) for a half-extension velocity of 5 mm/yr. The resulting margins are symmetric and wide with a COT magmatically dominated and perhaps underlain by some serpentinized mantle.

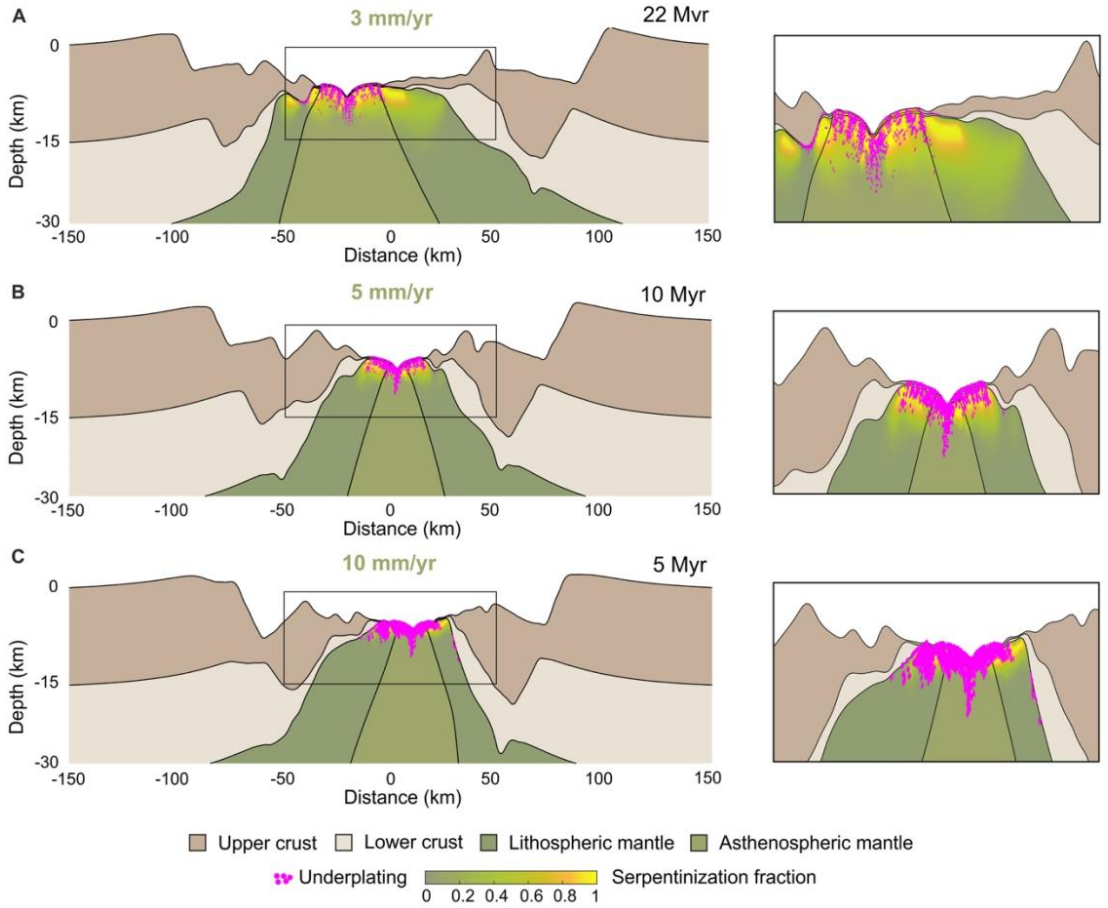

Figure S4. Numerical models with a mafic granulite lower crust and 35 km crustal thickness at a time step after break-up, for half-extension velocities of 3, 5 and 10 mm/yr. Crustal break-up occurs before lithospheric break-up for all these models, however the resulting nature of the COT is very different. Serpentinization starts earlier than melting for the model with 3 mm/yr, resulting in a COT with exhumed and serpentinized mantle, whereas melting starts earlier than serpentinization and is more abundant for the model with 10 mm/yr, resulting in a magmatically dominated COT. Right panel show zooms of the top surface of the models.

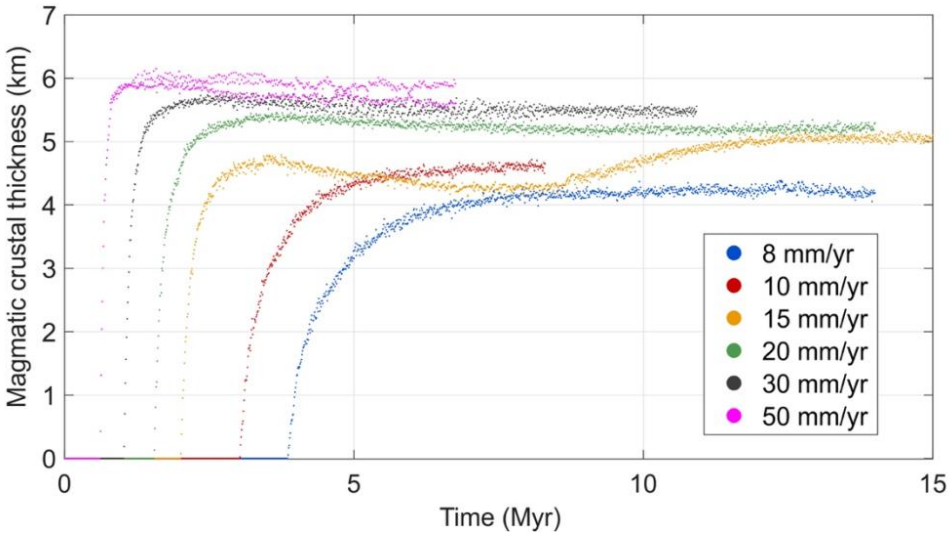

Figure S5. Magmatic crustal thicknesses for a model with 35 km crustal thickness, mafic granulite lower crust and half-extension velocities of 8, 10, 15, 20, 30 and 50 mm/yr.

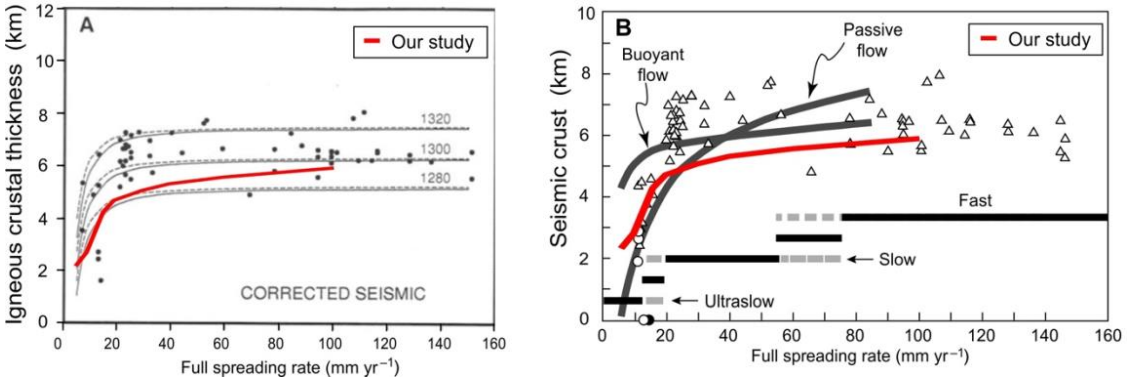

Figure S6. Oceanic crustal thickness versus full spreading rate data from: a) Bown & White (1995) and b) Dick et al. (2003). Our study results are superimposed with a red solid line. a) Our model results with a lithosphere-asthenosphere temperature of 1300℃ (red solid line) are in agreement with the predicted crustal thickness for mantle potential temperature of 1300℃, for assumed mantle viscosities of 10^{18} $Pa\ s$ (dashed lines) and 10^{20} $Pa\ s$ (solid lines). Dot are seismic observations. b) Our model results (red solid line) matches the predicted crustal thickness for a passive flow model at slow spreading rates and for a buoyant flow model at higher spreading rates. The passive and the buoyant model are based on Phipps Morgan et al. (1987) and Sotin & Parmentier (1989) respectively. Triangles show observations from White et al. (2001) and white circles from Jockat et al. (2003).

Supporting movies captions

Movie S1. Evolution of the numerical model with mafic granulite lower crust, 35 km crustal thickness and 3 mm/yr half-extension velocity. Top: Strain rate is depicted in grey shadow over the lithospheric layers. Middle: Serpentinization fraction and red contours delimiting the melting zone

in the mantle. Bottom: Magmatic crustal thickness over time. The initial deformation localizes at the rift center into conjugate large faults causing effective crustal thinning. At 11 Myr crustal faults that reach the mantle at temperatures suitable for serpentinization act as conduits for water and serpentinization starts ~3-4 km beneath the crust. At this time the thermal gradient is still too low for the mantle to melt. The narrow extensional mode dominates rifting and leads to symmetric narrow conjugate margins. An earlier onset of serpentinization than that of melting results in a COT dominated by exhumed serpentinized lithospheric mantle at the seafloor, underplated by a thin magmatic layer. The predicted magmatic crust reaches a constant value of ~1 km.

Movie S2. Evolution of the numerical model with mafic granulite lower crust, 40 km crustal thickness and 3 mm/yr half-extension velocity. Top: Strain rate is depicted in grey shadow over the lithospheric layers. Middle: Serpentinization fraction and red contours delimiting the melting zone in the mantle. Bottom: Magmatic crustal thickness over time. The model starts in narrow deformation mode with large faults localizing deformation. The initial degree of decoupling between crust and mantle promotes the later switch to sequential faulting mode after 10 Myr of extension. This mode occurs where deformation localizes in a single active fault and the lower crust is weak enough to flow to the fault tip. This inhibits crustal break-up by faulting and promotes the generation of a sequence of active faults that laterally migrate the rift center and dip oceanwards, resulting in asymmetric conjugate and earlier onset of serpentinization than that of melting. Eventually, conductive cooling embrittles the lower crust and allows crustal break-up to occur. The spatial extent of serpentinization beneath the thinned crust is much larger in the wide margin (20-30 km) than in the narrow one. Very little underplated magma is observed beneath the crust on both margin sides. The COT is characterized by exhumed serpentinized mantle at the seafloor, intruded and underplated by very little amounts of frozen magma. The predicted magmatic crust reaches a constant value of ~1 km.

Movie S3. Evolution of the numerical model wet quartzite lower crust, 35 km crustal thickness and 3 mm/yr half-extension velocity. Top: Strain rate is depicted in grey shadow over the lithospheric layers. Middle: Serpentinization fraction and red contours delimiting the melting zone in the mantle. Bottom: Magmatic crustal thickness over time. The large initial level of crust-mantle decoupling leads to distributed faulting over a wide zone, with uniform crustal and lithosphere mantle thinning, i.e., wide mode, from 0 to 11 Myr. A short phase of sequential faulting occurs until break-up. Melting starts at 17 Myr. The weak lower crustal flow inhibits the formation of crustal-scale faults, which delays the onset of serpentinization to 23 Myr. Break-up leads to conjugate margins that are mostly symmetric, where the slightly wider margin results from a last stage of sequential faulting. The COT is a magma-dominated domain where magma products can be found at the sea-floor and may be underlain by serpentinized mantle. The predicted magmatic crust reaches a constant value of ~2 km.

Movie S4. Evolution of the numerical model with wet quartzite lower crust, 40 km crustal thickness and 3 mm/yr half-extension velocity. Top: Strain rate is depicted in grey shadow over the lithospheric layers. Middle: Serpentinization fraction and red contours delimiting the melting zone in the mantle. Bottom: Magmatic crustal thickness over time. A great initial crust-mantle decoupling accommodates extension in core complex mode, localizing deformation in upper crustal detachment faults, whereas the lower crust and lithosphere mantle accommodates deformation over a wide region from 0 to 12 Myr. As extension continues, the deformation changes to wide mode until 32 Myr. Later cooling kicks in leading to localization of deformation where the crust is the thickest, as the cooled mantle in the thinned region is stronger, and switches to sequential faulting mode at 34 Myr. Melting starts at 19 Myr whereas serpentinization starts at 40 Myr. Sequential faulting in the last stages of extension leads to the formation of two asymmetric margins, where the hyper-extended wide margin is underplated by magma along much of its length ~150 km. The COT

is magma dominated, with magmatic products at the seafloor, perhaps underlain by some serpentinized mantle. The predicted magmatic crust reaches a constant value of ~1.5 km.

Movie S5. Comparison of the numerical models evolution MG35 and WQ40 (3 mm/yr half-extension). Model MG35 has a mafic granulite lower crust and 35 km crustal thickness. WQ40 has a wet quartzite lower crust and 40 km crustal thickness. Top panel shows velocity field for both models. Bottom panel shows predicted magmatic crustal thickness for both models (see Supplementary information for an explanation of how is calculated).

In fact, an essential part of the practical working of the scientific method is that new ideas be subjected to searching criticism.

Isaac Asimov

CHAPTER

6

General discussion and critical evaluation

6.1 Introduction

The main goal of this thesis is to investigate how the strength of the lower crust influences the different stages of magma-poor rift evolution and particularly the relation between the type of architecture and COT at rifted margins. 2D numerical experiments are used to test end-member scenarios to better understand the modes of extension during continental rifting and to provide a conceptual diagram based on the modelling results.

The formation of passive margins has been widely studied by 2D models despite being fundamentally a 3D problem, and mostly due to computational cost. Some 3D features of continental rifting show along strike symmetry and can be well approximated by 2D approaches (e.g., Huismans and Beaumont, 2011; Liao et al., 2013; Naliboff and Buiter, 2015; Naliboff et al., 2017; Petersen et al., 2015; Van Wijk and Cloetingh, 2002). However, the study of rift propagation, rift segmentation and oblique extension requires a 3D setting (e.g., Allken et al., 2011; Brune et al., 2014). For the end-member cases investigated in this thesis, a 2D approach is a convenient assumption for the analysis of the key parameters and processes that control magma-poor continental rifting (Brune, 2016). This is less computationally expensive because it reduces the complexity of the 3D system owing to the non-linearity of the lithospheric rheologies, and also allows for a higher resolution. Besides, the area of the South Atlantic investigated in this dissertation rifted in a nearly-orthogonal extension (Brune et al., 2012), so that in this case a 2D approach is justified.

In the following sections I critically evaluate the melting and serpentinization formulations included in the numerical code, the major model limitations for the natural representation of continental rifting and compare the model results with those from other published numerical studies. Throughout this discussion I also propose modelling improvements for future work.

6.2 Limitations of model assumptions

Model results are limited by the numerical approach, choice of input parameters and prescribed boundary conditions. This section extends the discussion in Chapter 3 about the model assumptions, which focused on the choice of initial thermo-rheological properties and the incorporation of mechanisms of strain localization. Despite these limitations, it is worth emphasizing that the model approach is mainly used to explore first-order characteristics of magma-poor rifted margins.

6.2.1 Mechanical boundary conditions

The imposed constant velocity at the sides of the 2D domain to model continental extension is conventionally used in numerical modelling. However, continental extension in natural systems is driven by tectonic forces such as the slab pull, ridge push or mantle drag (Forsyth and Uyeda, 1975). Therefore, a constant stress boundary condition can be used to account for the intrinsic tectonic forces available in Plate Tectonics. Recently, Brune et al. (2016) have used constant force boundary conditions to model extension of continents, which allows for self-consistent computation of velocity evolution. The authors found that rifting is characterized by an initial phase of slow rifting that speeds up during continental necking and leads to a second phase of fast rifting before break-up. Reproduction of successful and failed rifts depends on the applied constant force and the lithospheric strength. Their results match the extension history of typical worldwide passive margins in agreement with rapid absolute plate motion observed in plate reconstructions.

Future work will be the implementation of constant force boundary conditions and then to investigate if the link between the tectonic style and the type of COT proposed in Chapter 5 remains the same. The change of rifting velocity in a two-phases history will have strong implications on the relative timing and amounts of serpentinization and melting.

Additionally, since the range of extension velocities tested in this thesis has been reduced to the ultra-slow regime characteristic of magma-poor margins, an integrated study of passive margins could be done by exploring the role of the lower crustal strength also under faster velocities ($<$ 50 mm/yr half-extension).

6.2.2 Rheological behavior

The choice of rock materials in numerical modelling is crucial in the evolution of the model. Generally, it is justified by observations in the area of study where the model is intended to be applied or just a matter of preference. Here, the rheologies used for the lower crust are based on a

comparison of effective viscosities where mafic granulite and wet quartzite can ideally represent two end-member rheologies (see Appendix A). The choice of these rheologies also fit the crustal rheology for the central South Atlantic margins (see Chapter 5). In any case, there is an inherent uncertainty in extrapolating laboratory experiments to geological conditions and a difficulty in delimiting the creep mechanisms acting, what entails to interpret the model results with caution (Hopper and Buck, 1993). For instance, dynamic models of continental rifting generally use the power-law creep to simulate viscous behavior and the Drucker-Prager relationship for plasticity. Recent experiments on low temperature plasticity ($< 1000\ ^{\circ}C$) have shown the Peierls plasticity flow law limits the lithospheric mantle strength in high-stress regimes (for stresses larger than 200 MPa). It has been suggested to be of particular importance in the deformation of subducting slabs of low temperature and high stress (Karato et al., 2001). However, since only few experiments have been done (e.g., Goetze and Evans, 1979; Katayama and Karato, 2008; Mei et al., 2010), there are still large uncertainties associated.

Only few studies of continental rifting have included the Peierls mechanism, showing a decrease in the lithospheric mantle strength (e.g., Brune and Autin, 2013; Liao and Gerya, 2015). To have a better understanding of its influence during continental extension, further work could be a comparative study of the extensional models where the Peierls creep is applied. The evolution of the strength profiles of the end-member models discussed in this thesis (see movies E1, E3 and E3 in Electronic supporting information) suggest that the addition of this mechanism may impact the rift geometry at the early stages.

6.2.3 Initial weak seed

Chapter 5 shows how first-order characteristics of modelled rifted margins can be compared to natural examples. For instance, the width of the continental margin, the asymmetry of the conjugates, the fault associated subsidence and the faulting pattern. Throughout this study, I find that the margin width of the models is generally shorter than in the natural margins used for comparison. The crustal thinning gradient or crustal taper, which is measured from the unthinned continental crust to the highly extended distal margin (< 10 km thick), is more abrupt, even when weaker lower crustal rheologies are used in the models. This may be a consequence of the way the model is initialized. In nature, the initialization of the rift is highly controlled by the presence of pre-existing structures in the lithosphere, the so-called 'tectonic inheritance'. For instance, the presence of faults, shear zones, magmatic intrusions or detachment layers can be reactivated during early stages of rifting (Ziegler and Cloetingh, 2004; Zwaan and Schreurs, 2017). Some authors have introduced different types of heterogeneities in the pre-rift lithosphere, such as bimineralic

composition of rocks to simulate semibrittle/semiductile domains (Jammes and Lavier, 2016) or structural softening (Duretz et al., 2016). However, their conclusions only highlight the fact that pre-heterogeneities provide a first order control on the rift evolution and could explain some of the observed geological features at margins (i.e. continental ribbons or crustal scale anastomosing patterns). In practice, it is difficult to asses the inherited heterogeneities that were present in a pre-rift system and whether these were or not reactivated during rifting (Manatschal et al., 2015). Also, a laterally homogeneous lithospheric setup for the numerical models allows to test the key processes and parameters in a systematic way and isolate their contributions.

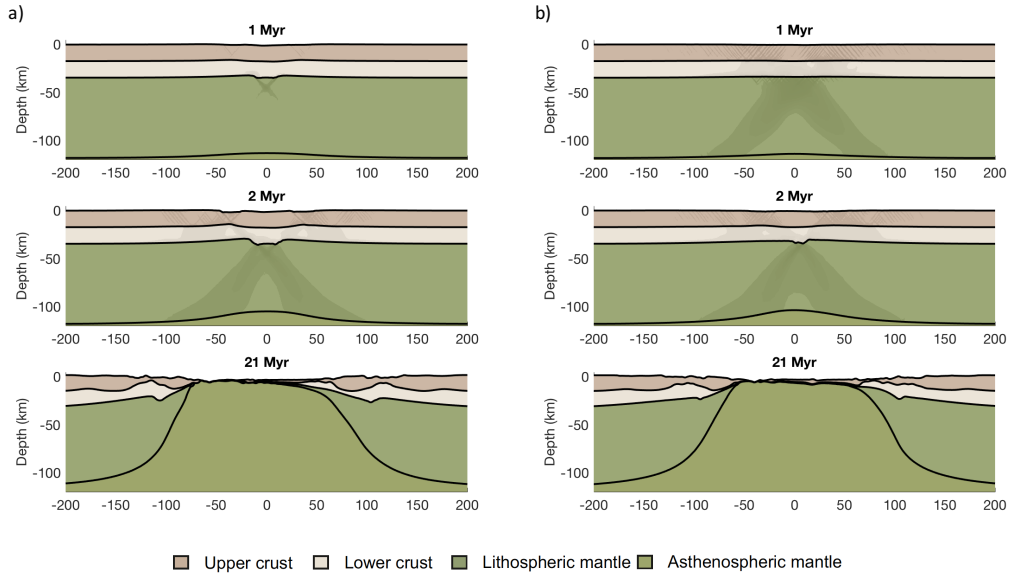

Figure 6.1: Evolution of the model with weak lower crust extended by 5 mm/yr and initialized with the weak seed described in a) this study and b) Brune et al. (2014). The strain rate field is shaded in gray.

In the models I showed, the rift is initialized with a central thermal weak seed that localizes deformation very fast. This could result in a more localized thinning and hence more abrupt crustal taper than using other type of weak seeds. The choice and role of this type of weak seed has been discussed previously in Section 3.2.3.2. However, the impact on the resulting crustal taper was not addressed. Following Brune et al. (2014), I also tested this type of weak seed, where the 1300 $°C$ isotherm is elevated as a triangular shape with 5 km of height and 20 km of width, and the initial stages were similar to the model results of Brune et al. (2014, 2017b). Deformation initially distributes over the whole domain until plastic softening coalescence. My results show more initial upper crustal faults (Fig. 6.1 at 1 and 2 Myr), indicating that the weak seed I normally use forces initial deformation to be more localized. However, the results show similar evolution and final crustal taper (Fig. 6.1a) and b) at 21 Myr).

6.2.4 Strain softening

The numerical model includes plastic and viscous strain softening for the simulation of faults and shear zones, respectively. These ad-hoc parametrizations are subject of debate since the effect of the different mechanisms contributing to strain softening (e.g., reduction in grain size, presence of fluids and mineralization) has not been quantified. Different assumptions are generally used in the literature regarding the values of the accumulated strain interval, angle of friction ϕ and cohesion C (see Table 6.1). The strain interval over which softening occurs can be considered for a total strain (e.g., Huismans and Beaumont, 2003), plastic strain and viscous strain (e.g., Brune et al., 2014) or historic second strain invariant (e.g., Ros et al., 2017). Additionally, some models include plastic healing through time (e.g., Elesin et al., 2010; Moresi et al., 2007; Naliboff and Buiter, 2015), which is based on the strengthening observed in natural shear zones (Hölker et al., 2002). This freedom in the approaching of strain softening could imply differences in the model results, since it has been shown that the onset of strain softening, the strength reduction and the softening rate can influence lithospheric deformation (e.g., Allken et al., 2011; Frederiksen and Braun, 2001). Therefore, a benchmark study between numerical codes for continental rifting is needed in order to bring some confidence on their applicability. Today, the reliability of these parametrizations largely relies on the reproduction of tectonic structures similar to those observed in the field. Consequently, further work in this direction has to be done in the numerical modelling community.

As previously shown in Section 3.2.3.1, I implemented a second type of plastic softening based on the finite plastic strain, as it is widely used in numerical modelling and it can facilitate comparisons between model results. However, due to the factor time, I could not integrate this softening in any of the two main studies of this thesis (Chapters 4 and 5) but I have included it in the ongoing study of the heat release effect.

Reference	Plastic softening			Viscous softening	
	C (MPa)	ϕ (°)	Interval	α	Interval
Brune et al. (2014)	5	27 to 0.3	0 to 1	1 to 30	0 to 1
Brune et al. (2017a)	5	27 to 0.3	0 to 0.5	1 to 10	0 to 0.5
Svartman Dias et al. (2015a)	44 to 4	30 to 5	0 to 1		
Ros et al. (2017)	10	30 to 15	0 to 1	1 to 30	0 to 1
Tetreault and Buiter (2017)	20	20 to 10	0.5 to 1.5		
Huismans and Beaumont (2003)		7 to 1	0.5 to 1.5	η to 0.1η	0.5 to 1.5
Huismans and Beaumont (2007)	20	7 to 1	0.5 to 1.5		
Huismans and Beaumont (2014)	0	15 to 2	0.5 to 1.5		

Table 6.1: Parameters for plastic and viscous softening included in different studies of continental rifting.

6.2.5 Melt formulation

Magma-poor margins, although less common than magma-rich margins (Menzies, 2002), present larger simplicity for the understanding of the undergoing processes. This is due to the lack of massive magmatism that strongly affects the rift evolution by changing the style of deformation, the rheological evolution or the localization of deformation. Moreover, natural magma-poor systems are not masked by voluminous magmatism, making more simple its comparison to numerical models, and being a tool for studying magma migration at earlier stages (Manatschal, 2004).

In our model, a first step forward has been done in the numerical modelling interplay between tectonic and magmatic processes. Although the applied melt model was already put in the context of previous melt models used in continental rift settings (supporting information of Chapter 5), below I expand the comparisons between our model and other previously used (e.g., Lavecchia et al., 2017; Schmeling, 2010; Simon et al., 2009).

The melt parametrization of Simon et al. (2009) includes the absorption of latent heat related to the phase change from solid to melt in the heat balance equation while we implement this temperature change in the melt function, so each node undergoing melt will change its temperature. Simon et al. (2009) also implement the density change related to melt retention and compositional depletion of the source. We implement only the second effect because we assume that all melt is moved beneath the Moho and no melt remains in situ in the source. As the maximum value of in situ melt is of 1% in Simon et al. (2009), we can predict that the inclusion of this melt retention effect would not affect our final results. Regarding the effect of melt on viscosity, they take ratio values of dry viscosity/ wet viscosity from Karato and Wu (1993) to increase the viscosity by simulating the dehydration and hence strengthening of the mantle source after melt is extracted. They also say that the effect of melt weakening on viscosity is potentially countered by dehydration strengthening. Therefore, we consider our parametrization comparable to theirs. In our melt code, we assume that initial wet olivine that depletes over 4% removes all the water and behaves as dry olivine. As a consequence, the rheology of this source is changed accordingly in the model. Simon et al. (2009) also include wet and dry melting, but we only include dry melting given the low amount produced by the wet solidus. Ultimately, our melting model is equivalent to the one of Simon et al. (2009), although perhaps, a bit more of melt would be produced by including the wet solidus.

The melt parametrization of Schmeling (2010) includes two-phase medium with melt and solid matrix. They use the generalized Darcy law for the melt equation of momentum. In the viscosity equation they include the effect of melt fraction. In the density equation they include the effect

of basaltic enrichment due to solidification, melt fraction and depletion. The first two terms are not included in our formulation, we do not change the density of the melt source but include the strengthening effect in the viscosity as explained above. Although they use a liquidus and a solidus like Lavecchia et al. (2017), in our formulation we account for the change in pressure and temperature at each time step by discretizing these two processes, which we consider better constraint. They extract all melt after 2% and emplace it in a melt layer on the top of the model following a bell shaped rate function. In our case, as we assume that all melt is vertically upwards in a 'dike', our final 'underplating layer' is different from their 'volcanics surface', since we are looking at different goals. Finally, they include solidification of ascended melt, this together with the Darcy's flow are recommended implementations for future work.

The melt parametrization of Lavecchia et al. (2017) changes the density of the melting rock according to the density of the depleted mantle and the extracted and intruded melt fraction. The solidus and liquidus are implemented in their melt formulation. The presence of melt has an effect on the rock strength, which Lavecchia et al. (2017) include at the emplacement level. They predict a drop in the plastic yield strength with a loss of cohesion and also a reduction in the viscosity. Finally, they include melt solidification and quantify the heat transported and released by moving melts at the emplacement level. The modelling of the decrease of plastic yield is interesting, but in our case it does not apply because we assume that all melt generated at each time step is instantaneously advected below the Moho and solidified in a dike. Although our melt emplacement formulation is ad-hoc, it is a valid first order approximation based on studies of melt migration paths as explained in Chapter 5.

Melt extraction could be a future implementation. In this study we preferred to consider the end-member model where all melt is localized below the Moho as a dike and at the COT-floor after crustal break-up. Incorporation of retained magma in the mantle, intrusion in the crust and extrusion will require the addition of more assumptions.

6.2.6 Melt emplacement

As shown in Section 2.5.2, I modelled two end-member scenarios for the emplacement of melt below the Moho, as vertical or horizontal columns of magma (i.e. dike and sill, respectively). Most studies of magma intrusion assume the dike scenario (Behn and Ito, 2008; Daniels et al., 2014), however, with initial continental extension, crustal thinning results in a decrease of crustal weight (Maccaferri et al., 2010) and this can lead to a counterbalance tectonic extension that rotates in 90° the principal axis at the rift axis. Therefore, horizontal sills could be found in the lower crust while dikes could be found at the rift flanks (Pagli et al., 2015). Since I could only show

studies including the dike approximation (Chapter 5), I leave for future work the comparison with the sill approximation.

Our assumption of instantaneous emplacement of a dike below the Moho is a first-order approximation equally valid to the models of dike injection using the M-factor (Behn and Ito, 2008; Behn et al., 2006) and similar (Bialas et al., 2010). But in order to have a more realistic formulation, models of dike propagation have to be integrated in models of continental rifting.

Additionally, our assumption that melt cannot penetrate serpentinized mantle is based on experimental work on the rheology and permeability of serpentinized peridotite in brittle and ductile conditions. As mentioned in Chapter 2 and 5, the assumption does not preclude that melt may eventually intrude the serpentinite layer and be extruded at the top basement, but that it will work as an additional barrier to melt extrusion and hence favor the occurrence of serpentinized peridotite at the top basement. In West Iberia it has been suggested that the serpentinized layer is only superficial and that it may be underlain by 2 km of melt. It is worth to note that permeability and non-dilatant deformation of serpentinite is not the only way serpentinite may act as a barrier, also devolatilization of serpentinite due to dike-serpentinite interaction may be another way. As this is the first time, to my knowledge, that modelling of both serpentinization and melting is included in a state-of-the-art 2D numerical model of extension, I think that it is a considerable step forward.

6.2.7 **Heat release of solidified melt**

The presence of magmatic intrusions within the lithosphere thermally weaken the rift zone. Based on this, I developed an algorithm to account for the heat release of the accumulated dikes beneath the crust (Section 2.5.3). Although I have worked on some preliminary tests, due to lack of time I could not perform a complete study for this dissertation. I suggest that the incorporation of heat release may have two contrasting roles: 1) it may localize deformation in a narrow rift, due to the increase heat that weakens the crust, and hence trigger crustal break-up or 2) it may enhance the flow of the lower crust and lead to wide or core complex rift, delaying crustal break-up.

Buck (2007) illustrates the effect of a magmatic intrusion in form of a dike as the combination of two localization processes. The first one is related to the stress exerted by the intrusion of the dike, which decreases the force needed for rifting. The second one is related to the heat input, which leads to advection of heat into the lithosphere plus the heat released when it solidifies. The effective temperature therefore would be addition of the magma temperature (about 1300 $^{\circ}C$) and the latent heat times the specific heat (about 300 $^{\circ}C$). For a set of dikes, this could significantly decrease the lithospheric strength and facilitate rifting.

At the moment, I am working on a new study that includes heat release of dikes, by analyzing how it affects viscosity and whether its incorporation can result in wider margins. This idea is based on the observations of magmatism in the wide margins of South China Basin and Santos.

6.2.8 Serpentinization formulation

Chapter 2 provides a sensitivity test of the 'active fault' parameter that defines which crustal faults are active during model extension. This implies the assumption that they act as water conduits to serpentinize the underlying mantle. We assume that brittle nodes under strain rates above a threshold value (defined in terms of the background strain rate and the active fault parameter) can be connected if they are within a radius of 4 km. Different values for the radius (i.e. 0.5, 1 and 4 km) resulted in slight variations of the amount of serpentinized mantle. Although this parametrization seems realistic as a first-order approximation, I think that it could be more accurate in the future by working on several aspects.

The first one is to introduce an adaptive mesh refinement so that the resolution is higher in the area of serpentinite generation. This will mainly affect the formation of faults and hence the resulting amount of serpentinized mantle. Even so, the latter will continue to be controlled mainly by the active fault parameter, which encompasses both the definition of active faults and the distance at which water can percolate to serpentinize. Perhaps, another valid approximation could be to define the active faults in terms of the plastic strain rate. A test comparing both approximations is needed to conclude if the onset of serpentinization will change significantly.

Besides, the current formulation does not include the effect of serpentinization on rheology. We modelled the instantaneous decrease in viscosity through the increase in temperature that results from the exothermic reaction of serpentinization. However, as serpentinites are weaker than peridotites, it would be more accurate to model a linear decrease in the coefficient of friction from 0 to 100% of serpentinization between the initial coefficient of friction and 0.2 (characteristic of serpentinites). This change in the rheology of the serpentinized region may localize further strain and trigger crustal break-up.

The reaction of serpentinization also involves a decrease in density which implies an increase in volume of approximately 40 %. A previous study on rifting and serpentinization used a relationship to decrease the density (Rüpke et al., 2013). This was based on the relative proportions of serpentine and magnetite during the reaction of serpentinization. The model results suggested that a relative basin uplift occurs when including the decrease of density for the serpentinites. However, for our incompressible model, I think that using the initial mantle density remains a good approximation .

Finally, in nature, circulation of seawater involves a hydrothermal cooling effect, which could be implemented by following Rüpke and Hasenclever (2017). Its implementation in the code will probably enhance the brittle behavior of the surrounding crust and modify the thermal structure of the mantle beneath.

The incorporations of all these suggestions may modify the onset of serpentinization for the different lithospheric setups but the relative timings should be similar.

6.2.9 Sedimentation and erosion

The numerical code used in this study includes water loading to approximate better the subsidence of the developing basins during continental rifting. However, this is an over simplistic approximation if we take into account that natural systems also obey to patterns of sedimentation and erosion. Through erosion the crust is unloaded and uplifted while through sedimentation the syn-rift basins are loaded and their subsidence increases. While it is necessary to separate the effects of the lithospheric strength and extension velocity (as investigated in this thesis) from the surface processes, the interaction of both and the effect on the final margin tectonic style is of great interest in order to advance more in the comprehension of the formation of magma-poor margins.

Lately, numerical modelling studies have focused on the role of sedimentation and erosion during continental rifting. Some concluding remarks are the following: 1) thermal blanketing effect of accumulated sediments in the rift basin leads to an increase of basement temperatures and enhance partial melting (Lizarralde et al., 2007), 2) higher sediment loading induce narrow rifting (Bialas and Buck, 2009), and 3) weaker lithospheres (i.e. weaker lower crust or thicker crusts) are more sensitive to the effects of sediment loading and thermal blanketing (Andrés-Martínez, personal communication).

Surfaces processes may change the tectonic style of the rifted margins, the conjugate asymmetry, the type of continent-ocean transition and the heat flow distribution. Therefore, these results complement my investigation.

6.3 Comparison with other model research

Due to the importance of the crustal structure and the extension velocity on rift evolution (e.g,. Brune et al., 2014; Buck, 1991; Huismans and Beaumont, 2014), more recent works have focused on systematically explore the interaction of these controls during margin formation. For example, Svartman Dias et al. (2016) and Tetreault and Buiter (2017) tested and described the evolution

of a suite of numerical models to help understanding how these controls influence the width and asymmetry of the final conjugate margins. However, these publications do not incorporate the modelling of melting and serpentinization. On the other hand, Davis and Lavier (2017) and Armitage et al. (2018) study the impact of the crustal structure and the extension velocity on the production and onset of melting, but they do not examine the tectonic style of the margins. This dissertation differ from the previous studies in that it explores whether it is possible to associate margin architectural styles to types of COT by including the processes of melting and serpentinization. Below I discuss the main results from the abovementioned publications in the context of my work.

6.3.1 Models from Svartman Dias et al. (2015) and Tetreault and Buiter (2017)

Both Svartman Dias et al. (2015a) and Tetreault and Buiter (2017) conducted 2D thermomechanical experiments by varying the initial crustal strength and extension velocity. Svartman Dias et al. (2015a) grouped the resulting conjugate margins into four end-members: (1) narrow asymmetric, (2) narrow near-symmetric, (3) wide asymmetric and (4) very wide highly asymmetric. Tetreault and Buiter (2017) also showed four groups: (1) narrow symmetric, (2) wide symmetric, (3) wide asymmetric and (4) rift jump, where a continental fragment is isolated. In this thesis, the conjugate margins classification includes: (1) narrow symmetric, (2) wide and narrow asymmetric, (3) wide near-symmetric, (4) ultra wide and narrow asymmetric and (5) very wide symmetric. Model results from the three publications (Table 6.2) indicate that a spectrum of conjugate margins styles can be produced by varying alone crustal strength and extension velocity.

	Svartman Dias et al. (2015a)	Tetreault and Buiter (2017)	Ros et al. (2017)
Conjugate margins type	width (km)	width (km)	width (km)
narrow symmetric	<100	∼100	∼100-150
narrow asymmetric	<100	-	∼150
wide symmetric	-	>100	>150
wide asymmetric	>100-300	>250	>200
very wide symmetric	-	-	>350
very wide asymmetric	200->350	(= wide asymmetric)	(= wide asymmetric)

Table 6.2: Conjugate margins classification from the modelling results of Svartman Dias et al. (2015a), Tetreault and Buiter (2017) and Ros et al. (2017) in terms of margin width and asymmetry.

Whether extension velocity or crustal strength controls the evolution of the rift will depend on the initial stratification and the range of velocity applied. In agreement with my modelling results (Fig. 4.11, Chapter 4), Svartman Dias et al. (2015a) found that faster extension velocities (10 mm/yr half-extension) tend to favor the development of more symmetric and narrower margins, while lower extension velocities ($<$ 5 mm/yr half-extension) are subject to the rheology in order to

lead to narrow or wide margins. Under the slower velocity range, it was concluded that an initial weak/thick crust includes a thick ductile lower crust that can form wide margins through a lateral migration of deformation, while a strong/thin crust includes a thin ductile lower crust that form narrow margins. I find an exception in the general trend of obtaining narrower margins for higher velocities with the model with weak and thin crust (WQ 35), which I discuss at the end of this section.

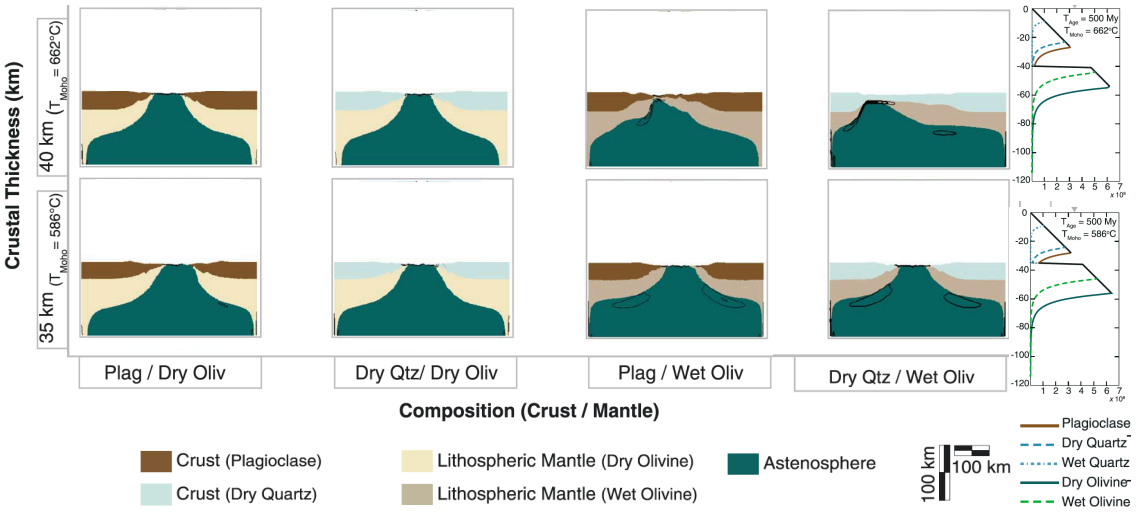

Figure 6.2: Initial yield strength envelopes (calculated for a strain rate of $10^{-14}s^{-1}$) and break-up snapshot of the models from Svartman Dias et al. (2015a) with the LAB at 114 km, extension velocity of 5 mm/yr, crustal thickness of 35 and 40 km, crustal rheology strong (plagioclase) and weak (dry quartz) and lithospheric mantle rheology strong (dry olivine) and weak (wet olivine). Modified from Svartman Dias et al. (2015a).

Svartman Dias et al. (2015a) does not show the model results for fast velocities, so I only gather the ones for an extension of 5 mm/yr in Figure 6.2. This shows the conjugate margins type for 8 models, with crustal thickness of 35 and 40 km, crustal rheology strong (plagioclase) and weak (dry quartz) and lithospheric mantle rheology strong (dry olivine) and weak (wet olivine). The results of these model setups are compared to some of the models presented in this thesis, shown in Figure 6.3, for the same extension velocity, crustal thickness of 35 and 40 km, lower crustal rheology strong (mafic granulite) and weak (wet quartzite) and strong lithospheric mantle.

Although the abovementioned general results are common to both studies, i.e. trends for thicker crusts or higher velocities, discrepancies arise when looking into the particular models. From the models of Svartman Dias et al. (2015a) shown in Figure 6.2, the two cases with thick crust and weak lithospheric mantle develop an asymmetry. In contrast, models in Ros et al. (2017) (Fig. 6.3) show asymmetry for a weak lower crust and strong lithospheric mantle, regardless of the crustal thickness. Therefore, on both studies, only the two cases with larger initial

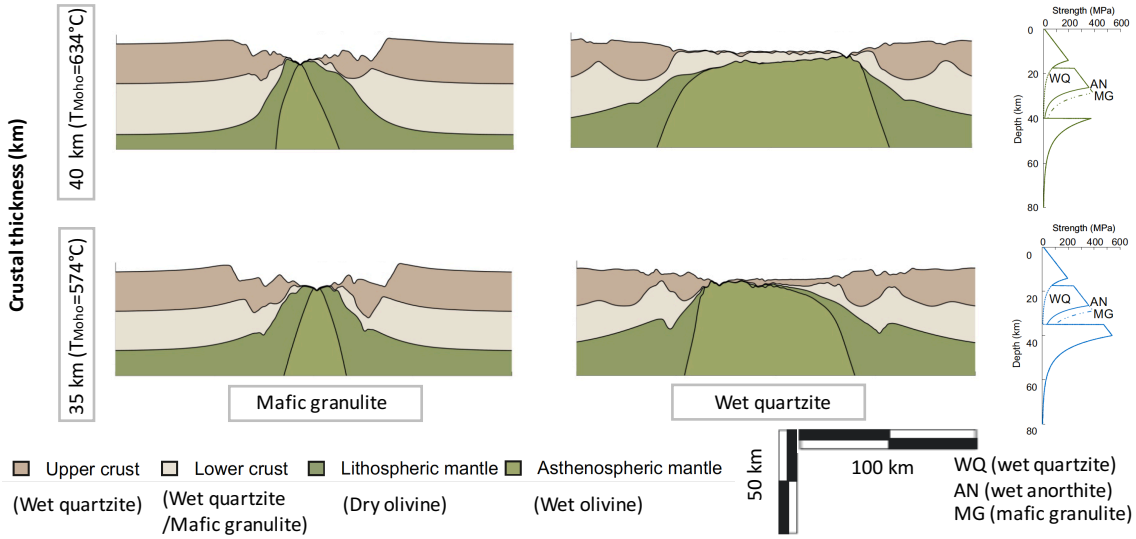

Figure 6.3: Initial yield strength envelopes (calculated for a strain rate of $10^{-14}s^{-1}$) and break-up snapshot of the models from Ros et al. (2017) with the LAB at 120 km, extension velocity of 5 mm/yr, crustal thickness of 35 and 40 km, lower crustal rheology strong (mafic granulite) and weak (wet quartzite).

crust-mantle decoupling result in asymmetric margins. These differences likely stems from the utilization of distinct end-member rheologies for the crust, initial thermal structure and treatment of strain softening. Svartman Dias et al. (2015a) model setups are slightly warmer with a thinner lithospheric mantle, which increases the thickness of the ductile lithospheric layers. This would result in a larger decoupling of the crust and mantle and could help in the formation of wide margins. On the other hand, models in Ros et al. (2017) include viscous strain softening that tend to form asymmetric margins (see Chapter 3). Therefore, during the extension of my models, the localization in ductile material is not only influenced by the power-law related strain rate softening but also by the viscous strain softening, unlike the models of Svartman Dias et al. (2015a) .

Tetreault and Buiter (2017) tested a suite of extension velocities, ranging from ultra-slow to fast, and four initial rheological structures, varying the amount of ductile crust. From those, I show in Figure 6.4 the conjugate margins of 9 models, with extension velocity of 2.5 mm/yr, 5 mm/yr and 10 mm/yr, crustal thickness of 39 km, and lower crustal rheology strong (wet feldspar) for Setup 2, intermediate (wet feldspar/10) for Setup 3 and weak (wet quartz) for Setup 4. I compare the type of conjugate margins that result for Setups 2 and 3, which show two initial ductile layers, to my models in Figure 11 of Chapter 4, with strong lower crust and thickness of 35 and 40 km. I also compare Setup 4, which shows an initial ductile middle-lower crust, to my models with weak lower crust and thickness of 35 km (Fig. 4.11).

Both Setup 2 and the model with strong and thin crust (MG 35), where crust and mantle are strongly coupled, result in narrow symmetric margins for all the velocities. However, the evolution

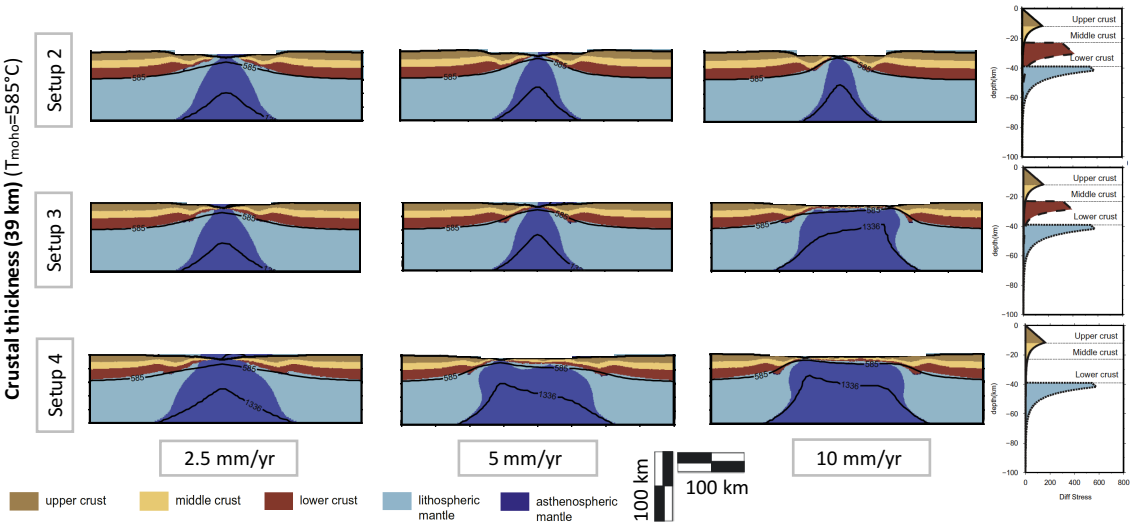

Figure 6.4: Initial yield strength envelopes (calculated for a strain rate of $10^{-15}s^{-1}$) and break-up snapshot of the models from Tetreault and Buiter (2017) with the LAB at 123 km, extension velocity of 2.5 mm/yr, 5 mm/yr and 10 mm/yr, crustal thickness of 39 km, lower crustal rheology strong (wet feldspar) for Setup 2, intermediate (wet feldspar/10) for Setup 3 and weak (wet quartz) for Setup 4. Modified from Tetreault and Buiter (2017).

of the models differs in terms of brittle versus ductile deformation. Tetreault and Buiter (2017) suggest that the models do not exhibit ductile deformation. Conversely, models in this thesis show crustal ductile deformation that is still highly coupled to the brittle parts, and that result in crustal-scale faults.

Setup 3 results in medium symmetric margins for 2.5 and 5 mm/yr and wide asymmetric margins for 10 mm/yr, where a jump rift is produced. For this initial rheological setup, Tetreault and Buiter (2017) suggest that rapid thermal thinning for higher velocities induce ductile behavior at late stages and leads to wider regions with highly thinned crust. When compared to the results for the strong and thick crust (MG 40) model, the opposite behavior is observed. Here, faster velocities results in an enhanced feedback between thermal thinning and strain softening, which localizes deformation in a narrow rift and results in narrow symmetric margins.

Finally, Setup 4 results in medium/wide symmetric margins for 2.5 mm/yr and asymmetric margins for 5 and 10 mm/yr, with a narrow and a very wide margin, where a rift jump occurs for the 5 mm/yr model. For 2.5 mm/yr, lithospheric cooling promotes a brittle behavior of the thinned crust at late stages. For 5 and 10 mm/yr, instead of thermal cooling, the rapid mantle upwelling weakens more the thinned crust and behaves more ductile. In Chapter 4, I also observe that faster velocities lead to wider asymmetric margins for the model with weak and thin crust (WQ 35). This behavior corroborates the findings of Brune et al. (2014), who suggested that faster velocities lead to more effective heat advection, which maintains for a longer time the low viscosity pocket

formed during the sequential faulting mode. As a consequence, wider hyperextended margins are produced.

Based on the models results, Tetreault and Buiter (2017) conclude that faster extension velocities lead to narrow symmetric margins for coupled models and to asymmetric margins with a highly thinned crust for decoupled models. In my models, only the decoupled crust-mantle model with weak and thin crust (WQ 35) follows the latter behavior. Although it is certain that the more decoupled model, with weak and thick crust (WQ 40), also shows asymmetric margins with a highly thinned crust, both the width of the wide margin and the degree of asymmetry decreases with increasing velocity. An important difference in the numerical modelling approach of Tetreault and Buiter (2017) with respect the modelling used in this study is the omission of elasticity, which has been demonstrated to be of great importance in the modelling of extensional systems (Olive et al., 2016). This could influence the different evolutions of the models.

These studies (i.e. Tetreault and Buiter (2017), Svartman Dias et al. (2015a), Ros et al. (2017) and Chapter 4) show an important interplay between crustal strength and extension velocity. The choice of rheology and thickness for the distinct crustal layers is crucial in the interaction of both key factors. In particular, through their impact on the lower crustal viscosity and crustal brittle-ductile transition, which leads to a more or less coupled lithosphere. It can be inferred that similar conjugate margin types can result from different combinations of these key factors if the behavior of the brittle versus ductile lithospheric parts is equivalent. The main differences from the model results discussed in this section may be strongly influenced by the type of strain softening considered (see Table 6.1). All these studies show models where the rift seems to migrate indefinitely without reaching final break-up. Svartman Dias et al. (2015a) explain this behavior by invoking a lack of magmatic input that finally helps breaking up the crust. However, I think it may be also a numerical artifact. I have investigated the evolution of the model WQ 35 extended by 10 mm/yr in order to constraint a possible cause. For instance, I checked the influence of shear heating, different ranges of plastic softening and the resolution of the model, among other parameters. I also analyzed if the condition imposed in the numerical modelling to separate two interfaces by a minimum of 200 m after remeshing was causing this stretching behavior. For that, I modelled a crustal setup where, instead of modelling independent upper and lower layers, I used a single crustal layer divided into two groups of tracers defining the corresponding material properties. I could not find a definite answer but I think one cause could be the use of plastic softening over an interval of accumulated plastic strain (see Huismans and Beaumont, 2003, for an exhaustive study on the relative effects of plastic and viscous strain softening).

6.3.2 Models from Davis and Lavier (2017)

Davis and Lavier (2017) conducted 2D thermomechanical numerical modelling experiments to investigate which are the controls on the formation of end-member rifted margins, i.e. magma-rich versus magma-poor. In their approach, a magma-rich margin was interpreted to form when magmatic emplacement began prior to crustal break-up, while a magma-poor margin formed when continental break-up occurred prior to magmatic emplacement. They tested several key potential factors to study the relative timing of crustal break-up and magmatic emplacement, of which crustal thickness, crustal rheology and extension velocity are of the interest of the present discussion. For that, the parameter space was reduced to a 'base model' and four subsequent models where only one variable was changed respect to the base model (Table 6.3). The base model is characterized by a LAB temperature of 1435°C, half-extension velocity of 5 mm/yr, crustal thickness of 35 km and crustal rheology of dry plagioclase. The additional runs comprise faster and slower velocities (10 and 2.5 km/yr respectively), thinner crust (30 km) and weaker crustal rheology (dry quartz). In order to compare my results to the ones of Davis and Lavier (2017), I summarize in Table 6.4 the equivalent models I have tested.

Results from Davis and Lavier (2017) show a predominance of magma-rich margins, while my results are all magma-poor. This difference comes, in the first place, from the definition of magma-rich and magma-poor, which in the case of Davis and Lavier (2017) is based on the relative timing of crustal break-up and magmatic emplacement while in Ros et al. (2017) comes from whether magmatism is more or less than expected from passive continental rifting of normal temperature mantle (i.e. undepleted mantle with a potential temperature of 1300°C according to Reston (2009a)). In the second place, the LAB temperature in my models is 1300°C and hence much lower. This difference strongly influences on the onset and amount of melting produced during the syn-rift. For example, McKenzie et al. (2005) showed that an enhance in mantle temperature of 12.5°C can increase the thickness by 1 km while Pérez-Gussinyé et al. (2006)

Variable	Model	Continental break-up (Myr)	Magmatic emplacement (Myr)	Relative timing (Myr)	Sea-floor spreading (Myr)	Magmatic character
Base	Base	15.05	11.00	4.05	13.10	Magma-rich
Extension rate	Fast (10 mm/yr)	5.65	5.55	0.10	7.00	Magma-rich
	Slow (2.5 mm/yr)	28.00	20.70	7.30	24.25	Magma-rich
Crustal thickness	Thin (30 km)	8.85	9.35	-0.50	11.60	Magma-poor
Crustal rheology	Weak (Dry quartz)	15.25	9.85	5.40	12.05	Magma-rich

Table 6.3: Timing of continental break-up, magmatic emplacement, relative timing between continental break-up and magmatic emplacement, sea-floor spreading for the models results of Davis and Lavier (2017) and their margin character.

Variable	Model	Crustal break-up (Myr)	Continental break-up (Myr)	Magmatic emplacement (Myr)	Relative timing (Myr)	Sea-floor spreading (Myr)	Magmatic character
Base	MG35 (5 mm/yr)	7.41	9.46	6.85	2.61	∼15	Magma-poor
Extension rate	Fast (MG35 10 mm/yr)	3.60	4.50	3.03	1.47	∼9	Magma-poor
	Slow (MG35 3 mm/yr)	16.95	17.79	14.16	3.63	∼28	Magma-poor
Crustal thickness	Thick (MG40)	8.73	9.89	6.87	3.02	∼15	Magma-poor
Crustal rheology	Weak (WQ35)	19.64	19.47	8.11	11.36	∼20	Magma-poor

Table 6.4: Timing of continental break-up, magmatic emplacement, relative timing between continental break-up and magmatic emplacement, sea-floor spreading for the models results of Ros et al. (2017) and their margin character.

suggested an increase of 18.5°C to achieve the same thickness. All our models are classified as magma-poor since the amount of melt is lower than the expected thickness produced in passive normal mantle upwelling, which typically leads to 6-7 km, i.e. the thickness of normal oceanic crust (e.g., Bown and White, 1995), besides the fact that in magma-rich margins the excessive magmatism usually results in the emplacement of igneous material with a thickness over 10 km (Kelemen and Holbrook, 1995; Reston and Manatschal, 2011).

According to all abovementioned, I agree that a rift that undergoes crustal and lithospheric mantle break-up before magmatic emplacement leads to magma-poor margins, as suggested by Davis and Lavier (2017), since all syn-rift melt is inhibited, however, magma-poor margins can also result from the opposite case as long as the amount of melt is low. In addition, the estimation of the onset of sea-floor spreading also changes for both studies. In the case of Davis and Lavier (2017), this onset is estimated for a magmatic thickness reaching 6 km, based on the tendency of melt production to balance at this thickness (Bown and White, 1995). However, in my study, the sea-floor spreading onset is assumed when the magmatic crustal thickness becomes constant with time. Although in average should be around 6 km, factors such as the potential mantle temperatures, depleted mantle or slow extension rates may limit the amount of melting during continental rifting (Pérez-Gussinyé et al., 2006), resulting in a maximum melt thickness between 1 and 6 km for ultraslow and slow velocities (Dick et al., 2003) similar to my results in Chapter 5. Regarding the figures of Davis and Lavier (2017), it would be interesting to show the continuation of the magmatic crustal thickness curve until a steady-state is reached.

Lastly, in my models magma emplacement occurs instantaneously while in Davis and Lavier (2017) occurs when regions of >2% melt are connected over a ≥3 km vertical thickness, as previously modelled by Schmeling (2006). Although the assumption is different, the model results would only be slightly affected.

Of the tested variables summarized in Table 6.3, Davis and Lavier (2017) find the crustal thickness as the most influential factor in the magmatic character of the margins. For a thinner crust, a

magma-poor character is expected while for a thicker crust a magma-rich character is favored. Following their criteria, the results agree with our modelling outcomes, which show how the onset of melting occurs earlier for larger coupling between crust and mantle, i.e. for thinner crusts and stronger rheologies, hence increasing the evidence of magmatism. However, in our model experiments, this does not imply a change from magma-poor to magma-rich margins.

For example, from the models of Ros et al. (2017), Table 6.4 shows that the thin model experiences a slightly earlier onset of melting than the thick model in addition to a shorter relative timing respect to continental break-up. This results in less accumulation of magma before break-up.

The second factor that highlights Davis and Lavier (2017) is the extension velocity, where faster velocities favor less pre-breakup melting. By comparing the relative timings in Table 6.3 and Table 6.4, our results also suggest this dependence, but, on the other hand, faster velocities increase the amount of melting generated, so that even if continental break-up is reached earlier for faster velocities, the accumulated melts are also larger, which may lead to more pre-breakup melting instead.

Finally, the last factor influencing the magmatic character is the crustal rheology (Davis and Lavier, 2017). The authors concluded that stronger rheologies may favor development of magma-poor margins. Both in this study and in Davis and Lavier (2017), the utilization of a weak rheology leads to a delay of continental break-up respect to the onset of melting and hence a higher accumulation of melts. In Ros et al. (2017) this translates into a more magmatic continent-ocean transition for models extended at fast velocities, but still under the magma-poor character.

6.3.3 Models from Armitage et al. (2018)

Armitage et al. (2018) developed 2D numerical models to explore the impact of crustal strength on melting during continental rifting. With this purpose, they tested two end-member rheologies for the lower crust, strong Columbia diabase and weak diabase (Fig. 6.5b). Numerical experiments by Armitage et al. (2018) have a crustal thickness of 35 km, with a 17.5 km upper crust and 17.5 lower crust. A wet quartzite rheology is used for the upper crust and models are extended at 7.5 mm/yr half-extension. Regarding the initial thermal lithosphere, the LAB is located at 100 km depth and three different potential temperatures are tested, which are 1350, 1400 and 1450°C. Although the thickness and the 'strong versus weak' composition of these models are similar to the thin-crust cases of Ros et al. (2017), i.e. models MG 35 and WQ 35, the pre-rift lithosphere is warmer.

Figure 6.5a shows the predicted melt thickness evolution over time for the different models of Armitage et al. (2018). The model results corroborate the finding of Ros et al. (2017) that crustal strength influences the onset of melting for ultra-slow velocities. For the different thermal structures, the onset of melting always starts earlier in the strong case. This result broadens to warmer lithospheres the conclusion found by Ros et al. (2017) that the onset of melting occurs earlier for strong lower crustal rheologies and it is delayed for larger decoupling between crust and mantle, which occurs with increasing crustal thickness or decreasing crustal strength. For the lowest potential temperature (1350°C) in Figure 6.5, the steady-state melt thickness is approximately 8 km for both crustal strengths. In the cases of Ros et al. (2017), the tested models use half-extension velocities of 3, 5 and 10 mm/yr, so the examples ran by Armitage et al. (2018) for a 7.5 km/yr velocity cannot be directly compared. The steady-state thickness for the cases with 5 and 10 mm/yr is of approximately 3.5 and 4.5 km respectively (Fig. 4 in Chapter 5).

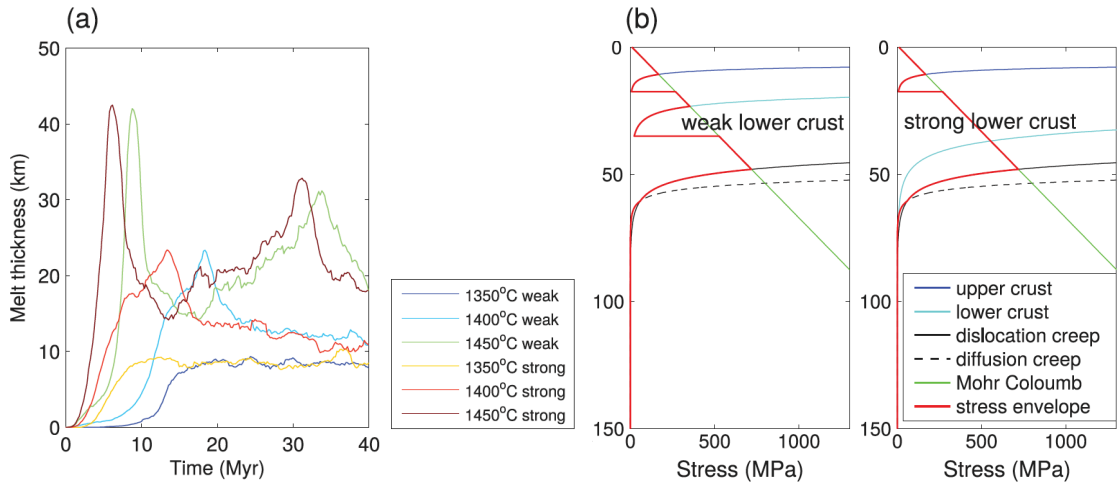

Figure 6.5: Model results from Armitage et al. (2018). a) Melt thickness as a function of time (half-extension velocity of 7.5 mm/yr). The mantle temperature is either 1350, 1400 or 1450°C and the lower crust is either strong or weak. b) Initial yield strength envelopes for the weak and strong models. The red line shows the strength envelope, the green line shows the Mohr Coulomb failure, the pale blue line shows the viscous flow law for the lower crust, the solid black line shows the dislocation creep law for the mantle, and the dashed black line shows the diffusion creep law. Modified from Armitage et al. (2018).

For larger velocities, the relative timing between the onset of melting for the different crustal strengths is much lower ($\leq$ 1Myr) than for the slowest case of 3 mm/yr ($>$ 1Myr). In contrast, the results of Armitage et al. (2018) show a relative timing of 10 Myr. This time difference is likely a result of the distinct end-member rheologies that have been tested and the 50°C thermal increase with respect to my models. In the supplementary of Ros et al. (2017), Figure S5 shows a steady-state melt thickness of 4.2 km for the strong model extended by 8 mm/yr. This result differs from the result of 8 km in Armitage et al. (2018) for the strong model, which may be a

consequence of the larger potential temperature used. This idea is supported by the models with 1400 and 1450°C potential temperatures of Armitage et al. (2018), which show larger amounts of melt than the models with 1350°C.

6.4 Comparison with natural rift examples

The thermomechanical evolution of continental rifting is controlled by a series of parameters whose individual influence is often difficult to isolate from observational data of natural examples. Therefore, progress has been made in the formulation of geodynamical modelling with the aim of investigate the control parameters involved in rift evolution. This has the advantage of having a virtual laboratory where multiple combinations of parameters can be tested and questioned in the context of geological observations.

This thesis is envisaged as a conceptual study to understand the interaction of key parameters during rifting and their control on the final margins, but also uses observational data from natural margins to constrain the initial and boundary conditions of the models (e.g., initial crustal thickness, extension velocity and rheological properties) since tectonic inheritance play an important role as well. The values of these parameters are based on the central South Atlantic margins, our study area. In Chapter 5 (Ros et al., 2017), first order characteristics of the rifted margins that result from numerical models are compared to seismic lines of three conjugate margins. Instead of using previous interpretations from the literature (e.g. Blaich et al., 2010, 2011; Kumar et al., 2013; Zalán et al., 2011), a reinterpretation of the lines was done in order to produce an integrated view of the conjugate margins in terms of asymmetry, thinning profile and faulting style. This included information from more recent publications on nature and thickness of onshore and offshore crustal deep structures (Assumpção et al., 2013a,b; Evain et al., 2015).

6.4.1 Continental rifted margin

A brief description of the first-order margin characteristics interpreted by the abovementioned publications is given here. For the Camamu-Gabon transect, the studies of Ros et al. (2017) and Blaich et al. (2010, 2011) (Fig. 6.6) show an asymmetric configuration with a narrow and abrupt crustal thinning along the Camamu margin and a wide and more gradual crustal thinning along the Gabon margin. In Ros et al. (2017), large blocks characterize the proximal margins and are related to large syn-tectonic subsidence. Also, faults dip mainly oceanward on both margins. In Blaich et al. (2010, 2011), the upper crust does not show marked brittle deformation, and large blocks and strong subsidence are interpreted.

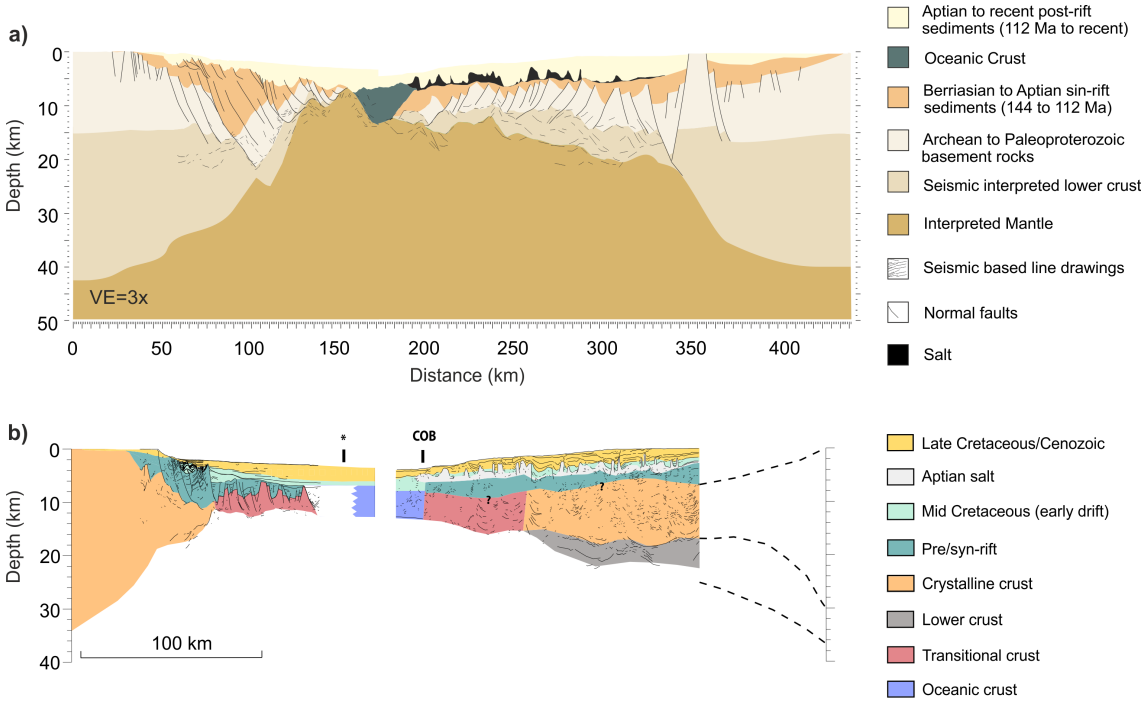

Figure 6.6: Conjugate transects along Camamu-Gabon basins a) from Ros et al. (2017) and b) modified from Blaich et al. (2011).

The interpretation of the Campos-Kwanza transect is discussed for the studies of Ros et al. (2017), Kumar et al. (2013) and Zalán et al. (2011) (Fig. 6.7). Kumar et al. (2013) show in Fig. 6.7b the conjugate lines on a South Atlantic reconstruction at 115 Ma. They interpret these lines as wide zones of thin continental crust with normal faulting of moderate to high angle, dipping mostly landward in the distal parts, few or none block rotation and limited syn-rift subsidence. The conjugate configuration is fairly symmetric with moderate crustal thinning. The interpretation of hyperextended crust and little syn-rift subsidence is also suggested by Ros et al. (2017), however the configuration of faults differ. In our interpretation faults dip both landward and basinward in the proximal parts, and oceanward in the distal parts. Even so, both studies agree that crustal thinning is partly produced by normal faulting and partly by lower crustal flow. On the other hand, Zalán et al. (2011) only show the interpretation of the Brazilian margin and also highlights the moderate crustal thinning and wide margin width. Faulting in this case is mostly oceanward.

Finally, the interpretation of the seismic line of North Santos is compared for the studies of Ros et al. (2017), Kumar et al. (2013) and Zalán et al. (2011) (Fig. 6.8). An extremely large margin with a wide zone of hyperextended continental is shown in the three studies. Ros et al. (2017) show a gentle crustal thinning, with horsts and grabens typically of small offsets and a related smooth syn-tectonic subsidence. The crustal thinning profile is more gradual in Kumar et al. (2013) and the normal faults die out against a mid crustal interface, which acts as a detachment horizon. Zalán

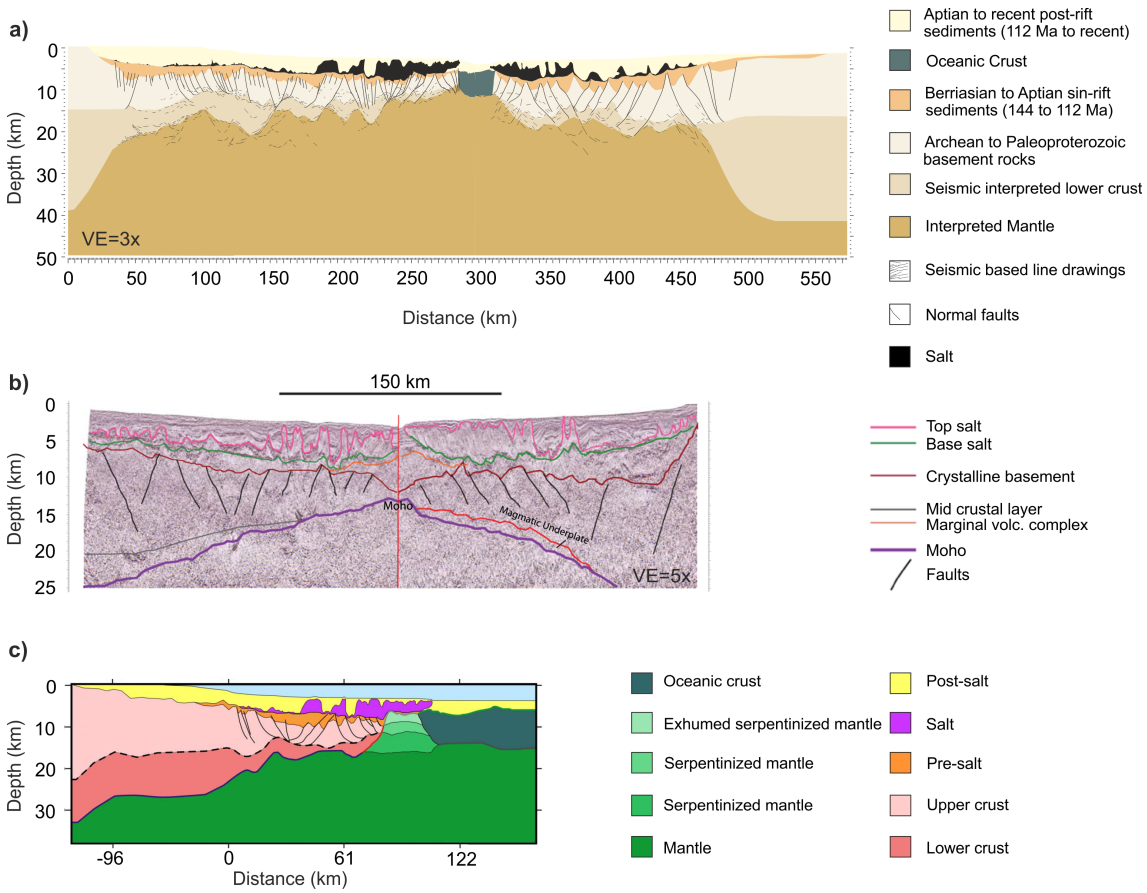

Figure 6.7: Conjugate transects along Campos-Kwanza basins a) from Ros et al. (2017) and b) modified from Kumar et al. (2013). c) Transect along Campos basin modified from Zalán et al. (2011).

et al. (2011) describe as highly irregular the observed crustal thinning, with a change from low to moderate gradient. Here, faults dip both ocean and landward in the proximal zone and mostly oceanward in the distal zone, as in Ros et al. (2017).

Some discrepancies between our interpretation and those of Zalán and Kumar rely on the data set used for the models. All interpretations are based on same MCS data set acquired by ION-GXT (line 1575), however, for our interpretation, the wide-angle refraction data (line SB01) from Evain et al. (2015) is also used. This recent data partly follows the tracks of the GXT line 1575 and extend it oceanward. Also, it is important to notice that our section landward starts with a 40 km thick continental crust, while in Kumar's starts with a 32 km thick and in Zalán's with 35 km. For example, we observe in our model some differences in the depth of the Moho with the models of Zalán et al. (2011) and Kumar et al. (2013). According to the study of Evain et al. (2015), these differences arise because both models constrained the position of the Moho mainly by gravity modelling. At the same time, we observe differences between the models of Zalán et al. (2011) and Kumar et al. (2013). This is because the data in Zalán et al. (2011) was depth processed only

to 25 km, while in Kumar et al. (2013) later acquired data of shallow water was used and merged to the earlier deep water lines, reprocessed and depth migrated to 40 km.

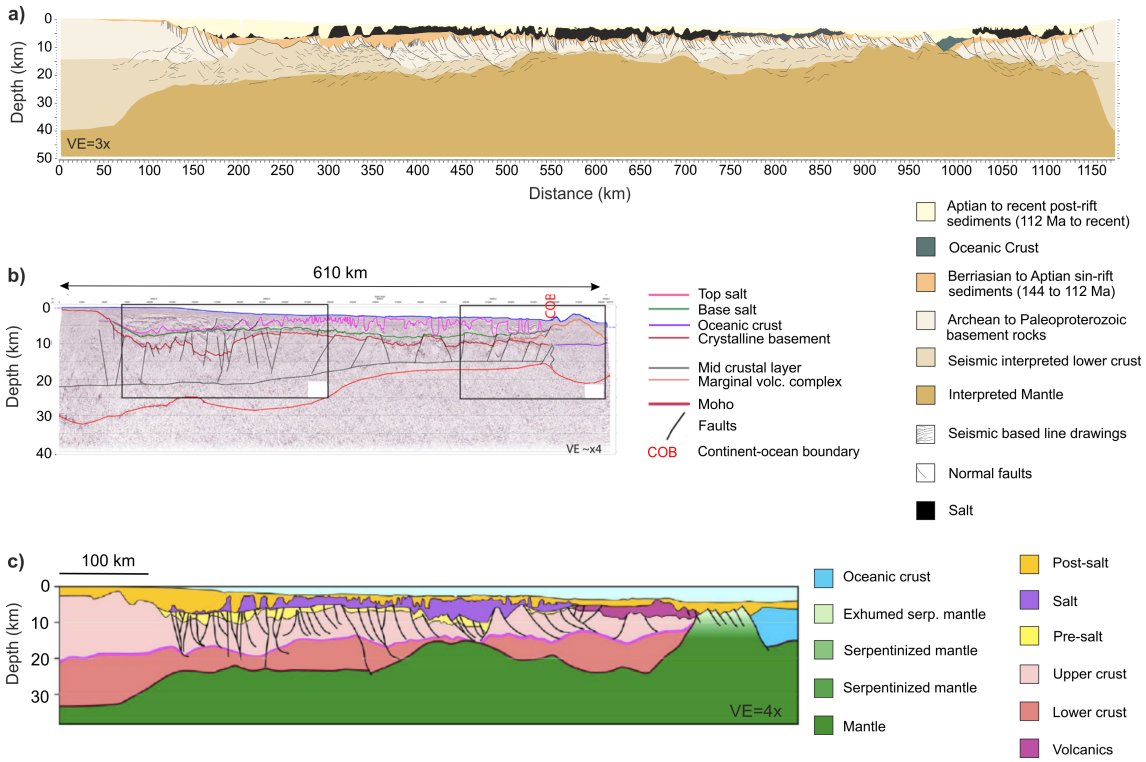

Figure 6.8: Conjugate transect along Santos-Kwanza basins a) from Ros et al. (2017). Transect along Santos basin modified from b) Kumar et al. (2013) and c) Zalán et al. (2011) and Svartman Dias et al. (2015b).

Nevertheless, it is not the intention of this study to refute any alternative interpretation but rather to discuss with models the first first-order controls on the localization of deformation, subsidence, magmatism and serpentinization, and their consequences for the variety of tectonic styles in rifted margins.

6.4.2 Continent-ocean transition

The nature of the COT along these central South Atlantic margins has been a topic of much debate in the recent years. For instance, Zalán et al. (2011) suggested a serpentinized exhumed mantle transition bordering the Santos and Campos basins while Kumar et al. (2013) interpreted an abrupt transition to Penrose-like oceanic crust accomplished by volcanic intrusions and extrusions. These different interpretations stress the need to sample the nature of the transition with closely spaced wide-angle, magnetic and gravity data, in order to image the relative proportions of magmatic versus serpentinized mantle material. At present, gravity models are used to interpret the nature

of the crust and are very ambiguous. Different models can obtain a good adjustment between measured and modelled anomalies. Most of the interpretations balance the high density contrast at the COT with a mixture of densities of basalt flows and crustal material.

Therefore, by understanding the key processes involved in rifting and oceanization, we propose that the use of numerical models that include mantle melting and serpentinization can aid interpretation of the COTs at the central South Atlantic segment. Here I compare the COT nature interpreted by Blaich et al. (2010, 2011), Kumar et al. (2013) and Zalán et al. (2011) and the predicted based on my model results (Ros et al., 2017).

According to Blaich et al. (2010, 2011) (Fig. 6.6b), the Camamu margin shows rotated fault-blocks and syn-rift sediment wedges, while in the Gabon conjugate margin the existence of salt deposits hinders the interpretation of the seismic signal and the recognition of similar structures. Their results suggest that the nature of the COT is continental and probably magmatically intruded. However, due to the non-uniqueness of the gravity anomalies, a gravity model with exhumed serpentinized mantle is also feasible, because of the broad range of densities that can have. Based on our modelling results, we suggest a COT characterized by exhumed serpentinized mantle (Fig. 6.6a).

For the Campos basin, Kumar et al. (2013) support the hypothesis of some magmatic underplating and no exposed serpentinized mantle (Fig. 6.7b). This is in agreement with Ros et al. (2017), that show a conceptual model with a COT dominated by magma and abrupt transition to oceanic crust (Fig. 6.7a). Conversely, Zalán et al. (2011) interpret exhumed mantle, which is divided into three zones of decreasing densities in order to reach a fit between measured and modelled gravity data (Fig. 6.7c). The latter interpretation is not totally discarded by Kumar et al. (2013), who, without seeing evidence of exhumed mantle, suggest that ambiguities in the seismic data could lead to another interpretation of the COT.

In the case of the Santos basin, Zalán et al. (2011) interpret 4 km of volcanic material above the 15 km thick continental crust in the Sao Paulo Plateau, just before the presence of exhumed mantle that transitions to oceanic crust (Fig. 6.8c). The exhumed mantle shows total serpentinization at the top and unknown decreasing percentage with depth. On the contrary, neither Ros et al. (2017) nor Kumar et al. (2013) notice evidence of exhumed mantle (Fig. 6.8a and b).

The approach of using dynamic models is to constrain interpretations that are not supported by physical processes. Even so, model results are subject to the assumptions of rheology, temperature and extension velocity, as well as melting and serpentinization parametrizations. These parameters are based on the few geological information we have. New studies are changing the paradigms, for example, Brune et al. (2016) recently proposed that the extension velocity accelerates during the

rift. This speed acceleration would result in the production of larger amounts of mantle melting in our models. On the other hand, the role of the Tristan da Cunha plume in the South Atlantic rift is still debated due to the controversial observation of magma-rich margins to the south of the Florianópolis Fracture Zone and magma-poor margins to the north (e.g., Fromm et al., 2015), where our study are is located. The impact of the plume during rifting would lead to more melt production. In short, both hypotheses could lead to more magmatism but in no case to the exhumation of serpentinized mantle.

6.5 Outlook

This dissertation investigates magma-poor continental rifting using 2D numerical modelling. The work focuses on the role of lower crustal strength and extension velocity on modes of continental lithosphere extension, i.e. narrow, sequential faulting, wide and core complex. The main results suggest that the predominance of one or other modes during extension is intimately linked to the tectonic style of the rifted conjugate margins and the nature of their COT. Characterization of the tectonic style is explained in terms of margin width, faulting style, fault associated subsidence and conjugate asymmetry, and it is related to the COT nature, based on the prevalence of magmatism or exposed serpentinized mantle.

For the characterization of the COT, the processes of melting and serpentinization were included in the numerical approach. The developed formulations for melt productivity, melt emplacement, underplating, heat release and serpentinization during continental rifting are explained in Chapter 2. The limitations of these implementations have been previously discussed in Sections 6.2.5, 6.2.6, 6.2.7 and 6.2.8. Nevertheless, they are valid as a first-order approximation and result in a wide variety of COTs.

Continental rifting is a multi-parametric and non-linear process. Therefore, to study the independent impact of a few parameters, it is necessary to define a pre-rift lithosphere. Chapter 3 discusses the available natural constraints for the setup of the model in terms of the rheological, thermal and compositional profiles. Additionally, sensitivity tests of important parameters influencing the model evolution were carried out. Special emphasis has been put on the sensitivity tests of strain localization mechanisms since understanding their influence on margin asymmetry is crucial for the evaluation of the model results. Numerous factors can influence continental extension, of which many have been broadly investigated, such as the initial Moho temperature (e.g., Svartman Dias et al., 2015a) or the depletion of the mantle (e.g., Armitage et al., 2013; Pérez-Gussinyé et al., 2006). Therefore, this chapter provides a framework for Chapters 4 and 5, with a careful choice of parameters common to all models presented in this thesis. Comparison of

the model results to previous studies can be certainly influenced by the assumed pre-conditions, but this can also shed light on the understanding of the different feedbacks between parameters.

Previous studies have shown how processes of strain localization concentrate deformation in a narrow rift while delocalization processes lead to the formation of a wide rift (e.g., Buck et al., 1999). Factors influencing these processes are strain softening, extension velocity and thickness of the brittle/ductile crust (e.g., Huismans and Beaumont, 2003; Kusznir and Park, 1987; Lavier and Buck, 2002; Tirel et al., 2008). Following these studies, Chapter 4 investigates the role of the lower crustal strength in localizing deformation into upper crustal faulting. A series of numerical experiments are run by systematically varying the crustal thickness, lower crustal rheology and extension velocity. Models results show that either very strong or very weak lower crustal strengths favour the development of upper crustal single faults. Very strong lower crust allows upper crustal faults to propagate through the lower crust and connect with upper mantle faults, forming a graben-like structure. Very weak lower crust allows a single fault to accommodate large offset as it abundantly flows toward the fault's tip, forming a core complex-like structure. In contrast, a lower crust that is enough weak but stronger than in the core complex mode, leads to a simultaneous development of faults distributed over a broad region. During the evolution of the models, the feedbacks between thermal thinning, strain softening and the elastic response of the lithosphere also influence the ability of the lower crust to flow and fill the accommodation space of the developing faults.

The type of lower crustal flow is linked to the formation of a low viscosity channel within the deep crust, whose extent and thickness varies with the mode of extension and is given by a threshold viscosity of $10^{21} Pa\,s$. For a strong lower crust, a restricted lower crustal flow leads to a narrow mode of extension, characterized by a very small and localized low viscosity area. For an intermediate strength, there is enough lower crustal flow within a small pocket of low viscosity in the hangingwall of the active fault that produces sequential faulting mode. For a weak lower crust, the flow is enough to distribute deformation over a broad region and lead to a wide mode, characterized by a thin and extended low viscosity layer. And for very weak lower crust, a massive flow results toward the tip of the fault, which is able to accumulate long offset and extend as a core complex mode, where the low-viscosity layer is very thick and distributed.

Another outcome of this work is the distinct distributions of crustal depth dependent thinning (DDT) for the different modes of extension. For the narrow, sequential faulting and wide modes, a small-scale crustal DDT is observed, which is induced by a lower crustal flow at a fault-block scale. In contrast, for the core complex mode, crustal DDT occurs at a large-scale, since the presence of a very weak lower crust results in its massive flow toward the rift axis. In order to infer what has happened to natural rift examples, we compare similar characteristics of those to

our models. We suggest that the presence of exhumed lower crust at the distal margins can be produced either by a large-scale crustal DDT as the one observed in the core complex mode of extension or by an initial lower crustal layer much thicker than the upper crust, without implying an abundant lower crustal flow. Moreover, we analyze the distribution of the surface heat flow with the lithospheric and crustal DDT for the different modes of extension. The results highlight how the sequential faulting mode implies a migration of the heat flow peak along the developing wide margin, reaching higher values for thicker upper crusts.

Natural systems show that upper crustal DDT is greatly exceed by that of the whole crust and lithosphere (Kusznir et al., 2005). I did not specifically addressed this problem in this work because Svartman Dias et al. (2016) already used geodynamic models to show that crustal DDT cannot explain alone the observed extension discrepancy, as previously anticipated by Reston (2009a) with the study of wide-angle seismic profiles. However, I find our crustal DDT results very interesting for the characterization of the modes of extension and heat flow distribution. These results could be integrated in kinematic models to constraint the heat flow and subsidence history.

This study also explores the influence of extension velocity on margin asymmetry, and shows how is subject to the strength of the lower crust. Although this type of study has been done alternatively by Tetreault and Buiter (2017) and Svartman Dias et al. (2015a) (as discussed in Section 6.3), my work was done independently of theirs. We show that two trends arise from increasing extension velocity in our models. The first one shows a change from asymmetric to symmetric margins for a strong or a very weak lower crustal rheology while the second one changes from asymmetric conjugates, with a relatively wide margin, to asymmetric conjugates and a wider margin, for a relatively weak lower crust. These changes are induced by the different proportions of brittle to ductile behavior of the lower crust as discussed in the chapter.

Motivated by the results of the study of the lower crustal strength and extension velocity and their impact on the rifted margins, Chapter 5 incorporates the generation of serpentinization, melting and underplating to relate these processes to the evolution and final stage of the rift. This study discusses the role of the lower crust on the link between the onset and amount of melting and serpentinization and the rift architecture.

This contribution is conceived, chiefly, as a general numerical study on the role of the lower crustal strength in controlling the rate of mantle upwelling versus the rate of crustal embrittlement, which in turn controls the onsets of melting and serpentinization respectively, and hence, the nature of the COT. To my knowledge, this is the first time that the impact of the lower crustal strength on serpentinization and melting and the relation to the architecture of the margins is studied.

We find that a change in lower crustal strength leads to differences on the relative timing between the onsets of melting and serpentinization, increasing for weaker rheologies that decouple more the crust and mantle. We demonstrate that models with slow extension velocity (3 mm/yr) and strong mafic granulite lower crust show serpentinization prior to melting and suggest that these models will present a COT characterized by exhumed and serpentinized mantle. In contrast, models with weaker wet quartzite lower crust undergo an earlier onset of melting than serpentinization at all velocities tested (3, 5 and 10 mm/yr half-extension), suggesting that a magmatically dominated COT would result.

Based on the numerical results, a conceptual model is proposed relating the extensional modes that a rifting goes through to the style of margins architecture and COTs. This model compares the implications of the two end-member rheologies tested for the lower crust: 1) a strong lower crust leads to a development of large faults mainly dipping oceanward, abrupt crustal thinning, large syn-rift subsidence and the onset of serpentinization prior to melting at low velocities, which results in a COT consisting of exhumed and serpentinized mantle and 2) a weak lower crust decreases the degree of coupling between crust and mantle, promotes the generation of small faults that dip both ocean- and landward, induces smooth crustal thinning, minor syn-rift subsidence and delays the onset of serpentinization more than it slows mantle upwelling and melting, which results in melting prior to serpentinization and a more magmatic COT.

By using what we learn from these numerical results, we make predictions of the COT nature at the central South Atlantic margins. We consider the width of these margins, their style of faulting and the degree of conjugate margin asymmetry as a diagnostic for whether the crust was strong or weak during rifting. We base these assumptions on the well-known modelling results of strong rheologies leading to narrow margins and weak rheologies to wide ones (see Chapter 4) and additionally support it by the geology of the study zone. The nature of COT is generally based on gravity models, which are very ambiguous, so several models can get good adjustment between measured and modelled anomalies. This leads to different interpretations for the COT depending on the type of modelling and the quality of the data. Therefore, we see modelling only as a tool to support interpretation of the COT. At present, there are not enough data to know how far the assumptions used in this type of modelling are really observed in the nature. The available data are not conclusive, neither on the width and nature of the COT nor on the appropriate rheology and structure of the crust and lithosphere onshore. However, what we can do is make simulations for specific parameters and compare the behavior of these simulations against observations.

In summary, this dissertation aims to better understand the evolution of present-day rifted margins by using numerical modelling as an additional tool in the study of the processes of extension of

magma-poor margins. The conceptual model shown in Figure 6.9 links the main outcomes of this study in an attempt to aid interpretation of natural rifted margins.

Despite the progress, it is still difficult to compare results from modelling with natural examples. The need to match observations of rifted margins leads to the use of kinematic models that can define a better evolution of a specific margin. However, comparing kinematic and dynamic models is still problematic (Karner et al., 2007). To better constraint observations, more detailed studies of wide-angle are required. These would allow for example to characterize better the boundary between upper and lower crust and hence the depth dependence of the crustal extensional mechanism. New wide angle seismic imaging techniques will help register S wave velocities, which provides useful information to distinguish lithologies. In particular, S waves are very important in the distinction between magmatic and serpentinized mantle rocks in the COT of magma-poor margins, where P wave velocities are very similar to the adjacent oceanic crust (Minshull, 2009).

A future challenge for research in magma-poor margins is to integrate studies of thermochronology, geomorphology, numerical modelling and analog experiments. A multi-scale view is also needed in order to improve the understanding of the feedbacks between the processes controlling continental rifting, from the rheology of polymineralic rocks to plate driving forces. This is nowadays the goal of many interdisciplinary geodynamic groups, like the COMPASS consortium group of which my PhD project is part.

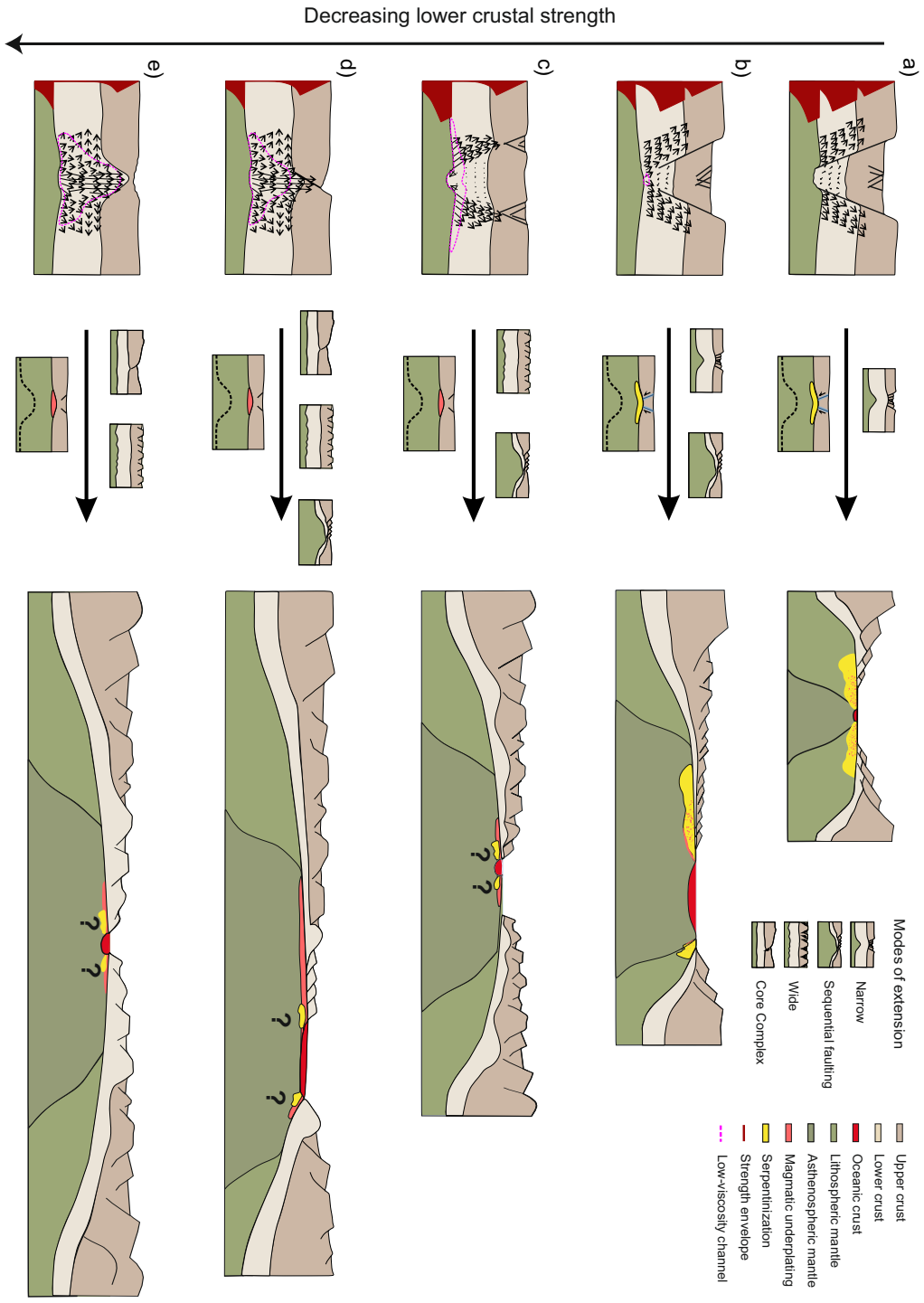

Figure 6.9: Conceptual model integrating the main results of the dissertation. Initial rift stage, transition between modes of extension implying an earlier onset of melt or serpentinization, and break-up stage. Extension velocity is 3 mm/yr. Cartoons show models with lower crustal strength ranging from strong (top panel) to very weak (bottom panel); (a) Mafic granulite and thin lower crust. (b) Mafic granulite and thick lower crust. (c) Wet quartzite and thin lower crust. (d) Wet quartzite and thick lower crust. (e) Dry quartzite (upper and lower crust) and thick lower crust.

CHAPTER

7

Conclusions

– A 2D numerical model is used to simulate magma-poor continental extension, gain insight into the key parameters and processes and explore the tectonic style and COT nature of the resulting rifted margins. By varying key parameters such as the initial crustal thickness, lower crustal rheology and extension velocity, the model results reproduce the observed variability of natural examples of magma-poor rifted margins, which ranges from narrow to wide widths, symmetric to asymmetric margins, strong to smooth subsidence, oceanward to landward dipping faulting and serpentinized to magmatic COT.

– Numerical models of continental extension may include viscous strain softening to account for the formation of lattice preferred orientations and the reduction in grain-size of the deforming rocks. The sensitivity results of this thesis show that viscous strain softening plays a role in controlling the mantle flow pattern and, in turn, the amount of melt generated by adiabatic decompression. However, when including a temperature dependence in the softening formulation, based on laboratory experiments, the development of mantle convection cells is delayed to the post-rift phase. This suggests that small-scale convection is not necessary present during magma-poor continental rifting.

– From the evolution of the tested models, four modes of extension are identified. Three of them may appear from the start of rifting or during extension, which are the narrow, wide and core complex modes, while the fourth mode, the sequential faulting one, only appears following another mode. The undergoing mode of extension is strongly dominated by the strength of the lower crust and hence its flow. For a strong lower crust, there is a restricted flow of lower crust that leads to a narrow mode. For an intermediate strength, there is enough flow of lower crust within a small pocket at the hangingwall of the dominant fault that helps the development of the sequential faulting mode. For a weak lower crust, there is flow distributing deformation over a broad region and producing a wide mode. And for a very weak lower crust, there is a massive flow toward the tip of the dominant fault that is

able to accumulate long offset and promote extension as a core complex mode. The strength of the lower crust may change during lithospheric thinning and trigger a transition to another mode of extension. Two types of modes transitions have been observed: 1) from strong to intermediate crustal strength, which results in a transition from narrow to sequential faulting mode and 2) from very weak to intermediate crustal strength, which results in a transition from core complex, to wide and to sequential faulting mode.

– The models show that localization of upper crustal brittle deformation into single or more faults depends on whether the topography around the fault can bend in response to slip, which in turn depends on the EET, strain softening and the ability of the lower crust to flow and fill the accommodation space. The latter is related to the formation of a low viscosity channel above the crust-mantle boundary, i.e. Moho, which extent limits the distance over which deformation can be transferred between both layers. The threshold viscosity that defines the thickness and extent of this low viscosity channel in the tested models is the isocontour $10^{21} Pa\,s$. The type of low viscosity channel can be used as a guide for determining the mode of extension: 1) the narrow mode is characterized by a very small and localized low viscosity area, 2) the sequential faulting mode by a low viscosity pocket in the hangingwall of the active fault, 3) the wide mode by a thin and extended low viscosity layer, and 4) the core complex mode by a very thick and distributed layer.

– The degree of margin asymmetry results from the interplay between extension velocity and lower crustal strength. Two trends arise from increasing extension velocity in the models: 1) a change from asymmetric to symmetric margins, for a strong or a very weak lower crustal rheology, and 2) a change from asymmetric conjugates with a relatively wide margin to asymmetric conjugates and a wider margin, for a relatively weak lower crust. These changes are induced by the different proportions of brittle to ductile behavior of the lower crust.

– All models present lithospheric and crustal DDT, where the amount of thinning of the lithospheric layers varies for the different modes of extension. The length scale of crustal DDT is large for the core complex mode, where the massive flow of the lower crust may lead to its exhumation, and small for the narrow, sequential faulting and wide modes, where the flow of the lower crust increases from the first to the last mode but always occurs at a fault-block scale. The model results also suggest that the presence of an initial lower crust thicker than the upper crust favors the exhumation of the lower crust without implying an abundant lower crustal flow. Therefore, large crustal DDT may be wrongly inferred at natural rifted margins when finding lower crustal exhumation, since it could be the result of the initial

proportion of upper- to lower-crust thickness and not of a large-scale flow of the lower crust during rifting.

– The distribution of surface heat flow also changes for the different modes of extension. The narrow and wide modes show similar values but in a localized or distributed region respectively. The sequential faulting mode implies the migration of the heat flow peak along the developing wide margin, where higher values are reached in models with thicker upper crusts due to the larger content in radioactive elements. Finally, the core complex mode localizes large heat flow values above the developing core complex.

– The results also show the importance of the lower crustal strength and the extension velocity in controlling the amount and onset of melting and serpentinization during magma-poor continental rifting. The more decoupled the crust-mantle system, the greater the delay of the onsets of melting and serpentinization, and this delay decreases with extension velocity. In addition, the relative timing between both onsets controls the nature of the COT. If serpentinization occurs prior to melting, the resulting COT is characterized by exhumed and serpentinized mantle, which occurs at very slow velocities for a strong lower crust such as mafic granulite. In contrast, if melting occurs prior to serpentinization, the resulting COT is predominantly magmatic, which occurs at velocities within the ultra-slow range of MORs for a weak lower crust such as wet quartzite.

– The COT nature is linked to the tectonic style of rifted margins through the modes of extension that continental lithosphere undergoes, which in turn depends on the strength of lower crust and extension velocity. Strong lower crusts lead to a development of large faults ($>$ 5 km) mainly dipping oceanward, abrupt crustal thinning, large syn-rift subsidence and onset of serpentinization prior to melting, which results in a COT consisting of exhumed and serpentinized mantle. Weaker rheologies decrease the degree of coupling between crust and mantle promoting initial distributed small faults ($<$ 5 km), dipping ocean- and landward, causing smooth crustal thinning and minor syn-rift subsidence. This delays serpentinization more than mantle upwelling and melting, so melting starts before serpentinization at any velocity within the ultra-slow range and leads to a more magmatic COT.

– The proposed conceptual model linking the COT nature and the tectonic style can be used as a predictive tool for the study of the nature of the COT in magma-poor rifted margins. In the central South Atlantic segment, the conjugate margins of Camamu-Gabon developed in a slow extension environment and are characterized by strong rheologies, this suggests they present a COT dominated by exhumed serpentinized mantle. However, the conjugates of Campos-Angola and North Santos-South Kwanza developed in a higher

extension environment and are characterized by weaker rheologies, which predicts a more magmatic COT with a rather abrupt transition to oceanic crust.

CHAPTER

A

Appendix

A.1 Numerical code overview

The FEM numerical code is divided into three main components: 1) the preprocessor that includes the input data and the generation of the mesh, 2) the processor that includes the mechanical and thermal solvers and 3) the postprocessor to analyze and visualize the results (Dabrowski et al., 2008). The main functions of the numerical code are summarized in the scheme below (after Andrés-Martínez, 2016).

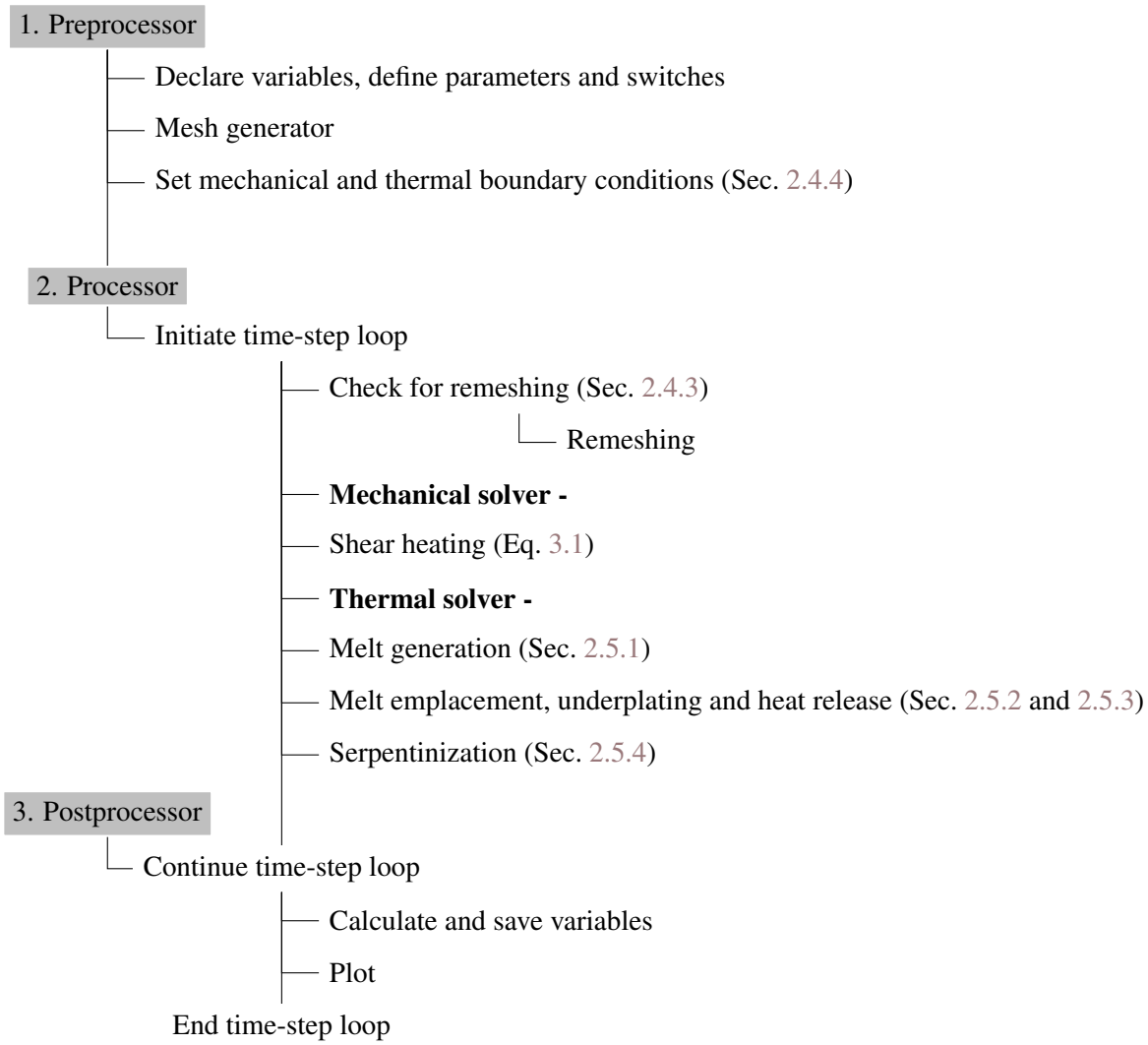
1. Preprocessor
Declare variables, define parameters and switches
Mesh generator
Set mechanical and thermal boundary conditions (Sec. 2.4.4)
2. Processor
Initiate time-step loop
Check for remeshing (Sec. 2.4.3)
Remeshing
Mechanical solver -
Shear heating (Eq. 3.1)
Thermal solver -
Melt generation (Sec. 2.5.1)
Melt emplacement, underplating and heat release (Sec. 2.5.2 and 2.5.3)
Serpentinization (Sec. 2.5.4)
3. Postprocessor
Continue time-step loop
Calculate and save variables
Plot
End time-step loop

- Mechanical solver

- Declare local variables
- Strain-rate iteration
  - Viscosity algorithm
    - Strain softening (Eqs. 3.7 and 3.8)
    - Calculate η_{eff}
  - Build stiffness matrix (A, Q, Q^T, M) and Rhs vector (F) (Sec. 2.4.2)
  - Reorder A and Rhs
  - Cholesky factorization of A
  - Uzawa-iteration solver
    - Solve velocities $v = A^{-1}Rhs$
    - Calculate the divergence $Div = Q^T M^{-1}$
    - Recalculate $Rhs = Rhs - \kappa * Div * Q$
  - End of Uzawa-iteration
  - Calculate historic strain ε_{II_h} for future strain softening
  - Calculate stress σ, deviatoric stress σ', strain ε, rigid-body rotation ω, strain rate $\dot{\varepsilon}$ and second invariants σ_{II} and $\dot{\varepsilon}_{II}$
- Check convergence and end the strain-rate iteration

- Thermal solver

- Declare local variables
- Build stiffness matrix (K_T)(Sec. 2.4.1)
- Reorder K_T and Rhs
- Solve temperatures $T = K_T^{-1}Rhs$

A.2 Lower crustal rheologies

For a given temperature and strain rate, the ductile strength of the crustal rock is determined by the material parameters. Figure A.1 represents the effective viscosity for a range of lower crustal rocks. For the typical range of temperatures within the lower crust at the start of continental rifting (300 to 700 $°C$) and a constant strain rate of $10^{-15}s^{-1}$, the strongest lower crust is given by the mafic granulite rheology and the weakest by dry quartzite. At the Moho temperature of our models ($\sim$ 600$°C$), the difference between this two end-members is of two orders of magnitude. Intermediates values are given by the rheologies of wet quartzite and dry diabase. For the numerical models of this thesis, I investigate the effects of the strong mafic granulite end-member and the weak wet quartzite, often used in studies of magma-poor continental rifting.

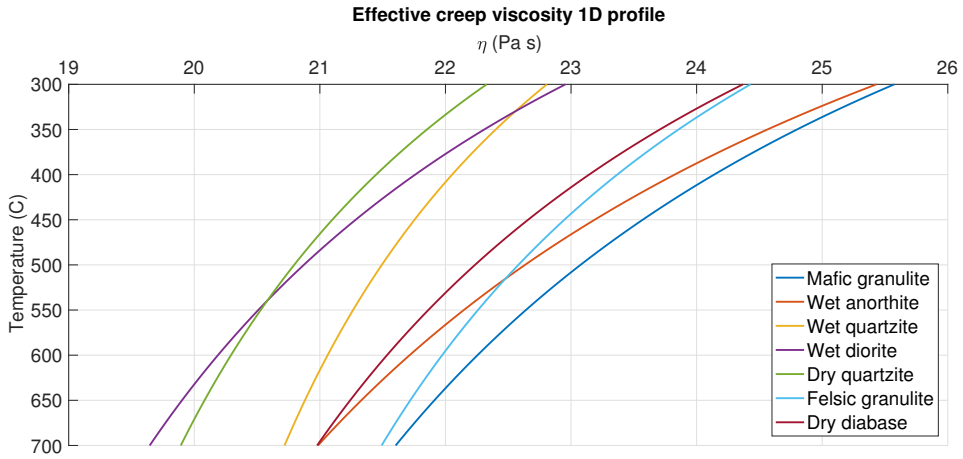

Figure A.1: Effective viscosity as a function of temperature based on laboratory measurements for mafic granulite (Wilks and Carter, 1990), wet anorthite (Rybacki and Dresen, 2000), wet quartzite (Gleason and Tullis, 1995), wet diorite (Tesauro et al., 2011), dry quartzite (Ranalli and Murphy, 1987), felsic granulite (Tejero and Ruiz, 2002), and dry diabase (Tesauro et al., 2011). Constant strain rate of $10^{-15}s^{-1}$.

Acknowledgements

I would like to thank all the people that made this Ph.D. journey more bearable. I would never have successfully completed this dissertation without their scientific, technical, and emotional help.

First of all, I would like to express my gratitude to Marta Pérez Gussinyé for giving me the opportunity to work on this fascinating project, for her continuous involvement and invaluable guidance and for the fruitful discussions concerning continental rifting, which helped me significantly in understanding the results of this thesis. Thanks also for inviting me to research at the University of Bremen upon your departure, this was a great experience.

I would like to acknowledge my second supervisor, Jason Phipps Morgan, for his support, advice and valuable explanations throughout these years.

I would also like to thank Miguel Andrés Martínez. He has been always enormously supportive, as a colleague, as a flatmate and as a friend. He is such a great person and scientist, who has helped me from coding in MATLAB to discussing geological interpretations.

Thanks to the COMPASS Research Group, for the three years of financial support, the great opportunity of attending international conferences such as the EGU and AGU, and the very interesting group meetings where I learnt a lot about different geological sub-disciplines. At the head of this group is Jürgen Adam, always there, with a big smile, and very enthusiast with the COMPASS group.

More people in the Earth Science Department has made my life easier as a Ph.D student. I acknowledge Lynne White, Diane Serpant, Julie Brown , Kevin D'Souza and Dan Parsonage for being always helpful with the administration, general doubts and the headaches from sending the computer abroad. I also acknowledge Frank Lehane and Mark Longbottom for their constant support with the technologies, this department clearly could not work without them and they deserve two big statues in the quad. I am also very grateful to Margaret Collinson, who has being of great assistance during the most critical period of my Ph.D. My sincere thanks also goes to

Javier Hernández-Molina and Robert Hall for giving me the opportunity to join them in Almería for two weeks and see first-hand how is to be a geologist on the field, which I really enjoyed. I am also grateful that Jenny Collier and Kenni D. Petersen agreed to act as examiners.

A huge *abrazo* goes to Juan and Miguel for hosting me in Madrid and make me feel part of the G.O. family.

I will be always in debt with the anonymous people of the coding and LaTex forums, valuable source of knowledge, and of the reggeaton sessions in YouTube that cheered me up during long working hours.

I want to send a big THANKS to all the Ph.D. friends who I have shared this experience with, most of them are already successful Doctors. In particular I would like to mention Albert de Montserrat, always inspiring with his helpful suggestions, engineering explanations and alcoholic invitations; Jorge Taramón, who with I share very good moments and who has supported me since the Master; Lucia Pérez, una 'todoterreno' from who to learn a lot and a great coffee-buddy; and Oris Rodriguez, forever-pusheen and great scientist.

Finally, I am very grateful to my BIG family, community and friends outside little Egham, always having a word of encouragement for me. And so much <3 to my mamá, my bro and mi pichón.

Panta rhei (Heraclitus)

Bibliography

V. Allken, R. S. Huismans, and C. Thieulot. Three-dimensional numerical modeling of upper crustal extensional systems. *Journal of Geophysical Research: Solid Earth*, 116(B10), 2011. 171, 175

M. Andrés-Martínez. *Rifted margin architecture and the interplay between mantle, crustal and surface processes from geodynamic numerical experiments*. PhD thesis, Royal Holloway, University of London, 2016. 67, 73, 205

M. Andrés-Martínez, J. P. Morgan, M. Pérez-Gussinyé, and L. Rüpke. A new free-surface stabilization algorithm for geodynamical modelling: Theory and numerical tests. *Physics of the Earth and Planetary Interiors*, 246:41–51, 2015. 28

J. Armitage, C. Jaupart, L. Fourel, and P. Allen. The instability of continental passive margins and its effect on continental topography and heat flow. *Journal of Geophysical Research: Solid Earth*, 118(4):1817–1836, 2013. 53, 195

J. J. Armitage. *Modelling the controls on melt generation during continental extension and breakup*. PhD thesis, University of Southampton, 2008. 70

J. J. Armitage, K. D. Petersen, and M. Pérez-Gussinyé. The role of crustal strength in controlling magmatism and melt chemistry during rifting and breakup. *Geochemistry, Geophysics, Geosystems*, 19(2):534–550, 2018. 181, 188, 189, 190

I. Artemieva. *The lithosphere: An interdisciplinary approach*. Cambridge University Press, 2011. 51

I. M. Artemieva. Global 1×1 thermal model tc1 for the continental lithosphere: implications for lithosphere secular evolution. *Tectonophysics*, 416(1):245–277, 2006. 52

I. M. Artemieva. The continental lithosphere: reconciling thermal, seismic, and petrologic data. *Lithos*, 109(1):23–46, 2009. 52

P. D. Asimow, M. Hirschmann, E. Stolper, and R. Nesbitt. An analysis of variations in isentropic melt productivity. *Philosophical Transactions: Mathematical, Physical and Engineering Sciences*, pages 255–281, 1997. 30

D. Aslanian, M. Moulin, J.-L. Olivet, P. Unternehr, L. Matias, F. Bache, M. Rabineau, H. Nouzé, F. Klingelheofer, I. Contrucci, et al. Brazilian and african passive margins of the central segment of the south atlantic ocean: Kinematic constraints. *Tectonophysics*, 468(1-4):98–112, 2009. 10

M. Assumpção, M. Bianchi, J. Julià, F. L. Dias, G. S. França, R. Nascimento, S. Drouet, C. G. Pavão, D. F. Albuquerque, and A. E. Lopes. Crustal thickness map of brazil: Data compilation and main features. *Journal of South American Earth Sciences*, 43:74–85, 2013a. 190

M. Assumpção, M. Feng, A. Tassara, and J. Julià. Models of crustal thickness for south america from seismic refraction, receiver functions and surface wave tomography. *Tectonophysics*, 609: 82–96, 2013b. 190

S. Bartzsch, S. Lebedev, and T. Meier. Resolving the lithosphere–asthenosphere boundary with seismic rayleigh waves. *Geophysical Journal International*, 186(3):1152–1164, 2011. 54

G. Bassi. Relative importance of strain rate and rheology for the mode of continental extension. *Geophysical Journal International*, 122(1):195–210, 1995. 6

G. Bayrakci, T. Minshull, D. Sawyer, T. J. Reston, D. Klaeschen, C. Papenberg, C. Ranero, J. Bull, R. Davy, D. Shillington, et al. Fault-controlled hydration of the upper mantle during continental rifting. *Nature Geoscience*, 9(5):384, 2016. 9, 43

C. Beaumont and S. J. Ings. Effect of depleted continental lithosphere counterflow and inherited crustal weakness on rifting of the continental lithosphere: general results. *Journal of Geophysical Research: Solid Earth*, 117(B8), 2012. 72

M. D. Behn and G. Ito. Magmatic and tectonic extension at mid-ocean ridges: 1. controls on fault characteristics. *Geochemistry, Geophysics, Geosystems*, 9(8), 2008. 36, 177, 178

M. D. Behn, W. R. Buck, and I. S. Sacks. Topographic controls on dike injection in volcanic rift zones. *Earth and Planetary Science Letters*, 246(3):188–196, 2006. 36, 178

R. W. Bialas and W. R. Buck. How sediment promotes narrow rifting: Application to the gulf of california. *Tectonics*, 28(4), 2009. 180

R. W. Bialas, W. R. Buck, and R. Qin. How much magma is required to rift a continent? *Earth and Planetary Science Letters*, 292(1-2):68–78, 2010. 178

O. Blaich, J. Faleide, F. Tsikalas, R. Lilletveit, D. Chiossi, P. Brockbank, and P. Cobbold. Structural architecture and nature of the continent-ocean transitional domain at the camamu and almada basins (ne brazil) within a conjugate margin setting. In *Geological Society, London,*

Petroleum Geology Conference series, volume 7, pages 867–883. Geological society of London, 2010. 190, 194

O. A. Blaich, J. I. Faleide, and F. Tsikalas. Crustal breakup and continent-ocean transition at south atlantic conjugate margins. *Journal of Geophysical Research: Solid Earth*, 116(B1), 2011. 190, 191, 194

B. Bos and C. J. Spiers. Frictional-viscous flow of phyllosilicate-bearing fault rock: Microphysical model and implications for crustal strength profiles. *Journal of Geophysical Research: Solid Earth*, 107(B2), 2002. 66, 67

R. Boutilier and C. Keen. Small-scale convection and divergent plate boundaries. *Journal of Geophysical Research: Solid Earth*, 104(B4):7389–7403, 1999. 3

J. W. Bown and R. S. White. Effect of finite extension rate on melt generation at rifted continental margins. *Journal of Geophysical Research: Solid Earth*, 100(B9):18011–18029, 1995. 2, 32, 187

K. Brodie and E. Rutter. The role of transiently fine-grained reaction products in syntectonic metamorphism: natural and experimental examples. *Canadian Journal of Earth Sciences*, 24 (3):556–564, 1987. 64

J. Brun and M. Beslier. Mantle exhumation at passive margins. *Earth and Planetary Science Letters*, 142(1-2):161–173, 1996. 6

S. Brune. Rifts and rifted margins: A review of geodynamic processes and natural hazards. *Plate Boundaries and Natural Hazards*, 219:13, 2016. 171

S. Brune and J. Autin. The rift to break-up evolution of the gulf of aden: Insights from 3d numerical lithospheric-scale modelling. *Tectonophysics*, 607:65–79, 2013. 173

S. Brune, A. A. Popov, and S. V. Sobolev. Modeling suggests that oblique extension facilitates rifting and continental break-up. *Journal of Geophysical Research: Solid Earth*, 117(B8), 2012. 72, 171

S. Brune, C. Heine, M. Pérez-Gussinyé, and S. V. Sobolev. Rift migration explains continental margin asymmetry and crustal hyper-extension. *Nature Communications*, 5, 2014. 6, 64, 72, 171, 174, 175, 180, 184

S. Brune, S. E. Williams, N. P. Butterworth, and R. D. Müller. Abrupt plate accelerations shape rifted continental margins. *Nature*, 536(7615):201, 2016. 172, 194

S. Brune, G. Corti, and G. Ranalli. Controls of inherited lithospheric heterogeneity on rift linkage: Numerical and analog models of interaction between the kenyan and ethiopian rifts across the turkana depression. *Tectonics*, 36(9):1767–1786, 2017a. 175

S. Brune, C. Heine, P. D. Clift, and M. Pérez-Gussinyé. Rifted margin architecture and crustal rheology: Reviewing iberia-newfoundland, central south atlantic, and south china sea. *Marine and Petroleum Geology*, 79:257–281, 2017b. 6, 72, 174

W. Buck. Dynamic processes in extensional and compressional settings: The dynamics of continental breakup and extension. 2007. 178

W. R. Buck. Modes of continental lithospheric extension. *Journal of Geophysical Research: Solid Earth*, 96(B12):20161–20178, 1991. 6, 51, 74, 180

W. R. Buck and L. L. Lavier. A tale of two kinds of normal fault: the importance of strain weakening in fault development. *Geological Society, London, Special Publications*, 187(1): 289–303, 2001. 66

W. R. Buck and A. N. Poliakov. Abyssal hills formed by stretching oceanic lithosphere. *Nature*, 392(6673):272, 1998. 67

W. R. Buck, L. L. Lavier, and A. N. Poliakov. How to make a rift wide. *Philosophical Transactions-Royal Society of London Series a Mathematical Physical and Engineering Sciences*, pages 671–689, 1999. 64, 74, 196

A. L. Cameselle, C. R. Ranero, D. Franke, and U. Barckhausen. The continent-ocean transition on the northwestern south china sea. *Basin Research*, 29(S1):73–95, 2017. 6

M. Cannat, G. Manatschal, D. Sauter, and G. Peron-Pinvidic. Assessing the conditions of continental breakup at magma-poor rifted margins: What can we learn from slow spreading mid-ocean ridges? *Comptes Rendus Geoscience*, 341(5):406–427, 2009. 8, 32

D. Chapman. Thermal gradients in the continental crust. *Geological Society, London, Special Publications*, 24(1):63–70, 1986. 52

D. Chian, K. E. Louden, and I. Reid. Crustal structure of the labrador sea conjugate margin and implications for the formation of nonvolcanic continental margins. *Journal of Geophysical Research: Solid Earth*, 100(B12):24239–24253, 1995. 3

D. Chian, K. E. Louden, T. A. Minshull, and R. B. Whitmarsh. Deep structure of the ocean-continent transition in the southern iberia abyssal plain from seismic refraction profiles: Ocean

drilling program (legs 149 and 173) transect. *Journal of Geophysical Research: Solid Earth*, 104(B4):7443–7462, 1999. 6, 43

I. Contrucci, F. Klingelhöfer, J. Perrot, R. Bartolome, M.-A. Gutscher, M. Sahabi, J. Malod, and J.-P. Rehault. The crustal structure of the nw moroccan continental margin from wide-angle and reflection seismic data. *Geophysical Journal International*, 159(1):117–128, 2004a. 3, 7

I. Contrucci, L. Matias, M. Moulin, L. Géli, F. Klingelhofer, H. Nouzé, D. Aslanian, J.-L. Olivet, J.-P. Réhault, and J.-C. Sibuet. Deep structure of the west african continental margin (congo, zaïre, angola), between 5 s and 8 s, from reflection/refraction seismics and gravity data. *Geophysical Journal International*, 158(2):529–553, 2004b. 3

C. A. Currie and R. D. Hyndman. The thermal structure of subduction zone back arcs. *Journal of Geophysical Research: Solid Earth*, 111(B8), 2006. 52

M. Dabrowski, M. Krotkiewski, and D. Schmid. Milamin: Matlab-based finite element method solver for large problems. *Geochemistry, Geophysics, Geosystems*, 9(4), 2008. 23, 26, 205

K. A. Daniels, I. Bastow, D. Keir, R. Sparks, and T. Menand. Thermal models of dyke intrusion during development of continent–ocean transition. *Earth and Planetary Science Letters*, 385: 145–153, 2014. 36, 177

J. K. Davis and L. L. Lavier. Influences on the development of volcanic and magma-poor morphologies during passive continental rifting. *Geosphere*, 13(5):1524–1540, 2017. 181, 186, 187, 188

J. De Bresser, J. Ter Heege, and C. Spiers. Grain size reduction by dynamic recrystallization: can it result in major rheological weakening? *International Journal of Earth Sciences*, 90(1):28–45, 2001. 64

A. de Montserrat, J. Hennig, J. Morgan, and R. Hall. "rapid cooling and exhumation of lower crust. insights from numerical models and application to se asia". 2018. 67

S. Dean, T. Minshull, R. Whitmarsh, and K. Louden. Deep structure of the ocean-continent transition in the southern iberia abyssal plain from seismic refraction profiles: The iam-9 transect at 40 20′ n. *Journal of Geophysical Research: Solid Earth*, 105(B3):5859–5885, 2000. 3

H. J. Dick, J. Lin, and H. Schouten. An ultraslow-spreading class of ocean ridge. *Nature*, 426 (6965):405–412, 2003. 3, 8, 9, 187

N. G. Direen, H. M. Stagg, P. A. Symonds, and J. B. Colwell. Dominant symmetry of a conjugate southern australian and east antarctic magma-poor rifted margin segment. *Geochemistry, Geophysics, Geosystems*, 12(2), 2011. 5

N. W. Driscoll and G. D. Karner. Lower crustal extension across the northern carnarvon basin, australia: Evidence for an eastward dipping detachment. *Journal of Geophysical Research: Solid Earth*, 103(B3):4975–4991, 1998. 6

D. C. Drucker and W. Prager. Soil mechanics and plastic analysis or limit design. *Quarterly of applied mathematics*, 10(2):157–165, 1952. 22

J. A. Dunbar and D. S. Sawyer. How preexisting weaknesses control the style of continental breakup. *Journal of Geophysical Research: Solid Earth*, 94(B6):7278–7292, 1989. 72

T. Duretz, B. Petri, G. Mohn, S. Schmalholz, F. Schenker, and O. Müntener. The importance of structural softening for the evolution and architecture of passive margins. *Scientific reports*, 6, 2016. 68, 77, 174

S. Dyksterhuis, P. Rey, R. Müller, and L. Moresi. Effects of initial weakness on rift architecture. *Geological Society, London, Special Publications*, 282(1):443–455, 2007. 72, 73, 74

R. A. Edwards, R. B. Whitmarsh, and R. A. Scrutton. The crustal structure across the transform continental margin off ghana, eastern equatorial atlantic. *Journal of Geophysical Research: Solid Earth*, 102(B1):747–772, 1997. 2

Y. Elesin, T. Gerya, I. M. Artemieva, and H. Thybo. Samovar: a thermomechanical code for modeling of geodynamic processes in the lithosphere—application to basin evolution. *Arabian journal of geosciences*, 3(4):477–497, 2010. 175

S. Emmanuel and B. Berkowitz. Suppression and stimulation of seafloor hydrothermal convection by exothermic mineral hydration. *Earth and Planetary Science Letters*, 243(3):657–668, 2006. 8, 45

J. Escartin, G. Hirth, and B. Evans. Effects of serpentinization on the lithospheric strength and the style of normal faulting at slow-spreading ridges. *Earth and Planetary Science Letters*, 151 (3-4):181–189, 1997. 46

M. Evain, A. Afilhado, C. Rigoti, A. Loureiro, D. Alves, F. Klingelhoefer, P. Schnurle, A. Feld, R. Fuck, J. Soares, et al. Deep structure of the santos basin-são paulo plateau system, se brazil. *Journal of Geophysical Research: Solid Earth*, 120(8):5401–5431, 2015. 7, 190, 192

U. H. Faul. Melt retention and segregation beneath mid-ocean ridges. *Nature*, 410(6831):920, 2001. 8

K. M. Fischer, H. A. Ford, D. L. Abt, and C. A. Rychert. The lithosphere-asthenosphere boundary. *Annual Review of Earth and Planetary Sciences*, 38:551–575, 2010. 54

D. Forsyth and S. Uyeda. On the relative importance of the driving forces of plate motion. *Geophysical Journal International*, 43(1):163–200, 1975. 172

S. Frederiksen and J. Braun. Numerical modelling of strain localisation during extension of the continental lithosphere. *Earth and Planetary Science Letters*, 188(1):241–251, 2001. 69, 72, 175

T. Fromm, L. Planert, W. Jokat, T. Ryberg, J. H. Behrmann, M. H. Weber, and C. Haberland. South atlantic opening: A plume-induced breakup? *Geology*, 43(10):931–934, 2015. 195

T. Funck, J. R. Hopper, H. C. Larsen, K. E. Louden, B. E. Tucholke, and W. S. Holbrook. Crustal structure of the ocean-continent transition at flemish cap: Seismic refraction results. *Journal of Geophysical Research: Solid Earth*, 108(B11), 2003. 3

T. Funck, H. R. Jackson, K. E. Louden, S. A. Dehler, and Y. Wu. Crustal structure of the northern nova scotia rifted continental margin (eastern canada). *Journal of Geophysical Research: Solid Earth*, 109(B9), 2004. 3

T. Gerya. *Introduction to numerical geodynamic modelling*. Cambridge University Press, 2009. 14, 21, 22, 53

T. Gerya and B. Stöckhert. Two-dimensional numerical modeling of tectonic and metamorphic histories at active continental margins. *International Journal of Earth Sciences*, 95(2):250–274, 2006. 20

G. C. Gleason and J. Tullis. A flow law for dislocation creep of quartz aggregates determined with the molten salt cell. *Tectonophysics*, 247(1):1–23, 1995. 50, 208

C. Goetze and B. Evans. Stress and temperature in the bending lithosphere as constrained by experimental rock mechanics. *Geophysical Journal International*, 59(3):463–478, 1979. 173

J. Goslin, P. Beuzart, J. Francheteau, and X. Le Pichon. Thickening of the oceanic layer in the pacific ocean. *Marine Geophysical Researches*, 1(4):418–427, 1972. 8

A. Gudmundsson. Deflection of dykes into sills at discontinuities and magma-chamber formation. *Tectonophysics*, 500(1):50–64, 2011. 33

F. Gueydan, C. Morency, and J.-P. Brun. Continental rifting as a function of lithosphere mantle strength. *Tectonophysics*, 460(1-4):83–93, 2008. 51

B. R. Hacker, P. B. Kelemen, and M. D. Behn. Continental lower crust. *Annual Review of Earth and Planetary Sciences*, 43:167–205, 2015. 52

V. Hamza and F. Vieira. Global distribution of the lithosphere-asthenosphere boundary: a new look. *Solid Earth*, 3(2):199, 2012. 52

J. Handin. Section 10: strength and ductility. *Geological Society of America Memoirs*, 97:223–290, 1966. 66

E. H. Hartz and Y. Y. Podladchikov. Toasting the jelly sandwich: The effect of shear heating on lithospheric geotherms and strength. *Geology*, 36(4):331–334, 2008. 77

J. Hasenclever. Modeling mantle flow and melting processes at mid-ocean ridges and subduction zones—development and application of numerical models. 2010. 28, 29, 30, 32, 33

C. Heine, J. Zoethout, and R. Müller. Kinematics of the south atlantic rift. *Solid Earth*, 4(2), 2013. 3, 52

M. Hirschmann, E. Stolper, and M. Ghiorso. Perspectives on shallow mantle melting from thermodynamic calculations. *Mineralogical Magazine*, 58(1):418–419, 1994. 29

M. M. Hirschmann. Water, melting, and the deep earth h2o cycle. *Annu. Rev. Earth Planet. Sci.*, 34:629–653, 2006. 62

G. Hirth and D. Kohlstedt. Rheology of the upper mantle and the mantle wedge: A view from the experimentalists. *Inside the subduction Factory*, pages 83–105, 2003. 19, 50, 54, 62

G. Hirth and D. L. Kohlstedt. Water in the oceanic upper mantle: implications for rheology, melt extraction and the evolution of the lithosphere. *Earth and Planetary Science Letters*, 144(1): 93–108, 1996. 19, 29, 63

A. B. Hölker, K. Holliger, G. Manatschal, and F. Anselmetti. Seismic reflectivity of detachment faults of the iberian and tethyan distal continental margins based on geological and petrophysical data. *Tectonophysics*, 350(2):127–156, 2002. 175

J. R. Hopper and W. R. Buck. The initiation of rifting at constant tectonic force: role of diffusion creep. *Journal of Geophysical Research: Solid Earth*, 98(B9):16213–16221, 1993. 173

J. R. Hopper and W. R. Buck. The effect of lower crustal flow on continental extension and passive margin formation. *Journal of Geophysical Research: Solid Earth*, 101(B9):20175–20194, 1996. 6

J. R. Hopper, J. C. Mutter, R. L. Larson, and C. Z. Mutter. Magmatism and rift margin evolution: Evidence from northwest australia. *Geology*, 20(9):853–857, 1992. 2

R. Huismans and C. Beaumont. Roles of lithospheric strain softening and heterogeneity in determining the geometry of rifts and continental margins. *Geological Society, London, Special Publications*, 282(1):111–138, 2007. 69, 72, 175

R. Huismans and C. Beaumont. Depth-dependent extension, two-stage breakup and cratonic underplating at rifted margins. *Nature*, 473(7345):74, 2011. 73, 171

R. S. Huismans and C. Beaumont. Asymmetric lithospheric extension: The role of frictional plastic strain softening inferred from numerical experiments. *Geology*, 30(3):211–214, 2002. 67, 69

R. S. Huismans and C. Beaumont. Symmetric and asymmetric lithospheric extension: Relative effects of frictional-plastic and viscous strain softening. *Journal of Geophysical Research: Solid Earth*, 108(B10), 2003. 64, 69, 72, 175, 185, 196

R. S. Huismans and C. Beaumont. Complex rifted continental margins explained by dynamical models of depth-dependent lithospheric extension. *Geology*, 36(2):163–166, 2008. 3

R. S. Huismans and C. Beaumont. Rifted continental margins: The case for depth-dependent extension. *Earth and Planetary Science Letters*, 407:148–162, 2014. 6, 73, 175, 180

G. Ito, J. Lin, and C. W. Gable. Dynamics of mantle flow and melting at a ridge-centered hotspot: Iceland and the mid-atlantic ridge. *Earth and Planetary Science Letters*, 144(1-2):53–74, 1996. 32

K. Iyer, L. H. Rüpke, J. Phipps Morgan, and I. Grevemeyer. Controls of faulting and reaction kinetics on serpentinization and double benioff zones. *Geochemistry, Geophysics, Geosystems*, 13(9), 2012. 8, 45

S. Jammes and L. L. Lavier. The effect of bimineralic composition on extensional processes at lithospheric scale. *Geochemistry, Geophysics, Geosystems*, 17(8):3375–3392, 2016. 174

S.-i. Karato. Rheology of the earth's mantle: A historical review. *Gondwana Research*, 18(1): 17–45, 2010. 62, 63

S.-i. Karato and P. Wu. Rheology of the upper mantle: A synthesis. *Science*, 260(5109):771–778, 1993. 19, 176

S.-i. Karato, M. R. Riedel, and D. A. Yuen. Rheological structure and deformation of subducted slabs in the mantle transition zone: implications for mantle circulation and deep earthquakes. *Physics of the Earth and Planetary Interiors*, 127(1-4):83–108, 2001. 173

G. Karner, G. Manatschal, and L. Pinheiro. Imaging, mapping and modelling continental lithosphere extension and breakup: an introduction. *Geological Society, London, Special Publications*, 282(1):1–8, 2007. 199

I. Katayama and S.-i. Karato. Low-temperature, high-stress deformation of olivine under water-saturated conditions. *Physics of the Earth and Planetary Interiors*, 168(3-4):125–133, 2008. 173

I. Katayama, K.-i. Hirauchi, K. Michibayashi, and J.-i. Ando. Trench-parallel anisotropy produced by serpentine deformation in the hydrated mantle wedge. *Nature*, 461(7267):1114, 2009. 45

B. J. Kaus. Factors that control the angle of shear bands in geodynamic numerical models of brittle deformation. *Tectonophysics*, 484(1):36–47, 2010. 21, 23

S. Kawano, I. Katayama, and K. Okazaki. Permeability anisotropy of serpentinite and fluid pathways in a subduction zone. *Geology*, 39(10):939–942, 2011. 45

P. Kelemen, G. Hirth, N. Shimizu, M. Spiegelman, and H. Dick. A review of melt migration processes in the adiabatically upwelling mantle beneath oceanic spreading ridges. *Philosophical Transactions of the Royal Society of London A: Mathematical, Physical and Engineering Sciences*, 355(1723):283–318, 1997. 8

P. B. Kelemen and W. S. Holbrook. Origin of thick, high-velocity igneous crust along the us east coast margin. *Journal of Geophysical Research: Solid Earth*, 100(B6):10077–10094, 1995. 2, 187

S. H. Kirby. Rock mechanics observations pertinent to the rheology of the continental lithosphere and the localization of strain along shear zones. *Tectonophysics*, 119(1-4):1–27, 1985. 67

F. Klingelhoefer, M. Evain, A. Afilhado, C. Rigoti, A. Loureiro, D. Alves, A. Leprêtre, M. Moulin, P. Schnurle, M. Benabdellouahed, et al. Imaging proto-oceanic crust off the brazilian continental margin. *Geophysical Journal International*, 200(1):471–488, 2014. 7

J. Korenaga. Mantle mixing and continental breakup magmatism. *Earth and Planetary Science Letters*, 218(3-4):463–473, 2004. 3

J. Korenaga. How does small-scale convection manifest in surface heat flux? *Earth and Planetary Science Letters*, 287(3-4):329–332, 2009. 84

J. Korenaga and T. H. Jordan. Physics of multiscale convection in earth's mantle: Evolution of sublithospheric convection. *Journal of Geophysical Research: Solid Earth*, 109(B1), 2004. 72

J. Korenaga and P. B. Kelemen. Major element heterogeneity in the mantle source of the north atlantic igneous province. *Earth and Planetary Science Letters*, 184(1):251–268, 2000. 3

N. Kumar, A. Danforth, P. Nuttall, J. Helwig, D. Bird, and S. Venkatraman. From oceanic crust to exhumed mantle: a 40 year (1970–2010) perspective on the nature of crust under the santos basin, se brazil. *Geological Society, London, Special Publications*, 369(1):147–165, 2013. 190, 191, 192, 193, 194

N. Kusznir and R. Park. The extensional strength of the continental lithosphere: its dependence on geothermal gradient, and crustal composition and thickness. *Geological Society, London, Special Publications*, 28(1):35–52, 1987. 3, 196

N. Kusznir, R. Hunsdale, A. Roberts, et al. Timing and magnitude of depth-dependent lithosphere stretching on the southern lofoten and northern vøring continental margins offshore mid-norway: implications for subsidence and hydrocarbon maturation at volcanic rifted margins. In *Geological Society, London, Petroleum Geology Conference series*, volume 6, pages 767–783. Geological Society of London, 2005. 197

A. Lavecchia, C. Thieulot, F. Beekman, S. Cloetingh, and S. Clark. Lithosphere erosion and continental breakup: Interaction of extension, plume upwelling and melting. *Earth and Planetary Science Letters*, 467:89–98, 2017. 176, 177

L. L. Lavier and W. R. Buck. Half graben versus large-offset low-angle normal fault: Importance of keeping cool during normal faulting. *Journal of Geophysical Research: Solid Earth*, 107 (B6), 2002. 196

L. L. Lavier and G. Manatschal. A mechanism to thin the continental lithosphere at magma-poor margins. *Nature*, 440(7082):324, 2006. 5, 6

L. L. Lavier, W. R. Buck, and A. N. Poliakov. Self-consistent rolling-hinge model for the evolution of large-offset low-angle normal faults. *Geology*, 27(12):1127–1130, 1999. 67

X. Le Pichon. Sea-floor spreading and continental drift. *Journal of Geophysical Research*, 73(12): 3661–3697, 1968. 9

C.-T. A. Lee, P. Luffi, and E. J. Chin. Building and destroying continental mantle. *Annual Review of Earth and Planetary Sciences*, 39:59–90, 2011. 63

P. H. Leloup, Y. Ricard, J. Battaglia, and R. Lacassin. Shear heating in continental strike-slip shear zones: model and field examples. *Geophysical Journal International*, 136(1):19–40, 1999. 78

J. Liao and T. Gerya. From continental rifting to seafloor spreading: insight from 3d thermo-mechanical modeling. *Gondwana Research*, 28(4):1329–1343, 2015. 173

J. Liao, T. Gerya, and Q. Wang. Layered structure of the lithospheric mantle changes dynamics of craton extension. *Geophysical research letters*, 40(22):5861–5866, 2013. 171

G. Lister, M. Etheridge, and P. Symonds. Detachment faulting and the evolution of passive continental margins. *Geology*, 14(3):246–250, 1986. 4

D. Lizarralde, G. J. Axen, H. E. Brown, J. M. Fletcher, A. González-Fernández, A. J. Harding, W. S. Holbrook, G. M. Kent, P. Paramo, F. Sutherland, et al. Variation in styles of rifting in the gulf of california. *Nature*, 448(7152):466, 2007. 180

G. Lu, B. J. Kaus, and L. Zhao. Thermal localization as a potential mechanism to rift cratons. *Physics of the Earth and Planetary Interiors*, 186(3):125–137, 2011. 51, 77

F. Maccaferri, M. Bonafede, and E. Rivalta. A numerical model of dyke propagation in layered elastic media. *Geophysical Journal International*, 180(3):1107–1123, 2010. 177

G. Mackenzie, H. Thybo, and P. Maguire. Crustal velocity structure across the main ethiopian rift: results from two-dimensional wide-angle seismic modelling. *Geophysical Journal International*, 162(3):994–1006, 2005. 8

J. Maclennan, T. Hulme, and S. C. Singh. Cooling of the lower oceanic crust. *Geology*, 33(5): 357–366, 2005. 8

L. E. Malvern. *Introduction to the Mechanics of a Continuous Medium*. Number Monograph. 1969. 67

G. Manatschal. New models for evolution of magma-poor rifted margins based on a review of data and concepts from west iberia and the alps. *International Journal of Earth Sciences*, 93(3): 432–466, 2004. 5, 176

G. Manatschal, L. Lavier, and P. Chenin. The role of inheritance in structuring hyperextended rift systems: Some considerations based on observations and numerical modeling. *Gondwana Research*, 27(1):140–164, 2015. 174

L. Mathieu, B. V. W. De Vries, E. P. Holohan, and V. R. Troll. Dykes, cups, saucers and sills: Analogue experiments on magma intrusion into brittle rocks. *Earth and Planetary Science Letters*, 271(1-4):1–13, 2008. 8

K. G. McDermott. *Mechanisms and recognition of hyper-extension at magma-poor rifted margins*. PhD thesis, University of Birmingham, 2013. 3

D. McKenzie. Some remarks on the development of sedimentary basins. *Earth and Planetary science letters*, 40(1):25–32, 1978. 4

D. McKenzie. The generation and compaction of partially molten rock. *Journal of Petrology*, 25 (3):713–765, 1984. 7

D. McKenzie, J. Jackson, and K. Priestley. Thermal structure of oceanic and continental lithosphere. *Earth and Planetary Science Letters*, 233(3-4):337–349, 2005. 186

D. P. McKenzie and R. L. Parker. The north pacific: an example of tectonics on a sphere. *Nature*, 216(5122):1276, 1967. 9

S. Mei, A. Suzuki, D. Kohlstedt, N. Dixon, and W. Durham. Experimental constraints on the strength of the lithospheric mantle. *Journal of Geophysical Research: Solid Earth*, 115(B8), 2010. 173

T. Menand. Physical controls and depth of emplacement of igneous bodies: A review. *Tectonophysics*, 500(1-4):11–19, 2011. 8

M. A. Menzies. *Volcanic rifted margins*, volume 362. Geological Society of America, 2002. 176

T. Minshull, S. Dean, R. White, and R. Whitmarsh. Anomalous melt production after continental break-up in the southern iberia abyssal plain. *Geological Society, London, Special Publications*, 187(1):537–550, 2001. 3

T. A. Minshull. Geophysical characterisation of the ocean–continent transition at magma-poor rifted margins. *Comptes Rendus Geoscience*, 341(5):382–393, 2009. 199

G. Mohn, G. Manatschal, M. Beltrando, E. Masini, and N. Kusznir. Necking of continental crust in magma-poor rifted margins: Evidence from the fossil alpine tethys margins. *Tectonics*, 31 (1), 2012. 5

L. Moresi, F. Dufour, and H.-B. Mühlhaus. A lagrangian integration point finite element method for large deformation modeling of viscoelastic geomaterials. *Journal of Computational Physics*, 184(2):476–497, 2003. 21

L. Moresi, H.-B. Mühlhaus, V. Lemiale, and D. May. Incompressible viscous formulations for deformation and yielding of the lithosphere. *Geological Society, London, Special Publications*, 282(1):457–472, 2007. 67, 175

J. P. Morgan. The generation of a compositional lithosphere by mid-ocean ridge melting and its effect on subsequent off-axis hotspot upwelling and melting. *Earth and Planetary Science Letters*, 146(1-2):213–232, 1997. 54, 63

W. J. Morgan. Rises, trenches, great faults, and crustal blocks. *Journal of Geophysical Research*, 73(6):1959–1982, 1968. 9

O. Müntener and G. Manatschal. High degrees of melt extraction recorded by spinel harzburgite of the newfoundland margin: The role of inheritance and consequences for the evolution of the southern north atlantic. *Earth and Planetary Science Letters*, 252(3):437–452, 2006. 3

O. Müntener, J. Hermann, and V. Trommsdorff. Cooling history and exhumation of lower-crustal granulite and upper mantle (malenco, eastern central alps). *Journal of Petrology*, 41(2):175–200, 2000. 9

J. C. Mutter, W. R. Buck, and C. M. Zehnder. Convective partial melting: 1. a model for the formation of thick basaltic sequences during the initiation of spreading. *Journal of Geophysical Research: Solid Earth*, 93(B2):1031–1048, 1988. 1, 3

J. Naliboff and S. J. Buiter. Rift reactivation and migration during multiphase extension. *Earth and Planetary Science Letters*, 421:58–67, 2015. 68, 72, 171, 175

J. B. Naliboff, S. J. Buiter, G. Péron-Pinvidic, P. T. Osmundsen, and J. Tetreault. Complex fault interaction controls continental rifting. *Nature communications*, 8(1):1179, 2017. 171

M. Nemčok. *Rifts and passive margins: Structural architecture, thermal regimes, and petroleum systems*. Cambridge University Press, 2016. 66, 67

M. Nemčok, S. Sinha, C. Stuart, C. Welker, M. Choudhuri, S. Sharma, A. Misra, N. Sinha, and S. Venkatraman. East indian margin evolution and crustal architecture: integration of deep reflection seismic interpretation and gravity modelling. *Geological Society, London, Special Publications*, 369(1):477–496, 2013. 5

T. K. Nielsen and J. R. Hopper. From rift to drift: Mantle melting during continental breakup. *Geochemistry, Geophysics, Geosystems*, 5(7), 2004. 8, 53

J.-A. Olive, M. D. Behn, E. Mittelstaedt, G. Ito, and B. Z. Klein. The role of elasticity in simulating long-term tectonic extension. *Geophysical Journal International*, 205(2):728–743, 2016. 185

S. Oller. *Nonlinear dynamics of structures*. Springer, 2014. 22

C. Pagli, F. Mazzarini, D. Keir, E. Rivalta, and T. O. Rooney. Introduction: Anatomy of rifting: Tectonics and magmatism in continental rifts, oceanic spreading centers, and transforms. *Geosphere*, 11(5):1256–1261, 2015. 177

M. Pérez-Gussinyé. A tectonic model for hyperextension at magma-poor rifted margins: an example from the west iberia–newfoundland conjugate margins. *Geological Society, London, Special Publications*, 369(1):403–427, 2013. 3

M. Pérez-Gussinyé and T. J. Reston. Rheological evolution during extension at nonvolcanic rifted margins: onset of serpentinization and development of detachments leading to continental breakup. *Journal of Geophysical Research: Solid Earth*, 106(B3):3961–3975, 2001. 8, 9, 43

M. Pérez-Gussinyé, J. P. Morgan, T. J. Reston, and C. R. Ranero. The rift to drift transition at non-volcanic margins: Insights from numerical modelling. *Earth and Planetary Science Letters*, 244(1-2):458–473, 2006. 3, 43, 186, 187, 195

G. Péron-Pinvidic and G. Manatschal. The final rifting evolution at deep magma-poor passive margins from iberia-newfoundland: a new point of view. *International Journal of Earth Sciences*, 98(7):1581–1597, 2009. 5

G. Peron-Pinvidic, G. Manatschal, and P. T. Osmundsen. Structural comparison of archetypal atlantic rifted margins: A review of observations and concepts. *Marine and Petroleum Geology*, 43:21–47, 2013. 5

G. Péron-Pinvidic, G. Manatschal, E. Masini, E. Sutra, J. M. Flament, I. Haupert, and P. Unternehr. Unravelling the along-strike variability of the angola–gabon rifted margin: a mapping approach. *Geological Society, London, Special Publications*, 438(1):49–76, 2017. 5

K. D. Petersen, J. Armitage, S. Nielsen, and H. Thybo. Mantle temperature as a control on the time scale of thermal evolution of extensional basins. *Earth and Planetary Science Letters*, 409: 61–70, 2015. 171

J. Phipps Morgan. Thermodynamics of pressure release melting of a veined plum pudding mantle. *Geochemistry, Geophysics, Geosystems*, 2(4), 2001. 29, 30

S. Pickup, R. Whitmarsh, C. Fowler, and T. Reston. Insight into the nature of the ocean-continent transition off west iberia from a deep multichannel seismic reflection profile. *Geology*, 24(12): 1079–1082, 1996. 6

J. Platt and W. Behr. Grainsize evolution in ductile shear zones: Implications for strain localization and the strength of the lithosphere. *Journal of Structural Geology*, 33(4):537–550, 2011. 64

M. Prada, V. Sallares, C. R. Ranero, M. Vendrell, I. Grevemeyer, N. Zitellini, and R. Franco. Seismic structure of the central tyrrhenian basin: Geophysical constraints on the nature of the main crustal domains. *Journal of Geophysical Research: Solid Earth*, 119(1):52–70, 2014. 6

J. Précigout and F. Gueydan. Mantle weakening and strain localization: Implications for the long-term strength of the continental lithosphere. *Geology*, 37(2):147–150, 2009. 65

G. Ranalli. *Rheology of the Earth*. Springer Science & Business Media, 1995. 14, 19, 20, 22, 23

G. Ranalli and D. C. Murphy. Rheological stratification of the lithosphere. *Tectonophysics*, 132 (4):281–295, 1987. 18, 208

C. R. Ranero and M. Pérez-Gussinyé. Sequential faulting explains the asymmetry and extension discrepancy of conjugate margins. *Nature*, 468(7321):294, 2010. 6

K. Regenauer-Lieb, R. F. Weinberg, and G. Rosenbaum. The effect of energy feedbacks on continental strength. *Nature*, 442(7098):67, 2006. 64, 77

I. Reid and H. Jackson. Oceanic spreading rate and crustal thickness. *Marine Geophysical Researches*, 5(2):165–172, 1981. 8, 29

T. Reston. The structure, evolution and symmetry of the magma-poor rifted margins of the north and central atlantic: a synthesis. *Tectonophysics*, 468(1-4):6–27, 2009a. 1, 2, 186, 197

T. Reston and G. Manatschal. Rifted margins: Building blocks of later collision. In *Arc-Continent Collision*, pages 3–21. Springer, 2011. 2, 187

T. J. Reston. The extension discrepancy and syn-rift subsidence deficit at rifted margins. *Petroleum Geoscience*, 15(3):217–237, 2009b. 3, 4, 7

T. J. Reston and J. P. Morgan. Continental geotherm and the evolution of rifted margins. *Geology*, 32(2):133–136, 2004. 3

E. Ros, M. Pérez-Gussinyé, M. Araújo, M. Thoaldo Romeiro, M. Andrés-Martínez, and J. P. Morgan. Lower crustal strength controls on melting and serpentinization at magma-poor margins: Potential implications for the south atlantic. *Geochemistry, Geophysics, Geosystems*, 2017. 70, 175, 181, 182, 183, 185, 186, 187, 188, 189, 190, 191, 192, 193, 194

L. Rüpke, J. Phipps Morgan, and J. Eaby Dixon. Implications of subduction rehydration for earth's deep water cycle. *Earth's Deep Water Cycle*, pages 263–276, 2006. 54, 62

L. H. Rüpke and J. Hasenclever. Global rates of mantle serpentinization and h2 production at oceanic transform faults in 3-d geodynamic models. *Geophysical Research Letters*, 44(13): 6726–6734, 2017. 180

L. H. Rüpke, D. W. Schmid, M. Perez-Gussinye, and E. Hartz. Interrelation between rifting, faulting, sedimentation, and mantle serpentinization during continental margin formation—including examples from the norwegian sea. *Geochemistry, Geophysics, Geosystems*, 14(10):4351–4369, 2013. 8, 43, 179

C. Ruppel. Extensional processes in continental lithosphere. *Journal of Geophysical Research: Solid Earth*, 100(B12):24187–24215, 1995. 51

S. Russell and R. Whitmarsh. Magmatism at the west iberia non-volcanic rifted continental margin: evidence from analyses of magnetic anomalies. *Geophysical Journal International*, 154(3):706–730, 2003. 6

E. Rybacki and G. Dresen. Dislocation and diffusion creep of synthetic anorthite aggregates. *Journal of Geophysical Research: Solid Earth*, 105(B11):26017–26036, 2000. 50, 208

D. S. Sawyer, M. F. Coffin, T. J. Reston, J. M. Stock, and J. R. Hopper. Cobboom: the continental breakup and birth of oceans mission. *Scientific Drilling*, 5:13–25, 2007. 1, 7

H. Schmeling. A model of episodic melt extraction for plumes. *Journal of Geophysical Research: Solid Earth*, 111(B3), 2006. 187

H. Schmeling. Dynamic models of continental rifting with melt generation. *Tectonophysics*, 480 (1-4):33–47, 2010. 176

C. Scholz and P. A. Cowie. Determination of total strain from faulting using slip measurements. *Nature*, 346(6287):837–839, 1990. 67

G. Schubert. *Treatise on geophysics*. Elsevier, 2015. 52

A. Sengör and K. Burke. Relative timing of rifting and volcanism on earth and its tectonic implications. *Geophysical Research Letters*, 5(6):419–421, 1978. 1

W. Sharples, L.-N. Moresi, M. Jadamec, and J. Revote. Styles of rifting and fault spacing in numerical models of crustal extension. *Journal of Geophysical Research: Solid Earth*, 120(6): 4379–4404, 2015. 6

J. R. Shewchuk. Triangle: Engineering a 2d quality mesh generator and delaunay triangulator. In *Applied computational geometry towards geometric engineering*, pages 203–222. Springer, 1996. 25, 27

R. H. Sibson. Conditions for fault-valve behaviour. *Geological Society, London, Special Publications*, 54(1):15–28, 1990. 67

K. Simon, R. S. Huismans, and C. Beaumont. Dynamical modelling of lithospheric extension and small-scale convection: implications for magmatism during the formation of volcanic rifted margins. *Geophysical Journal International*, 176(1):327–350, 2009. 176

A. Skelton, R. Whitmarsh, F. Arghe, P. Crill, and H. Koyi. Constraining the rate and extent of mantle serpentinization from seismic and petrological data: implications for chemosynthesis and tectonic processes. *Geofluids*, 5(3):153–164, 2005. 8

C. Sotin and E. Parmentier. Dynamical consequences of compositional and thermal density stratification beneath spreading centers. *Geophysical Research Letters*, 16(8):835–838, 1989. 32

D. W. Sparks, E. Parmentier, and J. P. Morgan. Three-dimensional mantle convection beneath a segmented spreading center: Implications for along-axis variations in crustal thickness and gravity. *Journal of Geophysical Research: Solid Earth*, 98(B12):21977–21995, 1993. 29

K. Stüwe. *Geodynamics of the lithosphere: an introduction*. Springer Science & Business Media, 2007. 18

A. E. Svartman Dias, L. L. Lavier, and N. W. Hayman. Conjugate rifted margins width and asymmetry: The interplay between lithospheric strength and thermomechanical processes. *Journal of Geophysical Research: Solid Earth*, 120(12):8672–8700, 2015a. 6, 51, 72, 175, 181, 182, 183, 185, 195, 197

A. E. Svartman Dias, N. W. Hayman, and L. L. Lavier. Thinning factor distributions viewed through numerical models of continental extension. *Tectonics*, 35(12):3050–3069, 2016. 180, 197

A. E. Svartman Dias et al. *The evolution of hyperextended rifted margins: linking variations on the width, asymmetry, and strain distribution to lithospheric strength and geodynamic processes*. PhD thesis, 2015b. 193

R. Tejero and J. Ruiz. Thermal and mechanical structure of the central iberian peninsula lithosphere. *Tectonophysics*, 350(1):49–62, 2002. 208

M. Tesauro, E. B. Burov, M. K. Kaban, and S. A. Cloetingh. Ductile crustal flow in europe's lithosphere. *Earth and Planetary Science Letters*, 312(1-2):254–265, 2011. 208

J. Tetreault and S. Buiter. The influence of extension rate and crustal rheology on the evolution of passive margins from rifting to break-up. *Tectonophysics*, 2017. 6, 175, 180, 181, 183, 184, 185, 197

H. Thybo and I. M. Artemieva. Moho and magmatic underplating in continental lithosphere. *Tectonophysics*, 609:605–619, 2013. 8, 34

C. Tirel, J.-P. Brun, and E. Burov. Dynamics and structural development of metamorphic core complexes. *Journal of Geophysical Research: Solid Earth*, 113(B4), 2008. 196

M. J. Tischer. *The structure and development of the continent-ocean transition zone of the Exmouth Plateau and Cuvier margin, Northwest Australia: implications for extensional strain partitioning*. 2006. 7

A. Tommasi, D. Mainprice, G. Canova, and Y. Chastel. Viscoplastic self-consistent and equilibrium-based modeling of olivine lattice preferred orientations: Implications for the upper mantle seismic anisotropy. *Journal of Geophysical Research: Solid Earth*, 105(B4):7893–7908, 2000. 64

B. E. Tucholke, J. Austin, E. Uchupi, A. Tankard, and H. Balkwill. Crustal structure and rift-drift evolution of the newfoundland basin. *Extensional tectonics and stratigraphy of the North Atlantic Margins*, 46:247–263, 1989. 6

D. Turcotte and G. Schubert. *Geodynamics (2nd)*. Cambridge University Press, Cambridge, 2002. 50

D. Turcotte and G. Schubert. *Geodynamics*. Cambridge University Press, 2014. 39

P. Unternehr, G. Péron-Pinvidic, G. Manatschal, and E. Sutra. Hyper-extended crust in the south atlantic: in search of a model. 2010. 5

H. J. Van Avendonk, W. S. Holbrook, G. T. Nunes, D. J. Shillington, B. E. Tucholke, K. E. Louden, H. C. Larsen, and J. R. Hopper. Seismic velocity structure of the rifted margin of the eastern grand banks of newfoundland, canada. *Journal of Geophysical Research: Solid Earth*, 111 (B11), 2006. 3

H. J. Van Avendonk, L. L. Lavier, D. J. Shillington, and G. Manatschal. Extension of continental crust at the margin of the eastern grand banks, newfoundland. *Tectonophysics*, 468(1):131–148, 2009. 68

B. A. Van der Pluijm and S. Marshak. Earth structure. *Physics of the Earth and Planetary Interiors*, 149:133–153, 2005. 15, 72

J. Van Wijk and S. Cloetingh. Basin migration caused by slow lithospheric extension. *Earth and Planetary Science Letters*, 198(3-4):275–288, 2002. 171

P. A. Vermeer and R. De Borst. Non-associated plasticity for soils, concrete and rock. *HERON, 29 (3), 1984*, 1984. 22

M. Wangen. *Physical principles of sedimentary basin analysis*. Cambridge University Press, 2010. 39

J. M. Warren and E. H. Hauri. Pyroxenes as tracers of mantle water variations. *Journal of Geophysical Research: Solid Earth*, 119(3):1851–1881, 2014. 62

B. Wernicke. Low-angle normal faults in the basin and range province: nappe tectonics in an extending orogen. *Nature*, 291(5817):645, 1981. 4

B. Wernicke. Uniform-sense normal simple shear of the continental lithosphere. *Canadian Journal of Earth Sciences*, 22(1):108–125, 1985. 4

N. White, M. Thompson, and T. Barwise. Understanding the thermal evolution of deep-water continental margins. *Nature*, 426(6964):334, 2003. 3

R. White, J. Bown, and J. Smallwood. The temperature of the iceland plume and origin of outward-propagating v-shaped ridges. *Journal of the Geological Society*, 152(6):1039–1045, 1995. 7

R. White, T. Minshull, M. Bickle, and C. Robinson. Melt generation at very slow-spreading oceanic ridges: Constraints from geochemical and geophysical data. *Journal of Petrology*, 42 (6):1171–1196, 2001. 8, 9

S. White, S. Burrows, J. Carreras, N. Shaw, and F. Humphreys. On mylonites in ductile shear zones. *Journal of Structural Geology*, 2(1-2):175–187, 1980. 51

R. Whitmarsh, G. Manatschal, and T. Minshull. Evolution of magma-poor continental margins from rifting to seafloor spreading. *Nature*, 413(6852):150, 2001. 5

J. v. Wijk, R. Huismans, M. Ter Voorde, and S. Cloetingh. Melt generation at volcanic continental margins: no need for a mantle plume? *Geophysical Research Letters*, 28(20):3995–3998, 2001. 2

C. Wijns, R. Weinberg, K. Gessner, and L. Moresi. Mode of crustal extension determined by rheological layering. *Earth and Planetary Science Letters*, 236(1-2):120–134, 2005. 6

K. R. Wilks and N. L. Carter. Rheology of some continental lower crustal rocks. *Tectonophysics*, 182(1-2):57–77, 1990. 50, 208

J. T. Wilson et al. Did the atlantic close and then re-open? 1966. 3, 9

P. V. Zalán, M. d. C. G. Severino, C. A. Rigoti, L. P. Magnavita, J. A. B. Oliveira, and A. R. Vianna. An entirely new 3d-view of the crustal and mantle structure of a south atlantic passive margin–santos, campos and espírito santo basins, brazil. In *AAPG annual conference and Exhibition*, pages 10–13, 2011. 5, 7, 190, 191, 192, 193, 194

C. A. Zelt, K. Sain, J. V. Naumenko, and D. S. Sawyer. Assessment of crustal velocity models using seismic refraction and reflection tomography. *Geophysical Journal International*, 153(3): 609–626, 2003. 3

P. A. Ziegler and S. Cloetingh. Dynamic processes controlling evolution of rifted basins. *Earth-Science Reviews*, 64(1-2):1–50, 2004. 173

F. Zwaan and G. Schreurs. How oblique extension and structural inheritance influence rift segment interaction: Insights from 4d analog models. *Interpretation*, 5(1):SD119–SD138, 2017. 173